

Alloy Catalysis across Composition Space

Submitted in partial fulfillment of the requirements for

the degree of

Doctor of Philosophy

in

Chemical Engineering

Irem Sen

B.S., Chemical Engineering, Bogazici University

M.S., Chemical Engineering, Bogazici University

Carnegie Mellon University
Pittsburgh, PA

December, 2017

© Copyright by Irem Sen 2017

All Rights Reserved

Acknowledgements

The past four and a half years would not have been meaningful without the help and support of many people. First of all, I would like to express my gratitude to my supervisor Andrew J. Gellman. Without his persistent help and encouragement, writing this thesis would not have been possible. I am grateful to have a chance to work with Jim Miller even for a short amount of time, he has been a constant source of help and guidance. I would also like to thank my thesis committee, Andrew J. Gellman (chair), Professor John Kitchin, Professor Gregory S. Rohrer, and Professor Neil Donahue for devoting their valuable time to comment on my research.

I want to thank everybody in DH 1202, my every day in the office would not be as enjoyable as it was without them. First of all, I want to thank Dr. Gamze Gumuslu for always being here for me during my graduate life. I have learned almost everything from her, she has been a great mentor and amazing friend. I have had no doubt of following her footsteps. I want to thank Dr. Petro Kondratyuk for his endless patience to my never-ending questions. It was a great privilege for me to share a working environment with such a valuable scientist. I was very lucky to be surrounded by great people like Xiaoxia Yu, Burcu Karagoz, Soham Dutta, Sasimas Katanyutanon, Nicholas Golio, Daniel Lee and Michael Radetic in Surface Science Group.

I also want to thank Janet Latini, Julie Tilton, Cynthia Vicker, Larry Hayhurst and Heather Depasquale for their help and support.

I would like to express my inexpressible gratitude to Dr. Harun Ferit Ozbakir for always being there for me during all the ups and downs of my life. I could not have come this far without his irreplaceable friendship. Also, Dr. Beyza Bulutoglu, we have had amazing adventures together. Her joy, endless support, and invaluable friendship always made me feel stronger. Harun and

Beyza provided me a second home in NYC full of laughter which always made me feel safe and loved.

Pittsburgh has given me so many great memories and great friends. First, I would like to thank Cihan Kaya. I have never felt alone here thanks to you. Burcu Beykal, thank you for becoming a sister to me. Thank you for always believing in me and supporting me no matter what. Burcu Karagoz, thank you for taking care of me in the office, in the lab or at home. I am grateful for all the memories we share. Gizem Ozbuyukkaya and Volkan Cirik, thank you for all the joyful moments. Irem Velibeyoglu and Onur Kibar, I am really glad to have you in my life, cheers to all the emergency ice cream runs with you.

I would like to thank all the amazing people in our department for making my every day a beautiful memory. Alex Bertuccio, Brittany Nordmark, Justin Weinberg, Rebecca Ball, Toni Bechtel, Blake Bleier, Travis Armiger, Sarah Guyer, Yuan Chen, Anirudth Subramanyam, Zack Wilson, Jacob Boes, Javier Lanauze, Nikos Lappas, John Michael, John Eason, Benjamin Sauk, Braulio Brunaud, Charles Sharkey, Chris Hanselman, Cristiana Lara, Dana McGuffin, Khalid Hajj, Nick Lamson, Qin Qu, Yun-Ru Huang, Steven Iasella and many more.

I am very lucky to have so many strong women in my life with whom I am proud to stand together. I cannot express how grateful I feel to have you in my life, Sevinc Genc, Seda Kizir, Merve Aygun, Selin Sezen, Nihan Unal, Begum Alaybeyoglu, Pinar Karatay and Deniz Kopru.

Last but not least I want to thank my family. I have been thousands of miles away from them for more than four years but I have always felt them near me. I am grateful to my father Recep Sen, who believed in me since my childhood. If I am about to finish my Ph.D., it is all thanks to him. Thank you, father, for devoting your life to us and for countless days that you followed me to school. I want to thank my mother, Ayfer Sen, for her endless love and patience,

for sending me those lovely messages every day. She is one of the strongest, kindest, warmest person I have ever known. Thank you for making our lives full of joy every second. And special thanks to my brother, Sait Can Sen. Always having a playmate is one the best privileges I have ever had, thank you for making me smile in any circumstances and thank you for making me feel blessed every second to have you by my side. I also appreciate the moral support and friendship of my dearest aunt Sadiye Sen, thank you for always taking care of our family.

Last but not least I would like to acknowledge the Department of Chemical Engineering at Carnegie Mellon University and National Science Foundation Grant No. CHE1566228, and Bertucci Graduate Fellowship for funding my research. Any opinions, findings, and conclusions or recommendations expressed in this thesis are those of the author(s) and do not necessarily reflect the views of the National Science Foundation.

Abstract

Alloys of transition metals often possess superior catalytic properties than their pure components. Finding new alloy catalysts with predictable and desirable catalytic properties is the major challenge in multicomponent catalyst design due to the need to perform many catalyst preparations, characterizations and reactivity measurements across composition space. To accelerate this search Composition Spread Alloy Films (CSAFs), thin multicomponent films that have composition gradients parallel to their surfaces, $A_xB_yC_{1-x-y}$ with $x = 0 \rightarrow 1$ and $y = 0 \rightarrow 1-x$, are prepared. Many otherwise intractable fundamental scientific problems in alloy science and catalysis can be effectively addressed through the use of CSAFs as high throughput materials libraries. High throughput characterization of composition and electronic structure of these CSAFs can be done using spatially resolved X-ray photoelectron spectroscopy (XPS). Coupling these techniques with a multichannel microreactor, we can sample product distributions from 100 different alloy catalysts across a CSAF in about 10 minutes.

We focused on Ag_xPd_{1-x} CSAFs and we investigated H_2 - D_2 exchange reaction across these libraries using our multichannel microreactor. We investigated the energetics of this reaction using a microkinetic model and successfully came up with a correlation between the catalytic activity, the composition of the alloy and the electronic structure of the alloy. For the next step, the same H_2 - D_2 exchange reaction was investigated experimentally across a $Cu_xAu_yPd_{1-x-y}$ composition space. Increasing Pd content was found to decrease adsorption barriers and to increase desorption barriers. The v -band center moves toward the Fermi level as Pd content increases and the barrier to dissociative adsorption of H_2 was found to decrease as the v -band energy increases. This data provides the first experimental correlation of elementary reaction barriers with valence band

energy across a continuous span of alloy composition space. We also tested our methodology for a more complex reaction, ethylene hydrogenation. Catalytic activity - composition of the alloy - electronic structure of the alloy correlation has been obtained across a continuous composition space of $\text{Cu}_x\text{Au}_y\text{Pd}_{1-x-y}$. This study is the first work to show this correlation experimentally.

All in all, in this study we have come up with a new methodology that can be applied to alloy catalysis studies. Using this methodology 100 different alloy compositions can be tested in one experiment which accelerates the search for a proper catalyst for a given application as well as provides a fundamental understanding of multicomponent materials.

Table of Contents

Acknowledgements	iii
Abstract	vi
List of Tables	xii
List of Figures	xiii
Chapter 1. Introduction	1
1.1 Summary	1
1.2 High throughput techniques	2
1.3 Hydrogen Separation by palladium based alloys	7
1.4 Ethylene hydrogenation	10
1.5 Scope of the thesis	15
1.6 References	16
Chapter 2. Experimental and Analytical Techniques	21
2.1 Summary	21
2.2 Experimental techniques	21
2.2.1 Composition spread alloy films (CSAFs)	21
2.2.1.1 CSAF deposition methods	23
2.2.1.2 Rotatable shadow mask deposition tool	24
2.2.2 Multichannel microreactor system	26
2.2.2.1 Design of the microreactor	27
2.2.2.2 Fabrication of the microreactor	29
2.2.2.3 Reactant gas delivery and product gas analysis	35

2.3 Analytical techniques	38
2.3.1 X-ray photoelectron spectroscopy	38
2.4 References	41
Chapter 3. Characterization of Composition, Electronic Structure and H ₂ -D ₂ Exchange Activity across Ag _x Pd _{1-x} Alloys	45
3.1 Chapter abstract	45
3.2 Introduction	46
3.3 Experimental	49
3.3.1 CSAF preparation	49
3.3.2 Characterization of CSAF composition and electronic structure	50
3.3.3 Characterization of H ₂ -D ₂ exchange activity across Ag _x Pd _{1-x} CSAF	51
3.4 Microkinetic model	53
3.5 Results and discussion	59
3.5.1 Characterization of CSAF composition	59
3.5.2 Characterization of CSAF electronic structure	60
3.5.3 H ₂ -D ₂ exchange on the Ag _x Pd _{1-x} CSAF	63
3.5.4 Kinetic parameters for H ₂ -D ₂ exchange on Ag _x Pd _{1-x}	68
3.5.5 Reaction rate for H ₂ -D ₂ exchange on Ag _x Pd _{1-x}	72
3.5.6 Correlation of activity and structure across composition space	76
3.6 Conclusions	78
3.7 Appendix: HD flow rate versus temperature across Ag _x Pd _{1-x} composition space	79
3.8 References	81

Chapter 4. Characterization of Composition, Electronic Structure and	
H ₂ -D ₂ Exchange Activity across Cu _x Au _y Pd _{1-x-y} Alloys	87
4.1 Chapter abstract	87
4.2 Introduction	88
4.3 Experimental	91
4.3.1 CSAF preparation	91
4.3.2 Characterization of CSAF composition and electronic structure	91
4.3.3 Characterization of CSAF H ₂ -D ₂ exchange activity	
across Cu _x Au _y Pd _{1-x-y} CSAF	92
4.4 Results and discussion	95
4.4.1 Performance of the microreactor	95
4.4.2 Characterization of CSAF composition	97
4.4.3 Characterization of CSAF electronic structure	99
4.4.4 H ₂ -D ₂ exchange on the Cu _x Au _y Pd _{1-x-y} CSAF	103
4.4.5 Kinetic parameters for H ₂ -D ₂ exchange on the Cu _x Au _y Pd _{1-x-y} CSAF	110
4.4.6 Reaction rate analysis of H ₂ -D ₂ exchange on Cu _x Au _y Pd _{1-x-y} CSAF	113
4.4.7 Correlation of activity and electronic structure across composition space	117
4.5 Conclusions	118
4.6 Appendix: HD flow rate versus temperature across Cu _x Au _y Pd _{1-x-y} CSAF	120
4.7 References	123

Chapter 5. Characterization of Composition, Electronic Structure and Ethylene Hydrogenation Activity across $\text{Cu}_x\text{Au}_y\text{Pd}_{1-x-y}$ Alloys	129
5.1 Chapter abstract	129
5.2 Introduction	131
5.3 Experimental	134
5.3.1 CSAF preparation	134
5.3.2 Characterization of CSAF composition and electronic structure	135
5.3.3 Characterization of C_2H_4 hydrogenation activity across $\text{Cu}_x\text{Au}_y\text{Pd}_{1-x-y}$ CSAF	135
5.4 Microkinetic model	138
5.5 Results and discussion	143
5.5.1 Characterization of CSAF composition	143
5.5.2 Characterization of CSAF electronic structure	145
5.5.3 C_2H_4 hydrogenation on $\text{Cu}_x\text{Au}_y\text{Pd}_{1-x-y}$ CSAF	146
5.5.4 Kinetic parameters for C_2H_4 hydrogenation on $\text{Cu}_x\text{Au}_y\text{Pd}_{1-x-y}$ CSAF	154
5.5.5 Correlation of activity and electronic structure across composition space	159
5.6 Conclusions	161
5.7 Appendix: Correlation of activity and electronic structure across composition space	162
5.7 References	163
Chapter 6. General Conclusions	168

List of Tables

Table 3. 1. Flow rates of H ₂ ($F_{\text{H}_2}^{\text{in}}$), D ₂ ($F_{\text{D}_2}^{\text{in}}$), and Ar ($F_{\text{Ar}}^{\text{in}}$) in the fourteen different gas conditions used during H ₂ -D ₂ exchange experiments at $P_{\text{tot}} = 1$ atm. Flow rates in one channel can be found by dividing the listed values into 100. Total flow rate is kept constant at 0.33 mL/min per channel.	51
Table 3.2. Experimental and theoretical reaction orders for different inlet conditions.	73
Table 4.1. Flow rates of H ₂ ($F_{\text{H}_2}^{\text{in}}$), D ₂ ($F_{\text{D}_2}^{\text{in}}$), and Ar ($F_{\text{Ar}}^{\text{in}}$) for the eleven different gas conditions used during H ₂ -D ₂ exchange experiments at $P_{\text{tot}} = 1$ atm. Flow rates in one channel can be found by dividing the listed values into 102. The total flow rate is kept constant at 0.15 mL/min per channel.	92
Table 4.2. Experimental and theoretical reaction orders for different inlet conditions.	115
Table 5. 1. Flow rates of H ₂ ($F_{\text{H}_2}^{\text{in}}$), C ₂ H ₄ ($F_{\text{C}_2\text{H}_4}^{\text{in}}$), and Ar ($F_{\text{Ar}}^{\text{in}}$) in the eleven different gas conditions used during C ₂ H ₄ hydrogenation experiments at $P_{\text{tot}} = 1$ atm. Flow rates in one channel can be found by dividing the listed values into 100. Total flow rate is kept constant at 0.1 mL/min per channel.	136

List of Figures

- Figure 1.1. a) Schematic representation of a CSAF with regions containing the entire ternary alloy composition space, $A_xB_yC_{1-x-y}$ ($x = 0 \rightarrow 1, y = 0 \rightarrow 1 - x$), all three binary alloys A_xB_{1-x} , A_xC_{1-x} , and B_xC_{1-x} ($x = 0 \rightarrow 1$) and all three pure components (A, B, and C). b) Photograph of the multichannel microreactor array built in our laboratory that allows characterization of reactivity at 100 discrete locations (100 different alloy compositions) on a CSAF. 2
- Figure 1.2. Comparison of H₂-D₂ exchange activity on five different catalysts. HD flows, out from the fixed bed of catalysts, show that the most active catalyst is FCC Pd₄₇Cu₅₃ and the least active is pure Cu. (The same reaction conditions, surface area and inlet flows. 4
- Figure 1.3. Comparison of H₂-D₂ exchange activity on 100 different Cu_xPd_{1-x} catalysts. H₂ conversions, out from the different locations on the CSAF, show that catalytic activity is increasing as Pd content increases. (The same reaction conditions, surface area and inlet flows. 5
- Figure 1.4. Energy barriers for H₂ adsorption (black) and desorption (red) as a function of Cu composition. Open symbols (blue) represent H₂ adsorption (square) and desorption (round) energy barriers estimated using experimental data from conventional fixed beds of single composition catalysts. These two datasets to be in good agreement is a good example to validate the high throughput methodology. 6
- Figure 1.5. Schematic representation of hydrogen transport through a Pd-based membrane. 9
- Figure 1.6. The Horiuti-Polanyi mechanism for ethylene hydrogenation over metal catalysts. 11
- Figure 1.7. The thermal evolution of adsorbed ethylene on Pt(111). The dehydrogenation proceeds from a) π -bonded ethylene at low temperature through b) di- σ -bonded ethylene to c) ethylidyne. 12
- Figure 1.8. Proposed mechanism for ethylene hydrogenation on Pt (111). 14
- Figure 2.1. Left: Schematic representation of a binary Ag_xPd_{1-x} CSAF. Middle: Schematic representation of a ternary Cu_xAu_yPd_{1-x-y} CSAF. Right: Photograph of a Cu_xAu_yPd_{1-x-y} CSAF. In color, the Cu, Au, and Pd regions are readily identifiable. 22
- Figure 2.2. Schematic representations of four different methods for deposition of composition spread alloy films. a) Chemical vapor deposition sources positioned close to the substrate such that lateral diffusion in the gas phase results in a gradient in flux to the surface from each source. b) Deposition of individual components in wedges using a sliding contact mask. c) Offset positioning of sources to generate nonuniform flux distributions across the substrate surface. d) Simultaneous 23

deposition of multiple components using fixed shadow masks to form the composition gradients.

Figure 2.3. a) Schematic of the operating principle of the rotating shadow mask CSAF deposition tool. b) 3D rendering of the tool. c) Picture of the tool in a UHV chamber. The four-leafed clover is a manually rotatable shutter. The automated, semicircular, rotatable shadow masks can be seen between the clover leaves. 25

Figure 2.4. a) An array of regions isolated by the microreactor across a CSAF. b) Photo of glass reactor arrays. c) An example of spatially resolved catalytic activity measurement for H₂-D₂ exchange reaction across a Cu_xAu_yPd_{1-x-y} ternary CSAF. H₂ conversion was chosen to be the indicator of the catalytic activity. Hence the ternary diagram here shows how catalytic activity changes across the CSAF as a function of Cu, Au and Pd composition. 27

Figure 2.5. The old configuration of the inlet and outlet channels that are micromachined into flat glass sheets. 27

Figure 2.6. The design of the 100-channel microreactor array used to deliver and withdraw gases from the CSAF surface. a) Input and output channels are machined into flat glass sheets. b) 10 input and 10 output layers are alternately bonded together with cover plates. c) The side of the multichannel microreactor array having 100 inlet and outlet channels is ground and polished. This side of the device is mated with a gasket having 100 holes which is then sandwiched between the glass reactor and the CSAF catalyst surface. 28

Figure 2.7. Depth profile of one of the random channels obtained using profilometer. 29

Figure 2.8. a) The stainless steel stand and b) the alignment aid used in the microreactor block preparation. 31

Figure 2.9. The schematic representation of the gluing process for the preparation of quartz capillaries that will be guiding flow to and from the microreactor. 32

Figure 2.10. The photograph of the microreactor after 100 inlet and 100 outlet capillaries are glued into the block and stainless steel inlet flow divider is prepared. 34

Figure 2.11. Illustration of the experimental setup. a) Mass flow controllers. b) A gasket is used in between the CSAF and the microreactor to isolate reaction volumes. A heater is placed on top of the CSAF and a thermocouple is attached to the CSAF substrate. c) Microfluidic reactor and illustration of the outlet channels. d) Automated sampler. A sampling capillary is placed on a robot arm that can move in x and y directions, i.e. capillary can move in and out of a channel and step to the next channel. e) Quadrupole mass spectrometer. 36

Figure 2.12. The optical image of the laser-machined elastomer gasket that is put on top of the microreactor array. The 700 μm × 800 μm rectangular windows in the 38

gasket define 100 reaction areas on the CSAF. In each isolated window a pair of inlet and outlet channel openings can be seen.

Figure 2.13. Schematic representation of X-ray photoemission process. An incident X-ray beam ejects a core level electron from an atom near the surface of the solid sample. The kinetic energy of the ejected photoelectron is related to the binding energy of the electron, which is characteristic of the atom from which the photoelectron originated. The mean free path of photoelectrons is ~ 1 to 10 nm, making XPS a surface-sensitive technique for characterizing the chemical composition in the near surface region of solid samples. 39

Figure 3.1. Pd composition (measured by XPS) versus position on the $\text{Ag}_x\text{Pd}_{1-x}$ binary CSAF. Black dots represent actual measurement points. 59

Figure 3.2. Background subtracted XP spectra of 169 different $\text{Ag}_x\text{Pd}_{1-x}$ compositions across the entire composition space. 61

Figure 3.3. XPS-derived average energy of the filled v -band relative to the Fermi level of $\text{Ag}_x\text{Pd}_{1-x}$ CSAF versus Pd (at. %) compositions. 63

Figure 3.4. HD flow rate versus temperature measured across $\text{Ag}_x\text{Pd}_{1-x}$ composition space. For all $\text{Ag}_x\text{Pd}_{1-x}$ compositions conversion increases with increasing T and decreasing x and y . Flow conditions in one channel are labeled on each figure. ($P_{tot} = 1$ atm) 64

Figure 3.5. H_2 - D_2 exchange conversion vs. T on $\text{Ag}_x\text{Pd}_{1-x}$ alloys for several discrete Ag compositions, x . H_2 conversion is increasing with increasing T and decreasing with Ag composition. Inlet flow was 0.1 mL/min H_2 , 0.1 mL/min D_2 and 0.13 mL/min Ar per channel. 65

Figure 3.6. H_2 - D_2 exchange conversion versus Ag composition at $T = 373$ K, 473 K and 593 K. Inlet flow was 0.1 mL/min H_2 , 0.1 mL/min D_2 and 0.13 mL/min Ar per channel. 66

Figure 3.7. a), b) HD flow rate in the outlet measured for two $\text{Ag}_x\text{Pd}_{1-x}$ alloy compositions ($x = 0.01, 0.36$) vs. T for four different inlet flow conditions. Solid squares are the experimental measurement points and the solid lines are the fits of the microkinetic model to the data. 67

Figure 3.8. Parity plot of the HD flow rates predicted by the microkinetic model vs. experimental measurements. Data are shown for all 90 $\text{Ag}_x\text{Pd}_{1-x}$ compositions ($x = 0 - 0.99$) at 14 different temperatures ($T = 333-593$ K) and 14 inlet flow conditions (Table 3.1). 68

Figure 3.9. Energy barriers for dissociative adsorption of H_2 , $\Delta E_{ads}^\ddagger(x)$, (black) and associative desorption of H_2 , $\Delta E_{des}^\ddagger(x)$, (red) as a function of $\text{Ag}_x\text{Pd}_{1-x}$ composition. 69

Figure 3.10. a) Plot of experimental HD production rate on five different $\text{Ag}_x\text{Pd}_{1-x}$ compositions at 593 K as a function of P_{D_2} with P_{H_2} constant at 30.39 kPa. b) Plot of 72

HD production rate on five different $\text{Ag}_x\text{Pd}_{1-x}$ compositions at 593 K as a function of P_{H_2} with P_{D_2} held constant at 0.03 kPa.

Figure 3.11. a) Total coverage of H and D atoms during H_2 - D_2 exchange reaction over three different $\text{Ag}_x\text{Pd}_{1-x}$ alloy compositions ($x = 0.01, 0.2, 0.37$) as a function of T . The flow contains 9 mL/min H_2 , 0.009 mL/min D_2 and 20.991 mL/min Ar. b) Total coverage of H and D atoms during H_2 - D_2 exchange reaction as a function of T for four different inlet flow compositions. The coverage is calculated using Eq. (8) and the kinetic parameters ν_{ads} , ν_{des} , ΔE_{ads}^\ddagger and ΔE_{des}^\ddagger extracted from the microkinetic model. 74

Figure 3.12. Energy barriers for dissociative adsorption of H_2 , $\Delta E_{ads}^\ddagger(x)$, (black) and associative desorption of H_2 , $\Delta E_{des}^\ddagger(x)$, (red) as a function of the ν -band center measured on 90 $\text{Ag}_x\text{Pd}_{1-x}$ positions. 76

Figure 3.13. HD flow rate versus temperature measured across $\text{Cu}_x\text{Au}_y\text{Pd}_{1-x-y}$ composition space. For all 100 $\text{Cu}_x\text{Au}_y\text{Pd}_{1-x-y}$ compositions conversion increases with increasing T and decreasing x and y . Flow conditions in one channel are labeled on each figure. ($P_{\text{tot}} = 1$ atm) 79

Figure 4.1. The measured gas transit times through each of the 100 microreactor channels. 95

Figure 4.2. In order to test the performance of the multichannel microreactor system in capturing catalytic activity across the CSAFs, H_2 - D_2 exchange across a pure Pd film was investigated. H_2 conversion was chosen to be the indicator of catalytic activity. The graph shows how catalytic activity changes across the Pd film. Uniform activity has been observed across the Pd surface. In the inset, the schematic representation of the H_2 - D_2 exchange reaction is given. 96

Figure 4.3. Photograph of the ternary $\text{Cu}_x\text{Au}_y\text{Pd}_{1-x-y}$ CSAF with an overlaid grid of real-space coordinates across which the XPS measurements are performed. 97

Figure 4.4. Concentration distribution (at. %) obtained with XPS for Cu, Au, and Pd across a $\text{Cu}_x\text{Au}_y\text{Pd}_{1-x-y}$ CSAF. 98

Figure 4.5. a) $\text{Cu}_x\text{Au}_y\text{Pd}_{1-x-y}$ alloy compositions across 14×14 mm² substrate surface (a 13×13 grid with 1 mm spacing). b) $\text{Cu}_x\text{Au}_y\text{Pd}_{1-x-y}$ alloy compositions covered in ternary space. Each of the red dots represents a different alloy composition corresponding to the 100 different microreactor channels. 98

Figure 4.6. Background subtracted XP spectra of 169 different $\text{Cu}_x\text{Au}_y\text{Pd}_{1-x-y}$ compositions across the entire composition space. 99

Figure 4.7. Background subtracted XPS spectra for the three extreme compositions across the $\text{Cu}_x\text{Au}_y\text{Pd}_{1-x-y}$ CSAF. These three compositions represent pure Cu, pure Au and pure Pd. 100

Figure 4.8. XPS-derived average energy of the filled v -band relative to the Fermi level of $\text{Cu}_x\text{Au}_y\text{Pd}_{1-x-y}$ CSAF versus Pd (at. %) compositions.	102
Figure 4.9. HD flow rate in the outlet measured at four different positions across the $\text{Cu}_x\text{Au}_y\text{Pd}_{1-x-y}$ CSAF versus temperature for two successive experiments. The inlet flow rate contains 0.05 mL/min H_2 , 0.05 mL/min D_2 and 0.05 mL/min Ar per channel. The closeness of black and red data points shows that the surface is giving reproducible reactivity.	103
Figure 4.10. HD flow rate versus temperature measured across $\text{Cu}_x\text{Au}_y\text{Pd}_{1-x-y}$ composition space. For all 100 $\text{Cu}_x\text{Au}_y\text{Pd}_{1-x-y}$ compositions, conversion increases with increasing T and decreasing x and y . Flow conditions in one channel are labeled on each figure. ($P_{tot} = 1$ atm)	104
Figure 4.11. Ternary composition space showing how the catalytic activity of the H_2 - D_2 exchange reaction changes with Cu, Au and Pd composition across the $\text{Cu}_x\text{Au}_y\text{Pd}_{1-x-y}$ CSAF. H_2 conversion was selected to be the indicator of activity and was measured at 533 K for the inlet flow 0.05 mL/min $\text{H}_2 + 0.05$ mL/min $\text{D}_2 + 0.05$ mL/min Ar.	106
Figure 4.12. H_2 - D_2 exchange conversion across the real physical space of the $\text{Cu}_x\text{Au}_y\text{Pd}_{1-x-y}$ CSAF at $T = 333$ K, 433 K and 533 K. Inlet flow was 0.05 mL/min H_2 , 0.05 mL/min D_2 , and 0.05 mL/min Ar per channel.	107
Figure 4.13. a), b) HD flow rate in the outlet measured for two $\text{Cu}_x\text{Au}_y\text{Pd}_{1-x-y}$ alloy compositions vs. T for five inlet flow conditions. Solid squares are the experimental measurement points and the solid lines are the fits of the data to the microkinetic model.	108
Figure 4.14. Parity plot of the HD flow rates predicted by the microkinetic model vs. experimental measurements. Data are shown for all 100 $\text{Cu}_x\text{Au}_y\text{Pd}_{1-x-y}$ compositions ($x = 0 - 1$, $y = 0 - (1 - x)$) at 11 different temperatures ($T = 333-533$ K) and 11 inlet flow conditions (Table 4.1).	109
Figure 4.15. a) Barriers for H_2 adsorption as a function of $\text{Cu}_x\text{Au}_y\text{Pd}_{1-x-y}$ alloy composition and b) standard errors (SE) on estimated adsorption barriers.	110
Figure 4.16. a) Barriers for H_2 desorption as a function of $\text{Cu}_x\text{Au}_y\text{Pd}_{1-x-y}$ alloy composition and b) standard errors (SE) on estimated desorption barriers for all 100 different points across the CSAF. c) ΔE_{des}^\ddagger as a function of $\text{Cu}_x\text{Au}_y\text{Pd}_{1-x-y}$ alloy composition and d) standard errors (SE) on estimated desorption barriers after discarding the points giving very high SEs.	111
Figure 4.17. Plot of experimental HD production rate on five different $\text{Cu}_x\text{Au}_y\text{Pd}_{1-x-y}$ compositions (as listed on the figure) at 433 K as a function of P_{H_2} with P_{D_2} constant at 34 kPa.	113

Figure 4.182. Plot of experimental HD production rate on five different $\text{Cu}_x\text{Au}_y\text{Pd}_{1-x-y}$ compositions (as listed on the figure) at 433 K as a function of P_{D_2} with P_{H_2} constant at 0.34 kPa.	114
Figure 4.193. Total coverage of H and D atoms during $\text{H}_2\text{-D}_2$ exchange reaction over three different $\text{Ag}_x\text{Pd}_{1-x}$ alloy compositions ($x = 0.01, 0.2, 0.37$) as a function of T . The flow contains 9 mL/min H_2 , 0.009 mL/min D_2 and 20.991 mL/min Ar.	116
Figure 4.20. Total coverage of H and D atoms during $\text{H}_2\text{-D}_2$ exchange as a function of T for four different inlet flow compositions. The coverage is calculated using Equation (3.14) and the kinetic parameters, ν_{ads} , ν_{des} , $\Delta E_{\text{ads}}^\ddagger$ and $\Delta E_{\text{des}}^\ddagger$, are extracted from the microkinetic model.	116
Figure 4.21. Energy barriers for dissociative adsorption of H_2 , $\Delta E_{\text{ads}}^\ddagger(x, y)$, (black) and associative desorption of H_2 , $\Delta E_{\text{des}}^\ddagger(x, y)$, (red) as a function of ν -band center energy measured across the $\text{Cu}_x\text{Au}_y\text{Pd}_{1-x-y}$ CSAF.	118
Figure 4.22. HD flow rate versus temperature measured across $\text{Cu}_x\text{Au}_y\text{Pd}_{1-x-y}$ composition space. For all 100 $\text{Cu}_x\text{Au}_y\text{Pd}_{1-x-y}$ compositions conversion increases with increasing T and decreasing x and y . Flow conditions in one channel are labeled on each figure. ($P_{\text{tot}} = 1$ atm)	120
Figure 5.1. Ethylene hydrogenation mechanism proposed by Horiuti-Polanyi. In this mechanism, H_2 adsorbs dissociatively and C_2H_4 (ethylene) adsorbs molecularly. Adsorbed H combine with adsorbed C_2H_4 to form C_2H_5 (ethyl) and then another H is added to C_2H_5 to produce C_2H_6 (ethane).	132
Figure 5.2. Fragmentation patterns of ethylene and ethane.	138
Figure 5.3. Concentration distribution (at. %) obtained with XPS for Cu, Au, and Pd across a $\text{Cu}_x\text{Au}_y\text{Pd}_{1-x-y}$ CSAF.	143
Figure 5.4. a) $\text{Cu}_x\text{Au}_y\text{Pd}_{1-x-y}$ alloy compositions across 14×14 mm ² substrate surface (a 13×13 grid with 1 mm spacing). b) $\text{Cu}_x\text{Au}_y\text{Pd}_{1-x-y}$ alloy compositions covered in ternary space. Each of the red dots represents a different alloy composition corresponding to the 100 different microreactor channel.	144
Figure 5.5. XPS-derived average energy of the filled ν -band relative to the Fermi level of $\text{Ag}_x\text{Pd}_{1-x}$ CSAF versus Pd (at. %) compositions.	145
Figure 5.6. Ethylene conversion versus temperature measured at one randomly picked alloy composition across $\text{Cu}_x\text{Au}_y\text{Pd}_{1-x-y}$ composition space. The measured conversion values belong to 3 randomly picked experiments in order to show the reproducibility of the reactivity across the CSAF surface. The inlet flow rate contains 0.004 mL/min C_2H_4 , 0.004 mL/min H_2 and 0.022 mL/min Ar per channel.	146

Figure 5.7. Ethylene conversion versus time measured at one randomly picked alloy composition across $\text{Cu}_x\text{Au}_y\text{Pd}_{1-x-y}$ composition space. No catalyst deactivation was observed.	147
Figure 5.8. C_2H_6 flow rate versus temperature measured across $\text{Cu}_x\text{Au}_y\text{Pd}_{1-x-y}$ composition space. For all 100 $\text{Cu}_x\text{Au}_y\text{Pd}_{1-x-y}$ compositions activity increases with increasing T and decreasing x and y . Flow conditions in one channel are labeled on each figure. ($P_{tot} = 1$ atm)	148
Figure 5.9. Ternary composition space showing how the catalytic activity of the C_2H_4 hydrogenation reaction changes with Cu, Au and Pd composition across the $\text{Cu}_x\text{Au}_y\text{Pd}_{1-x-y}$ CSAF. C_2H_4 conversion was selected to be the indicator of the activity and measured at 433K for the inlet flow 0.013 mL/min C_2H_4 + 0.013 mL/min H_2 + 0.076 mL/min Ar.	150
Figure 5.10. C_2H_4 hydrogenation conversion across the real physical space of $\text{Cu}_x\text{Au}_y\text{Pd}_{1-x-y}$ CSAF at $T = 313$ K, 373 K and 433 K. Inlet flow was 0.013 mL/min C_2H_4 + 0.013 mL/min H_2 + 0.074 mL/min Ar per channel.	151
Figure 5.11. C_2H_6 flow rate in the outlet measured for three $\text{Cu}_x\text{Au}_y\text{Pd}_{1-x-y}$ alloy compositions vs. $P_{\text{C}_2\text{H}_4}$. Catalytic activities are normalized to the catalytic activities observed at standard conditions ($T = 373$ K, $P_{\text{H}_2} = 13.33$ kPa, $P_{tot} = 1$ atm).	152
Figure 5.12. Effects of P_{H_2} on C_2H_6 flow rate in the outlet measured for three $\text{Cu}_x\text{Au}_y\text{Pd}_{1-x-y}$ alloy compositions. ($T = 373$ K, $P_{\text{C}_2\text{H}_4} = 6.67$ kPa, $P_{tot} = 1$ atm).	153
Figure 5.13. a) Barriers for H_2 adsorption as a function of $\text{Cu}_x\text{Au}_y\text{Pd}_{1-x-y}$ alloy composition and b) Barriers for H_2 desorption as a function of $\text{Cu}_x\text{Au}_y\text{Pd}_{1-x-y}$ alloy composition.	154
Figure 5.14. a) Barriers for C_2H_4 adsorption as a function of $\text{Cu}_x\text{Au}_y\text{Pd}_{1-x-y}$ alloy composition and b) Barriers for C_2H_4 desorption as a function of $\text{Cu}_x\text{Au}_y\text{Pd}_{1-x-y}$ alloy composition.	156
Figure 5.15. a) Barriers for C_2H_4 hydrogenation to C_2H_5 as a function of $\text{Cu}_x\text{Au}_y\text{Pd}_{1-x-y}$ alloy composition and b) Barriers for C_2H_5 dissociation as a function of $\text{Cu}_x\text{Au}_y\text{Pd}_{1-x-y}$ alloy composition.	157
Figure 5.16. Barriers for C_2H_5 hydrogenation to C_2H_6 as a function of $\text{Cu}_x\text{Au}_y\text{Pd}_{1-x-y}$ alloy composition.	158
Figure 5.17. Energy barriers for all 7 elementary steps in the C_2H_4 hydrogenation mechanism, $\Delta E_i^\ddagger(x, y)$, as a function of ν -band center energy measured across nine different alloy compositions across the $\text{Cu}_x\text{Au}_y\text{Pd}_{1-x-y}$ CSAF. The corresponding elementary reaction is labeled next to each dataset.	159
Figure 5.18. Energy barriers for H_2 and C_2H_4 adsorption steps in the C_2H_4 hydrogenation mechanism, $\Delta E_i^\ddagger(x, y)$, as a function of ν -band center energy	162

measured across the $\text{Cu}_x\text{Au}_y\text{Pd}_{1-x-y}$ CSAF. The corresponding elementary reaction is labeled next to each dataset.

Figure 5.19. Energy barriers for two successive hydrogenation steps in the C_2H_4 hydrogenation mechanism, $\Delta E_i^\ddagger(x, y)$, as a function of ν -band center energy measured across the $\text{Cu}_x\text{Au}_y\text{Pd}_{1-x-y}$ CSAF. The corresponding elementary reaction is labeled next to each dataset.

163

CHAPTER 1

Introduction

1.1 Summary

Alloys and multicomponent materials are often used as catalysts instead of using pure metals since metallic alloys are often shown to possess superior catalytic and mechanical properties compared to their pure components due to ligand, strain and ensemble effects [1, 2]. The interactions between the different elements in an alloy (ligand effects), the change in lattice parameters due to alloying (strain effects) and the spatial distribution of atomic sites (ensemble effects) influence the distinctive physical and electronic features of the alloy, making it possible to adjust the reaction activity and selectivity of the alloy catalyst [3].

Alloys of transition metals are often better catalysts than the pure metal components themselves and the reaction activity of an alloy catalyst can be tuned by either changing its components or adjusting its alloy composition [4]. But the reasons why these multi-component materials are better catalysts than their pure components are not yet very well understood due to the lack of experimental studies that correlate the catalytic activity of alloys with their electronic properties over a range of compositions.

This thesis focuses on the application of high throughput methodology that has been developed in our laboratory to conduct reaction kinetics studies of H₂-D₂ exchange and ethylene hydrogenation reactions on binary and ternary Pd-based alloys surfaces. In this chapter, the literature relevant to the objective of this thesis is reviewed and the scope of this thesis is outlined.

1.2 High throughput techniques

Correlation of the catalytic activity of alloys with their composition and electronic structures is a challenging process mainly due to the difficulties in preparation and characterization of a range of single composition samples using conventional methods. Conventional approaches study one composition at a time, which not only slows the process of data measurement but also limits the scope of the research to a small number of distinct alloy compositions. The preparation of samples with different compositions also increases the research expenditure. For example, 11 catalyst samples are needed in order to span the composition space of a binary alloy with 10% composition resolution. Spanning composition space for a ternary alloy with 10% composition resolution requires $\sim 10^2$ samples. In general, the problem for an n -component alloy catalyst requires sampling of a continuous, $n-1$ dimensional, composition space.

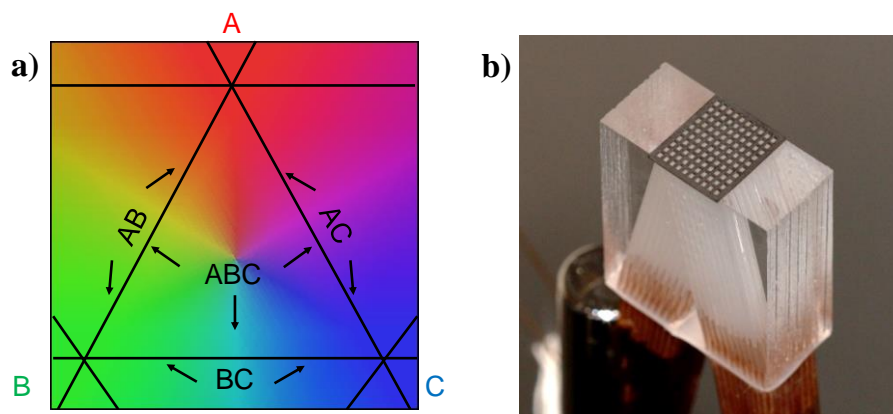


Figure 1.1. a) Schematic representation of a CSAF with regions containing the entire ternary alloy composition space, $A_xB_yC_{1-x-y}$ ($x = 0 \rightarrow 1, y = 0 \rightarrow 1 - x$), all three binary alloys A_xB_{1-x} , A_xC_{1-x} , and B_xC_{1-x} ($x = 0 \rightarrow 1$) and all three pure components (A, B, and C). b) Photograph of the multichannel microreactor array built in our laboratory that allows characterization of reactivity at 100 discrete locations (100 different alloy compositions) on a CSAF.

Finding the optimal catalyst composition for a given application is the major challenge in multicomponent catalyst design. Conventional methods concentrate on a limited number of discrete alloy compositions and are very slow because handling one sample at a time is time-consuming. For example, in the early 1900's, Haber and Bosch spent years testing ~2000 different ammonia synthesis catalysts before determining that Fe as the most active [5]. Compared to the conventional ways, high throughput techniques offer great advantages in studying multicomponent systems [6, 7]. They enable characterization of reaction activity of all different alloy compositions in one single experiment based on the use of composition spread alloy films (CSAFs) [8-10]. Figure 1.1-a shows a schematic representation of a ternary CSAF. CSAF is one kind of high throughput library, which contains all possible compositions of an alloy in the form of a thin film deposited on a substrate. By using a multichannel micro-reactor that has been developed in our group (Figure 1.1-b), the catalytic activity of an alloy catalyst for a specific reaction can be measured at 100 different locations on the CSAF surface, which correspond to 100 different alloy compositions, in one single experiment.

One example to show the potential of high throughput methods can be the investigation of H₂-D₂ exchange reaction. O'Brien performed a detailed analysis of H₂-D₂ exchange kinetics on fixed beds of Pd, Cu, Pd₄₇Cu₅₃ (BCC and FCC) and Pd₇₀Cu₃₀ using a conventional flow reactor [11]. The results showed that the order of H₂-D₂ exchange activity of the catalysts increases as follows: Cu << Pd < BCC Pd₄₇Cu₅₃ < Pd₇₀Cu₃₀ < FCC Pd₄₇Cu₅₃ (Figure 1.2). According to these results, the structure of the alloy, as well as the composition of the alloy, influence the activity. Experiments were performed in a fixed bed reactor containing the catalyst foil to be tested at near ambient pressure and over a temperature range of 200-800 K. In all experiments, equivolumetric flows of H₂ and D₂ were used. Among all the catalysts used, the exchange reaction was observed

to be limited by the rate of H_2 adsorption only over Cu. The rate was limited by desorption on all of the Pd-containing alloys. This work provides a good understanding about the H_2 - D_2 exchange reaction, but the number of different catalysts was limited hence it is not easy to extract actual correlation between the composition and catalytic activity for the entire composition span of CuPd alloys. Also since it takes a lot of time to run the tests, only three equimolar inlet flow conditions were tested, hence the effect of the changes in the partial pressures of the reactant gases could not be detected thoroughly.

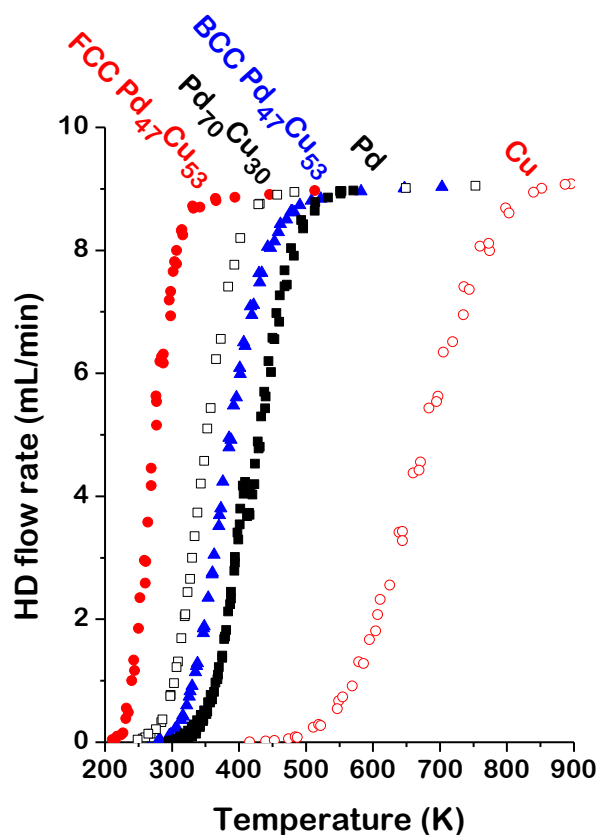


Figure 1.2. Comparison of H_2 - D_2 exchange activity on five different catalysts. HD flows, out from the fixed bed of catalysts, show that the most active catalyst is FCC Pd₄₇Cu₅₃ and the least active is pure Cu. (The same reaction conditions, surface area and inlet flows.)

For speeding up the data collection process, Gumuslu investigated the same H₂-D₂ exchange reaction across a CuPd binary CSAF [8]. She was able to collect reactivity data on 100 discrete compositions across the Cu_xPd_{1-x} binary CSAF as a function of temperature using the multichannel microreactor array as shown in Figure 1.3. The data shown in Figure 1.3 was can be collected in about 6 hours. Across the CSAF, HD exchange activity was observed to increase with increasing temperature for all cases. The alloy became more active with increasing Pd concentration; maximum conversion was achieved at approximately 70% Pd.

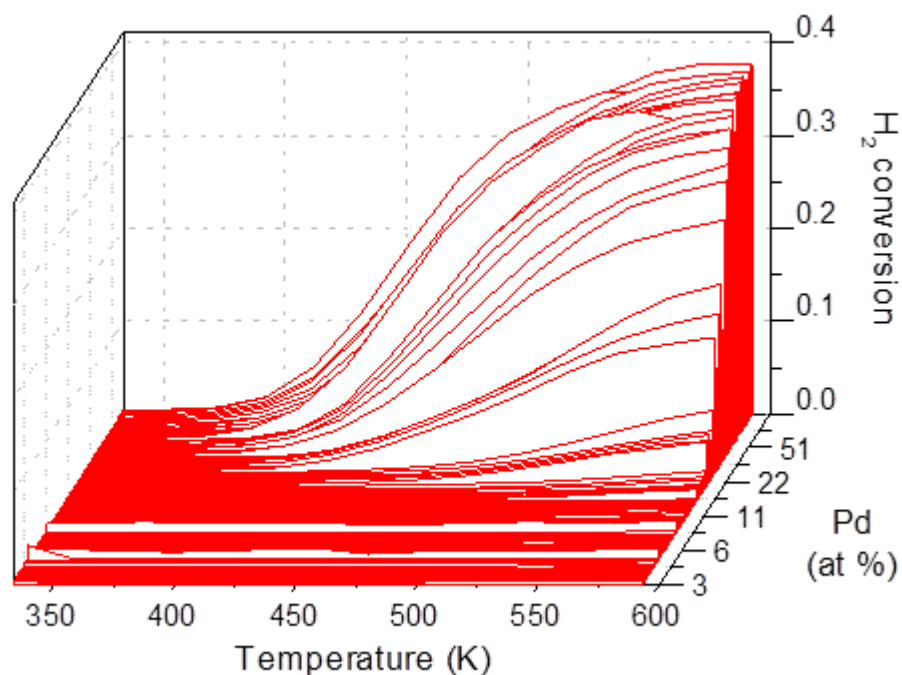


Figure 1.3. Comparison of H₂-D₂ exchange activity on 100 different Cu_xPd_{1-x} catalysts. H₂ conversions, out from the different locations on the CSAF, show that catalytic activity is increasing as Pd content increases. (The same reaction conditions, surface area and inlet flows.)

In both of these works, the collected reactivity data is fit into a microkinetic model and fundamental kinetics parameters were calculated. The calculated energy barriers for H₂ adsorption (ΔE_{ads}^\ddagger) and desorption (ΔE_{des}^\ddagger) were plotted as a function of Cu composition in Figure 1.4. The blue hollow data points belongs to the energy barriers obtained on fixed beds of Pd, Cu, Pd₄₇Cu₅₃ and Pd₇₀Cu₃₀. From this dataset containing only 4 points, a general trend in energy barriers versus composition can be observed however it is very difficult to obtain the general correlation between these variables. The filled data points belong to the energy barriers calculated through a well resolved continuous composition library of CuPd alloys across the CSAF. The comparison of these two set of results shows that the calculated energy barriers are in a very good agreement with each other, validating the use of high-throughput methods.

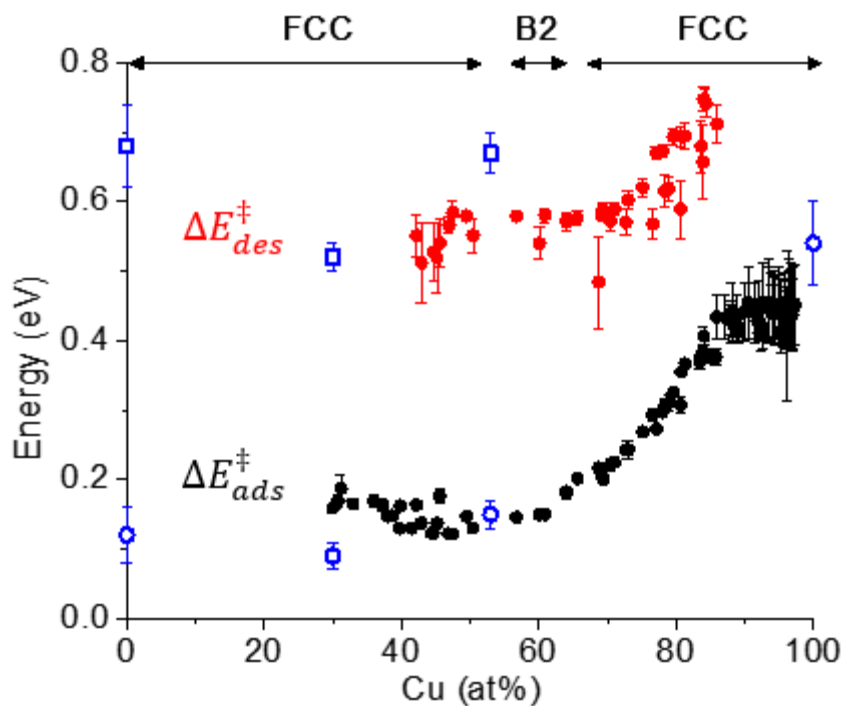


Figure 1.4. Energy barriers for H₂ adsorption (black) and desorption (red) as a function of Cu composition. Open symbols (blue) represent H₂ adsorption (square) and desorption (round) energy barriers estimated using experimental data from conventional fixed beds of single composition catalysts. These two datasets to be in good agreement is a good example to validate the high throughput methodology.

1.3 Hydrogen separation by palladium based alloys

The high throughput techniques can be applied to develop better catalysts for industrial separation of hydrogen. Hydrogen plays a significant role in advanced energy systems, such as being the energy source for fuel cells. In general, the main methods for hydrogen production are electrolysis of water, steam reforming of methane, gasification of coal or partial oxidation of oil or natural gas [3]. In processes where fossil fuels are involved, hydrogen has to be separated from a CO₂-rich gas mixture. Common technologies used for hydrogen separation include solvent adsorption, pressure swing adsorption and cryogenic recovery, all of which require large capital and energy expenditures [12, 13]. However, membrane separation has many advantages such as reducing operating costs, minimizing unit operations and lowering energy consumption [14]. Membranes made of Ni, Pd and Pt have the ability to dissociate and dissolve H₂. Among these metals, Pd membranes are known to have high permeability because hydrogen has a higher solubility over a wide temperature range in Pd than in Pt and Ni [2].

Pd membranes have reasonable membrane cost and high hydrogen selectivity relative to other gases [15, 16]. Several Pd or Pd-alloy membranes were reported to be stable for several months under H₂ flow in the temperature range 350-500°C [1, 17]. There are also some limitations of Pd-based membranes. Adsorption of hydrogen below its critical point of 298°C and 2 MPa produces α -PdH and β -PdH phases. Phase transitions cause a change in lattice parameter which may lead to the formation of bulk and grain boundary defects [18]. As for the Pd membranes, hydrogen embrittlement, in which dissolved hydrogen tends to cause lattice expansion in the metal, eventually cause the membrane to rupture on repeated pressure and temperature cycling [19, 20]. Also, exposure to H₂ can reduce the ductility of the metal which causes embrittlement [21]. Interactions with carbon-containing species and exposure to sulfur or carbon monoxide may

deactivate the Pd surface [14, 22]. Alloying Pd with other metals such as Ag, Au, Cu, Fe, Ni, Pt or Y can prevent these problems. Addition of 5% Au increased H₂ permeability by ~28%, but above 40% Au, a decrease in permeability was reported [23]. Au was also found the sulfur tolerance significantly compared to other metals[24]. But it must be noted that despite these benefits of Au addition, the cost of Au limits its usability and makes Ag and Cu more attractive options [25]. Alloying Pd with Cu increased the structural stability and sulfur tolerance of the membrane without significant reduction in H₂ permeability [26-31]. Alloying Pd with Ag was found to be less brittle in the presence of hydrogen compared to pure Pd [19, 32, 33]. Another advantage of alloying Pd is that Ag addition remarkably increases the permeability of palladium to hydrogen [19, 20, 34]. Addition of 23 (at.)% Ag to pure Pd was reported to decrease the critical temperature and pressure for the α -PdH to β -PdH transition and to increase hydrogen solubility dramatically[33, 34]. The permeability of Ag-Pd membrane was compared to Pd-Cu and Pd-Au. Pd-Ag was found to show higher permeability than the others at the specified temperature and pressure which is 1.7 times higher than the Pd permeability value[34]. Sieverts et al. measured the solubility of H₂ in Au-Pd, Ag-Pd and Pt-Pd alloys and found out that Ag-Pd has the highest solubility amongst them [35, 36]. Also to take advantage of the favorable surface chemistry of both Pd-Cu and Pd-Au binary alloys, the idea of preparing and testing ternary alloys was proposed [37]. In one study, the permeability of Pd₇₀Cu₂₆Au₄ was predicted to be 2.5-5 times higher than Pd₇₀Cu₃₀ over the temperature range 323-923°C [37]. With conventional techniques which require preparing and characterizing each sample individually, the search for the optimum ternary alloy composition would be very expensive and time-consuming. Applying high throughput methods can accelerate this search while also generating a fundamental understanding of multicomponent catalysts.

The transport mechanism through the membrane involves three main steps as shown in Figure 1.5 [38]. H_2 adsorbs dissociatively on the upstream side of the membrane surface, H atoms diffuse through the metal and recombine so that H_2 desorbs from the downstream surface [39, 40]. The bulk diffusion step has been investigated extensively in the literature [41-43]. However dissociative adsorption and associative desorption processes are not yet very well understood on Pd-based surfaces. H_2 - D_2 exchange ($H_2 + D_2 \rightarrow HD$) reaction a very good model reaction that can provide a valuable information about those steps. So, our work, high throughput characterization of H_2 - D_2 exchange reaction on Ag_xPd_{1-x} and $Cu_xAu_yPd_{1-x-y}$ alloys happens to be very crucial to understand hydrogen purification via Pd-based membranes.

When the high throughput reaction kinetics experiments are combined with high throughput characterization techniques, the correlation of the changes in catalytic activity with the alloy composition and the electronic structure of the alloy can be done. Ligand effects are described by the change in the width and/or the center of the d -band. It is known that changes in the position of d -band center relative to the Fermi level, lead to changes in the energy barrier for adsorption, which leads a change in activity[44, 45]. For a higher activity, the center of the d -band

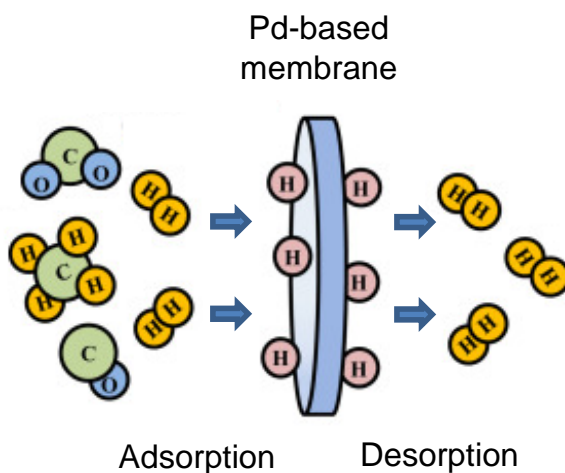


Figure 1.5. Schematic representation of hydrogen transport through a Pd-based membrane.

must be high above the Fermi level which means as the number of d-states above the Fermi level increases, the alloy becomes more active [45]. Ligand effects can be observed with the use of electronic spectroscopic methods such as X-ray photoelectron spectroscopy (XPS) [1, 44]. Using spatially resolved XPS we can estimate the average energy of the filled states of the valence band (s-, p-, and d-bands) across composition space, $\varepsilon_v(x)$. Using the v-band energies as an experimental proxy for the d-band energy, we can correlate reaction barriers (ΔE_{ads}^\ddagger and ΔE_{des}^\ddagger) with $\varepsilon_v(x)$ across the entire composition space.

1.4 Ethylene hydrogenation

High-throughput techniques can be used to characterize the activity of alkene hydrogenation reactions over different alloy catalysts. Catalytic hydrogenation is extensively used in a wide range of industrial applications such as the production of fuels, improving the combustion properties, increasing the stability of biofuels, to convert alkenes to saturated alkanes which are less toxic and less reactive [46]. Since its discovery at the end of the 19th century, alkene hydrogenation over metal surfaces has been studied extensively in the literature with ethylene as a model reactant [47-52]. Ethylene is the smallest hydrocarbon containing carbon-carbon bond which makes it a very good candidate for probing catalytic reactivity of larger hydrocarbons [53]. Adsorption of ethylene on metal surfaces has been investigated on metal surfaces by various methods [54, 55]. For ethylene decomposition and hydrogenation, single-crystal surfaces of Pt and Rh were found to be very active [56-60]. The hydrogenation of ethylene over transition metals has been defined as a deceptively simple reaction which in fact possesses an extremely rich and complicated chemistry [61]. In this work, ethylene hydrogenation has been chosen to be investigated using the high-throughput methods developed in our laboratory. This catalytic

reaction involves simple reactants, can proceed at ambient temperature and only produces ethane [62]. Also, it has been studied on binary alloy catalysts before [63-67]. With the existing knowledge about these reactions, the development of a high throughput experimental strategy for understanding and designing ternary alloy catalysts is the goal of this work.

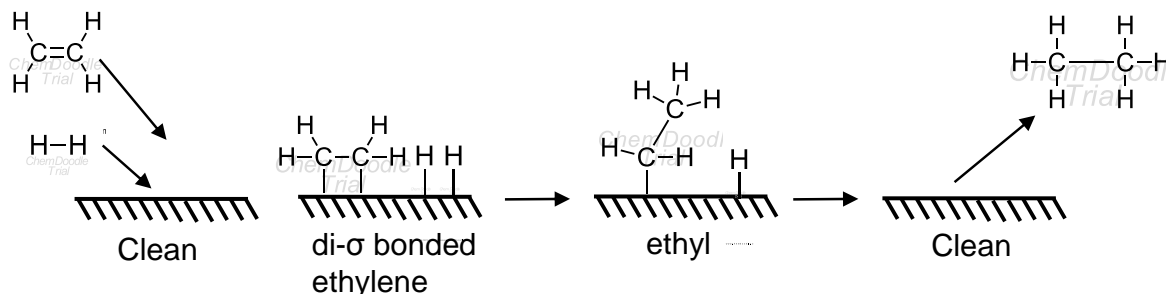


Figure 1.6. Horiuti-Polanyi mechanism for ethylene hydrogenation over metal catalysts.

Sabatier and Senderens observed the catalytic hydrogenation of ethylene over platinum at the end of the nineteenth century and since then a continuous effort has been put to understand this simplest alkene hydrogenation reaction [68]. In 1934, Horiuti and Polanyi proposed their famous four-step ethylene hydrogenation mechanism. In this mechanism, ethylene adsorbs on the transition metal surface by using one of the carbon-carbon double bonds (by breaking one of the carbon-carbon bonds) and forming two σ bonds with the underlying metal surface. This is followed with hydrogenation with an atomic hydrogen to produce ethyl intermediate and then another hydrogenation with another atomic hydrogen to produce ethane which is immediately desorbed from the surface [69] (Figure 1.6).

In the 1950s, the evidence for an ethyl intermediate was found by Kemball et al. using deuterium labeling that showed ethylene molecules readily exchange hydrogen atoms during the hydrogenation process [70]. And with the advances of surface spectroscopy techniques, three distinct surface species were observed to be formed upon adsorption of ethylene on Pt: 1) a π -adsorbed intermediate, 2) a di- σ -adsorbed intermediate and 3) a partially dehydrogenated ethylidyne species [71]. Ultraviolet photoemission spectroscopy (UPS) showed that ethylene physisorbs through its π -orbital (π -bonded species) on clean Pt(111) at low temperatures [72]. With increase in temperature, ethylene irreversibly breaks this π -bond and forms two σ bonds on the metal surface (di- σ -bonded species) [73]. And above 240K, di- σ -bonded ethylene dehydrogenates to ethylidyne by transferring one hydrogen from one carbon to the other and losing a hydrogen [60] (Figure 1.7).

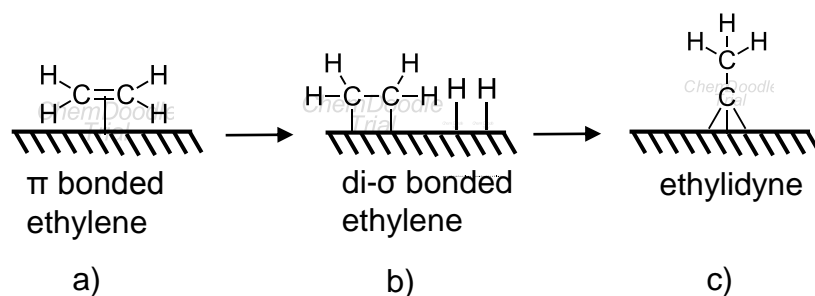


Figure 1.7. The thermal evolution of adsorbed ethylene on Pt(111). The dehydrogenation proceeds from **a)** π -bonded ethylene at low temperature through **b)** di- σ -bonded ethylene to **c)** ethylidyne.

The role of ethylidyne has been investigated on Pt (111) and on supported Pt catalyst. On Pt (111), it was reported that hydrogenation of ethylidyne was several orders of magnitude slower than that of hydrogenation of ethylene to ethane [74]. On Pt/Cab-O-Sil, it was reported that ethylidyne was not involved in the reaction [75]. Both of these studies show that ethylidyne is

only a spectator species which does not involve in ethylene hydrogenation mechanism [75-77]. When it comes to π -bonded and σ -bonded ethylene, it was reported that when the Pt catalyst surface was precovered with these species, they are both hydrogenated when H_2 is flowing over. If the catalyst surface is annealed in the absence of hydrogen, it was found that only di- σ -bonded species was converted to ethylidyne while the π -bonded ethylene remains unaffected [78]. Cremer et al. monitored ethylene hydrogenation on Pt (111) in situ at high pressures using sum frequency generation (SFG) method. Their obtained SFG spectra showed that the decrease in the concentration of di- σ -bonded ethylene does not cause a decrease in the rate of hydrogenation. This observation basically tells us that di- σ -bonded ethylene is not an important intermediate in ethylene hydrogenation. They reported that di- σ -bonded species compete directly with ethylidyne for sites. Once ethylidyne species are formed they also block the adsorption sites for di- σ -bonded species. Since it is known that ethylidyne has no effect on ethylene hydrogenation, di- σ -bonded species can also be eliminated from the mechanism. However, π -bonded species was found not to be affected by the ethylidyne concentration. So, it can be said that π -bonded species is likely to be a key intermediate in ethylene hydrogenation [61, 76]. The proposed mechanism can be found in Figure 1.8.

Ethylene hydrogenation has been investigated for a long time and there is a very rich literature about this reaction especially on Pt. Also, most of these studies have been conducted under ultra-high vacuum conditions and they mostly focus on identifying surface species. In this reaction kinetics study, we aim to fully investigate the reaction mechanism of ethylene hydrogenation across Pd-based alloys at high-pressure conditions.

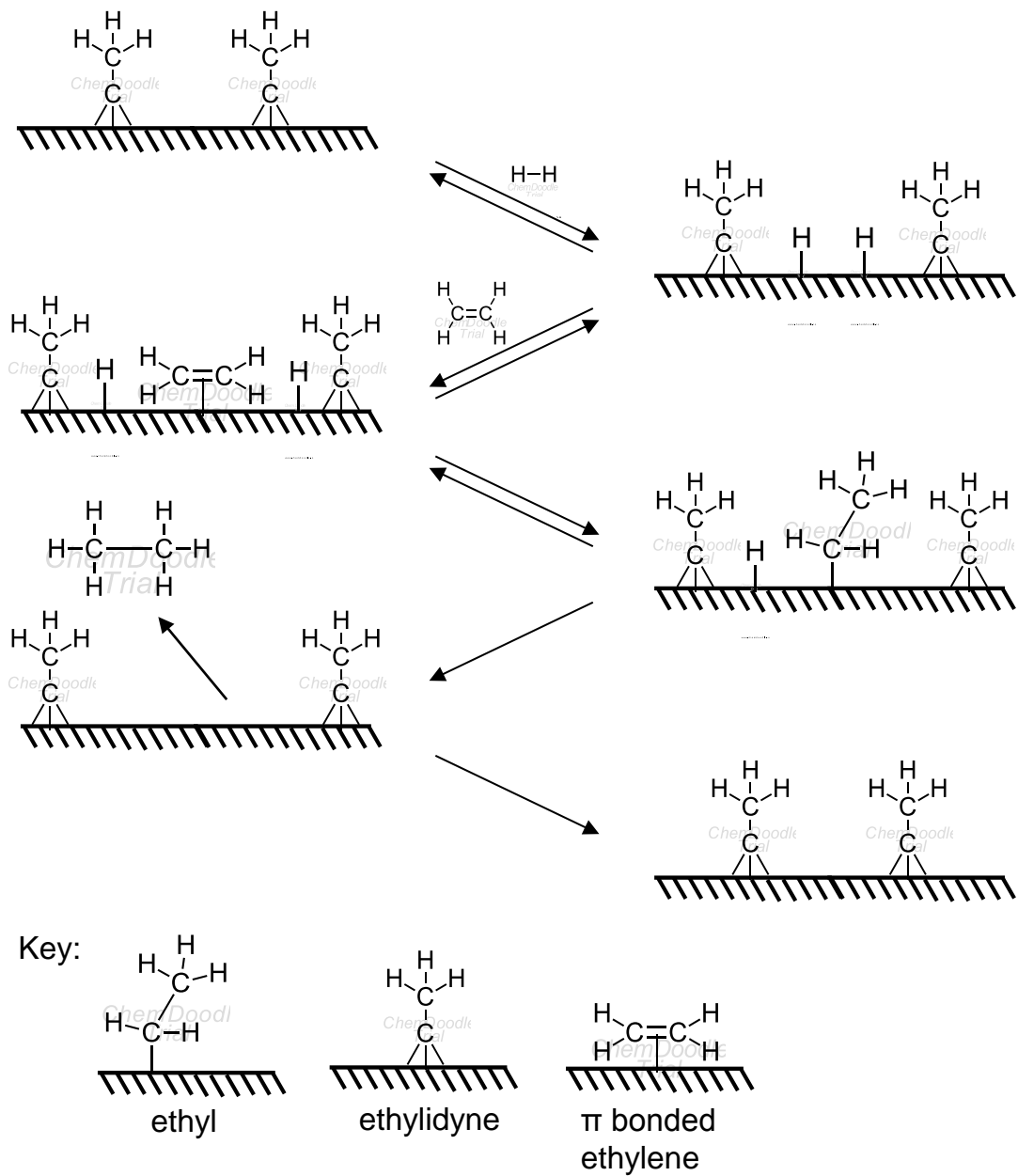


Figure 1.8. Proposed mechanism for ethylene hydrogenation on Pt (111).

1.5 Scope of the thesis

In this thesis, the adsorption and desorption characteristics of H₂ via H₂-D₂ exchange reaction as well as ethylene hydrogenation reaction were investigated across Pd-based alloy surfaces. We proposed a high throughput methodology for the reaction kinetics studies which depends on the usage of materials libraries (CSAFs) as catalysts coupled with a multichannel microreactor array. We aim to validate the use of this high throughput methodology and to present a correlation between catalytic activity, catalyst composition and its electronic structure for both H₂-D₂ exchange and ethylene hydrogenation reactions.

In Chapter 2, a detailed description of the fabrication of the multichannel microreactor array as well as the experimental and analytical techniques that are used in this work is described. The derivation of the microkinetic model for H₂- D₂ exchange reaction is also given in detail. In Chapters 3 and 4, the detailed analysis of H₂-D₂ exchange reaction across Ag_xPd_{1-x} and Cu_xAu_yPd_{1-x-y} surfaces is provided respectively. The catalytic activity – composition – electronic structure correlation for both Ag_xPd_{1-x} binary and Cu_xAu_yPd_{1-x-y} ternary alloys have been reported respectively in Chapters 3 and 4.

In Chapters 5, the detailed analysis of ethylene hydrogenation reaction across Cu_xAu_yPd_{1-x-y} surfaces is provided. After our high throughput methodology is validated investigating H₂-D₂ exchange reaction, it was shown in this chapter that the same methodology can be applied to more complex reactions. The catalytic activity – composition – electronic structure correlation has been deduced for ethylene hydrogenation reaction across Cu_xAu_yPd_{1-x-y} ternary alloys.

1.6 References

1. Wei, T., J. Wang, and D.W. Goodman, *Characterization and Chemical Properties of Pd–Au Alloy Surfaces*. The Journal of Physical Chemistry C, 2007. **111**(25): p. 8781-8788.
2. Hammer, B. and J.K. Norskov, *Why gold is the noblest of all the metals*. Nature, 1995. **376**(6537): p. 238-240.
3. Chen, J.G., C.A. Menning, and M.B. Zellner, *Monolayer bimetallic surfaces: Experimental and theoretical studies of trends in electronic and chemical properties*. Surface Science Reports, 2008. **63**(5): p. 201-254.
4. Sinfelt, J.H., *Kinetics of Ethylene Hydrogenation over a Platinum—Silica Catalyst*. The Journal of Physical Chemistry, 1964. **68**(4): p. 856-860.
5. Roberts, M.W., *Industrial developments (1950-1999)*. Catalysis Letters, 2000. **67**(1): p. 67-73.
6. Farrusseng, D., *High-throughput heterogeneous catalysis*. Surface Science Reports, 2008. **63**(11): p. 487-513.
7. Corma, A., et al., *Integrating high-throughput characterization into combinatorial heterogeneous catalysis: unsupervised construction of quantitative structure/property relationship models*. Journal of Catalysis, 2005. **232**(2): p. 335-341.
8. Gumuslu, G., et al., *Correlation of Electronic Structure with Catalytic Activity: H₂–D₂ Exchange across CuxPd1–x Composition Space*. ACS Catalysis, 2015. **5**(5): p. 3137-3147.
9. Kondratyuk, P., et al., *A microreactor array for spatially resolved measurement of catalytic activity for high-throughput catalysis science*. Journal of Catalysis, 2013. **300**(Supplement C): p. 55-62.
10. Boes, J.R., et al., *Estimating Bulk-Composition-Dependent H₂ Adsorption Energies on CuxPd1–x Alloy (111) Surfaces*. ACS Catalysis, 2015. **5**(2): p. 1020-1026.
11. O'Brien, C.P., et al., *The Kinetics of H₂–D₂ Exchange over Pd, Cu, and PdCu Surfaces*. The Journal of Physical Chemistry C, 2011. **115**(49): p. 24221-24230.
12. Adhikari, S. and S. Fernando, *Hydrogen membrane separation techniques*. Industrial & Engineering Chemistry Research, 2006. **45**(3): p. 875-881.
13. Lanning, B., et al., *Un-supported Palladium Alloy Membranes for the Production of Hydrogen*, in *Inorganic Membranes for Energy and Environmental Applications*, A. Bose, Editor. 2009, Springer New York. p. 203-219.
14. Paglieri, S.N. and J.D. Way, *Innovations in palladium membrane research*. Separation and Purification Methods, 2002. **31**(1): p. 1-169.
15. Aasberg-Petersen, K., C.S. Nielsen, and S.L. Jorgensen, *Membrane reforming for hydrogen*. Catalysis Today, 1998. **46**(2): p. 193-201.

16. Derossset, A.J., *Processing Industrial Gas Streams at High Pressures ... Diffusion of Hydrogen through Palladium Membranes*. Industrial and Engineering Chemistry, 1960. **52**(6): p. 525-528.
17. Sinfelt, J.H., *Bimetallic Catalysts: Discoveries, Concepts, and Application*. 1983, New York: Wiley.
18. Lewis, F.A., *The Palladium Hydrogen System - Structures near Phase-Transition and Critical-Points*. International Journal of Hydrogen Energy, 1995. **20**(7): p. 587-592.
19. Jayaraman, V. and Y.S. Lin, *Synthesis and hydrogen permeation properties of ultrathin palladium-silver alloy membranes*. Journal of Membrane Science, 1995. **104**(3): p. 251-262.
20. Shu, J., et al., *Catalytic palladium-based membrane reactors: A review*. The Canadian Journal of Chemical Engineering, 1991. **69**(5): p. 1036-1060.
21. Rogers, H.C., *Hydrogen Embrittlement of Metals*. Science, 1968. **159**(3819): p. 1057-&.
22. Collins, J.P., et al., *Catalytic dehydrogenation of propane in hydrogen permselective membrane reactors*. Industrial & Engineering Chemistry Research, 1996. **35**(12): p. 4398-4405.
23. L, M.D., *Method for hydrogen separation and purification*. 1969, Google Patents.
24. Roa, F., et al., *Preparation and characterization of Pd-Cu composite membranes for hydrogen separation*. Chemical Engineering Journal, 2003. **93**(1): p. 11-22.
25. Yun, S. and S. Ted Oyama, *Correlations in palladium membranes for hydrogen separation: A review*. Journal of Membrane Science, 2011. **375**(1): p. 28-45.
26. Kamakoti, P., et al., *Prediction of hydrogen flux through sulfur-tolerant binary alloy membranes*. Science, 2005. **307**(5709): p. 569-573.
27. Kulprathipanja, A., et al., *Pd and Pd-Cu membranes: inhibition of H₂ permeation by H₂S*. Journal of Membrane Science, 2005. **254**(1-2): p. 49-62.
28. Morreale, B.D., et al., *Effect of hydrogen-sulfide on the hydrogen permeance of palladium-copper alloys at elevated temperatures*. Journal of Membrane Science, 2004. **241**(2): p. 219-224.
29. Nam, S.E. and K.H. Lee, *Hydrogen separation by Pd alloy composite membranes: introduction of diffusion barrier*. Journal of Membrane Science, 2001. **192**(1-2): p. 177-185.
30. Piper, J., *Diffusion of Hydrogen in Copper-Palladium Alloys*. Journal of Applied Physics, 1966. **37**(2): p. 715-&.
31. Uemiya, S., et al., *Separation of Hydrogen through Palladium Thin-Film Supported on a Porous-Glass Tube*. Journal of Membrane Science, 1991. **56**(3): p. 303-313.
32. Amandusson, H., L.-G. Ekedahl, and H. Dannetun, *Hydrogen permeation through surface modified Pd and PdAg membranes*. Journal of Membrane Science, 2001. **193**(1): p. 35-47.

33. Uemiya, S., T. Matsuda, and E. Kikuchi, *Hydrogen permeable palladium-silver alloy membrane supported on porous ceramics*. Journal of Membrane Science, 1991. **56**(3): p. 315-325.
34. Knapton, A.G., *Palladium Alloys for Hydrogen Diffusion Membranes*. Platinum Metal Reviews, 1977. **21**(2): p. 44-50.
35. E. Jurisch, A.M., and A. Sieverts, Z. Anorg. Allgem. Chem., 1915. **92**(4): p. 329.
36. Hagen, A.S.a.H., Z. Phys. Chem., 1935. **174A**(3-4): p. 247.
37. Semidey-Flecha, L., C. Ling, and D.S. Sholl, *Detailed first-principles models of hydrogen permeation through PdCu-based ternary alloys*. Journal of Membrane Science, 2010. **362**(1-2): p. 384-392.
38. Al-Mufachi, N.A., N.V. Rees, and R. Steinberger-Wilkens, *Hydrogen selective membranes: A review of palladium-based dense metal membranes*. Renewable and Sustainable Energy Reviews, 2015. **47**(Supplement C): p. 540-551.
39. O'Brien, C.P., et al., *The Kinetics of H-2-D-2 Exchange over Pd, Cu, and PdCu Surfaces*. Journal of Physical Chemistry C, 2011. **115**(49): p. 24221-24230.
40. O'Brien, C.P., et al., *H-2-D-2 Exchange Kinetics in the Presence of H₂S over Pd₄S, Pd₇₀Cu₃₀, and Pd₄₇Cu₅₃ Surfaces*. Journal of Physical Chemistry C, 2012. **116**(33): p. 17657-17667.
41. Hurlbert, R.C. and J.O. Konecny, *Diffusion of Hydrogen through Palladium*. The Journal of Chemical Physics, 1961. **34**(2): p. 655-658.
42. Jewett, D.N. and A.C. Makrides, *Diffusion of hydrogen through palladium and palladium-silver alloys*. Transactions of the Faraday Society, 1965. **61**(0): p. 932-939.
43. Pyun, S.-I., W.-J. Lee, and T.-H. Yang, *Hydrogen diffusion through palladium-gold alloy coatings electrodeposited on palladium substrate under permeable boundary condition*. Thin Solid Films, 1997. **311**(1): p. 183-189.
44. Baber, A.E., H.L. Tierney, and E.C.H. Sykes, *Atomic-Scale Geometry and Electronic Structure of Catalytically Important Pd/Au Alloys*. ACS Nano, 2010. **4**(3): p. 1637-1645.
45. Hammer, B. and J.K. Nørskov, *Theoretical surface science and catalysis—calculations and concepts*, in *Advances in Catalysis*. 2000, Academic Press. p. 71-129.
46. Heard, C.J., et al., *Kinetic Regimes in Ethylene Hydrogenation over Transition-Metal Surfaces*. ACS Catalysis, 2016. **6**(5): p. 3277-3286.
47. Beeck, O., *Hydrogenation catalysts*. Discussions of the Faraday Society, 1950. **8**(0): p. 118-128.
48. Zaera, F. and G.A. Somorjai, *Hydrogenation of ethylene over platinum (111) single-crystal surfaces*. Journal of the American Chemical Society, 1984. **106**(8): p. 2288-2293.
49. Bos, A.N.R. and K.R. Westerterp, *Mechanism and kinetics of the selective hydrogenation of ethyne and ethene*. Chemical Engineering and Processing: Process Intensification, 1993. **32**(1): p. 1-7.

50. Godbey, D., et al., *Hydrogenation of chemisorbed ethylene on clean, hydrogen, and ethynidyne covered platinum (111) crystal surfaces*. Surface Science, 1986. **167**(1): p. 150-166.
51. Riekert, L., G. C. Bond, *Catalysis by Metals*. 519 Seiten mit 128 Abbildungen. Academic Press, London und New York 1962. Preis: Ln. 100 s. Zeitschrift für Elektrochemie, Berichte der Bunsengesellschaft für physikalische Chemie, 1962. **66**(8-9): p. 771-771.
52. Horiuti, J. and K. Miyahara, *Hydrogenation of ethylene on metallic catalysts*. 1968: US Department of Commerce, National Bureau of Standards.
53. Saliccioli, M., Y. Chen, and D.G. Vlachos, *Microkinetic Modeling and Reduced Rate Expressions of Ethylene Hydrogenation and Ethane Hydrogenolysis on Platinum*. Industrial & Engineering Chemistry Research, 2011. **50**(1): p. 28-40.
54. J. C. Bertolini, J.M., *The Chemical Physics of Solid Surfaces and Heterogeneous Catalysis*, ed. D.P.W. D.A. King. Vol. 3B. 1984, New York: Elsevier.
55. Sheppard, N., *Vibrational Spectroscopic Studies of the Structure of Species Derived From the Chemisorption of Hydrocarbons on Metal Single-Crystal Surfaces*. Annual Review of Physical Chemistry, 1988. **39**(1): p. 589-644.
56. Somorjai, G.A., M.A. Van Hove, and B.E. Bent, *Organic monolayers on transition-metal surfaces: the catalytically important sites*. The Journal of Physical Chemistry, 1988. **92**(4): p. 973-978.
57. Steininger, H., H. Ibach, and S. Lehwald, *Surface reactions of ethylene and oxygen on Pt(111)*. Surface Science, 1982. **117**(1): p. 685-698.
58. Kesmodel, L.L., L.H. Dubois, and G.A. Somorjai, *LEED analysis of acetylene and ethylene chemisorption on the Pt(111) surface: Evidence for ethynidyne formation*. The Journal of Chemical Physics, 1979. **70**(5): p. 2180-2188.
59. Zaera, F., *Mechanisms for ethylene hydrogenation and hydrogen-deuterium exchange over platinum(111)*. The Journal of Physical Chemistry, 1990. **94**(12): p. 5090-5095.
60. Cremer, P., et al., *The conversion of di- σ bonded ethylene to ethynidyne on Pt(111) monitored with sum frequency generation: evidence for an ethynidene (or ethyl) intermediate*. Surface Science, 1995. **328**(1): p. 111-118.
61. Cremer, P.S. and G.A. Somorjai, *Surface science and catalysis of ethylene hydrogenation*. Journal of the Chemical Society, Faraday Transactions, 1995. **91**(20): p. 3671-3677.
62. Cortright, R.D., et al., *Kinetic study of ethylene hydrogenation*. Journal of Catalysis, 1991. **127**(1): p. 342-353.
63. Mei, D., M. Neurock, and C.M. Smith, *Hydrogenation of acetylene–ethylene mixtures over Pd and Pd–Ag alloys: First-principles-based kinetic Monte Carlo simulations*. Journal of Catalysis, 2009. **268**(2): p. 181-195.
64. Sheth, P.A., M. Neurock, and C.M. Smith, *First-Principles Analysis of the Effects of Alloying Pd with Ag for the Catalytic Hydrogenation of Acetylene–Ethylene Mixtures*. The Journal of Physical Chemistry B, 2005. **109**(25): p. 12449-12466.

65. Anderson, J., *Chemisorption and reactions on metallic films*. Vol. 1. 2012: Elsevier.
66. Campbell, J.S. and P.H. Emmett, *The catalytic hydrogenation of ethylene on nickel-copper and nickel-gold alloys*. Journal of Catalysis, 1967. **7**(3): p. 252-262.
67. Frankenburg, W.G., V.I. Komarewsky, and E.K. Rideal, *Advances in catalysis*. Vol. 4. 1952: Academic Press.
68. P. Sabatier, J.B.S., *Comptes Rendus Chimie*, 1897. **124**: p. 1358.
69. Horiuti, I. and M. Polanyi, *Exchange reactions of hydrogen on metallic catalysts*. Transactions of the Faraday Society, 1934. **30**(0): p. 1164-1172.
70. Kemball, C., *146. The deuteration and exchange of ethylene on evaporated metal catalysts at low temperatures*. Journal of the Chemical Society (Resumed), 1956(0): p. 735-743.
71. Dumesic, J.A., *The Microkinetics of heterogeneous catalysis*. 1993.
72. Cassuto, A., J. Kiss, and J.M. White, *On the orientation of low temperature π -bonded ethylene on Pt(111)*. Surface Science, 1991. **255**(3): p. 289-294.
73. Döll, R., et al., *Structure of disordered ethylene adsorbed on Pt(111) analyzed by diffuse LEED: asymmetrical di- σ bonding favored*. Surface Science, 1997. **374**(1): p. 151-161.
74. Davis, S.M., et al., *Radiotracer and thermal desorption studies of dehydrogenation and atmospheric hydrogenation of organic fragments obtained from [14C]ethylene chemisorbed over Pt(111) surfaces*. Journal of Catalysis, 1985. **92**(2): p. 240-246.
75. Rekoske, J.E., et al., *Microkinetic analysis of diverse experimental data for ethylene hydrogenation on platinum*. The Journal of Physical Chemistry, 1992. **96**(4): p. 1880-1888.
76. Cremer, P.S., et al., *Ethylene Hydrogenation on Pt(111) Monitored in Situ at High Pressures Using Sum Frequency Generation*. Journal of the American Chemical Society, 1996. **118**(12): p. 2942-2949.
77. Beebe, T.P. and J.T. Yates, *An in situ infrared spectroscopic investigation of the role of ethylidyne in the ethylene hydrogenation reaction on palladium/alumina*. Journal of the American Chemical Society, 1986. **108**(4): p. 663-671.
78. Mohsin, S.B., M. Trenary, and H.J. Robota, *Infrared identification of the low-temperature forms of ethylene adsorbed on platinum/alumina*. The Journal of Physical Chemistry, 1988. **92**(18): p. 5229-5233.

CHAPTER 2

Experimental and Analytical Techniques

2.1 Summary

In this thesis, a variety of experimental and analytical techniques were used to prepare and characterize Pd-based alloy catalysts. In Section 2.2, we describe the preparation of CSAFs and the design of the multichannel microreactor system used for the reaction kinetics studies. The fabrication process for the microreactor block is described in detail in Section 2.2.2. In Section 2.3, we describe the analytical methods used in this work. X-ray photoelectron spectroscopy (XPS) was used to characterize the composition and electronic structure of the CSAF surface. A description of the experimental and analytical techniques, and the principles of operation of the analytical instruments is explained in this chapter.

2.2 Experimental techniques

2.2.1 Composition spread alloy films (CSAFs)

Catalysts are complex multicomponent materials whose properties depend on many materials characteristics such as elemental composition, morphology and the surface atomic structure. And the catalytic activity and selectivity depend on operation conditions such as temperature, pressure, reactant feed condition and flow rate. The traditional approach to establishing catalyst characterization-catalytic activity relationship hence requires a preparation of a series of single-composition samples. So that sampling, complex multidimensional composition

spaces with high composition resolution can be a very time consuming and costly process. In order to accelerate this process and also provide a fundamental understanding of the multicomponent materials, high throughput approaches have been developed. These high throughput methods are based on preparation and parallel characterization of combinatorial materials libraries. This combinatorial approach has been successfully implemented for discovery and optimization of new pharmaceuticals, catalysts, polymers, superconductors, magnetic materials, structural materials and coatings [1-4].

High throughput methods are already making important contributions to catalysis science. Many different types of catalyst libraries have been developed and a variety of methods for screening catalyst activity within a library have been proposed and tested [5]. The composition spread alloy film (CSAF) is a high throughput sample library with a composition that is continuously variable across a single, compact substrate. Figure 2.1 shows an illustrations of a binary $\text{Ag}_x\text{Pd}_{1-x}$ and a ternary $\text{Cu}_x\text{Au}_y\text{Pd}_{1-x-y}$ CSAFs. For example, on a ternary CSAF (Figure 2.1-middle), it is possible to study catalysis on CuAuPd ternary composition space, as well as on CuAu,

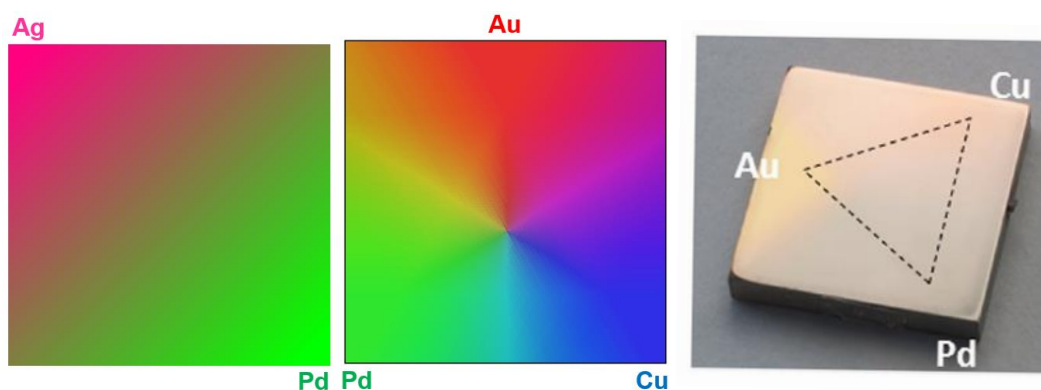


Figure 2.1. **Left:** Schematic representation of a binary $\text{Ag}_x\text{Pd}_{1-x}$ CSAF. **Middle:** Schematic representation of a ternary $\text{Cu}_x\text{Au}_y\text{Pd}_{1-x-y}$ CSAF. **Right:** Photograph of a $\text{Cu}_x\text{Au}_y\text{Pd}_{1-x-y}$ CSAF. In color, the Cu, Au, and Pd regions are readily identifiable.

CuPd and AuPd binary composition spaces and on pure Cu, Au and Pd metals. These films have been used to study inorganic materials before [2, 6-9]. Most previous work has focused on the characterization of composition, electronic structure or materials properties of those films [10-16]. However, none of the studies involve usage of these films in order to depict the relation between the fundamental kinetics parameters and composition across the entire composition spread.

2.2.1.1 CSAF deposition methods

Composition spread alloy films are typically prepared using a set of chemically distinct, single-component physical vapor deposition sources. In literature there can be found a couple of different strategies for controlling the flux distribution at the substrate surface which ultimately determines the lateral distribution of the CSAF composition as shown in Figure 2.2. One simple method that allows codeposition of components for intimate mixing uses chemical vapor deposition (CVD) as shown in Figure 2.2-a. In this method, CVD precursor inlets are positioned

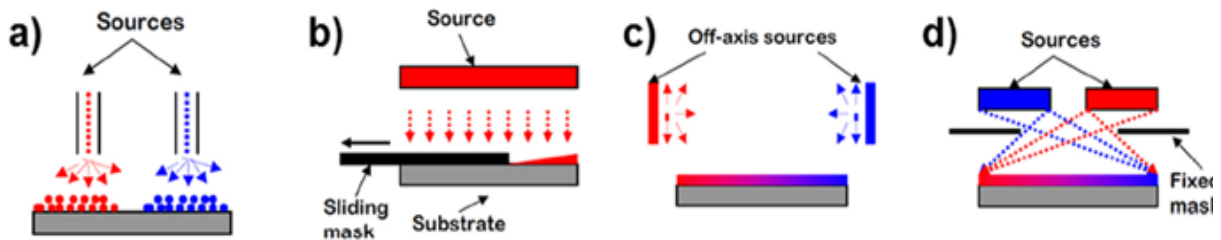


Figure 2.2. Schematic representations of four different methods for deposition of composition spread alloy films. **a)** Chemical vapor deposition sources positioned close to the substrate such that lateral diffusion in the gas phase results in a gradient in flux to the surface from each source. **b)** Deposition of individual components in wedges using a sliding contact mask. **c)** Offset positioning of sources to generate nonuniform flux distributions across the substrate surface. **d)** Simultaneous deposition of multiple components using fixed shadow masks to form the composition gradients.

closed to the substrate and diffusive, gas-phase intermixing is allowed to create the composition gradient on the substrate in the region between the two sources [17, 18]. This method allows limited control of the composition span for a given film and generates films of nonuniform thickness.

One other approach as illustrated in Figure 2.2-b uses a contact mask between the sources and the substrate. The mask slides across the substrate surface so that thickness varies across the substrate. Components cannot be co-deposited using this method and complete mixing may not be achieved by subsequent annealing [7, 19, 20]. As shown in Figure 2.2-c, off-axis sources can be used to create CSAFs as well, by doing that gradients in their fluxes across the substrate can be achieved [21, 22]. Using this idea, we have developed a simple, compact offset filament deposition tool on our laboratory which can deposit up to four components [23]. The tool is capable of repeatable, quantitative production of thin (≤ 100 nm) CSAFs on substrates that are up to ~ 12 mm in diameter. The tool can be used to deposit metals that are evaporable at temperature up to ~ 1500 K and can produce fluxes that vary by an order of magnitude across the substrate surface. This method benefits from the codeposition of several components however it does not allow the full span of composition space to be accessed on a single CSAF [24-27]. CSAFs that span the entire composition space can be prepared by using the shadow mask deposition method which allows codeposition of components with flux gradients (Figure 2.2-d) [28, 29].

2.2.1.2 Rotatable shadow mask deposition tool

In the rotatable shadow mask deposition method developed by our research group, components are evaporated from e-beam evaporation sources (Mantis Deposition Ltd.) and deposited as a thin film on a substrate. As shown in Figure 2.3, shadow masks are positioned with

an angle between the sources and the substrate. Up to four components can be deposited simultaneously with their masks oriented to deposit composition gradients in any desired direction. The positioning of the shadow mask between the source and the substrate determines the location and the spatial extent of the flux gradient at the substrate surface. The orientation of the shadow mask can also be used to control the direction of the flux gradient across the substrate. Also being able to rotate those shadow masks, leads a better control at net flux at either end of the gradient spread. A quartz crystal microbalance (Maxtek) was used to calibrate the fluxes from all the sources to be the same. Calibration was done by adjusting the power to each source according to the information from the quartz crystal microbalance. So using this deposition tool, a binary, ternary or quaternary CSAF that spans the entire composition space can be created [30]. $\text{Ag}_x\text{Pd}_{1-x}$ binary and $\text{Cu}_x\text{Au}_y\text{Pd}_{1-x-y}$ ternary CSAFs used in this work were prepared using this rotatable shadow mask deposition tool. The CSAF substrates are $14 \times 14 \text{ mm}^2$ of 2 mm thick Mo. Mo was chosen as a substrate since it does not interfere with the alloy but stabilizes the film against dewetting at annealing temperature [25, 31-33]. The deposited films that have a thickness of approximately 100 nm are annealed at 800 K for about an hour in the UHV chamber they are deposited.

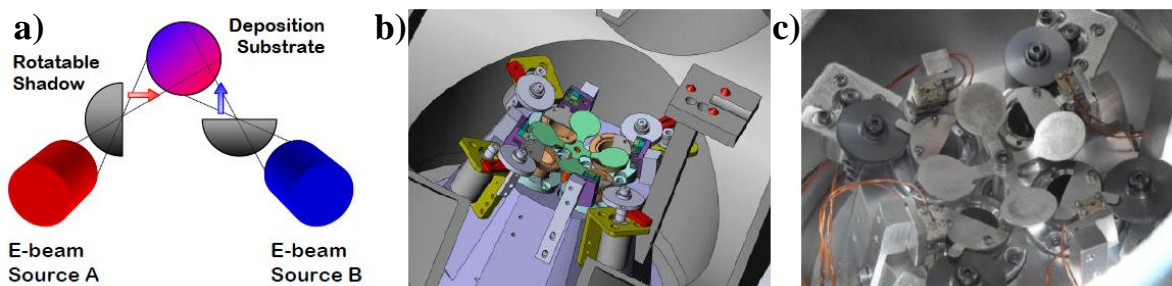


Figure 2.3. a) Schematic of the operating principle of the rotating shadow mask CSAF deposition tool. b) 3D rendering of the tool. c) Picture of the tool in an UHV chamber. The four-leafed clover is a manually rotatable shutter. The automated, semicircular, rotatable shadow masks can be seen between the clover leaves.

2.2.2 Multichannel microreactor system

In order to make spatially resolved catalytic activity measurements across the CSAF surfaces, a multichannel microreactor array was designed and constructed. For high throughput reaction kinetics studies, a different examples of reactor systems have been reported in literature. A standard six-flow reactor set-up was used by Moulijn et al., for environmental catalysis research. In this system the temperature and inlet composition was kept constant while the pressure and space velocity can be varied [34]. Morra et al., reported a 16 channel multi-tubular reactor which can test activity in 16 different packed beds. The temperature and inlet flow conditions can be varied in each of the reactors which enhances the diversity of the experiments that can be carried out [35]. Both of these two reaction systems are good examples for process intensification of using traditional flow reactors which have channel diameters around 7 mm. As reactor parallelization gains more attraction, the channel sizes become smaller and this leads to more compact designs. In one example a compact and metallic 1 channel-microreactor unit has been developed which favors better heat transfer along the catalyst layer which is utilized efficiently during the reactions without the formation of any hot or cold spots [36, 37]. This concept is then applied to a multi-parallel multichannel reactor system in which two reactions can be coupled to heat the endothermic and cool the exothermic reaction [38]. Finally, Senkan et al., came up with an 80-channel microreactor system which allows to activity measurements across 80 different catalyst beds in about 10 minutes [39].

In this study, we propose a 100-channel microreactor array (Figure 2.4-b) which can be used to make spatially resolved reactivity measurements (Figure 2.4-c) across the prepared CSAFs. The finished reactor array is composed of 100 inlet-outlet pairs, each pair defining a reaction

volume with a footprint of 700×800 microns, in a 10×10 array across the CSAF surface as shown as black squares in Figure 2.4-a.

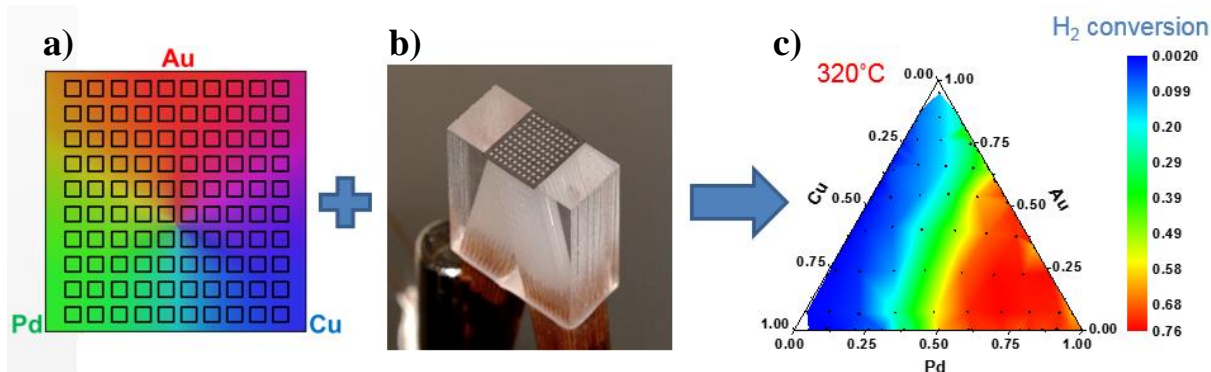


Figure 2.4. a) Array of regions isolated by the microreactor across a CSAF. b) Photo of glass reactor arrays. c) An example of spatially resolved catalytic activity measurement for H_2 - D_2 exchange reaction across a $Cu_xAu_yPd_{1-x-y}$ ternary CSAF. H_2 conversion was chosen to be the indicator of the catalytic activity. Hence the ternary diagram here shows how catalytic activity changes across the CSAF as a function of Cu, Au and Pd composition.

2.2.2.1 Design of the microreactor

The fabrication of the reactor is based on bonding glass sheets (Shott Borofloat®, 36 mm \times 27 mm \times 500 μ m thick) on which inlet and outlet channels had been micromachined. In our previous design, there were two types of glass layers in the microreactor device that differ in their

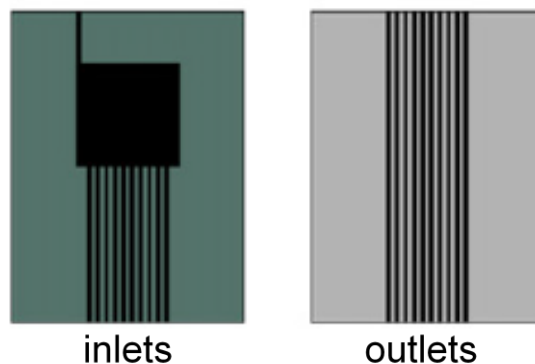


Figure 2.5. The old configuration of the inlet and outlet channels that are micromachined into flat glass sheets.

channel patterns as shown in Figure 2.5. Inlet layers are used for the delivery of reactant gas to the CSAF surface. There was a single inlet stream on one layer and then this main stream was divided into 10 parallel reactant channels. Outlet layers which route the product gas streams away from the CSAF surface to the gas analysis system have 10 parallel channels. This configuration of channels puts a lower limit on the allowable flow rates. The total flow rate was usually kept higher than 30 mL/min (or 0.30 mL/min per channel) in order to prevent the back-diffusion of the product gases into the inlet streams of neighboring channels. In order to eliminate this flow disadvantage of the microreactor, we have changed the configuration of the inlet and outlet channels and came up with the new design which contains 10 channels on the inlet plate and 10 channels on the outlet plate as shown in Figure 2.6-a. The details about the old microreactor structure can be found elsewhere [40].

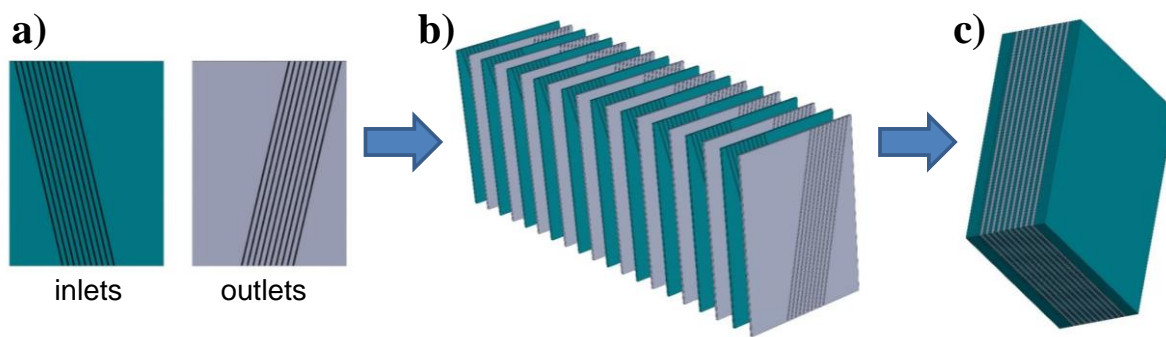


Figure 2.6. The design of the 100-channel microreactor array used to deliver and withdraw gases from the CSAF surface. **a)** Input and output channels are machined into flat glass sheets. **b)** 10 input and 10 output layers are alternately bonded together with cover plates. **c)** The side of the multichannel microreactor array having 100 inlet and outlet channels is ground and polished. This side of the device is mated with a gasket having 100 holes which is then sandwiched between the glass reactor and the CSAF catalyst surface.

2.2.2.2 Fabrication of the Microreactor

The construction of the multichannel microreactor array with the new design of inlet and outlet plates is shown schematically in Figure 2.6. 24 glass layers were used to prepare a microreactor block. This, flat borosilicate glass sheets (Shott Borofloat®, 36 mm × 27 mm × 500 μm thick) were used as the starting material for the layers. The channels are roughly rectangular in cross-section, measuring 500 μm wide and about 200 μm deep. The depth profiles of the channels are obtained using a profilometer and the consistency of these dimensions are checked. The surface topography of one random example channel can be seen in Figure 2.7. The cross-sectional area and shape of the channels do not influence the flow rate through the channel, because the channels provide much less resistance to gas flow than the glass capillaries connected to them to deliver and extract the gases. Ten of the inlet layers are used to deliver the reactant gases to the

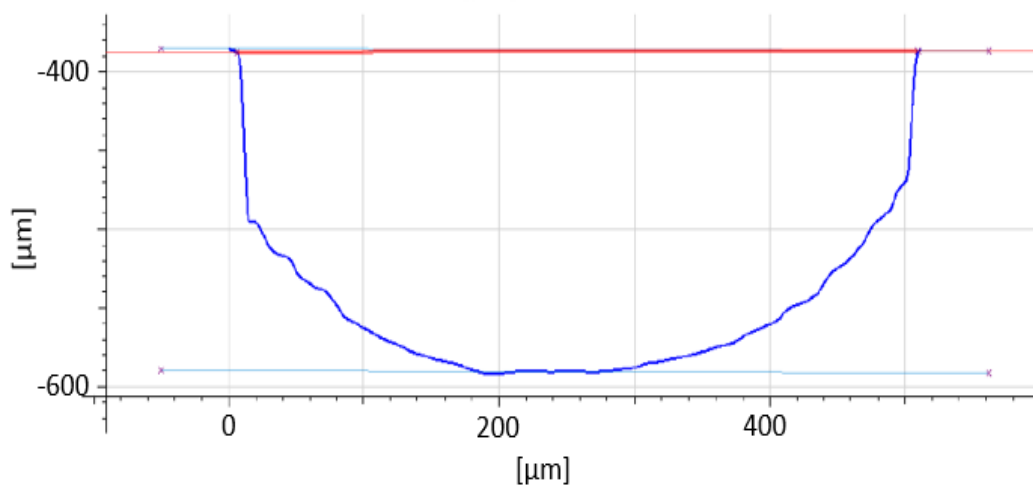


Figure 2.7. Depth profile of one of the random channels obtained using profilometer.

CSAF surface. Ten of the outlet layers are used to route the product gases away from the CSAF surface to the gas analysis system. The 10 inlet layers and 10 outlet layers are stacked alternately (Figure 2.6-b) and the device is completed by adding two non-channeled glass cover plates at the two sides.

The 24 glass layers were bonded together using a procedure that was developed to produce reliable bonding between many layers. The process does not use any bonding agents. It relies in the fact that flat, clean glass plates can bond to one another after appropriate chemical treatment [41]. The detailed bonding procedure steps are as follows:

- 1) The glass plates are placed into the stainless steel stand (Figure 2.8-a), the stand is placed into the beaker that is filled with deionized water and the beaker is placed into the sonicator (Branson). The glass plates are sonicated for 15 minutes.
- 2) Then the stand containing the glass plates is soaked into the 20% aqueous NaOH solution for 1 hour.
- 3) After soaking in NaOH solution, the glass plates are rinsed with deionized water. The stand is again put into a beaker that is filled with deionized water and sonicated for another 15 minutes. After this step, the glass plates are already bonded to each other but not very tightly.
- 4) The glass plates are stacked in the correct order under running deionized water. Immediately after bonding, the bonded glass plates are placed into the alignment aid (Figure 2.8-b) and aligned from both sides by pressing against the metal walls. The bonded block left overnight to allow water to evaporate.
- 5) The remainder of the water is evaporated in a vacuum oven (Fischer Scientific, 280A) first at room temperature for 2 hours, then at 90 °C for 2 hours and finally at 180 °C for 3 hours

as suggested in literature [42, 43]. The stacked plates are let to cool down to room temperature under vacuum. Drying, evaporation of water from bonded interface, is an important step in bonding which makes the bond strong. So usage of a vacuum environment along with increased temperature helps to speed up the drying process.

- 6) The microfluidic device is then put into the muffle furnace (Thermolyne) and annealed at 620 °C for 1 hour. An iron container with a cap was made for holding the bonded glass while it is inside the furnace. At this temperature, the glass plates become soft enough so that permanent bonds can form between the layers but not soft enough for the distortion of the channel structure. After it cooled down to room temperature, the multichannel microreactor block is ready.

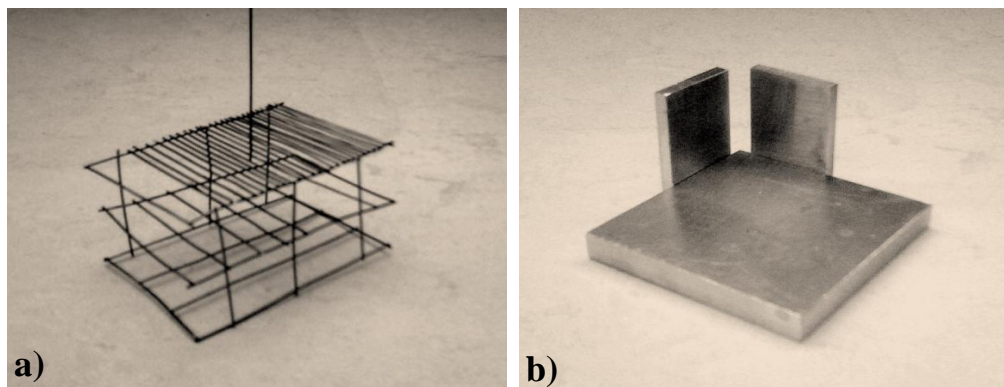


Figure 2.8. a) The stainless steel stand and b) the alignment aid used in the microreactor block preparation.

Using this 6-step procedure, totally 8 multichannel microreactor blocks have been prepared. Some bonding defects have been observed as interference fringes, however they usually occur at the edges of the glass sheets and do not impact the channel structure. Previously, we have tried chemical treatment consisting of soaking the glass plates into sulfuric acid solution as well as piranha solution. We found that in the case of borosilicate glass, treatment with NaOH solution

gives better results than the other options. So using this procedure, a 100-channel microreactor can be prepared in about 2 days, most of the time is spent during overnight drying of the glass plates after chemical treatment and during overnight cooling after the block is annealed in the muffle furnace.

After bonding, the side of the array having 100 reactant gas inlets and 100 product gas outlets (Figure 2.6-c) is polished to a high degree of flatness. This polished side of the device will ultimately be mated via a gasket with the CSAF surface. The opposite side of the microreactor block is also polished. This side contains 100 inlet holes and 100 outlet holes. Gases flow to and from the microreactor array through quartz capillaries. The detailed procedure to attach those capillaries into the microreactor block is as follows:

- 1) 100 pieces of 45 cm-long-capillaries (Polymicro Technologies, Inc., OD: 430 μm - ID: 320 μm) are cut. These are going to be used as the outlet channels.
- 2) 100 pieces of 20 cm-long-capillaries (Polymicro Technologies, Inc., OD: 430 μm - ID: 320 μm) are cut. These are going to be used as the inlet channels.
- 3) 200 pieces of 12 cm-long-capillaries (Polymicro Technologies, Inc., OD: 160 μm - ID: 100 μm) are cut (100 for the inlets and 100 for the outlets).



Figure 2.9. The schematic representation of the gluing process for the preparation of quartz capillaries that will be guiding flow to and from the microreactor.

- 4) 100 μm -ID capillaries are glued into the 320 μm -ID ones one by one using a silicon sealant capable of withstanding temperatures up to 250 °C (Silicone Solutions, SS-6001F). Insert 5 mm of the thinner capillary into the thicker one and glue them into each other using a very small amount of glue as shown in Figure 2.9. The silicone is usually cured in 5 to 10 minutes but overnight drying is suggested.
- 5) The prepared outlet capillaries should be labeled from 0 to 99.
- 6) First the prepared inlet capillaries are inserted into the microreactor. All 7 mm portion of the tiny capillaries should fully be inside the microreactor channels.
- 7) After all 100 inlet capillaries are in their right holes on the microreactor block, the side of the microreactor with the outlet channel openings should be covered with Kapton tape. Also all other sides of the microreactor is suggested to be covered with the same tape in order to protect the microreactor block from the silicone that is going to be used to glue the inlet capillaries into the microreactor.
- 8) Now, the inlet capillaries can be glued to the microreactor using the silicone sealant (Silicone Solutions, SS-6001F). The best way is to pour a lot of glue between each row of the inlets while one person is keeping the rows apart from each other, and the other one is pouring glue into the opening. It should be noted that the glue solidifies within 5 minutes. After pouring glue into each row, a tiny wire that can go between each row should be used to make sure that glue reaches to the microreactor surface completely. Be careful not to move the capillaries, you do not want them to come out of the microreactor openings. The block needs to be let dry overnight.
- 9) The same procedure needs to be followed for the outlet capillaries. And again the block needs to be let dry overnight.

10) The inlet capillaries need to be glued into each other from their free sides which do not glued into the microreactor. And also two separate 50 cm-long-capillaries (Polymicro Technologies, Inc., OD: 430 μm - ID: 320 μm) should be cut and glued together with the inlets. These two extra channels will be used as the reference channels for the product analysis part of the experiments. And then these glued-into-each-other 102 capillaries needs to be glued to the stainless steel tube (ID: 1/4"). This stainless steel tube will be used as the inlet flow divider. In this process Devcon 5-minute epoxy is used. While gluing inlets into each other, one needs to be sure that each of the 102 capillaries gets wet with epoxy individually. Otherwise leaks will be seen while operating the reactor. This gluing process should be done pretty quickly. Attaching the capillaries into the stainless steel tube while the epoxy blob around them is still fluid is strongly suggested.

11) After drying overnight, the microreactor is ready (Figure 2.10).



Figure 2.10. The photograph of the microreactor after 100 inlet and 100 outlet capillaries are glued in to the block and stainless steel inlet flow divider is prepared.

2.2.2.3 Reactant gas delivery and product gas analysis

The schematic representation of the experimental system is shown in Figure 2.11. The reactant gas mixture is delivered to the microreactor via 360 μm ID polyimide-coated quartz capillaries and flow rates are controlled by mass flow controllers (Aalborg Instruments, GFC-17). The inlet flow is then distributed equally to all 100 inlet channels. Each inlet and outlet pair of channels is isolated from its neighbors by a Kalrez 7075 (Dupont) flexible gasket which has 10×10 array of $700 \mu\text{m} \times 800 \mu\text{m}$ holes on it [44] (Figure 2.12). The gasket is compressed between the microreactor and the CSAF sample under study. The effectiveness of the gasket for the elimination of the intermixing of the gases between neighboring reaction channels is illustrated somewhere else [40]. Perfluoroelastomer Kalrez 7075 was found to be the most suitable material since it is soft enough to provide gas-tight seal and it does not distort at temperatures up to 590 K. The CSAF was heated by a heater placed on top of it (Figure 2.11-b) and the temperature of the reaction was monitored and controlled by a thermocouple spot-welded to one side of the CSAF substrate.

The product gas streams from each of the 100 microchannels are independently accessible for analysis using an automated sampler which has a stepper arm that can move in x and y directions (Figure 2.11-d). A 10 μm ID quartz capillary is mounted on this stepper arm which serves as the sampling capillary. The stepper arm is connected to an x-y positioning stage. Its two orthogonal linear motion stages, each driven by a programmable stepper motor, insert the sampling capillary into the gas stream from 100 output capillaries carrying the product gas from the multichannel microreactor array. To guide the end of the sampling capillary, tapered stainless steel tubes are connected to the ends of the 100 output capillaries. Product gases are transported to the quadrupole mass spectrometer (Stanford Research Systems RGA-200). From the open

sampling end of the output capillaries, there is a possibility to observe air diffusion against the product gas flow especially in the case of light product gases (for example, H₂, HD, or D₂). Similar problems with air back diffusion was observed in literature [45]. This can be minimized by increasing total flow rate.

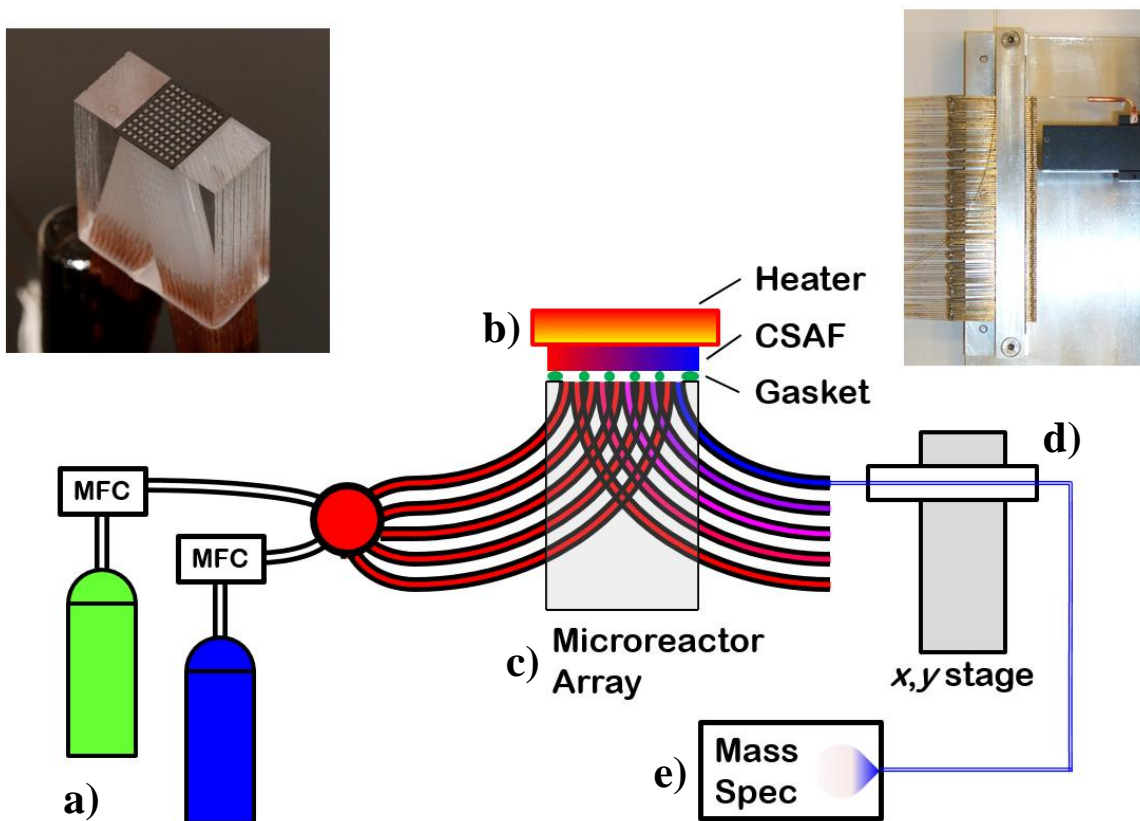


Figure 2.11. Illustration of the experimental setup. **a)** Mass flow controllers. **b)** A gasket is used in between the CSAF and the microreactor to isolate reaction volumes. A heater is placed on top of the CSAF and a thermocouple is attached to the CSAF substrate. **c)** Microfluidic reactor and illustration of the outlet channels. **d)** Automated sampler. A sampling capillary is placed on a robot arm that can move in x and y directions, i.e. capillary can move in and out of a channel and step to the next channel. **e)** Quadrupole mass spectrometer.

As mentioned at the 10th step of the microreactor fabrication procedure above, there are actually 102 inlet capillaries instead of 100 inlet channel present in the microreactor block. The presence of these 2 extra channels that are bypassing the microreactor constitutes one of the unique features of our reaction system. Through one of these extra channels a sample of the inlet flow is directly sent to the mass spectrometer for the gas analysis. This channel is giving information about the reaction that is under investigation when there is no conversion. To the second one of these extra channels, a coiled stainless tube (OD: 0.028” - ID: 0.02”) which is filled with pure Pd wire (ESPI Metals, Diameter: 0.004”, Purity: 3N5) is attached. This Pd filled tube is actually acting as a conventional flow reactor. This simple coiled reactor is coupled with a hemispherical heating mantle so that the temperature of the reactor can be adjusted as desired. The amount of the Pd and the operation temperature is adjusted such that in this reactor the reaction that is under investigation always reaches to the full conversion. The outlet of this reactor is sent to the mass spectrometer for the quantification of the product gases. So these two extra channels are providing information for the specific reaction when there is zero and full conversions have been observed. These values can be used as the reference points in order to calculate the conversions at each of the 100 different channels in the multichannel microreactor array. Also being able to quantify the amount of air diffusing against the product gas flow in those two reference channels enhances the quality of the product quantification calculations.

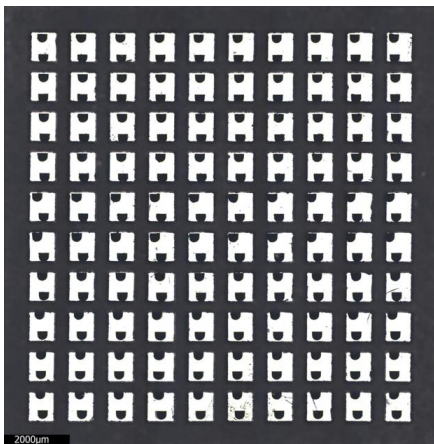


Figure 2.12. The optical image of the laser-machined elastomer gasket that is put on top of the microreactor array. The $700\ \mu\text{m} \times 800\ \mu\text{m}$ rectangular windows in the gasket define 100 reaction areas on the CSAF. In each isolated window a pair of inlet and outlet channel openings can be seen.

2.3 Analytical techniques

2.3.1 X-ray photoelectron spectroscopy

X-ray photoelectron spectroscopy (XPS) is a technique to obtain qualitative and quantitative information of the elemental composition of surfaces. It can be used to determine the chemical composition in the near-surface region (~ 1 to $10\ \text{nm}$) of CSAFs as well as density of electronic states. XPS analysis of the CSAFs was performed in a ThetaProbe chamber (Thermo-Fisher Scientific Inc.).

The physics of the XPS technique is schematically shown in Figure 2.13. An X-ray beam is pointed at the target surface and ejects core-level electrons (photoelectrons) from the atoms in the sample. Only photoelectrons in the near-surface region have enough kinetic energy to escape the sample.

The kinetic energy of these photoelectrons is measured by an electron energy analyzer and is related to the binding energy of the core-level electrons according to:

$$E_K = E_{h\nu} - E_B - \phi \quad (1)$$

where E_K is the kinetic energy of the photoelectron, $E_{h\nu}$ is the energy of the incident X-ray beam, E_B is the binding energy of the electron, and ϕ is the work function of the spectrometer. The binding energy of the core-level electrons is characteristic of the atom which the photoelectron was generated. Therefore, XPS is a technique for characterizing the chemical composition in the

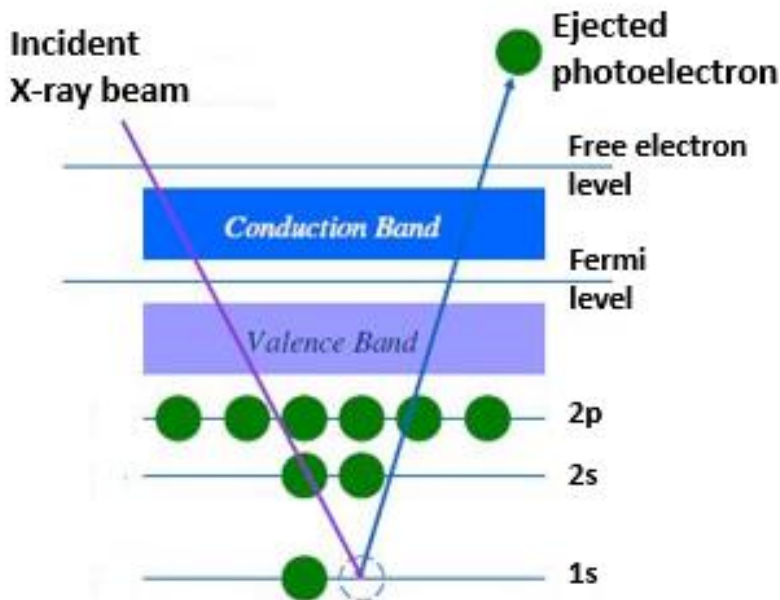


Figure 2.13. Schematic representation of X-ray photoemission process. An incident X-ray beam ejects a core level electron from an atom near the surface of the solid sample. The kinetic energy of the ejected photoelectron is related to the binding energy of the electron, which is characteristic of the atom from which the photoelectron originated. The mean free path of photoelectrons is ~1 to 10 nm, making XPS a surface-sensitive technique for characterizing the chemical composition in the near surface region of solid samples.

near surface regions of solid samples. Kinetic energies of the emitted photoelectrons determine the mean free paths of the photoelectrons. Only the photoelectrons that are in the near surface region (~ 1 to 10 nm) can escape from the surface and this fact makes XPS a very useful technique to characterize the near surface composition of the solid surfaces (up to 7 atomic layers into the surface)[46-48]. We use XPS to determine the composition of our binary $\text{Ag}_x\text{Pd}_{1-x}$ and ternary $\text{Cu}_x\text{Au}_y\text{Pd}_{1-x-y}$ CSAFs in terms of atomic fractions of Ag, Au, Cu and Pd at discrete positions on the CSAF surface.

In order to perform XPS measurements the CSAF sample was mounted onto a sample holder that can be heated up to 1000 K. The sample can be moved by an automated stage in the ThetaProbe so that the analysis of the CSAF at a set of predetermined points (CSAF compositions) can be done. Spatially resolved maps of the Ag $3d_{5/2}$, Au $4f_{7/2}$, Cu $2p_{3/2}$, and Pd $3d_{3/2}$ XP spectra were obtained by lateral translation of the CSAF such that its plane intersected the source-analyzer focal point. The X-ray spot size was arranged to be around 200 μm . The pass energy of the hemispherical energy analyzer was set to 40 eV. Atomic fractions of the components were estimated using Avantage Data System software provided by the manufacturer of the ThetaProbe. This software contains a library of peak positions and relative intensities of the pure metals which is used to identify the components and their compositions from the measured spectra.

XPS was also used to map the valence band electronic structure of the prepared CSAFs. The density of the filled states was mapped as a function of energy with respect to fermi level, which is located at zero on the energy scale.

The XPS-derived average energy of the filled v-band (ε_v) were calculated from the background subtracted v-band spectra obtained from the CSAFs based on

$$\varepsilon_v = \frac{\int N(\varepsilon) \varepsilon d\varepsilon}{\int N(\varepsilon) d\varepsilon} \quad (2)$$

where ε is the energy of filled state in the valence band relative to the Fermi level, ε_v is the average energy of the valence band and $N(\varepsilon)$ is the density of filled states at the energy, ε , which is proportional to the intensity of v-band spectrum. The v-band spectra were collected at binding energies in range from 0 to 25 with analyzer pass energy of 40 eV.

2.4 References

1. Hogan Jr, J.C., *Combinatorial chemistry in drug discovery*. 1997. **15**: p. 328.
2. Cui, J., et al., *Combinatorial search of thermoelastic shape-memory alloys with extremely small hysteresis width*. Nat Mater, 2006. **5**(4): p. 286-290.
3. Stanton, M.L. and J.A. Holcombe, *Array-Based Split-Pool Combinatorial Screening of Potential Catalysts*. Journal of Combinatorial Chemistry, 2007. **9**(3): p. 359-365.
4. Zech, T., et al., *Design, fabrication, and application of a massively parallel single-bead microreactor system for high-throughput experimentation in heterogeneous catalysis*. Review of Scientific Instruments, 2005. **76**(6): p. 062215.
5. Farrusseng, D., *High-throughput heterogeneous catalysis*. Surface Science Reports, 2008. **63**(11): p. 487-513.
6. Takeuchi, I., et al., *Identification of novel compositions of ferromagnetic shape-memory alloys using composition spreads*. Nat Mater, 2003. **2**(3): p. 180-184.
7. Ohkubo, I., et al., *Continuous composition-spread thin films of transition metal oxides by pulsed-laser deposition*. Applied Surface Science, 2004. **223**(1): p. 35-38.
8. Löbel, R., et al., *Combinatorial fabrication and high-throughput characterization of a Ti–Ni–Cu shape memory thin film composition spread*. Materials Science and Engineering: A, 2008. **481-482**(Supplement C): p. 151-155.
9. Famodu, O.O., et al., *Combinatorial Investigation of Ferromagnetic Shape-Memory Alloys in the Ni–Mn–Al Ternary System Using a Composition Spread Technique*. MATERIALS TRANSACTIONS, 2004. **45**(2): p. 173-177.

10. Green, M.L., I. Takeuchi, and J.R. Hattrick-Simpers, *Applications of high throughput (combinatorial) methodologies to electronic, magnetic, optical, and energy-related materials*. Journal of Applied Physics, 2013. **113**(23): p. 231101.
11. Grochla, D., et al., *Time- and space-resolved high-throughput characterization of stresses during sputtering and thermal processing of Al–Cr–N thin films*. Journal of Physics D: Applied Physics, 2013. **46**(8): p. 084011.
12. Hamann, S., M. Ehmann, and A. Ludwig, *High-throughput characterization of stresses in thin film materials libraries using Si cantilever array wafers and digital holographic microscopy*. Review of Scientific Instruments, 2011. **82**(6): p. 063903.
13. Guerin, S., et al., *Combinatorial Electrochemical Screening of Fuel Cell Electrocatalysts*. Journal of Combinatorial Chemistry, 2004. **6**(1): p. 149-158.
14. Strasser, P., *Combinatorial Optimization of Ternary Pt Alloy Catalysts for the Electrooxidation of Methanol*. Journal of Combinatorial Chemistry, 2008. **10**(2): p. 216-224.
15. *Doped Titanium Dioxide Films Prepared by Pulsed Laser Deposition Method*. International Journal of Photoenergy, 2012. **2012**: p. 8.
16. Sun, S., et al., *Application of parallel synthesis and high throughput characterization in photocatalyst discovery*. Combinatorial chemistry & high throughput screening, 2011. **14**(3): p. 160-172.
17. Wang, Q., F. Liu, and D. Han, *High-Throughput Chemical Vapor Deposition System and Thin-Film Silicon Library*. Macromolecular Rapid Communications, 2004. **25**(1): p. 326-329.
18. Wang, Q., et al., *A combinatorial study of materials in transition from amorphous to microcrystalline silicon*. Solid State Communications, 1999. **113**(3): p. 175-178.
19. Yamada, Y., et al., *Fabrication of Ternary Phase Composition-Spread Thin Film Libraries and Their High-Throughput Characterization: $Ti_{1-x-y}Zr_xHf_yO_2$ for Bandgap Engineering*. Journal of Superconductivity, 2005. **18**(1): p. 109-113.
20. Bäte, M., et al., *Combinatorial Investigation of the Vapor Deposition Polymerization of Aromatic Polyimides*. Macromolecular Rapid Communications, 2004. **25**(1): p. 371-376.
21. Kennedy, K., et al., *Rapid Method for Determining Ternary-Alloy Phase Diagrams*. Journal of Applied Physics, 1965. **36**(12): p. 3808-3810.
22. van Dover, R.B. and L.F. Schneemeyer, *The Codeposited Composition Spread Approach to High-Throughput Discovery/Exploration of Inorganic Materials*. Macromolecular Rapid Communications, 2004. **25**(1): p. 150-157.
23. Priyadarshini, D., et al., *Compact tool for deposition of composition spread alloy films*. Journal of Vacuum Science & Technology A: Vacuum, Surfaces, and Films, 2012. **30**(1): p. 011503.
24. Gumuslu, G., et al., *Correlation of Electronic Structure with Catalytic Activity: H₂–D₂ Exchange across Cu_xPd_{1-x} Composition Space*. ACS Catalysis, 2015. **5**(5): p. 3137-3147.

25. Priyadarshini, D., et al., *High-Throughput Characterization of Surface Segregation in Cu_xPd_{1-x} Alloys*. The Journal of Physical Chemistry C, 2011. **115**(20): p. 10155-10163.
26. Boes, J.R., et al., *Estimating Bulk-Composition-Dependent H_2 Adsorption Energies on Cu_xPd_{1-x} Alloy (111) Surfaces*. ACS Catalysis, 2015. **5**(2): p. 1020-1026.
27. Boes, J.R., et al., *Core level shifts in $Cu-Pd$ alloys as a function of bulk composition and structure*. Surface Science, 2015. **640**: p. 127-132.
28. Guerin, S. and B. Hayden, *Vapour Deposition Method*. 2007, Google Patents.
29. Guerin, S. and B.E. Hayden, *Physical Vapor Deposition Method for the High-Throughput Synthesis of Solid-State Material Libraries*. Journal of Combinatorial Chemistry, 2006. **8**(1): p. 66-73.
30. Fleutot, B., J.B. Miller, and A.J. Gellman, *Apparatus for deposition of composition spread alloy films: The rotatable shadow mask*. Journal of Vacuum Science & Technology A: Vacuum, Surfaces, and Films, 2012. **30**(6): p. 061511.
31. Wei, T., J. Wang, and D.W. Goodman, *Characterization and Chemical Properties of $Pd-Au$ Alloy Surfaces†*. The Journal of Physical Chemistry C, 2007. **111**(25): p. 8781-8788.
32. He, J.W., et al., *Surface chemistry of monolayer metallic films on $Re(0001)$ and $Mo(110)$* . Journal of Vacuum Science & Technology A: Vacuum, Surfaces, and Films, 1990. **8**(3): p. 2435-2444.
33. Park, C., E. Bauer, and H. Poppa, *Growth and alloying of Pd films on $Mo(110)$ surfaces*. Surface Science, 1985. **154**(2): p. 371-393.
34. Moulijn, J.A., et al., *High-throughput experimentation in catalyst testing and in kinetic studies for heterogeneous catalysis*. Catalysis Today, 2003. **81**(3): p. 457-471.
35. Morra, G., et al., *High-throughput gas phase transient reactor for catalytic material characterization and kinetic studies*. Chemical Engineering Journal, 2008. **138**(1): p. 379-388.
36. Sen, I. and A.K. Avci, *Simulation of exhaust gas reforming of propane in a heat exchange integrated microchannel reactor*. International Journal of Hydrogen Energy, 2014. **39**(2): p. 844-852.
37. Sen, I. and A.K. Avci, *Exhaust Gas Reforming of Methane in a Catalytic Microchannel Reactor*. Industrial & Engineering Chemistry Research, 2014. **53**(5): p. 1760-1767.
38. Cao, C., et al., *Catalyst screening and kinetic studies using microchannel reactors*. Catalysis Today, 2007. **125**(1): p. 29-33.
39. Senkan, S., et al., *High-Throughput Testing of Heterogeneous Catalyst Libraries Using Array Microreactors and Mass Spectrometry*. Angewandte Chemie International Edition, 1999. **38**(18): p. 2794-2799.
40. Kondratyuk, P., et al., *A microreactor array for spatially resolved measurement of catalytic activity for high-throughput catalysis science*. Journal of Catalysis, 2013. **300**(Supplement C): p. 55-62.

41. Jia, Z.-J., Q. Fang, and Z.-L. Fang, *Bonding of Glass Microfluidic Chips at Room Temperatures*. Analytical Chemistry, 2004. **76**(18): p. 5597-5602.
42. Zhuang, G., et al., *A low temperature bonding of quartz microfluidic chip for serum lipoproteins analysis*. Biomedical Microdevices, 2006. **8**(3): p. 255-261.
43. Pan, C.T., et al., *A low-temperature wafer bonding technique using patternable materials*. Journal of Micromechanics and Microengineering, 2002. **12**(5): p. 611.
44. Kondratyuk, P., et al., *A microreactor array for spatially resolved measurement of catalytic activity for high-throughput catalysis science*. Journal of Catalysis, 2013. **300**: p. 55-62.
45. Claus, P., D. Hönicke, and T. Zech, *Miniaturization of screening devices for the combinatorial development of heterogeneous catalysts*. Catalysis Today, 2001. **67**(4): p. 319-339.
46. Ertl, G. and J. Küppers, *Low energy electrons and surface chemistry*. 1985, Weinheim, Federal Republic of Germany; Deerfield Beach, FL, USA: VCH.
47. Miller, J.B., C. Matranga, and A.J. Gellman, *Surface segregation in a polycrystalline Pd70Cu30 alloy hydrogen purification membrane*. Surface Science, 2008. **602**(1): p. 375-382.
48. Miller, J.B., B.D. Morreale, and A.J. Gellman, *The effect of adsorbed sulfur on surface segregation in a polycrystalline Pd70Cu30 alloy*. Surface Science, 2008. **602**(10): p. 1819-1825.

CHAPTER 3

Characterization of Composition, Electronic Structure and H₂-D₂

Exchange Activity across Ag_xPd_{1-x} Alloys

3.1 Chapter Abstract

Finding the optimal catalyst composition for a given application is the major challenge in multicomponent catalyst design due to the need to perform many catalyst preparations, characterization and reactivity measurements across composition space. To accelerate this search, thin multicomponent films called Composition Spread Alloy Films (CSAFs) are prepared, which have composition gradients parallel to their surfaces, A_xB_{1-x} with $x = 0 \rightarrow 1$ and $y = 0 \rightarrow 1-x$. In order to study alloy catalysis across a CSAF, a 100 channel microreactor array has been developed to run steady state catalytic reactions at different positions or alloy compositions on the CSAF. Ag_xPd_{1-x} CSAFs spanning all of the binary composition space have been prepared using a rotating shadow mask CSAF deposition tool developed in-house.

The relationship between alloy catalyst activity and the electronic structure was investigated experimentally across Ag_xPd_{1-x} CSAFs. H₂-D₂ exchange kinetics were measured at 90 discrete compositions on the CSAFs over a temperature range of 333 – 593 K. Characterization of the CSAFs was done using X-ray photoelectron spectroscopy. H₂ conversion was chosen to be the indicator of activity and it was found to increase with increasing Pd content. A microkinetic model was used to estimate the energy barriers to dissociative adsorption and associative desorption of H₂ as functions of alloy composition, x . Across the Ag_xPd_{1-x} CSAF, increasing Pd

content from 0 to 1 was found to decrease the adsorption barrier from 0.40 to 0.02 eV and also decrease the desorption barrier from 0.64 to 0.84 eV, which suggests H₂-D₂ exchange is limited by H₂ desorption. Spatially resolved X-ray photoelectron spectra obtained from the CSAFs were used to estimate the energy of the valence-band center as a function of alloy composition. The v-band center shifted monotonically from -3.4 to -6.2 eV across the Ag_xPd_{1-x} CSAF. The barrier to dissociative adsorption of H₂ was found to decrease as the v-band energy increases. This data provides the first experimental correlation of elementary reaction barriers with valence band energy across a continuous span of Ag-Pd binary alloy composition space.

3.2 Introduction

Pd is a good membrane material to obtain high purity H₂ [1]. It has high ability to dissociate and dissolve H₂, a high H₂ selectivity versus other gases and the membrane costs are competitive [2, 3]. However, Pd has some drawbacks such as H₂ embrittlement with temperature and sulfur poisoning [4-8]. These drawbacks often can be eliminated by alloying Pd with other metals such as Ag, Cu, Au, Fe, Y [9-16]. Alloying Pd with Ag enhances its mechanical strength [6, 15, 16] and increases H atom permeability [6, 7, 17]. Addition of 23 at.% Ag to pure Pd was reported to decrease the critical temperature and pressure for the α -PdH to β -PdH transition and to increase H₂ solubility dramatically [15, 17]. The H atom permeability of Ag-Pd membranes was found to be 1.7 times higher than that of Cu-Pd and Au-Pd [17]. Sieverts *et al.* showed that Ag-Pd has a higher H₂ solubility than Au-Pd, Cu-Pd and Pt-Pd alloys and that this is, in part, responsible for the high permeability of Ag-Pd membranes [18, 19].

H₂ transport through Pd membranes involves three main steps, H₂ adsorbs dissociatively on the upstream side of the membrane surface, H atoms diffuse through the membrane and then H₂ recombinatively desorbs from the downstream surface [20, 21]. This transport is known to be limited by the bulk diffusion of H atoms as manifested by its ½-order dependence on H₂ pressure, P_{H₂} [22]. Decreasing the membrane thickness increases the order of the pressure dependence and increases the permeability through Ag-Pd alloys [6, 15, 22]. For ultrathin Ag-Pd alloy films with thicknesses less than 500 nm, H₂ transport was reported to be first-order in P_{H₂} over the temperature range 373 K < T < 523 K [6]. This result indicates that surface reactions, i.e. the H₂ adsorption and desorption steps at the upstream and downstream surface, dictate the rate of hydrogen transport through ultrathin Ag-Pd membranes. The bulk diffusion step has been investigated extensively in the literature [23-25]. However, the dissociative adsorption and associative desorption processes are not yet well understood on Pd-based alloy surfaces. The kinetics of the H₂-D₂ exchange (H₂ + D₂ → 2HD) reaction can provide valuable information about those steps. Hence, our high throughput characterization of the kinetics of the H₂-D₂ exchange reaction on Ag_xPd_{1-x} alloys provides important insight into hydrogen purification by Pd-based membranes.

H₂ is known to dissociate on Pd without significant activation barriers [26-30]. However, molecular H₂ does not adsorb dissociatively on Ag [31-33]. Dissociative adsorption of H₂ does not occur at room temperature on Ag single crystal surfaces [34] and dissociation of H₂ on Ag surfaces is predicted to be an endothermic process [35-38]. This lack of affinity of Ag toward H₂ is usually attributed to the filled *d*-band of Ag [39-41] and the fact that adsorbed species interact with *d*-band electrons of metal surfaces [1, 42, 43]. However, the effect of alloying Pd with Ag on the energetics of the H₂ dissociation reaction has not been investigated. Hence, the activity-

electronic structure–composition relationship for Ag-Pd alloys that we present in this paper provides benchmarks for further experimental and theoretical studies.

In this study, a $\text{Ag}_x\text{Pd}_{1-x}$ CSAF that spans a continuous range of compositions ($x = 0 \rightarrow 1$) was used to characterize the activity for H_2 - D_2 exchange. Quantitative kinetic data has been obtained and analyzed to elucidate the mechanism and extract fundamental kinetic parameters for H_2 - D_2 exchange as functions of alloy composition. H_2 - D_2 exchange is an ideal model reaction to demonstrate the correlation of kinetics parameters with alloy characteristics, such as electronic structure. Within the Langmuir-Hinshelwood framework for modeling surface reaction kinetics, H_2 - D_2 exchange has the simplest possible reaction mechanism parameterized by just two rate constants: k_{ads} , for the dissociative adsorption of H_2 and D_2 and k_{des} , for the recombinative desorption of H_2 and D_2 . By measuring these two rate constants over a range of temperature, the activation barriers to dissociative adsorption (ΔE_{ads}^\ddagger) and recombinative desorption (ΔE_{des}^\ddagger) can be estimated across $\text{Ag}_x\text{Pd}_{1-x}$ alloy composition space.

In this work, H_2 - D_2 exchange kinetics on a $\text{Ag}_x\text{Pd}_{1-x}$ CSAF have been measured to determine values of ΔE_{ads}^\ddagger and ΔE_{des}^\ddagger as functions of alloy composition. In addition, the barriers have been correlated with the valence band electronic structure of the alloy at each composition. Ligand effects on catalytic activity are determined by the width and/or the center of the d -band. It is known that changes in the position of d -band center relative to the Fermi level, lead to changes in the energy barriers for adsorption, which lead to a change in activity [44, 45]. As the center of the occupied states in the d -band increases towards the Fermi-level, the alloy becomes more active [45]. The valence band electronic structure can be measured using electronic spectroscopic methods such as X-ray photoelectron spectroscopy (XPS) or UV photoelectron spectroscopy (UPS) [44, 46]. Using XPS we have estimated the average energy of the filled states of the valence

band (s -, p -, and d -bands), $\epsilon_v(x)$, across composition space and shown that the v -band shifts toward the Fermi level as the Ag fraction decreases. Using the v -band energies as an experimental proxy for the d -band energy, we can correlate reaction barriers (ΔE_{ads}^\ddagger and ΔE_{des}^\ddagger) with $\epsilon_v(x)$ across the entire $\text{Ag}_x\text{Pd}_{1-x}$ composition space. We have observed that as Ag content decreases, the d -band center shifts toward the Fermi level, consistent with the observed decrease in the reaction barriers. This work demonstrates a high-throughput experimental methodology for correlation of fundamental kinetic parameters, such as ΔE_{ads}^\ddagger and ΔE_{des}^\ddagger , with the electronic structure of multicomponent alloy catalysts. This general methodology should be applicable to a wide-range of catalytic reactions.

3.3 Experimental

3.3.1 CSAF Preparation

The CSAF samples were prepared by evaporative deposition of Pd and Ag onto a $14 \times 14 \times 2 \text{ mm}^3$ polished Mo substrate (Valley Design Corp.) using a rotatable shadow mask CSAF deposition tool that has been described in detail previously [47]. Electron beam evaporation sources containing Pd and Ag were positioned on opposite sides of the substrate. Deposition rates from both sources were controlled by filament heating power and measured using a QCM. The film thickness ($\sim 100 \text{ nm}$ in this work) was controlled by the deposition time. The position and orientation of the shadow masks between the sources and the substrate result in a flux gradient across the substrate. Mo was chosen as a substrate material because it does not alloy with Ag or Pd and stabilizes the film against dewetting at annealing temperatures [46, 48-50]. CSAFs were deposited and then annealed (800 K for 1 h) under ultrahigh vacuum (UHV) conditions.

3.3.2 Characterization of CSAF Composition and Electronic Structure

XPS analysis of the $\text{Ag}_x\text{Pd}_{1-x}$ CSAF was performed in a ThetaProbe™ (Thermo-Fisher Scientific Inc.) to map the local composition and the valence band electronic structure across the sample surface. In order to perform XPS measurements, the CSAF sample was mounted onto a sample holder. The sample can be moved by an automated stage in the ThetaProbe allowing analysis (composition and valence band spectra) of the CSAF at a set of predetermined points. Spatially resolved maps of the Ag $3d_{5/2}$, and Pd $3d_{3/2}$ XP spectra were obtained by lateral translation of the CSAF such that its plane intersected the source-analyzer focal point. The x-ray spot size was ~ 200 μm in diameter. The pass energy of the hemispherical energy analyzer was set to 40 eV. Atomic fractions of the components were estimated using the Avantage™ Data System software package. This software contains a library of the binding energies and the relative intensities of XPS features from the pure metals. These are used to identify the components and their compositions from the measured XP spectra.

XPS was also used to map the valence band electronic structure of the CSAFs as a function of composition. The density of the filled states was mapped as a function of binding energy with respect to Fermi level. The ν -band spectra were collected at binding energies in the range 0 to 25 eV with an analyzer pass energy of 40 eV. The XPS-derived average energy of the filled ν -band (ϵ_ν) was calculated from the background subtracted ν -band spectra obtained from the CSAFs [51].

3.3.3 Characterization of H₂-D₂ Exchange Activity across Ag_xPd_{1-x} CSAF

The H₂-D₂ exchange activity of the Ag_xPd_{1-x} CSAFs was measured by flowing H₂, D₂, and Ar through a 100-channel microreactor array. The experimental setup used was explained in detail in Section 2.2.2. Mass flow controllers (Aalborg GFC 17) were used to regulate the flow rates of H₂ (99.999%, Valley National Gases), D₂ (99.999%, Valley National Gases) and Ar (99.999%, Valley National Gases) through the microreactor to the CSAF surface. A surface

Table 3.1. Flow rates of H₂ ($F_{H_2}^{in}$), D₂ ($F_{D_2}^{in}$), and Ar (F_{Ar}^{in}) in the fourteen different gas conditions used during H₂-D₂ exchange experiments at $P_{tot} = 1$ atm. Flow rates in one channel can be found by dividing the listed values into 100. Total flow rate is kept constant at 0.33 mL/min per channel.

	$F_{H_2}^{in}$ (mL/min)	$F_{D_2}^{in}$ (mL/min)	F_{Ar}^{in} (mL/min)	P_{H_2} (kPa)	P_{D_2} (kPa)
1	9.00	9.00	12.00	30.4	30.4
2	9.00	4.50	16.50	30.4	15.2
3	9.00	3.00	18.00	30.4	10.1
4	9.00	1.50	19.50	30.4	5.07
5	9.00	1.00	20.00	30.4	3.38
6	9.00	0.45	20.55	30.4	1.52
7	9.00	0.18	20.81	30.4	0.61
8	9.00	0.09	20.91	30.4	0.30
9	9.00	0.05	20.96	30.4	0.15
10	9.00	0.02	20.98	30.4	0.06
11	9.00	0.01	20.99	30.4	0.03
12	4.50	0.01	25.49	15.2	0.30
13	2.25	0.01	27.74	7.60	0.30
14	0.90	0.01	29.09	3.04	0.30

area corresponding to one catalyst composition across the ternary CSAF was approximately 0.006 cm². The inlet flow rates of H₂, D₂, and Ar were adjusted to the conditions listed in Table 3.1.

The H₂-D₂ exchange activity of Ag_xPd_{1-x} CSAF was measured at atmospheric pressure and over a temperature range from 333-593 K with H₂ partial pressures ranging from 3.04 to 30.4 kPa and D₂ partial pressures ranging from 0.03 to 30.4 kPa. The temperature was increased in 20 K increments, and the reaction was allowed to reach steady state by waiting for 4 minutes at each temperature before beginning the analysis of the product gases. The product gas mixture from each of the 100 different reaction volumes was sent to the mass spectrometer for quantification. The CSAF surface was pretreated with H₂ prior to the experiments. Also, during a different set of experiments the CSAF surface was left in contact with flowing H₂.

The composition of the reaction products was calculated by assuming that the mass spectrometer signals at $m/q = 2, 3,$ and 4 amu obtained from the product gas samples were proportional to the H₂, HD and D₂ partial pressures between the baseline and equilibrium conversion. Baseline (0% conversion) signals at $m/q = 2, 3$ and 4 amu were collected by sampling the feed gases directly without contacting the CSAF surface. At equilibrium, the composition of the product gases H₂, HD and D₂ is given by

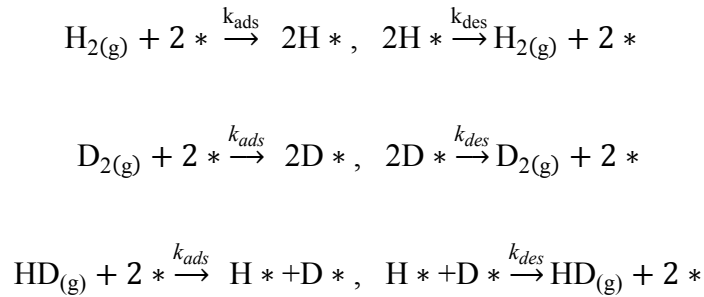
$$\frac{P_{HD}^2}{P_{H_2}P_{D_2}} = 4.16 \exp\left(\frac{-77.7}{T}\right) \quad (3.1)$$

where P_{H_2} , P_{D_2} and P_{HD} are the partial pressures of H₂, D₂ and HD, respectively [52].

H₂ conversions were measured at 100 channels at T = 333-593 K at 14 different inlet flow conditions specified in Table 3.1. The measured conversions were used to calculate the kinetic parameters and the activation barriers to dissociative adsorption (ΔE_{ads}^\ddagger) and recombinative desorption (ΔE_{des}^\ddagger) for the catalytic H₂-D₂ exchange reaction as a function of Ag_xPd_{1-x} alloy composition.

3.4 Microkinetic Model

Microkinetic analysis of the H₂-D₂ exchange reaction on Ag_xPd_{1-x} was performed using the entire dataset (across 90 different alloy compositions, at 14 different temperatures and at 14 different inlet flow conditions) obtained from the CSAF to estimate the kinetic parameters v_{ads} , v_{des} , ΔE_{ads}^\ddagger and ΔE_{des}^\ddagger as a function of alloy composition, x . The model was derived based on a Langmuir-Hinshelwood mechanism:



In the reactions, * stands for a vacant site on the surface; H* and D* showed adsorbed H and D, respectively. This is a two-step, reversible mechanism that occurs through dissociative adsorption and recombinative desorption of H₂, D₂ and HD requiring two sites, *. The rate constants have an Arrhenius form:

$$k_{ads} = v_{ads} \exp(-\Delta E_{ads}^{\ddagger}/k_B T) \quad (3.2)$$

$$k_{des} = v_{des} \exp(-\Delta E_{des}^{\ddagger}/k_B T) \quad (3.3)$$

where v_{ads} is the adsorption pre-exponent, $\Delta E_{ads}^{\ddagger}$ is the adsorption energy barrier, v_{des} is the desorption pre-exponent, $\Delta E_{des}^{\ddagger}$ is the desorption barrier, k_B is the Boltzmann constant, and T is the temperature.

H₂-D₂ exchange was modeled considering only dissociative adsorption and recombinative desorption of H₂, D₂ and HD under steady-state conditions. Isotopic effects were ignored, so the adsorption and desorption rate constants were taken to be the same for H₂, D₂ and HD. Also, it was assumed that the activation barriers and pre-exponents in the rate constants for adsorption and desorption were independent of coverage and temperature. The inlet conditions are defined as

$$P_{H_2}^{in} = \alpha P_H^{tot} \quad (3.4)$$

$$P_{D_2}^{in} = (1 - \alpha) P_H^{tot} \quad (3.5)$$

$$P_H^{tot} = P_{H_2}^{in} + P_{D_2}^{in} = P_{H_2} + P_{D_2} + P_{HD} \quad (3.6)$$

where $P_{H_2}^{in}$ and $P_{D_2}^{in}$ are the partial pressure of H₂ and D₂ at the inlet mixture, respectively. P_H^{tot} is the pressure of all hydrogen isotopes. The fraction of H₂ in the inlet H₂-D₂ mixture is denoted as α .

The steady state surface coverages of H and D can be calculated by

$$\frac{d\theta_H}{dt} = 2k_{ads}P_{H_2}(1 - \theta_H - \theta_D)^2 - 2k_{des}\theta_H^2 + k_{ads}P_{HD}(1 - \theta_H - \theta_D)^2 - 2k_{des}\theta_H\theta_D \quad (3.7)$$

$$\frac{d\theta_D}{dt} = 2k_{ads}P_{D_2}(1 - \theta_H - \theta_D)^2 - 2k_{des}\theta_D^2 + k_{ads}P_{HD}(1 - \theta_H - \theta_D)^2 - 2k_{des}\theta_H\theta_D \quad (3.8)$$

where k_{ads} is the rate constant for dissociative molecular adsorption of H_2 or D_2 and k_{des} is the rate constant for recombinative desorption of H_2 or D_2 . The rate constant for recombinative desorption of HD from recombination of H and D is denoted as $2k_{des}$. θ_H is the surface coverage of H atoms and θ_D is the surface coverage of D atoms. The total coverage of H and D atoms, θ , can be defined as

$$\theta = \theta_H + \theta_D \quad (3.9)$$

$$\theta_H = \alpha\theta \quad (3.10)$$

$$\theta_D = (1 - \alpha)\theta \quad (3.11)$$

Adding Equation 3.7 and 3.8 gives

$$\frac{d\theta}{dt} = 2k_{ads}P_H^{tot}(1 - \theta)^2 - 2k_{des}\theta^2 \quad (3.12)$$

At steady state Equation 3.12 gives

$$0 = k_{ads}P_H^{tot}(1 - \theta)^2 - k_{des}\theta^2 \quad (3.13)$$

$$\theta = \frac{\sqrt{k_{ads}P_H^{tot}/k_{des}}}{1 + \sqrt{k_{ads}P_H^{tot}/k_{des}}} \quad (3.14)$$

This is exactly what would be expected from a second order Langmuir isotherm. The rate equation for HD production can be defined as

$$r_{HD} = 2k_{des}\theta_H\theta_D - k_{ads}P_{HD}(1 - \theta_H - \theta_D)^2 \quad (3.15)$$

$$r_{HD} = 2k_{des}\alpha(1 - \alpha)\theta^2 - k_{ads}P_{HD}(1 - \theta)^2 \quad (3.16)$$

$$P_{HD} = \frac{F_{HD}P^{tot}}{F^{tot}} \quad (3.17)$$

$$P^{tot} = P_{H_2}^{in} + P_{D_2}^{in} + P_{buffer} \quad (3.18)$$

where F_{HD} is the molar flow rate of HD produced, P^{tot} is the total pressure in the reactor ($P^{tot} = P_{H_2}^{in} + P_{D_2}^{in} + P_{Ar}^{in} = P_{H_2} + P_{D_2} + P_{HD} + P_{Ar}$), and F^{tot} is total molar gas flow rate through the reactor. P_{buffer} is the partial pressure of the inert gas in the gas flow.

With these definitions, the rate equation transforms into

$$r_{HD} = 2k_{des}\alpha(1 - \alpha)\theta^2 - k_{ads}F_{HD}P^{tot}(1 - \theta)^2/F^{tot} \quad (3.19)$$

F_{HD}^{out} , which is the HD flow rate exiting the microreactor, can be calculated by solving the flow equation.

$$A = \int_0^{F_{HD}^{out}} \frac{dF'}{\alpha - \beta F'} \quad (3.20)$$

$$\alpha = 2k_{des}\alpha(1 - \alpha)\theta^2 \quad (3.21)$$

$$\beta = k_{ads}P^{tot}(1 - \theta)^2/F^{tot} \quad (3.22)$$

$$F_{HD}^{out} = \frac{\alpha}{\beta} [1 - \exp(-\beta A)] \quad (3.23)$$

$$F_{HD}^{out} = 2\alpha(1 - \alpha) \frac{F^{tot}P_H^{tot}}{P^{tot}} \left[1 - \exp\left(\frac{-k_{ads}P^{tot}A}{F^{tot} \left(1 + \sqrt{k_{ads}P_H^{tot}/k_{des}} \right)^2} \right) \right] \quad (3.24)$$

$$P_{HD}^{out} = 2\alpha(1 - \alpha)P_H^{tot} \left[1 - \exp\left(\frac{-k_{ads}P^{tot}A}{F^{tot} \left(1 + \sqrt{k_{ads}P_H^{tot}/k_{des}} \right)^2} \right) \right] \quad (3.25)$$

where A is the catalyst surface area.

The H_2 conversion can be determined experimentally using mass spectrometer signals and the microkinetic model with known reaction conditions and selected values of v_{ads} , v_{des} , ΔE_{ads}^\ddagger and ΔE_{des}^\ddagger by

$$X_{H_2} = \frac{F_{HD}}{2F_{H_2}^{in}} \quad (3.26)$$

The model prediction of conversion, X_{model} , was fit to the experimental H_2 conversion, X_{exp} , data at each catalyst composition, for all inlet flow conditions and temperatures simultaneously. The fit was performed by minimizing the sum of squared errors (SSE) between the calculated and experimental conversions by changing the four parameters v_{ads} , v_{des} , ΔE_{ads}^\ddagger and ΔE_{des}^\ddagger .

$$SSE = \sum_{i,j} [X_{exp}(F_i, T_j) - X_{model}(F_i, T_j)]^2 \quad (3.27)$$

The fit of the model prediction of conversions to experimental values was performed in MATLAB using non-linear fitting subroutine *lsqcurvefit* which utilizes a “trust-region-reflective” least squares algorithm which is based on an interior-reflective Newton Method. Termination tolerance on the SSE function was set to 10^{-12} . A central finite difference method was used to calculate gradients. The confidence intervals for the nonlinear least squares parameter estimates were calculated using the MATLAB function *nlparci*.

3.5 Results and Discussion

3.5.1 Characterization of CSAF Composition

The near surface composition of the $\text{Ag}_x\text{Pd}_{1-x}$ CSAF was mapped by X-ray photoelectron spectroscopy (XPS) as a function of position on the Mo substrate across a 13×13 grid with 1 mm spacing. Although the CSAF is deposited onto a $14 \times 14 \text{ mm}^2$ Mo substrate, the region of interest is the $10 \times 10 \text{ mm}^2$ area spanned by the 10×10 array of microreactor channels. The composition map corresponding to the area on the CSAF used for the measurement of catalytic reaction kinetics is given in Figure 3. 1. The CSAF has been deposited such that the iso-composition lines are oriented at an angle with respect to the edge of the substrate, which is aligned with the microreactors. This tilted configuration was used so that each channel of the microreactor would

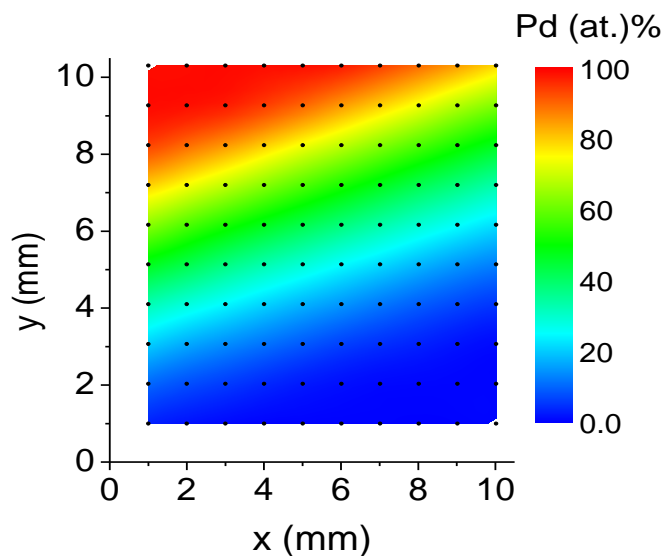


Figure 3. 1. Pd composition (measured by XPS) versus position on the $\text{Ag}_x\text{Pd}_{1-x}$ binary CSAF. Black dots represent actual measurement points.

sample a different alloy composition. Thus, we have 90 reaction zones sampling 90 different $\text{Ag}_x\text{Pd}_{1-x}$ compositions, simultaneously (one row of ten channels was blocked). In the region sampled by the microreactor array, the $\text{Ag}_x\text{Pd}_{1-x}$ CSAF spanned the composition range $x = 0 \rightarrow 1$. The tilt can be seen in Figure 3. 1 and illustrates the ability of our rotatable shadow mask deposition tool to prepare CSAFs with composition gradients oriented in any desired direction [47, 53].

3.5.2 Characterization of CSAF Electronic Structure

XPS was used to map the valence band electronic structure of the $\text{Ag}_x\text{Pd}_{1-x}$ CSAF at the same points of $\text{Ag}_x\text{Pd}_{1-x}$ composition space that were used for measurement of $\text{H}_2\text{-D}_2$ exchange kinetics. Figure 3.2 illustrates the background subtracted ν -band spectra mapped at 169 discrete locations across the $\text{Ag}_x\text{Pd}_{1-x}$ CSAF. The spectra are plotted as functions of energy with respect to the Fermi level, which is located at zero on the energy scale. It can be clearly seen that the density of states shifts towards the Fermi level as the Pd composition increases.

The XPS-derived average energy of the filled ν -band, $\varepsilon_\nu(x)$, was calculated (Equation 3.28) from the background subtracted ν -band XP spectra (Figure 3.2) obtained from $\text{Ag}_x\text{Pd}_{1-x}$ CSAF [51].

$$\varepsilon_\nu = \frac{\int N(\varepsilon) \varepsilon d\varepsilon}{\int N(\varepsilon) d\varepsilon} \quad (3.28)$$

The quantity ε is the energy of filled state in the valence band relative to the Fermi level and $N(\varepsilon)$ is the density of filled states, which is taken to be proportional to the intensity of the ν -band XP spectrum.

The XPS-derived average energies of the filled ν -band (ε_ν) were calculated for each alloy composition over the binding energy range -10 to 0 eV. It should be noted that XP spectra only probe the density of filled states, not the empty states. However, the valence band in $\text{Ag}_x\text{Pd}_{1-x}$ alloys is dominated by filled states; i.e. the Ag d -band is full and Pd d -band is almost full (having nine to ten electrons). In this case, the valence band energy obtained from the XP spectra only slightly underestimates the average energy of the entire valence band.

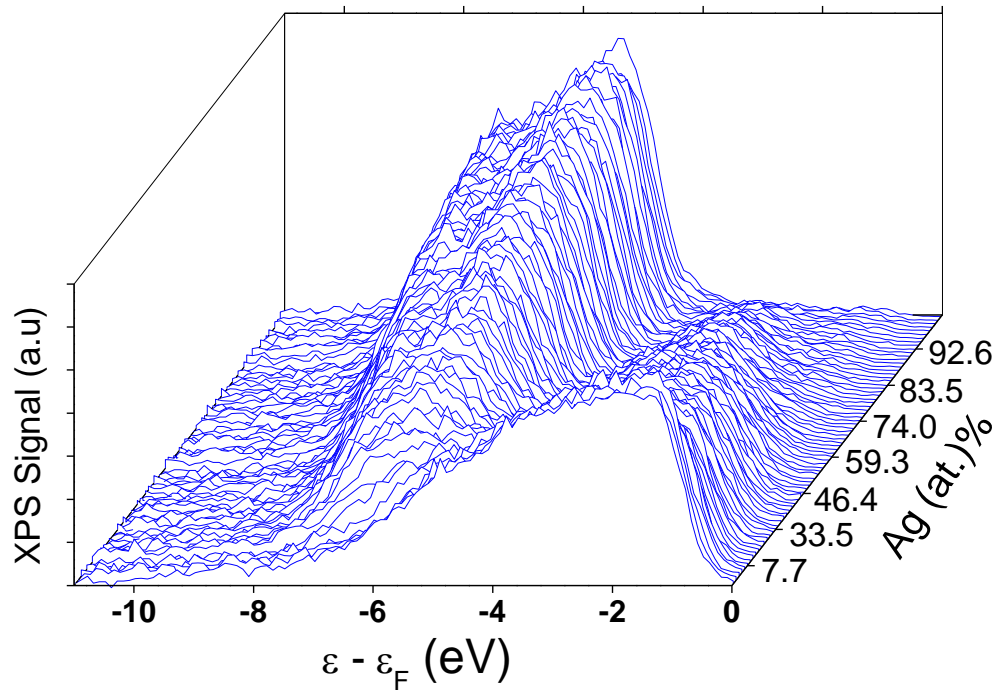


Figure 3.2. Background subtracted XP spectra of 169 different $\text{Ag}_x\text{Pd}_{1-x}$ compositions across the entire composition space.

The $\text{Ag}_x\text{Pd}_{1-x}$ v -band energies shift linearly with alloy composition (Figure 3.3). The average energy of the $\text{Ag}_x\text{Pd}_{1-x}$ v -band shifts toward the Fermi level as the Pd content increases. This result is in good agreement with the observation from Figure 3.2. Estimates of d -band center values for pure metals (Pd or Ag) are available in the literature, most of which were obtained from electronic structure calculations. The range of d -band energies reported for Ag is $\varepsilon_d = -5.28$ to -4.28 eV [42, 54, 55], roughly 1 eV higher than our measurement of $\varepsilon_v^{\text{Ag}} = -6.2$ eV. For Pd, $\varepsilon_d = -2.64$ to -2.02 eV [42, 54-57], which is ~ 1 eV higher than our measurement of $\varepsilon_v^{\text{Pd}} = -3.4$ eV. The ~ 1 eV offset between the literature values of d -band center and our measurements may arise from the calculation approaches which causes variations in the density of states (DOS) [58]. For a given DOS, the choice of upper and lower integration limits can result in differences in the predicted values of d -band center [42, 59]. Another reason for the offset may be an incomplete background subtraction of secondary electrons contributing to the XP spectra at high binding energies. Finally, the offset may also arise from the fact that our experimental measurements include photoemission from the s - and p -bands. These issues aside, the offset is not critical to our use of the XPS derived estimations of $\varepsilon_v(x)$, as we are principally interested in correlating the composition dependence of catalytic barriers with the composition dependence of $\varepsilon_v(x)$. The fact that XPS and DFT both give the same magnitude of ε_v shift with composition is sufficient.

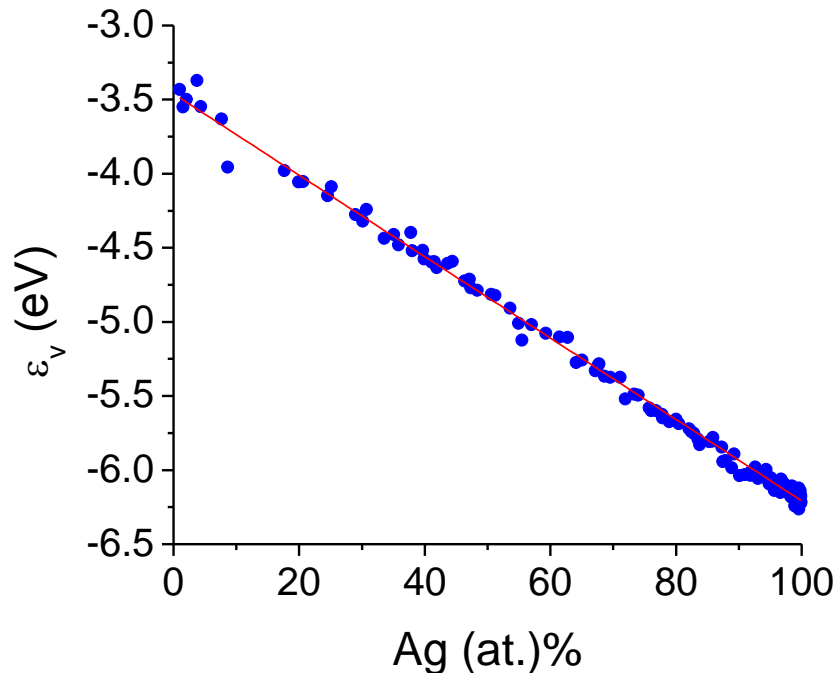


Figure 3.3. XPS-derived average energy of the filled v-band relative to the Fermi level of $\text{Ag}_x\text{Pd}_{1-x}$ CSAF versus Pd (at. %) compositions.

3.5.3 H_2 - D_2 Exchange on the $\text{Ag}_x\text{Pd}_{1-x}$ CSAF

H_2 - D_2 exchange over the $\text{Ag}_x\text{Pd}_{1-x}$ CSAF was carried out by flowing H_2 , D_2 , and Ar mixtures into the microreactor at a constant temperature, partial pressures and flow rates while monitoring the product gas composition by mass spectrometry. Mass spectrometer signals were converted to H_2 conversion, X , for 90 different $\text{Ag}_x\text{Pd}_{1-x}$ compositions, x , at 14 different temperatures, T , and 14 different flow conditions. The $\text{Ag}_x\text{Pd}_{1-x}$ binary CSAF displayed stable activity during the course of the experiments. Collected X versus T for all the inlet conditions listed in Table 3.1 are converted to flow rates of produced HD using Equation 3.26. The measured HD flow rates for one sample inlet flow condition across all 90 different $\text{Ag}_x\text{Pd}_{1-x}$ compositions

are given in Figure 3.4-a. HD flow rates are also predicted using the microkinetic model explained in Section 3.4. The fits for the example dataset is given in Figure 3.4-b. The data for the other inlet flow conditions can be found in the Appendix.

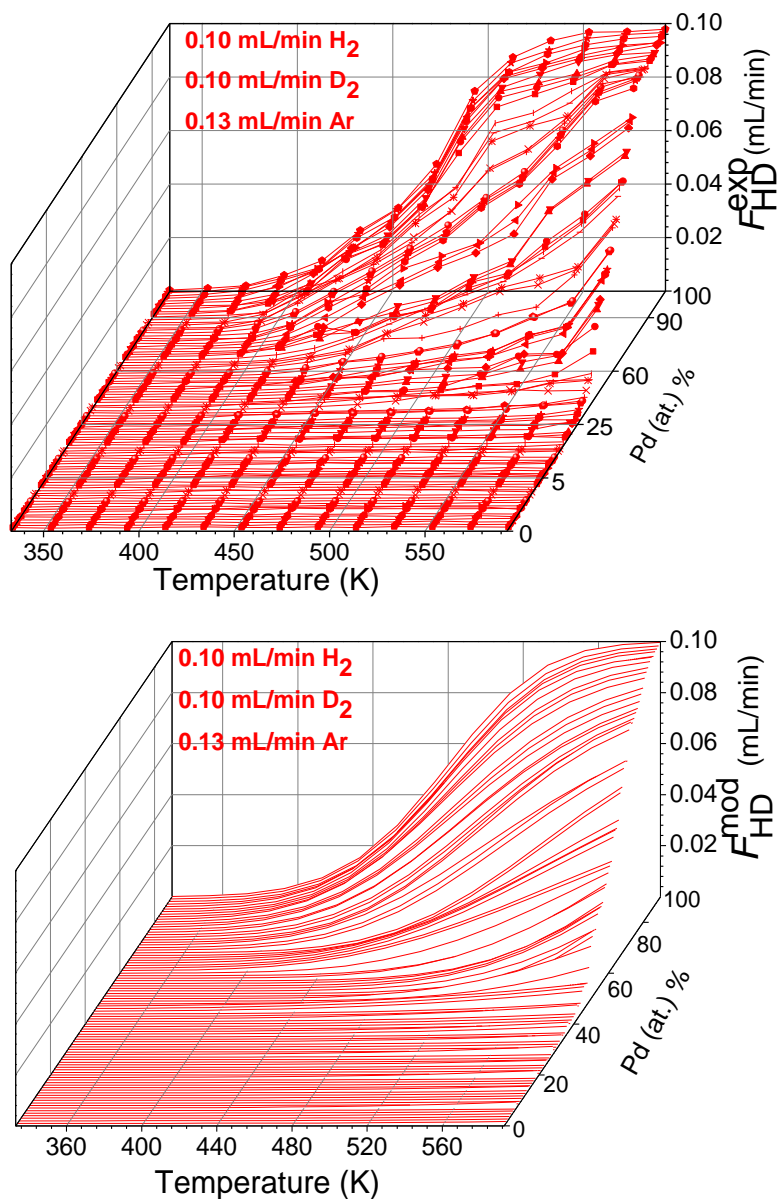


Figure 3.4. HD flow rate vs. temperature across Ag_xPd_{1-x} composition space. For all Ag_xPd_{1-x} compositions conversion increases with increasing T and decreasing x . Flow conditions in each channel are labeled on each figure ($P_{tot} = 1$ atm). Top figure gives the measured values and the bottom one gives the model predictions.

Conversion versus temperature curves, $X(T)$, for all inlet flow conditions were investigated at each of the 90 different alloy compositions. One example is shown in Figure 3.5 for the inlet flow consisting of 0.1 mL/min H_2 , 0.1 mL/min D_2 , and 0.13 mL/min Ar per channel for five discrete alloy compositions. Note that equilibrium corresponds to a conversion of $X = 0.489$ at 593 K for all equimolar H_2 and D_2 inlet cases. Across the CSAF, H_2 - D_2 exchange activity increases with increasing T and decreasing Ag content. At $T = 333$ K, the conversion was $X \approx 0$ at all alloy compositions. Equilibrium conversion was reached at the Pd-rich end of the CSAF for $T > 525$ K. As the Pd content decreases, the temperature at which equilibrium is reached increases. For Pd compositions < 0.80 , equilibrium was not achieved, even at the highest temperature used, $T = 593$ K. For low compositions of Pd, near-zero HD production activity was observed at $T < 375$ K. Each data point in Figure 3.5 was collected under isothermal conditions; the CSAF

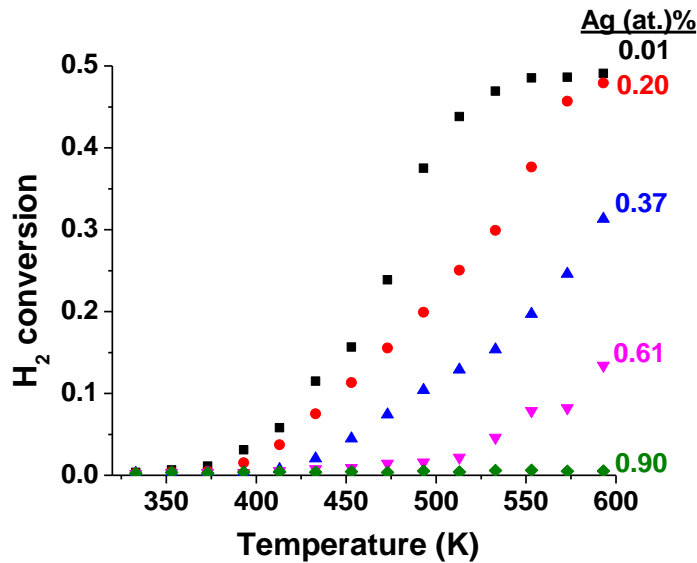


Figure 3.5. H_2 - D_2 exchange conversion vs. T on Ag_xPd_{1-x} alloys for several discrete Ag compositions, x . H_2 conversion is increasing with increasing T and decreasing with Ag composition. Inlet flow was 0.1 mL/min H_2 , 0.1 mL/min D_2 and 0.13 mL/min Ar per channel.

was heated at 1 K/s and then held at constant temperature for ~4 min to reach steady state before sampling HD production across all 90 alloy compositions.

Figure 3.6 shows H₂ conversion versus Ag composition on the Ag_xPd_{1-x} CSAF at three different temperatures. At $T = 593$ K, the activity increases as the Pd content of the alloy increases, reaching equilibrium for Pd compositions greater than 0.80. For $T < 373$ K, H₂ conversion is $X \approx 0$ across the entire CSAF.

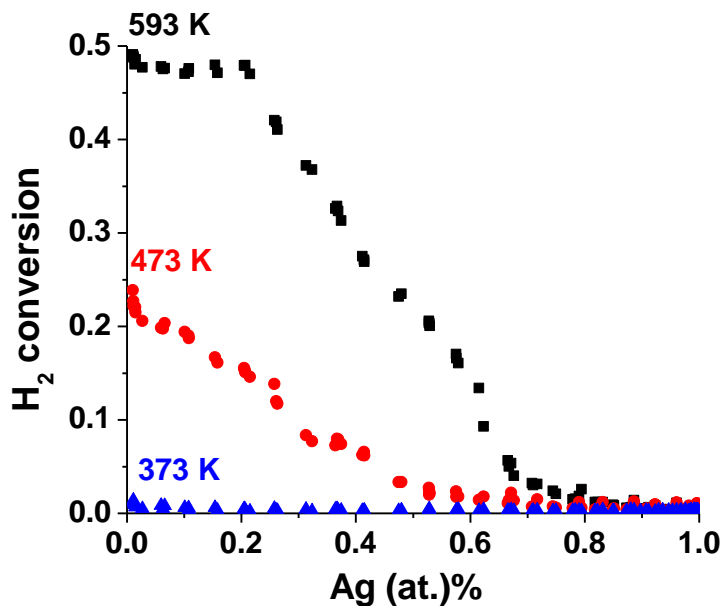


Figure 3.6. H₂-D₂ exchange conversion versus Ag composition at $T = 373$ K, 473 K and 593 K. Inlet flow was 0.1 mL/min H₂, 0.1 mL/min D₂ and 0.13 mL/min Ar per channel.

The pressure dependence of HD production from H₂-D₂ exchange over Ag_xPd_{1-x} alloys has been investigated across the temperature range $T = 333 - 593$ K by varying P_{H_2} and P_{D_2} independently. The first 11 rows of Table 3.1 corresponds to the inlet conditions where P_{H_2} was kept constant while changing P_{D_2} . The last 4 rows of Table 3.1 corresponds to the inlet conditions

where P_{D_2} was kept constant while changing P_{H_2} . For all these cases, activity was found to increase with T and decrease with Ag content, x . Figure 3.7 shows HD flow rates, F_{HD}^{out} obtained for three Ag_xPd_{1-x} compositions and the four different feed gas conditions where F_{H_2} was kept constant at 0.1 mL/min in each channel. F_{D_2} was changed from 0.1 mL/min to 0.01 mL/min per channel. The total flow rate per channel was kept constant at 0.3 mL/min. In Figure 3.8, experimental values of the HD flowrates for the four different feed conditions are shown as the discrete data points and the fits from the microkinetic model are illustrated as the solid lines. The quality of the fit can be assessed using these F_{HD}^{out} versus T plots. A parity plot (Figure 3. 8) comparison of the modeled HD flow rates (solid lines) and the experimental HD flow rates shows that the model fits the experimental data (17640 values of F_{HD}^{out}) well for all catalyst compositions across the entire temperature range of the experiment ($T = 333 - 593$ K).

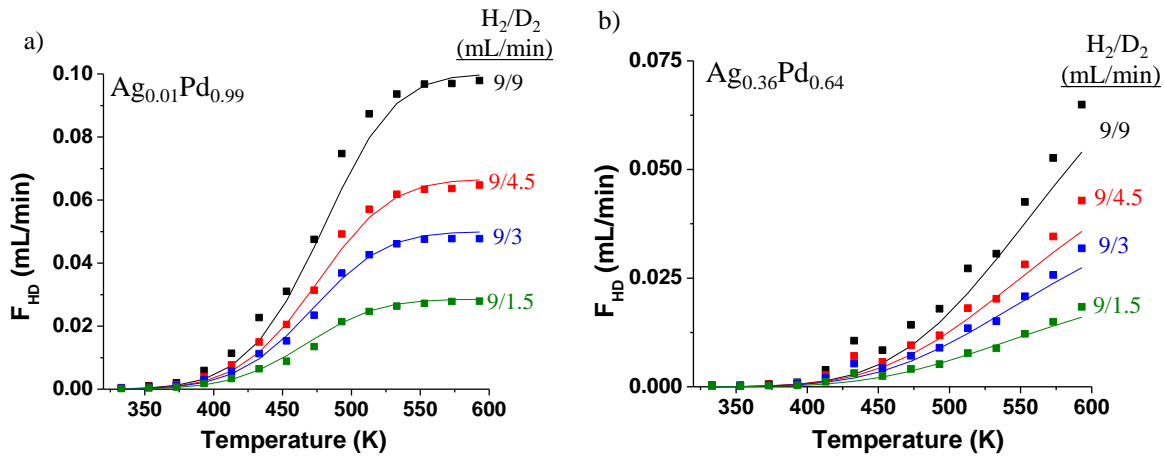


Figure 3.7. a), b) HD flow rate in the outlet measured for two Ag_xPd_{1-x} alloy compositions ($x = 0.01, 0.36$) vs. T for four different inlet flow conditions. Solid squares are the experimental measurement points and the solid lines are the fits of the microkinetic model to the data.

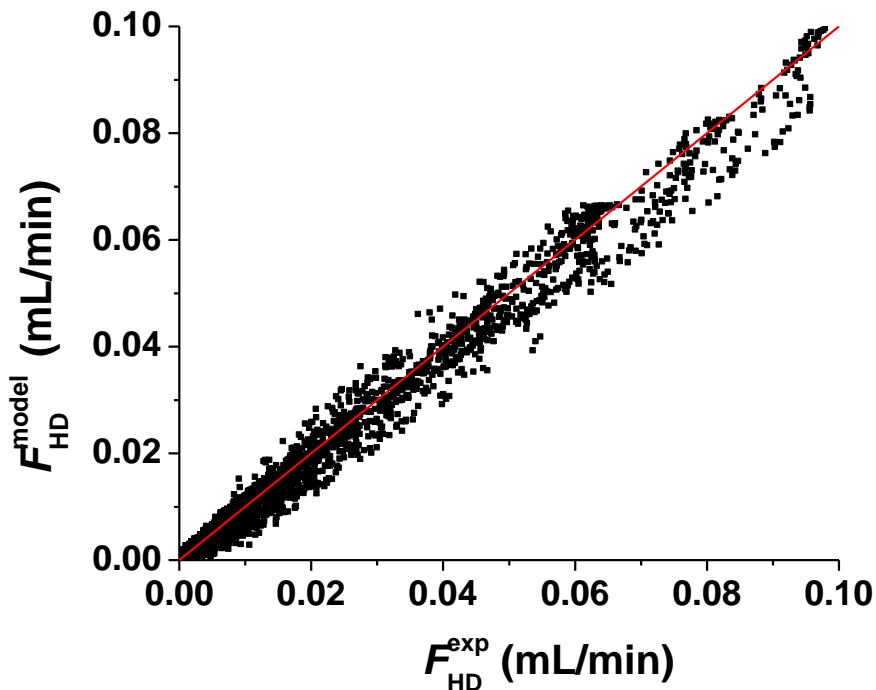


Figure 3. 8. Parity plot of the HD flow rates predicted by the microkinetic model vs. experimental measurements. Data are shown for all 90 $\text{Ag}_x\text{Pd}_{1-x}$ compositions ($x = 0 - 0.99$) at 14 different temperatures ($T = 333\text{--}593$ K) and 14 inlet flow conditions (Table 3.1).

3.5.4 Kinetic Parameters for $\text{H}_2\text{-D}_2$ Exchange on $\text{Ag}_x\text{Pd}_{1-x}$

The comprehensive dataset obtained using high throughput methods and the microkinetic model are used to estimate the kinetic parameters, v_{ads} , v_{des} , ΔE_{ads}^\ddagger and ΔE_{des}^\ddagger for each $\text{Ag}_x\text{Pd}_{1-x}$ alloy composition. In the previous studies, it has been proven that pre-exponential factors are fairly independent of alloy composition [20, 60]. Therefore, in this study, the model fit was performed by fixing the pre-exponents to their transition state theory values of $v_{ads} = 10^{-4}$ mol/m²/s/Pa and $v_{des} = 10^6$ mol/m²/s [61] and only varying ΔE_{ads}^\ddagger and ΔE_{des}^\ddagger .

The obtained values of ΔE_{ads}^\ddagger and ΔE_{des}^\ddagger are plotted in Figure 3.9. It is observed that both ΔE_{ads}^\ddagger and ΔE_{des}^\ddagger vary nonlinearly with $\text{Ag}_x\text{Pd}_{1-x}$ alloy composition. The value of ΔE_{ads}^\ddagger rises from ~ 0 to ~ 0.4 eV and the value of ΔE_{des}^\ddagger rises from ~ 0.65 to ~ 0.85 over the composition range $x = 0 \rightarrow 1$. Over the composition range $x > 0.4$, $\Delta E_{ads}^\ddagger(x) \ll \Delta E_{des}^\ddagger(x)$, which suggests that the rate-limiting step of the $\text{H}_2\text{-D}_2$ exchange reaction is recombinative desorption of HD. For the composition range $x < 0.4$, the microkinetic modeling of $\text{H}_2\text{-D}_2$ exchange kinetics yielded a large uncertainty in ΔE_{des}^\ddagger that was greater than the magnitude of ΔE_{des}^\ddagger itself, $\sigma E_{des}^\ddagger > \Delta E_{des}^\ddagger$. This can be interpreted as an insensitivity of $\text{H}_2\text{-D}_2$ kinetics to the value of ΔE_{des}^\ddagger on Ag, which indicates that the dissociative adsorption reaction is rate-limiting step in this region.

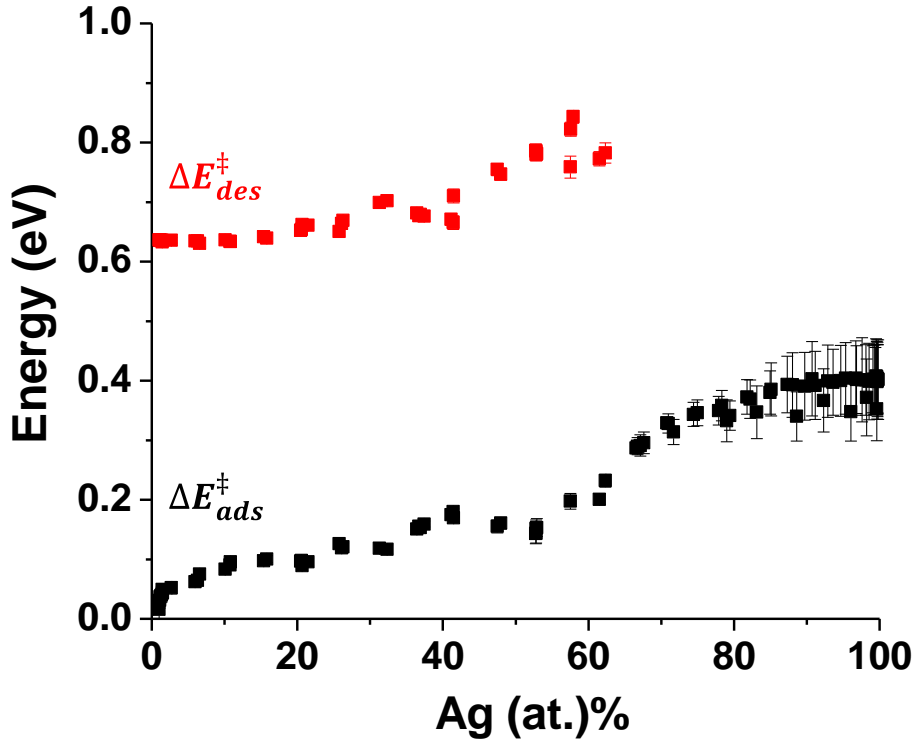


Figure 3.9. Energy barriers for dissociative adsorption of H_2 , $\Delta E_{ads}^\ddagger(x)$, (black) and associative desorption of H_2 , $\Delta E_{des}^\ddagger(x)$, (red) as a function of $\text{Ag}_x\text{Pd}_{1-x}$ composition.

This observation suggests that at a composition of $x \approx 0.4$, the rate-limiting step changes from recombinative desorption of HD ($x < 0.4$) to dissociative adsorption of H₂/D₂ ($x > 0.4$).

Pure Ag appears to be the least active H₂-D₂ exchange catalyst among the composition space examined in this study. This is due to the large activation barrier to H₂ adsorption on Ag ($\Delta E_{ads}^\ddagger = 0.4 \pm 0.07 eV$). In contrast, the barrier to H₂ adsorption on Pd is very close to zero ($\Delta E_{ads}^\ddagger = 0.02 \pm 0.01 eV$). The order of decreasing H₂-D₂ exchange activity of the desorption-limited catalysts ($x = 1 \rightarrow 0.4$) closely follows the order of increasing activation barriers ($x = 1 \rightarrow 0.4$) for Ag_xPd_{1-x} alloys.

O'Brien et al. measured the values of v_{ads} , v_{des} , ΔE_{ads}^\ddagger and ΔE_{des}^\ddagger for steady state catalytic H₂-D₂ exchange reaction over fixed beds of Cu, Cu_{0.53}Pd_{0.47}, Cu_{0.30}Pd_{0.70}, and Pd in a conventional flow reactor [20]. In that study, the adsorption barrier for pure Pd was reported to be $\Delta E_{ads}^\ddagger = 0.12 \pm 0.04 eV$ and the desorption barrier for pure Pd was reported to be $\Delta E_{des}^\ddagger = 0.68 \pm 0.06 eV$. Although, our calculated adsorption barrier differs slightly from the reported value, the desorption barriers are comparable. This observation suggests that CSAFs are effective tools that can be used to investigate catalytic reactions on pure metals and alloys. Many experimental studies of H₂ adsorption have been reported in literature, most of which the have been conducted under ultrahigh vacuum conditions [27, 30, 62-68]. The studies conducted on polycrystalline Pd surfaces at near-ambient pressures reported adsorption barriers very close to 0 eV when the surface is not saturated with H [66-68]. In Figure 3.11, we showed that the surface coverages are less than 1, so our calculated adsorption barrier, $\Delta E_{ads}^\ddagger = 0.02 \pm 0.01 eV$ is in good agreement with the literature values. The activation barriers to desorption on Pd (111) and PdH surfaces are reported to be in the range of 0.67 – 0.85 eV [66, 69, 70]. While, it is not

straightforward to compare our calculated desorption barrier for pure Pd with these studies, ours is within this range, $\Delta E_{des}^{\ddagger} = 0.68 \pm 0.06 \text{ eV}$.

Gumuslu et al. measured the values of ν_{ads} , ν_{des} , $\Delta E_{ads}^{\ddagger}$ and $\Delta E_{des}^{\ddagger}$ for steady state catalytic H₂-D₂ exchange reaction across Cu_xPd_{1-x} CSAF with a minimum Cu composition of $x = 0.3$. In that study, the adsorption barrier for Cu_{0.3}Pd_{0.7} was reported to be $\Delta E_{ads}^{\ddagger} \approx 0.15 \text{ eV}$ and desorption barrier for Cu_{0.3}Pd_{0.7} to be $\Delta E_{des}^{\ddagger} \approx 0.55 \text{ eV}$. In our study, adsorption barrier for Ag_{0.31}Pd_{0.69} was reported to be $\Delta E_{ads}^{\ddagger} = 0.12 \text{ eV} \pm 0.01$ and desorption barrier for Ag_{0.31}Pd_{0.69} to be $\Delta E_{des}^{\ddagger} = 0.70 \pm 0.01 \text{ eV}$. Despite having calculated slightly higher desorption barriers, the values are quite comparable. This result is in accordance with the fact that Ag and Cu have similar H₂ adsorption characteristics.

We were able to calculate the adsorption barriers on pure Ag as $\Delta E_{ads}^{\ddagger} = 0.4 \pm 0.07 \text{ eV}$. This is a relatively high barrier when compared to pure Pd. Adsorption of hydrogen is known to be negligible [33, 71, 72] on Ag, although when it occurs, it is known to be an endothermic process [35]. In one study that used density-functional theory, the minimum barrier to dissociative adsorption of H₂ on Ag(100) was reported to be 1.1 eV [35]. In another study, which investigated the interaction of atomic hydrogen with the Ag (111) surface using low-energy electron diffraction (LEED), high-resolution electron-loss spectroscopy (HREELS), thermal desorption spectroscopy and work function measurements, an adsorption barrier of 0.6 eV was reported [73]. The adsorption barrier calculated in this work is lower than these reported values. Considering the differences in the crystal structures of these surfaces, we were able to capture the difficulty of quantifying/characterizing dissociative adsorption of H₂ on Ag.

3.5.5 Reaction Rate for H₂-D₂ Exchange on Ag_xPd_{1-x}

Figure 3.10 displays the experimental HD production rate of five different Ag_xPd_{1-x} compositions at 593 K as a function of H₂ or D₂ partial pressure with a) P_{H_2} held constant at 30.39 kPa and a variable P_{D_2} , and b) P_{D_2} held constant at 0.03 kPa and a variable P_{H_2} . A positive dependence of the HD production rate was observed at all temperatures tested, as well as on the growing P_{D_2} (from a low partial pressure) while P_{H_2} remained constant (at a relatively high pressure). The calculated slopes are very close to 1, which suggest that the reaction is first order with respect to the low pressure component, P_{D_2} . In contrast, a zero slope is detected when increasing the partial pressure of the high pressure component, P_{H_2} while P_{D_2} is held constant low partial pressure.

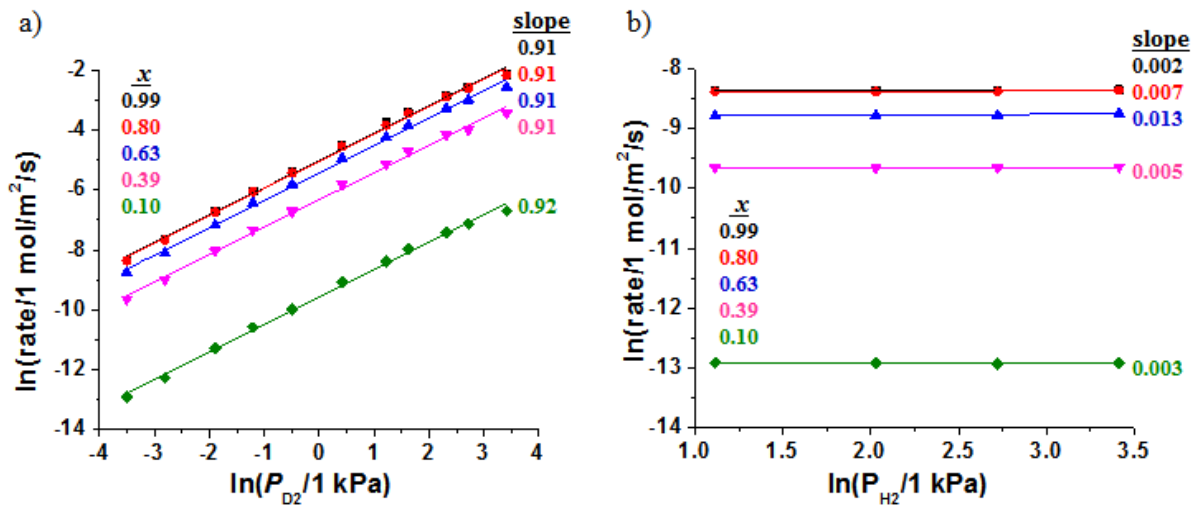


Figure 3.10. a) Plot of experimental HD production rate on five different Ag_xPd_{1-x} compositions at 593 K as a function of P_{D_2} with P_{H_2} constant at 30.39 kPa. b) Plot of HD production rate on five different Ag_xPd_{1-x} compositions at 593 K as a function of P_{H_2} with P_{D_2} held constant at 0.03 kPa.

The experimental formal reaction orders and the reaction orders predicted by the classical Langmuir-Hinshelwood model for H₂/D₂ pressures are summarized in Table 3.2. The theoretical reaction orders are derived analytically using the Langmuir-Hinshelwood based microkinetic model described in the Appendix. For the inlet conditions where P_{H_2} is constant and P_{D_2} is changing, the reaction orders obtained experimentally match the analytical solution of the Langmuir-Hinshelwood model. For the other case where P_{D_2} is constant and P_{H_2} is changing, there is disagreement between the experimental reaction orders and the ones predicted by the Langmuir-Hinshelwood model. The experimentally observed reaction order is found to be 0, however, the Langmuir-Hinshelwood model predicts a -1 reaction order when the surface coverage is close to 1, $\theta_{H/D} \approx 1$, and a 0 reaction order when the surface coverage is close to 0, $\theta_{H/D} \approx 0$. So it can be said that the classical Langmuir-Hinshelwood model predicts the HD production rate accurately when the coverage of the surface species is low.

The total coverage of H and D atoms during H₂-D₂ exchange over the 90 different Ag_xPd_{1-x} alloy compositions was calculated using Equation 3.14, and the kinetic parameters, ΔE_{ads}^\ddagger and ΔE_{des}^\ddagger , were extracted from the microkinetic model. Figure 3.11-a shows the total coverage of H and D atoms on three different Ag_xPd_{1-x} alloy compositions and Figure 3.11-b shows the total

Table 3.2. Experimental and theoretical reaction orders for different inlet conditions.

Inlet conditions	Experiment	Langmuir-Hinshelwood
Constant P_{H_2} (Changing P_{D_2})	$+0.917 \pm 0.08$	~1
Constant P_{D_2} (Changing P_{H_2})	$+0.009 \pm 0.04$	~ - 1 or 0

coverage of H and D atoms on $\text{Ag}_{0.2}\text{Pd}_{0.8}$ for four different inlet gas conditions across the temperature range $T = 333\text{-}593$ K. At low temperature (~ 350 K), the catalyst surface is nearly saturated with H and D atoms for different $\text{Ag}_x\text{Pd}_{1-x}$ alloy compositions where $x < 0.4$. As temperature increases, the total coverage decreases for all these feed conditions. Keeping P_{D_2} constant and reducing P_{H_2} (going from the black solid line to the green solid line in Figure 3.11-b) reduces the rate of H_2 adsorption, decreasing the total coverage of H and D atoms. It can be said that under low surface coverages and when the Pd content of the $\text{Ag}_x\text{Pd}_{1-x}$ alloy is more than 40 (at.%) , $x > 0.4$, the Langmuir-Hinshelwood model does well at predicting the reaction order. The reason for such good agreement is that at high temperatures, only surface H and D species are present (no subsurface H and D) [74].

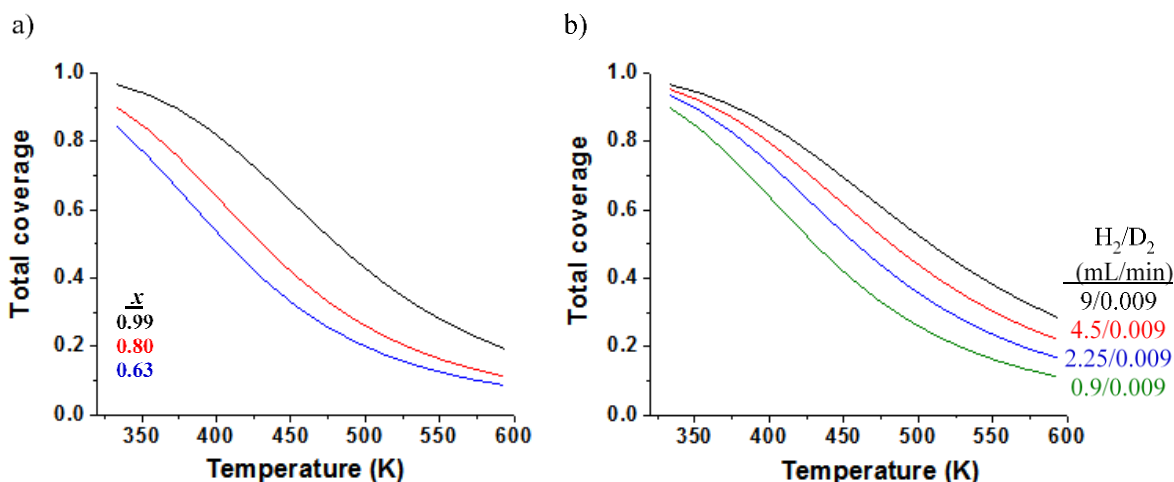


Figure 3.11. a) Total coverage of H and D atoms during $\text{H}_2\text{-D}_2$ exchange reaction over three different $\text{Ag}_x\text{Pd}_{1-x}$ alloy compositions ($x = 0.01, 0.2, 0.37$) as a function of T . The flow contains 9 mL/min H_2 , 0.009 mL/min D_2 and 20.991 mL/min Ar. **b)** Total coverage of H and D atoms during $\text{H}_2\text{-D}_2$ exchange reaction as a function of T for four different inlet flow compositions. The coverage is calculated using Eq. (8) and the kinetic parameters ν_{ads} , ν_{des} , ΔE_{ads}^\ddagger and ΔE_{des}^\ddagger extracted from the microkinetic model.

Slightly positive orders were observed experimentally for experiments with constant P_{D_2} while changing H_2 flow conditions across the CSAF. However, when the total coverage of H and D are close to unity, the Langmuir-Hinshelwood model predicts a negative dependence of HD production rate on H_2 partial pressure in the low temperature regime. If the surface is saturated with H and D atoms, an increase in P_{H_2} would decrease the surface concentration of D due to competitive adsorption with H atoms. In this case, the Langmuir-Hinshelwood model would predict a decrease in the HD production rate, hence a negative reaction order. So the experimentally observed apparently zero reaction order cannot be explained with this model. Therefore, only taking the surface species into account does not work for this system. There has been an ongoing debate about the possibility of the involvement of subsurface H atoms in surface reactions, especially on transition metals, including Pd [75, 76], which could explain the discrepancy.

Schauermann et al. have recently reported a slightly positive dependency of HD production rate on the species' partial pressure under conditions where the surface H/D coverage approaches saturation and subsurface H/D is present. Comparison of this study to our work is not straightforward since they used Pd nanoparticles and a Pd (111) single crystal in ultrahigh vacuum conditions and we studied a binary CSAF at atmospheric pressure. The agreement of these experimental observations draws attention to the importance of understanding subsurface hydrogen to characterize properly hydrogen's interaction with transition metals on an atomic level.

3.5.6 Correlation of Activity and Structure across Composition Space

The main goal of this study has been to correlate fundamental kinetic parameters for the catalytic H₂-D₂ exchange reaction over Ag_xPd_{1-x} alloys with details of their electronic structure. Computationally this can be achieved using DFT for various catalytic processes by correlating the calculated mean energy of the *d*-band, ε_d , of various metals with calculated barriers, ΔE^\ddagger , to the elementary reaction steps on their surfaces [1, 42, 54, 77]. In this work, we have used XP spectra from a Ag_xPd_{1-x} CSAF to measure the energy of the filled valence band center, $\varepsilon_v(x)$, and microkinetic modeling to calculate the ΔE_{ads}^\ddagger and ΔE_{des}^\ddagger for the H₂-D₂ exchange reaction. The correlation between these parameters are plotted in Figure 3. 12 for 90 different Ag_xPd_{1-x} alloy

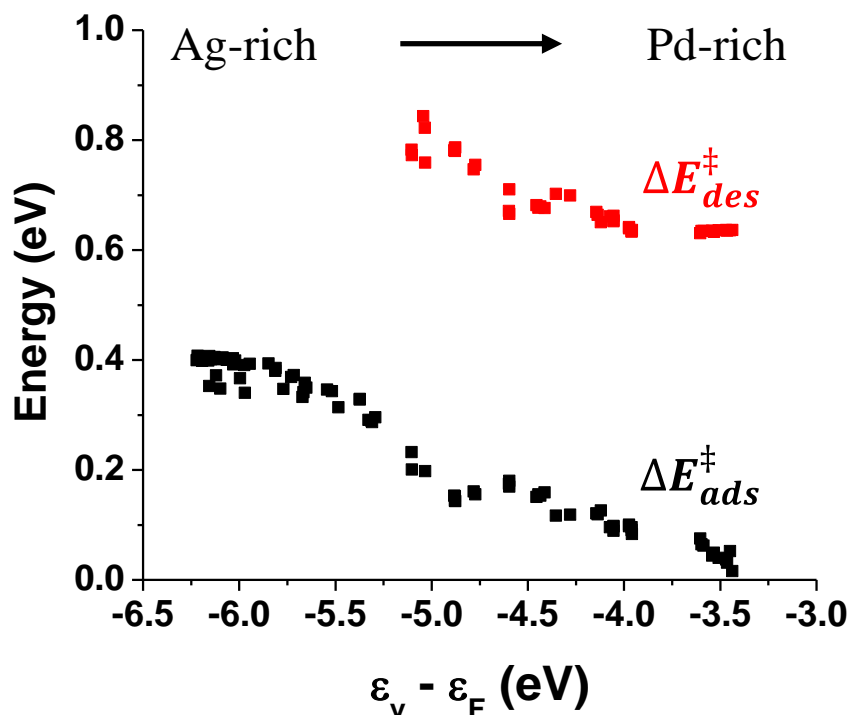


Figure 3. 12. Energy barriers for dissociative adsorption of H₂, $\Delta E_{ads}^\ddagger(x)$, (black) and associative desorption of H₂, $\Delta E_{des}^\ddagger(x)$, (red) as a function of the *v*-band center measured on 90 Ag_xPd_{1-x} positions.

compositions. The overall correlation shows that as ε_v shifts toward the Fermi level, $\Delta E_{ads}^\ddagger(\varepsilon_v)$ and $\Delta E_{des}^\ddagger(\varepsilon_v)$ decrease, as suggested from DFT studies [54, 78-83]. To the best of our knowledge, this is the first experimental study that correlates fundamental kinetic parameters for the H₂-D₂ exchange reaction over Ag_xPd_{1-x} alloys with details of their electronic structure.

Figure 3.11 shows that there is a clear correlation between the adsorption energy and the ν -band center; both H₂ adsorption and desorption barriers decrease linearly with increasing ε_v across the entire Ag_xPd_{1-x} composition space. It can also be seen that ΔE_{des}^\ddagger is slightly less sensitive to changes in ε_v than ΔE_{ads}^\ddagger . The center of the ν -band moves toward the Fermi level as more Pd is alloyed with Ag. In this direction, adsorption becomes more stable and an increase in activity is observed. This trend has also been reported from previous theoretical studies [78, 79, 84]. The heat of adsorption ($\Delta E_{ads} = \Delta E_{ads}^\ddagger - \Delta E_{des}^\ddagger$) of H₂ was found to change from 0.2 to 0.64 eV at different adsorption sites on Ag. These values become negative as more Pd is added, which proves that adsorption becomes more stable as Pd is added to the alloy [85].

The positions of the valence band derived from the XP spectra (Figure 3.2) exhibit a linear dependence on Ag_xPd_{1-x} alloy composition. However, the dependence of ΔE_{ads}^\ddagger and ΔE_{des}^\ddagger on alloy composition slightly deviates from linearity. This result suggests that there are some processes, such as segregation, that are not captured in the computational model. Surface enrichment of Ag was reported for Ag-Pd alloys in vacuum or inert atmosphere [86, 87]. However, reverse segregation has been reported for Ag-Pd alloys in hydrogen-rich atmosphere, experimentally [88] and theoretically [89, 90]. It is known that hydrogen treatment results in a chemical shift of around 0.1 - 0.2 eV of the Pd 3d core level, but no change occurs in the Ag 3d level. XPS analysis supports this result showing that Pd segregates to the membrane surface in conditions of high hydrogen pressure [88]. Under our reaction conditions, we cannot address this segregation issue directly,

but segregation may be responsible from the non-linear behavior of ΔE_{ads}^\ddagger , especially for $\text{Ag}_x\text{Pd}_{1-x}$ alloy compositions in the range of $x = 0.3 - 0.6$.

3.6 Conclusions

In this study, the catalytic $\text{H}_2\text{-D}_2$ exchange reaction was investigated across $\text{Ag}_x\text{Pd}_{1-x}$ composition space by using high throughput methodology. A materials library spanning $\text{Ag}_x\text{Pd}_{1-x}$ composition space from $x = 0 \rightarrow 1$ was prepared using the rotatable shadow mask deposition tool, as explained in Section 2.2.1.2. The characterization of composition and electronic structure across the CSAF was done using XPS. Also, catalytic reactivity at 90 discrete positions (90 different alloy compositions) across the CSAF was measured using the multichannel microreactor array, as described in Section 2.2.2. Coupling spatially resolved characterization techniques and the high throughput reaction system, composition – catalytic activity – electronic structure correlation for Ag-Pd alloys has been investigated across a continuous composition space. We found that the activity increased with increasing Pd at.%. Microkinetic analysis of the reaction showed that the $\text{H}_2\text{-D}_2$ exchange reaction was limited by the rate of adsorption below 30 at. % Pd and desorption limited above that value. Obtained v-band spectra showed that the v-band center moved closer to the Fermi level with increasing Pd content in the alloy. With the correlation between the kinetic parameters and electronic structure, i.e. ΔE_{ads}^\ddagger and ΔE_{des}^\ddagger vs ϵ_v , it was observed that both adsorption and desorption barriers decreased as the v-band center moved closer to the Fermi level. With these results we were able to show that we have successfully developed a high throughput methodology that can be applied to catalysis studies. Using this technique, we were able to correlate the fundamental kinetic parameters for the $\text{H}_2\text{-D}_2$ exchange reaction with electronic structure of the binary alloy catalyst across the entire composition range.

3.7 Appendix: HD Flow Rate versus Temperature across $\text{Ag}_x\text{Pd}_{1-x}$ Composition Space

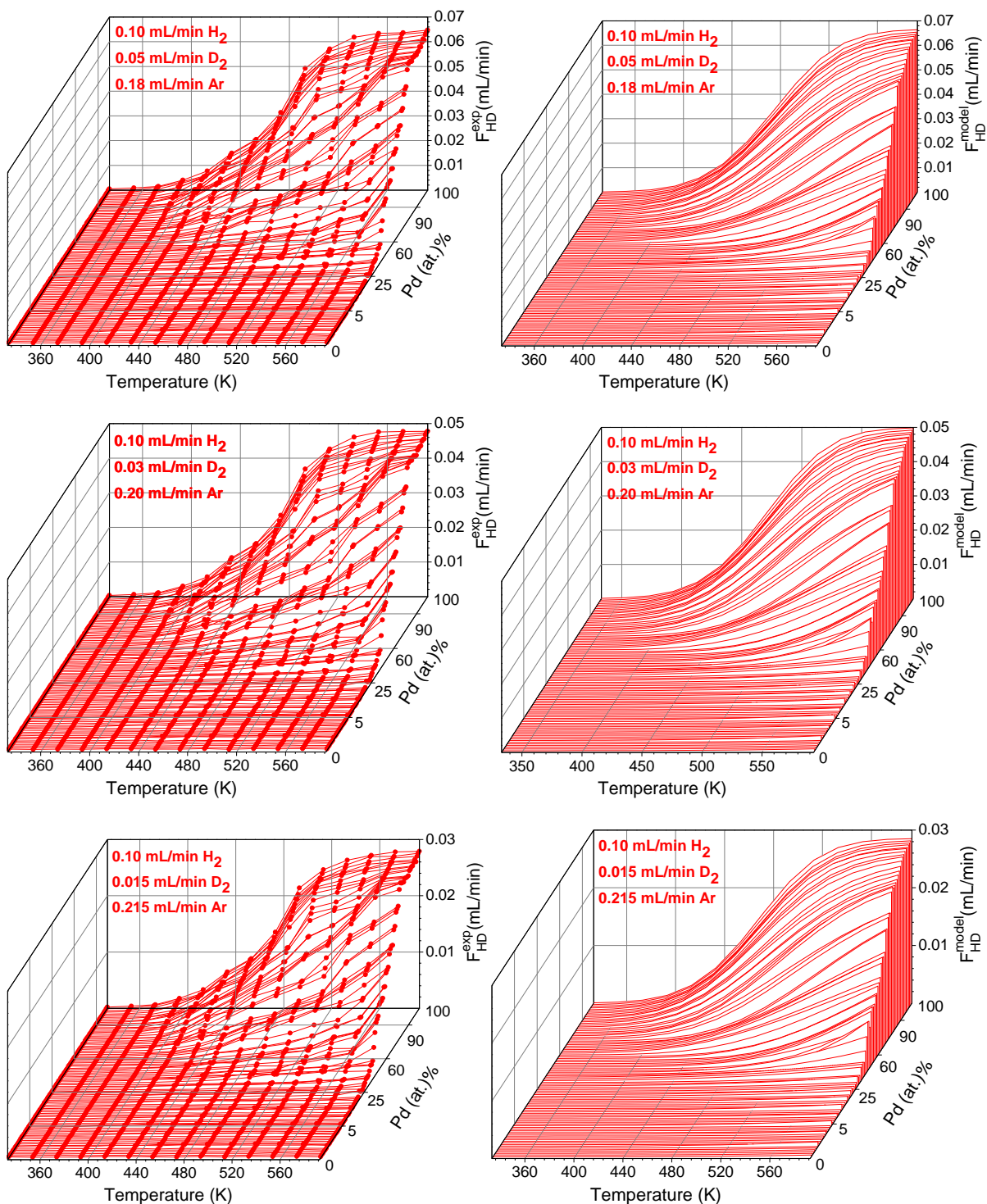
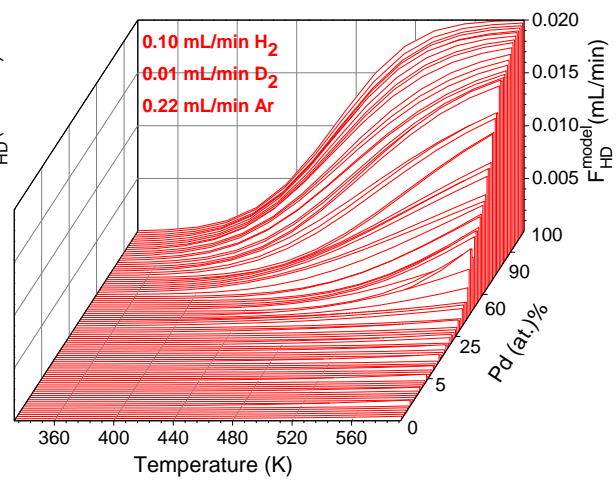
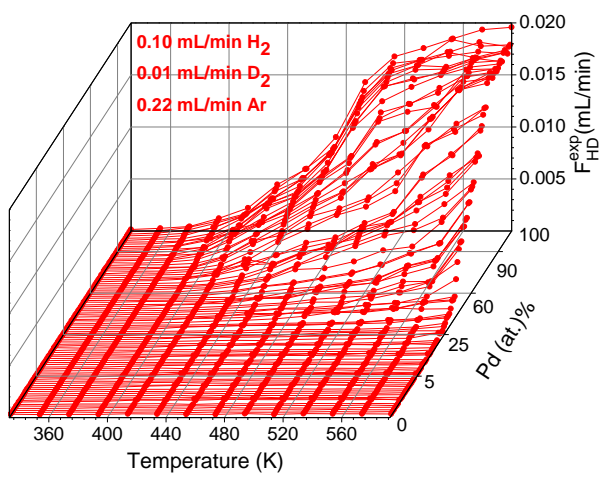


Figure 3.13. HD flow rate versus temperature measured across $\text{Ag}_x\text{Pd}_{1-x}$ composition space. For all $\text{Ag}_x\text{Pd}_{1-x}$ compositions conversion increases with increasing T and decreasing x and y . Flow conditions in one channel are labeled on each figure ($P_{\text{tot}} = 1 \text{ atm}$).



3.8 References

1. Hammer, B. and J.K. Norskov, *Why gold is the noblest of all the metals*. Nature, 1995. **376**(6537): p. 238-240.
2. Aasberg-Petersen, K., C.S. Nielsen, and S.L. Jørgensen, *Membrane reforming for hydrogen*. Catalysis Today, 1998. **46**(2): p. 193-201.
3. deRosset, A.J., *Diffusion of Hydrogen through Palladium Membranes*. Industrial & Engineering Chemistry, 1960. **52**(6): p. 525-528.
4. Paglieri, S.N. and J.D. Way, *INNOVATIONS IN PALLADIUM MEMBRANE RESEARCH*. Separation and Purification Methods, 2002. **31**(1): p. 1-169.
5. Lewis, F.A., *The palladium-hydrogen system: Structures near phase transition and critical points*. International Journal of Hydrogen Energy, 1995. **20**(7): p. 587-592.
6. Jayaraman, V. and Y.S. Lin, *Synthesis and hydrogen permeation properties of ultrathin palladium-silver alloy membranes*. Journal of Membrane Science, 1995. **104**(3): p. 251-262.
7. Shu, J., et al., *Catalytic palladium-based membrane reactors: A review*. The Canadian Journal of Chemical Engineering, 1991. **69**(5): p. 1036-1060.
8. Collins, J.P., et al., *Catalytic Dehydrogenation of Propane in Hydrogen Permselective Membrane Reactors*. Industrial & Engineering Chemistry Research, 1996. **35**(12): p. 4398-4405.
9. Roa, F., et al., *Preparation and characterization of Pd-Cu composite membranes for hydrogen separation*. Chemical Engineering Journal, 2003. **93**(1): p. 11-22.
10. Kamakoti, P., et al., *Prediction of Hydrogen Flux through Sulfur-Tolerant Binary Alloy Membranes*. Science, 2005. **307**(5709): p. 569-573.
11. Kulprathipanja, A., et al., *Pd and Pd-Cu membranes: inhibition of H₂ permeation by H₂S*. Journal of Membrane Science, 2005. **254**(1): p. 49-62.
12. Morreale, B.D., et al., *Effect of hydrogen-sulfide on the hydrogen permeance of palladium-copper alloys at elevated temperatures*. Journal of Membrane Science, 2004. **241**(2): p. 219-224.
13. Nam, S.-E. and K.-H. Lee, *Hydrogen separation by Pd alloy composite membranes: introduction of diffusion barrier*. Journal of Membrane Science, 2001. **192**(1): p. 177-185.
14. Piper, J., *Diffusion of Hydrogen in Copper-Palladium Alloys*. Journal of Applied Physics, 1966. **37**(2): p. 715-721.
15. Uemiya, S., T. Matsuda, and E. Kikuchi, *Hydrogen permeable palladium-silver alloy membrane supported on porous ceramics*. Journal of Membrane Science, 1991. **56**(3): p. 315-325.
16. Amandusson, H., L.-G. Ekedahl, and H. Dannetun, *Hydrogen permeation through surface modified Pd and PdAg membranes*. Journal of Membrane Science, 2001. **193**(1): p. 35-47.

17. Knapton, A.G., *Palladium Alloys for Hydrogen Diffusion Membranes*. Platinum Metal Reviews, 1977. **21**(2): p. 44-50.
18. E. Jurisch, A.M., and A. Sieverts, *Z. Anorg. Allgem. Chem.*, 1915. **92**(4): p. 329.
19. Hagen, A.S.a.H., *Z. Phys. Chem.*, 1935. **174A**(3-4): p. 247.
20. O'Brien, C.P., et al., *The Kinetics of H₂-D₂ Exchange over Pd, Cu, and PdCu Surfaces*. The Journal of Physical Chemistry C, 2011. **115**(49): p. 24221-24230.
21. O'Brien, C.P., et al., *H₂-D₂ Exchange Kinetics in the Presence of H₂S over Pd₄S, Pd₇₀Cu₃₀, and Pd₄₇Cu₅₃ Surfaces*. The Journal of Physical Chemistry C, 2012. **116**(33): p. 17657-17667.
22. Lewis, F.A., *The palladium hydrogen system*. 1967, London; New York: Academic Press.
23. Hurlbert, R.C. and J.O. Konecny, *Diffusion of Hydrogen through Palladium*. The Journal of Chemical Physics, 1961. **34**(2): p. 655-658.
24. Jewett, D.N. and A.C. Makrides, *Diffusion of hydrogen through palladium and palladium-silver alloys*. Transactions of the Faraday Society, 1965. **61**(0): p. 932-939.
25. Pyun, S.-I., W.-J. Lee, and T.-H. Yang, *Hydrogen diffusion through palladium-gold alloy coatings electrodeposited on palladium substrate under permeable boundary condition*. Thin Solid Films, 1997. **311**(1): p. 183-189.
26. Bartczak, W.M. and J. Stawowska, *Interaction of Dihydrogen with Transition Metal (Pd, Ni, Ag, Cu) Clusters*. Structural Chemistry, 2004. **15**(5): p. 447-459.
27. Cattania, M.G., et al., *Interaction of hydrogen with a palladium (110) surface*. Surface Science, 1983. **126**(1): p. 382-391.
28. Dong, W., G. Kresse, and J. Hafner, *Dissociative adsorption of H₂ on the Pd(111) surface*. Journal of Molecular Catalysis A: Chemical, 1997. **119**(1): p. 69-76.
29. Lozano, A., A. Groß, and H.F. Busnengo, *Molecular dynamics study of H₂ dissociation on H-covered Pd(100)*. Physical Review B, 2010. **81**(12): p. 121402.
30. Muschiol, U., P.K. Schmidt, and K. Christmann, *Adsorption and absorption of hydrogen on a palladium (210) surface: a combined LEED, TDS, ΔΦ and HREELS study*. Surface Science, 1998. **395**(2): p. 182-204.
31. Benton, A.F. and L.C. Drake, *Kinetics of Reaction and Adsorption in the System Silver—Oxygen*. Journal of the American Chemical Society, 1934. **56**(2): p. 255-263.
32. Benton, A.F. and J.C. Elgin, *THE CATALYTIC SYNTHESIS OF WATER VAPOR IN CONTACT WITH METALLIC SILVER*. Journal of the American Chemical Society, 1926. **48**(12): p. 3027-3046.
33. Drake, L.C. and A.F. Benton, *Adsorption of Carbon Dioxide and Hydrogen on Bare and Oxygen-covered Silver Surfaces*. Journal of the American Chemical Society, 1934. **56**(3): p. 506-511.
34. Zhukov, V., K.D. Rendulic, and A. Winkler, *Coadsorption of hydrogen and potassium on silver single crystal surfaces*. Vacuum, 1996. **47**(1): p. 5-11.

35. Eichler, A., et al., *Trends in the chemical reactivity of surfaces studied by ab initio quantum-dynamics calculations*. Physical Review B, 1999. **59**(20): p. 13297-13300.
36. Eichler, A., G. Kresse, and J. Hafner, *Ab-initio calculations of the 6D potential energy surfaces for the dissociative adsorption of H₂ on the (100) surfaces of Rh, Pd and Ag*. Surface Science, 1998. **397**(1): p. 116-136.
37. Montoya, A., A. Schlunke, and B.S. Haynes, *Reaction of Hydrogen with Ag(111): Binding States, Minimum Energy Paths, and Kinetics*. The Journal of Physical Chemistry B, 2006. **110**(34): p. 17145-17154.
38. Greeley, J. and M. Mavrikakis, *Surface and Subsurface Hydrogen: Adsorption Properties on Transition Metals and Near-Surface Alloys*. The Journal of Physical Chemistry B, 2005. **109**(8): p. 3460-3471.
39. Duś, R. and E. Nowicka, *Atomic deuterium (hydrogen) adsorption on thin silver films*. Progress in Surface Science, 2003. **74**(1): p. 39-56.
40. Manzoor, D. and S. Pal, *Reactivity and Catalytic Activity of Hydrogen Atom Chemisorbed Silver Clusters*. The Journal of Physical Chemistry A, 2015. **119**(24): p. 6162-6170.
41. Mikovskys, R.J., M. Boudart, and H.S. Taylor, *Hydrogen-Deuterium Exchange on Copper, Silver, Gold and Alloy Surfaces I*. Journal of the American Chemical Society, 1954. **76**(14): p. 3814-3819.
42. Hammer, B. and J.K. Nørskov, *Theoretical surface science and catalysis—calculations and concepts*, in *Advances in Catalysis*. 2000, Academic Press. p. 71-129.
43. Ruban, A., et al., *Surface electronic structure and reactivity of transition and noble metals I Communication presented at the First Francqui Colloquium, Brussels, 19–20 February 1996. I*. Journal of Molecular Catalysis A: Chemical, 1997. **115**(3): p. 421-429.
44. Baber, A.E., H.L. Tierney, and E.C.H. Sykes, *Atomic-Scale Geometry and Electronic Structure of Catalytically Important Pd/Au Alloys*. ACS Nano, 2010. **4**(3): p. 1637-1645.
45. Hammer, B. and J.K. Nørskov, *Theoretical surface science and catalysis—calculations and concepts*, in *Advances in Catalysis*. 2000, Academic Press. p. 71-129.
46. Wei, T., J. Wang, and D.W. Goodman, *Characterization and Chemical Properties of Pd–Au Alloy Surfaces†*. The Journal of Physical Chemistry C, 2007. **111**(25): p. 8781-8788.
47. Fleutot, B., J.B. Miller, and A.J. Gellman, *Apparatus for deposition of composition spread alloy films: The rotatable shadow mask*. Journal of Vacuum Science & Technology A: Vacuum, Surfaces, and Films, 2012. **30**(6): p. 061511.
48. Priyadarshini, D., et al., *High-Throughput Characterization of Surface Segregation in CuxPd1-x Alloys*. The Journal of Physical Chemistry C, 2011. **115**(20): p. 10155-10163.
49. He, J.W., et al., *Surface chemistry of monolayer metallic films on Re(0001) and Mo(110)*. Journal of Vacuum Science & Technology A, 1990. **8**(3): p. 2435-2444.
50. Park, C., E. Bauer, and H. Poppa, *Growth and alloying of Pd films on Mo(110) surfaces*. Surface Science, 1985. **154**(2): p. 371-393.

51. Li, X., Z. Zhang, and V.E. Henrich, *Inelastic electron background function for ultraviolet photoelectron spectra*. Journal of Electron Spectroscopy and Related Phenomena, 1993. **63**(3): p. 253-265.
52. McQuarrie, D.A., *Statistical Mechanics*. 2000: University Science Books.
53. Yin, C., et al., *Detection of CuAuPd Phase Boundaries Using Core Level Shifts*. The Journal of Physical Chemistry B, 2017.
54. Hammer, B., Y. Morikawa, and J.K. Norskov, *CO chemisorption at metal surfaces and overlayers*. Phys Rev Lett, 1996. **76**(12): p. 2141-2144.
55. Hofmann, T., et al., *Using Photoelectron Spectroscopy and Quantum Mechanics to Determine d-Band Energies of Metals for Catalytic Applications*. The Journal of Physical Chemistry C, 2012. **116**(45): p. 24016-24026.
56. Gorzkowski, M.T. and A. Lewera, *Probing the Limits of d-Band Center Theory: Electronic and Electrocatalytic Properties of Pd-Shell–Pt-Core Nanoparticles*. The Journal of Physical Chemistry C, 2015. **119**(32): p. 18389-18395.
57. Zhou, W.P., et al., *Size effects in electronic and catalytic properties of unsupported palladium nanoparticles in electrooxidation of formic acid*. The Journal of Physical Chemistry B, 2006. **110**(27): p. 13393-13398.
58. Gajdoš, M., A. Eichler, and J. Hafner, *CO adsorption on close-packed transition and noble metal surfaces: trends from ab initio calculations*. Journal of Physics: Condensed Matter, 2004. **16**(8): p. 1141.
59. Toyoda, E., et al., *The d-Band Structure of Pt Nanoclusters Correlated with the Catalytic Activity for an Oxygen Reduction Reaction*. The Journal of Physical Chemistry C, 2011. **115**(43): p. 21236-21240.
60. Gumuslu, G., et al., *Correlation of Electronic Structure with Catalytic Activity: H₂–D₂ Exchange across CuxPd1–x Composition Space*. ACS Catalysis, 2015. **5**(5): p. 3137-3147.
61. James, A.D., *The Microkinetics of heterogeneous catalysis*. 1993: Washington, DC : American Chemical Society, 1993.
62. Cobden, P.D., B.E. Nieuwenhuys, and V.V. Gorodetskii, *Adsorption of some small molecules on a Pd field emitter*. Applied Catalysis A: General, 1999. **188**(1): p. 69-77.
63. Gdowski, G.E., T.E. Felter, and R.H. Stulen, *Effect of surface temperature on the sorption of hydrogen by Pd(111)*. Surface Science, 1987. **181**(3): p. L147-L155.
64. Okuyama, H., et al., *Path and mechanism of hydrogen absorption at Pd(100)*. Surface Science, 1998. **401**(3): p. 344-354.
65. Fogelberg, J., et al., *Kinetic modeling of hydrogen adsorption/absorption in thin films on hydrogen-sensitive field-effect devices: Observation of large hydrogen-induced dipoles at the Pd-SiO₂ interface*. Journal of Applied Physics, 1995. **78**(2): p. 988-996.
66. Johansson, M., et al., *Hydrogen adsorption on palladium and palladium hydride at 1bar*. Surface Science, 2010. **604**(7): p. 718-729.

67. Johansson, M., O. Lytken, and I. Chorkendorff, *The sticking probability of hydrogen on Ni, Pd and Pt at a hydrogen pressure of 1 bar*. Topics in Catalysis, 2007. **46**(1): p. 175-187.
68. Johansson, M., O. Lytken, and I. Chorkendorff, *The sticking probability for H₂ in presence of CO on some transition metals at a hydrogen pressure of 1bar*. Surface Science, 2008. **602**(10): p. 1863-1870.
69. Engel, T. and H. Kuipers, *A molecular-beam investigation of the scattering, adsorption and absorption of H₂ and D₂ from/on/in Pd(111)*. Surface Science, 1979. **90**(1): p. 162-180.
70. Ratajczykowa, I., *The influence of CO on hydrogen sorption by Pd(111) single crystals*. Surface Science, 1986. **172**(3): p. 691-714.
71. Holden, S.J. and D.R. Rossington, *Hydrogen Adsorption on Silver, Gold, and Aluminum. Studies of Parahydrogen Conversion*. The Journal of Physical Chemistry, 1964. **68**(5): p. 1061-1067.
72. Masel, R.I., *Principles of adsorption and reaction on solid surfaces*. 1996: New York (N.Y.) : Wiley.
73. Lee, G. and E.W. Plummer, *Interaction of hydrogen with the Ag(111) surface*. Physical Review B, 1995. **51**(11): p. 7250-7261.
74. Wilde, M., et al., *Hydrogen absorption in oxide-supported palladium nanocrystals*. Physical Review B, 2008. **77**(11): p. 113412.
75. Savara, A., *Kinetic Evidence for a Non-Langmuir-Hinshelwood Surface Reaction: H/D Exchange over Pd Nanoparticles and Pd(111)*. Chemphyschem, 2013. **14**(8): p. 1686-1695.
76. Ludwig, W., et al., *Subsurface Hydrogen Diffusion into Pd Nanoparticles: Role of Low-Coordinated Surface Sites and Facilitation by Carbon*. The Journal of Physical Chemistry C, 2012. **116**(5): p. 3539-3544.
77. Hammer, B. and J.K. Nørskov, *Theoretical surface science and catalysis—calculations and concepts*. Advances in catalysis, 2000. **45**: p. 71-129.
78. Gauthier, Y., et al., *Adsorption Sites and Ligand Effect for CO on an Alloy Surface: A Direct View*. Physical Review Letters, 2001. **87**(3): p. 036103.
79. Mavrikakis, M., B. Hammer, and J.K. Nørskov, *Effect of Strain on the Reactivity of Metal Surfaces*. Physical Review Letters, 1998. **81**(13): p. 2819-2822.
80. Lambert, R.M. and G. Pacchioni, *Chemisorption and Reactivity on Supported Clusters and Thin Films.: Towards an Understanding of Microscopic Processes in Catalysis*. Vol. 331. 2013: Springer Science & Business Media.
81. Kratzer, P., B. Hammer, and J.K. Nørskov, *Geometric and electronic factors determining the differences in reactivity of H₂ on Cu(100) and Cu(111)*. Surface Science, 1996. **359**(1): p. 45-53.

82. Kratzer, P., B. Hammer, and J.K. Nørskov, *A theoretical study of CH₄ dissociation on pure and gold-alloyed Ni(111) surfaces*. The Journal of Chemical Physics, 1996. **105**(13): p. 5595-5604.
83. Hammer, B., O.H. Nielsen, and J.K. Nørskov, *Structure sensitivity in adsorption: CO interaction with stepped and reconstructed Pt surfaces*. Catalysis Letters, 1997. **46**(1): p. 31-35.
84. Liu, P. and J.K. Nørskov, *Ligand and ensemble effects in adsorption on alloy surfaces*. Physical Chemistry Chemical Physics, 2001. **3**(17): p. 3814-3818.
85. Løvvik, O.M. and R.A. Olsen, *Density functional calculations of hydrogen adsorption on palladium-silver alloy surfaces*. The Journal of Chemical Physics, 2003. **118**(7): p. 3268-3276.
86. Reniers, F., M. Jardinier-Offergeld, and F. Bouillon, *Auger electron spectroscopy study of the surface segregation in silver-palladium alloys*. Surface and Interface Analysis, 1991. **17**(6): p. 343-351.
87. Yamamura, M., K. Kaneda, and T. Imanaka, *Preparation of Pd-Ag thin films by the RF-sputtering method and its catalysis for oxidative dehydrogenation of allylic alcohols*. Catalysis Letters, 1989. **3**(3): p. 203-208.
88. Shu, J., et al., *Surface segregation of Pd-Ag membranes upon hydrogen permeation*. Surface Science, 1993. **291**(1): p. 129-138.
89. González, S., et al., *On the Promoting Role of Ag in Selective Hydrogenation Reactions over Pd-Ag Bimetallic Catalysts: A Theoretical Study*. The Journal of Physical Chemistry C, 2007. **111**(18): p. 6852-6856.
90. Løvvik, O.M. and S.M. Opalka, *Reversed surface segregation in palladium-silver alloys due to hydrogen adsorption*. Surface Science, 2008. **602**(17): p. 2840-2844.

CHAPTER 4

Characterization of Composition, Electronic Structure and H₂-D₂

Exchange Activity across Cu_xAu_yPd_{1-x-y} Alloys

4.1 Chapter abstract

Finding the optimal catalyst composition for a given application is the major challenge in multicomponent catalyst design due to the need to perform many catalyst preparation, characterization and reactivity measurements across composition space. To accelerate this search, thin multicomponent films called Composition Spread Alloy Films (CSAFs) are prepared, which have composition gradients parallel to their surfaces, A_xB_yC_{1-x-y} with $x = 0 \rightarrow 1$ and $y = 0 \rightarrow 1 - x$. In order to study alloy catalysis across a CSAF, a 100 channel microreactor array has been developed to run steady state catalytic reactions at different positions or alloy compositions on the CSAF. Cu_xAu_yPd_{1-x-y} CSAFs spanning all of binary and ternary composition space have been prepared using a rotating shadow mask CSAF deposition tool developed in house.

The relationship between alloy catalyst activity and electronic structure is investigated experimentally across Cu_xAu_yPd_{1-x-y} CSAFs. H₂-D₂ exchange kinetics were measured at 100 discrete compositions on the CSAFs over a temperature range of 333 – 593 K. Characterization of the CSAFs was done using X-ray photoelectron spectroscopy. H₂ conversion was chosen to be the indicator of activity and it was found to increase with increasing Pd content. A microkinetic model was used to estimate the energy barriers to dissociative adsorption and recombinative desorption of H₂ as functions of alloy composition, x and y . Across the Cu_xAu_yPd_{1-x-y} CSAF,

increasing Pd content was found to decrease the adsorption barrier from 0.6 to 0.15 eV and increase the desorption barrier from 0.6 to 0.9 eV, which suggests H₂-D₂ exchange reaction is limited by H₂ desorption. Spatially resolved X-ray photoelectron spectra obtained from the CSAFs were used to estimate the energy of the valence-band center as a function of alloy composition. The v-band center shifted monotonically from -3.4 to -5.7 eV across the Cu_xAu_yPd_{1-x-y} CSAF. This data provides the first experimental correlation of elementary reaction barriers with valence band energy across a continuous span of ternary alloy composition space.

4.2 Introduction

Pd is a good membrane material to obtain high purity H₂ [1]. It has a strong ability to dissociate and dissolve H₂, a high H₂ selectivity versus other gases and the membrane costs are competitive [2, 3]. However, Pd has some drawbacks such as H₂ embrittlement with temperature and sulfur poisoning [4-8]. These drawbacks often can be eliminated by alloying Pd with other metals such as Ag, Cu, Au, Fe, Y [9-16]. Alloying Pd with Au was reported to increase permeability of the membrane [17] and make the membrane more sulfur tolerant [9]. However, its high cost limits its usability [18]. Cu, on the other hand, can reduce the cost while still improving the properties of the pure Pd membranes [12, 19, 20].

H₂ transport through Pd membranes involves three main steps, H₂ adsorbs dissociatively on the upstream side of the membrane surface, H atoms diffuse through the membrane and then H₂ recombinatively desorbs from the downstream surface [21, 22]. The energetics of H₂ dissociation over pure Pd, pure Cu and pure Au have been well characterized. H₂ is known to dissociate on Pd without significant activation barriers [23-27]. However H₂ dissociation over Cu is hindered by a large activation barrier (~0.5-0.7 eV) [28-33]. Au, known as the noblest metal,

is actually the least active one for dissociative adsorption of H₂ [34]. Recently, Au nanoparticles have received significantly more attention than bulk Au surfaces due to their remarkable catalytic performance [35]. However, it is known that H₂ does not adsorb on the Au(310) surfaces [36], H₂ adsorption is an endothermic process on the Au(111) surface [37] and that H₂ does not readily dissociate on Au (110) surfaces [38]. The lack of affinity of Cu and Au to H₂ is usually attributed to the electronic structures of the surfaces and the fact that adsorbed species interact with *d*-band electrons of metal surfaces [1, 39, 40]. Cu has filled anti-bonding states, so the *d*-contribution of the bond is not attractive [41, 42]. Au also has a filled *d*-band, so when H₂ comes in contact with the surface, it is repelled [43].

Alloying Pd with Cu enhances membrane characteristics, as explained before. In one study that was conducted using scanning tunneling microscopy, evaporating a small amount of Pd atoms on Cu (111) surfaces was shown to largely enhance the dissociative sticking probability of low energy H₂ molecules with respect to the inert Cu(111) surface [44]. A very similar result was also observed utilizing molecular dynamics calculations based on density functional theory, showing that isolated Pd atoms on Cu (111) significantly increase the reactivity of the otherwise inert, pure Cu surface. The calculated energy barrier for H₂ dissociation in this study is smaller than the previously reported values on Cu (111) by a factor of two: 0.23 eV vs ~0.46 eV [45]. O'Brien et al. showed that some Cu-Pd binary alloys were more active than pure Pd for the dissociation of H₂ [21]. Further, Gumuslu et al. managed to characterize the H₂-D₂ exchange reaction across a continuous composition space of Cu_xPd_{1-x} alloys [46].

Neurock et al., examined examine the effect of alloying Pd and Au on the kinetics of ethylene hydrogenation over well-defined Pd and Pd-Au surfaces using a first-principles-based dynamic Monte Carlo simulation method. They found that the apparent turnover frequency

remained more or less constant with Au composition up to 12.5%. Increasing the surface composition of Au was shown to weaken the strength of the metal–hydrogen bonds and also shut down sites for H₂ adsorption and activation [47]. There are also other experimental and theoretical studies investigating different reactions across Au-Pd binary metals [48-51]. However, the effect of alloying Pd with Au and Cu on the energetics of the H₂ dissociation reaction has not been investigated. Hence, the activity-electronic structure–composition relationship for Cu-Au-Pd alloys that we present in this work provides benchmarks for further experimental and theoretical studies.

In this study, a Cu_xAu_yPd_{1-x-y} CSAF that spans a continuous range of compositions ($x = 0 \rightarrow 1$ and $y = 0 \rightarrow 1$) was used to characterize the activity for H₂-D₂ exchange. Quantitative kinetic data has been obtained and analyzed to elucidate the mechanism and extract fundamental kinetic parameters for H₂-D₂ exchange as functions of alloy composition. Within the Langmuir-Hinshelwood framework for modeling surface reaction kinetics, H₂-D₂ exchange has the simplest possible reaction mechanism parameterized by just two rate constants: k_{ads} , for the dissociative adsorption of H₂ and k_{des} , for the recombinative desorption of H₂. By measuring these two rate constants over a range of temperatures, the activation barriers to dissociative adsorption (ΔE_{ads}^\ddagger) and recombinative desorption (ΔE_{des}^\ddagger) can be estimated across Cu_xAu_yPd_{1-x-y} alloy composition space. In addition, the valence band electronic structures of the alloys at each composition are obtained using X-ray photoelectron spectroscopy. Overall, by combining our materials library CSAFs, our multichannel microreactor array, and our spatially resolved surface characterization techniques, we can correlate reaction barriers (ΔE_{ads}^\ddagger and ΔE_{des}^\ddagger) with $\epsilon_v(x)$ across the entire Cu_xAu_yPd_{1-x-y} composition space.

4.3 Experimental

4.3.1 CSAF preparation

The CSAF samples were prepared by evaporative deposition of Cu, Au and Pd onto a $14 \times 14 \times 2 \text{ mm}^3$ polished Mo substrate (Valley Design Corp.) using a rotatable shadow mask CSAF deposition tool that has been described in detail previously [52]. Electron beam evaporation sources containing Cu, Au and Pd were positioned 120° apart from each other. Deposition rates from all three sources were controlled by filament heating power and measured using a QCM. The film thickness ($\sim 100 \text{ nm}$ in this work) was controlled by the deposition time. The positions and orientations of the shadow masks between the sources and the substrate result in a flux gradient across the substrate. Mo was chosen as a substrate material because it does not alloy with Au, Cu or Pd and stabilizes the film against dewetting at annealing temperatures [53-56]. CSAFs were deposited at room temperature over periods of 6 to 8 h, annealed at 800 K for 1 h to induce crystallization and sputtered using a He^+ beam under ultrahigh vacuum (UHV) conditions.

4.3.2 Characterization of CSAF composition and electronic structure

XPS analysis of the $\text{Cu}_x\text{Au}_y\text{Pd}_{1-x-y}$ CSAF was performed in a ThetaProbe™ (Thermo-Fisher Scientific Inc.) to map the local composition and the valence band electronic structure across the sample surface. XPS characterization process was the same as described in Section 3.3.2. Spatially resolved maps of the Cu $2p_{3/2}$, Au $4f_{7/2}$ and Pd $3d_{3/2}$ XP spectra were obtained by lateral translation of the CSAF such that its plane intersected the source-analyzer focal point. The obtained composition and valence band maps across the CSAF are given in the Results section (Section 4.4).

4.3.3 Characterization of H₂-D₂ exchange activity across Cu_xAu_yPd_{1-x-y} CSAF

The H₂-D₂ exchange activity of the Cu_xAu_yPd_{1-x-y} CSAFs was measured by flowing H₂, D₂, and Ar through a 100-channel microreactor array. The experimental setup used was explained in detail in Section 2.2.2. Cu_xAu_yPd_{1-x-y} was prepared as explained in Section 2.2.2. Mass flow controllers (Aalborg GFC 17) were used to regulate the flow rates of H₂ (99.999%, Valley National Gases), D₂ (99.999%, Valley National Gases) and Ar (99.999%, Valley National Gases) through the channels to the CSAF surface. The area within each microreactor and corresponding to one catalyst composition across the ternary CSAF was approximately 0.006 cm². The inlet flow rates of H₂, D₂, and Ar were adjusted to the conditions listed in Table 4.1.

Table 4.1. Flow rates of H₂ ($F_{H_2}^{in}$), D₂ ($F_{D_2}^{in}$), and Ar (F_{Ar}^{in}) for the eleven different gas conditions used during H₂-D₂ exchange experiments at $P_{tot} = 1$ atm. Flow rates in one channel can be found by dividing the listed values into 102. The total flow rate is kept constant at 0.15 mL/min per channel.

	$F_{D_2}^{in}$ (mL/min)	$F_{H_2}^{in}$ (mL/min)	F_{Ar}^{in} (mL/min)	P_{D_2} (kPa)	P_{H_2} (kPa)
1	5.00	5.00	5.00	33.8	33.8
2	5.00	1.00	9.00	33.8	6.75
3	5.00	0.50	9.50	33.8	3.38
4	5.00	0.20	9.90	33.8	0.67
5	5.00	0.10	9.80	33.8	1.35
6	5.00	0.05	9.95	33.8	0.34
7	10.00	0.05	4.95	67.5	0.34
8	2.50	0.05	12.45	16.9	0.34
9	1.00	0.05	13.95	6.75	0.34
10	5.00	1.00	4.00	50.7	10.1
11	5.00	1.00	14.00	25.3	4.05

The CSAF was heated by a thermocouple spot-welded to one of its sides. The experiments were performed over a temperature range of 333 K to 533 K with 20 K increments and at atmospheric pressure. At each temperature, approximately 4 minutes were required to allow the system to reach steady state. The product gas mixture from each of the 100 different reaction volumes was sent to the mass spectrometer for quantification. The CSAF surface was pretreated with H₂ prior to the experiments. Also, between each set of experiments the CSAF surface was left in contact with flowing H₂.

The composition of the reaction products was calculated using the mass spectrometer signals at $m/q = 2, 3,$ and 4 amu obtained from the product gas samples. Two extra channels were added to the microreactor system, one of which is an empty capillary, which allows the reactant gas mixture to bypass the microreactor. This channel gave the signals at $m/q = 2, 3,$ and 4 amu when there is no H₂-D₂ exchange activity. These signals are our baseline, which indicates zero conversion. The second channel is also a capillary through which the reactant gas mixture bypasses the microreactor. A coiled flow reactor filled with Pd is attached to the end of this extra channel. By heating the Pd wire to a temperature that ensures equilibrium conversion of the product gases, we can collect signals of $m/q = 2, 3,$ and 4 amu at equilibrium conversion. With these extra channels, the mass spectrometer signals can be calibrated after each experiment. The composition of the product gases can be calculated by assuming that the H₂, HD, and D₂ mass spectrometer signals sampled from the product gas are proportional to the H₂, HD, and D₂ partial pressures exiting the microreactor between zero and equilibrium conversion.

$$S_2 = (1 - X)S_2^{zero} + XS_2^{eq} \quad (4.1)$$

$$S_3 = (1 - X)S_3^{zero} + XS_3^{eq} \quad (4.2)$$

$$S_4 = (1 - X)S_4^{zero} + XS_4^{eq} \quad (4.3)$$

where X is conversion and S is the mass spectrometer signal collected. Subscripts 2, 3, and 4 show the m/q values. Superscript *zero* represents our baseline, the signals collected from the zero conversion channel. Superscript *eq* represents the signals collected when the reaction has reached equilibrium, or full conversion. Linear least squares regression is used to calculate conversions. At equilibrium, the composition of the product gases H_2 , HD , and D_2 can be calculated by

$$\frac{P_{HD}^2}{P_{H_2}P_{D_2}} = 4.16 \exp\left(\frac{-77.7}{T}\right) \quad (4.4)$$

where T is temperature (K); and P_{H_2} , P_{D_2} and P_{HD} are the partial pressures of H_2 , D_2 and HD , respectively [57].

H_2 conversions were measured at 100 channels at $T = 333 - 593$ K at 11 different inlet flow conditions specified in Table 4.1. The measured conversions were used to calculate the kinetic parameters, i.e. the activation barriers to dissociative adsorption (ΔE_{ads}^\ddagger) and recombinative desorption (ΔE_{des}^\ddagger) for the catalytic H_2 - D_2 exchange reaction as a function of $Cu_xAu_yPd_{1-x-y}$ alloy composition. A detailed explanation of the microkinetic model and calculation methods has been given in Section 3.4.

4.4 Results and discussion

4.4.1 Performance of the microreactor

During the course of this work, we have developed a new design for our microreactors as explained in detail in the Experimental section (Section 2.2.2). After the multichannel microreactor system is set up, the first step was to measure the flow rates through individual channels. Using an automated valve, the gas flow of Ar and N₂ was alternated at the inlets to the microreactor and the time for N₂ to reach the end of the output capillary for each channel was measured. The measured transit times through each of the 100 individual channels are shown in Figure 4.1. The measured transit times depend on the flow rates used ($F_{N_2} = F_{Ar} = 10$ mL/min) and the volumes of each channel. The mean transit time was measured to be approximately 42 seconds. The standard deviation of the transit times for the 100 channels was found to be 2.3% of

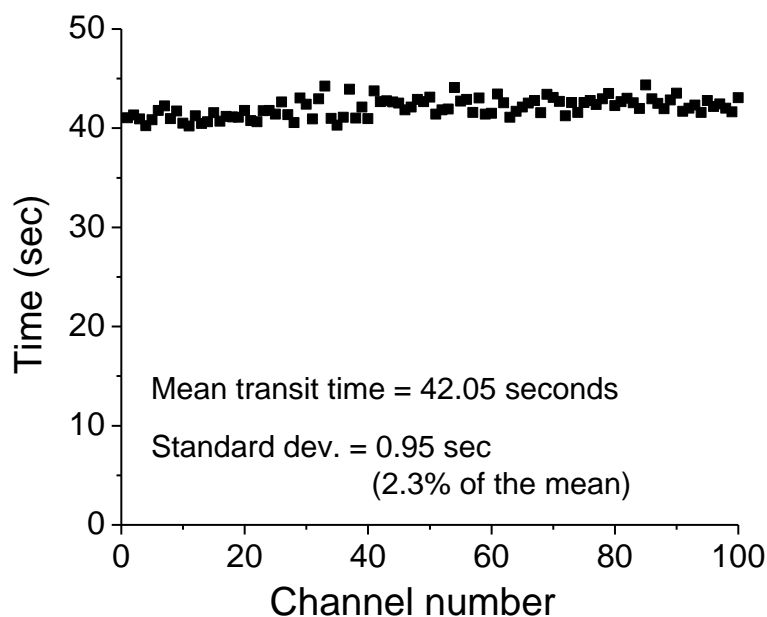


Figure 4.1. The measured gas transit times through each of the 100 microreactor channels.

their mean value. Since transit time and flow through the channel are inversely related, this number also characterizes the standard deviation in flow rate through the microreactor array.

The ability of the multichannel microreactor system to characterize the catalytic activity across CSAFs was also tested. The H_2 - D_2 exchange reaction, which has the simplest possible reaction mechanism (shown schematically at the inset of Figure 4.2), was chosen to run preliminary reaction kinetics experiments across a pure Pd film. As seen in Figure 4.2, uniform activity was observed across the pure Pd film at the specified reaction temperature. Changing the reaction temperature and the reactant flow rates, permits collection of a large amount of kinetic data for comparisons of catalytic activity in a short amount of time.

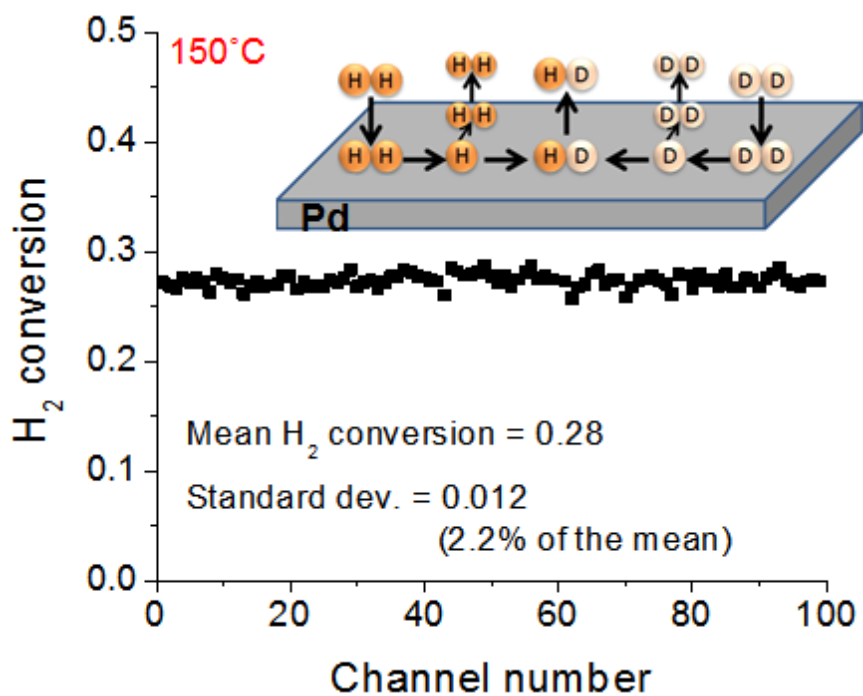


Figure 4.2. In order to test the performance of the multichannel microreactor system in capturing catalytic activity across the CSAFs, H_2 - D_2 exchange across a pure Pd film was investigated. H_2 conversion was chosen to be the indicator of catalytic activity. The graph shows how catalytic activity changes across the Pd film. Uniform activity has been observed across the Pd surface. In the inset, the schematic representation of the H_2 - D_2 exchange reaction is given.

4.4.2 Characterization of CSAF composition

Spatially resolved measurements of $\text{Cu}_x\text{Au}_y\text{Pd}_{1-x-y}$ composition were made using XPS across a 13×13 grid with 1 mm spacing, as shown in Figure 4.3.

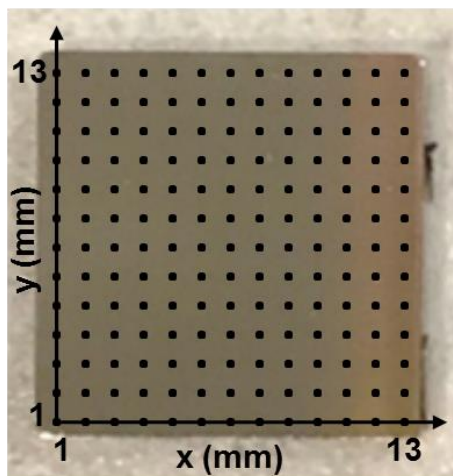


Figure 4.3. Photograph of the ternary $\text{Cu}_x\text{Au}_y\text{Pd}_{1-x-y}$ CSAF with an overlaid grid of real-space coordinates across which the XPS measurements are performed.

The generated composition maps for all three components, Cu, Au, and Pd, are given in Figure 4.4. Composition changes from 0% to almost 100%, which shows that nearly the full composition range for Cu, Au and Pd was covered. The gradient is widespread, which makes it possible to analyze a large amount of distinct ternary alloy compositions. This can be seen by looking at the ternary composition map in Figure 4.5, where the measurement points are marked as black squares. The even distribution of points shows that CSAF spans all ternary alloy composition space. Having several data points on the edges shows that we also have all three binary alloys (Cu-Pd, Au-Pd, and Cu-Au) on the CSAF. The CSAF surface is $14 \times 14 \text{ mm}^2$, however, our multichannel microreactor array only covers $10 \times 10 \text{ mm}^2$ at the center of the CSAF substrate. The alloy compositions on the 10×10 reactor grid are determined using a composition

distribution model (CDM), which was developed in our group. CDM provides a quantitative basis for estimating composition continuously at all locations across the CSAF from a set of discrete measurements, and is based on simplifying assumptions regarding the evaporative flux profiles produced by the rotatable shadow mask deposition tool. The details of the model can be found elsewhere [58]. The composition space showing all the 100 different alloy compositions that corresponds to each of the 100 channels in the multichannel microreactor array can be seen in Figure 4.5-b.

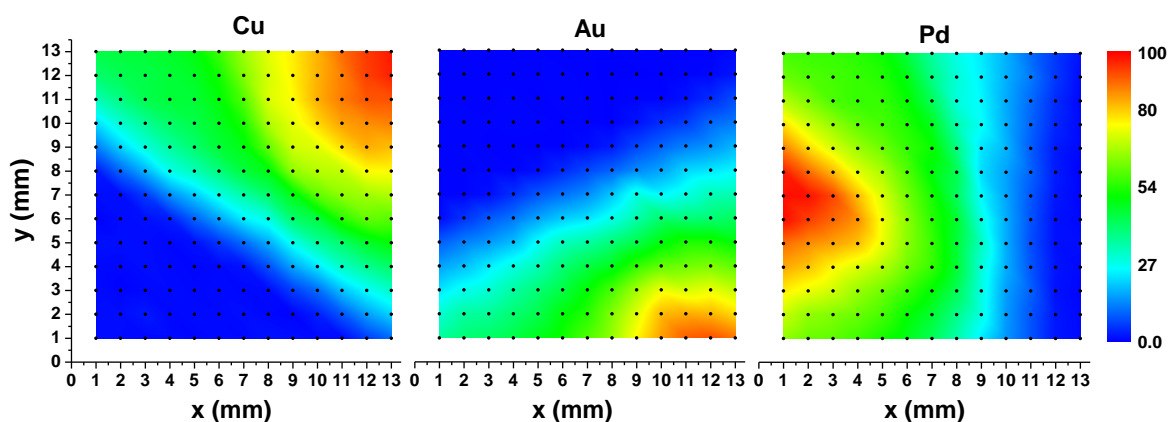


Figure 4.4. Concentration distribution (at. %) obtained with XPS for Cu, Au, and Pd across a $\text{Cu}_x\text{Au}_y\text{Pd}_{1-x-y}$ CSAF.

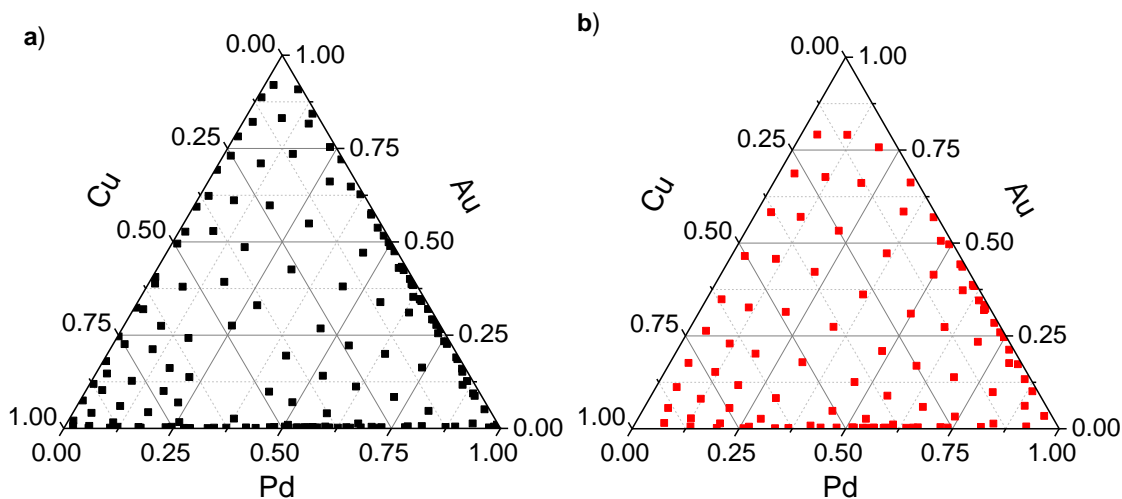


Figure 4.5. a) $\text{Cu}_x\text{Au}_y\text{Pd}_{1-x-y}$ alloy compositions across $14 \times 14 \text{ mm}^2$ substrate surface (a 13×13 grid with 1 mm spacing). **b)** $\text{Cu}_x\text{Au}_y\text{Pd}_{1-x-y}$ alloy compositions covered in ternary space. Each of the red dots represent a different alloy composition corresponding to the 100 different microreactor channels.

4.4.3 Characterization of CSAF electronic structure

XPS was used to map the valence band electronic structure of the $\text{Cu}_x\text{Au}_y\text{Pd}_{1-x-y}$ CSAF across a 13×13 grid with 1 mm spacing, as shown in Figure 4.3. Figure 4.6 illustrates the background subtracted ν -band spectra mapped at 169 discrete locations across the $\text{Cu}_x\text{Au}_y\text{Pd}_{1-x-y}$ CSAF. The spectra are plotted as functions of energy with respect to the Fermi level (ε_F), which is located at zero on the energy scale. Since we have a ternary alloy, it is not straightforward to interpret this data, however, it can be said that the density of states shifts towards the Fermi level as the Pd composition increases.

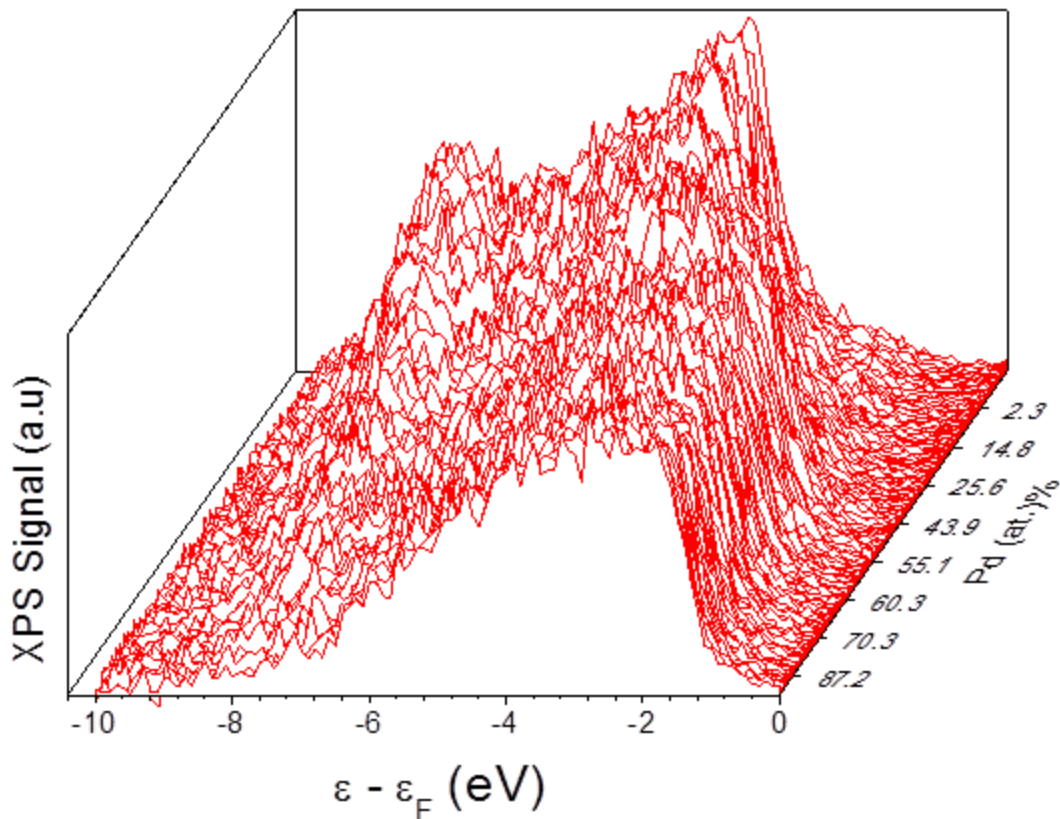


Figure 4.6. Background subtracted XP spectra of 169 different $\text{Cu}_x\text{Au}_y\text{Pd}_{1-x-y}$ compositions across the entire composition space.

Cu and Au have filled d -bands whereas Pd has almost full d -band (9 to 10 electrons). Interesting feature of Pd is that it has broader d -bands than Au or Cu. For Pd, the bottom of the valence s -band is situated below the binding energy of -5 eV and the top of the sp -band is above ε_F , leaving the energy range of 0–3 eV below ε_F for the d -bands [59]. We have obtained a very similar energy range for Pd (red line of Figure 4.7). Figure 4.7 shows the obtained XPS spectra for almost pure Cu, almost pure Au, and almost pure Pd. Using the spectrum for Pd in Figure 4.7, we can say that as the Pd concentration of the alloy increases, more states closer to the Fermi level are filled. In contrast, as the amount of Cu and Au in the alloy increases, the density of filled states shifts further away from Fermi level. When the spectrum of $\text{Cu}_{0.98}\text{Au}_0\text{Pd}_{0.02}$ (almost pure Cu, black

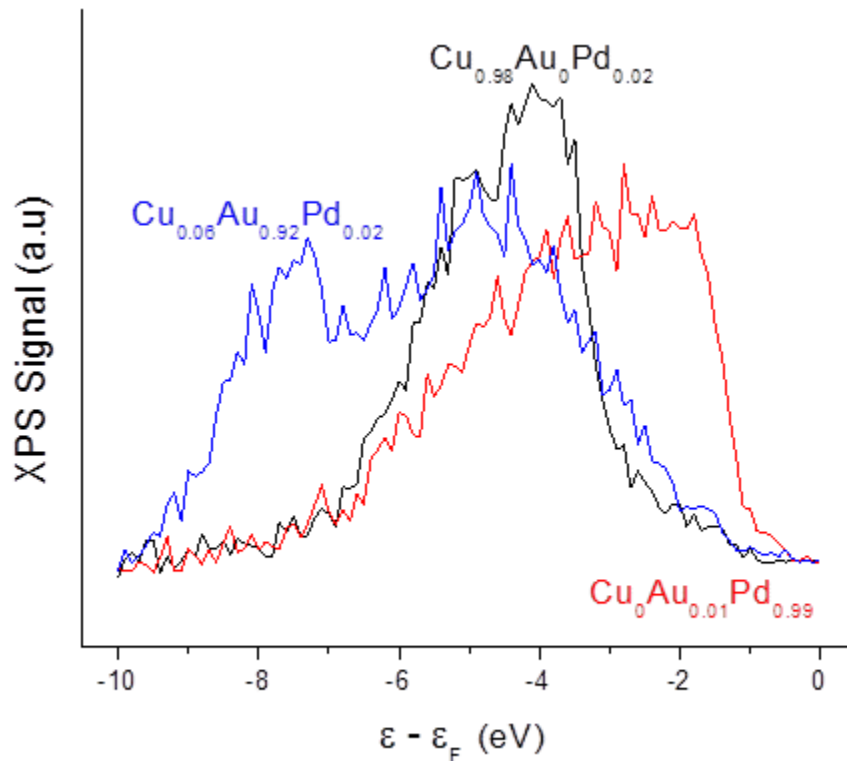


Figure 4.7. Background subtracted XPS spectra for the three extreme compositions across the $\text{Cu}_x\text{Au}_y\text{Pd}_{1-x-y}$ CSAF. These three compositions represent pure Cu, pure Au and pure Pd.

line of Figure 4.7) is compared with $\text{Cu}_{0.06}\text{Au}_{0.92}\text{Pd}_{0.02}$ (almost pure Au, blue line of Figure 4.7), it is obvious that Au has a distinct peak at around -8 eV. From the detailed analysis of the spectra given in Figure 4.6, we observed that as Au content increases in the alloy, the intensity of this peak also increases.

The XPS-derived average energy of the filled ν -band, $\varepsilon_\nu(x)$, was calculated (Equation 4.5) from the background subtracted ν -band spectra (Figure 4.6) obtained from the $\text{Cu}_x\text{Au}_y\text{Pd}_{1-x-y}$ CSAF [60].

$$\varepsilon_\nu = \frac{\int N(\varepsilon) \varepsilon d\varepsilon}{\int N(\varepsilon) d\varepsilon} \quad (4.5)$$

where ε is the energy of the filled state in the valence band relative to the Fermi level (ε_F) and $N(\varepsilon)$ is the density of filled states at that energy which is proportional to the intensity of ν -band spectrum. The XPS-derived average energy of the filled ν -band (ε_ν) was calculated over the binding energy range -10 to 0 eV. The change in ν -band energy with respect to $\text{Cu}_x\text{Au}_y\text{Pd}_{1-x-y}$ composition can be observed in Figure 4.8. The results on two different ternary diagrams were obtained across two different $\text{Cu}_x\text{Au}_y\text{Pd}_{1-x-y}$ CSAFs and show high degree of reproducibility. The average energy of the $\text{Cu}_x\text{Au}_y\text{Pd}_{1-x-y}$ ν -band shifts toward the Fermi level as the Pd content increases, i.e. as the color changes from green to red. This result is in good agreement with the observation from Figure 4.6. Estimates of d -band center values for pure metals (Cu, Au, or Pd) are available in the literature, most having been obtained from electronic structure calculations. The range of d -band energies reported for pure Cu is $\varepsilon_d = -3.6 - 2.0$ eV [61-66], roughly 1 eV higher than our measurement of $\varepsilon_\nu^{\text{Cu}} = -4.5$ eV (Figure 4.8). For Au, a wide range of d -band energies are reported, $\varepsilon_d = -4.45$ to -2.5 eV [39, 40, 42, 63, 66-71]. There is an offset between

these values and the one measured in our study, $\varepsilon_v^{Au} = -5.3$ eV. For Pd, values in the range $\varepsilon_d = -2.64$ to -2.02 eV [39, 62, 63, 69, 72-74] were reported, which is about 1 eV higher than our measurement of $\varepsilon_v^{Pd} = -3.4$ eV. There are significant differences between the literature values of d -band center and our measurements. This may be because of the use of different calculation approaches which causes variations in the density of states (DOS) [75]. For a given DOS, the choice of upper and lower integration limits can cause differences in the values of d -band center [39, 76]. Another reason for this offset may be an incomplete background subtraction of secondary electrons contributing to the XP spectra at high binding energies. We can say that the composition dependence of the XPS-derived v -band energy is a very good proxy for the d -band energy since the shift in the energy of the filled portion of the total DOS follows that of the d -band, as determined using electronic structure calculations.

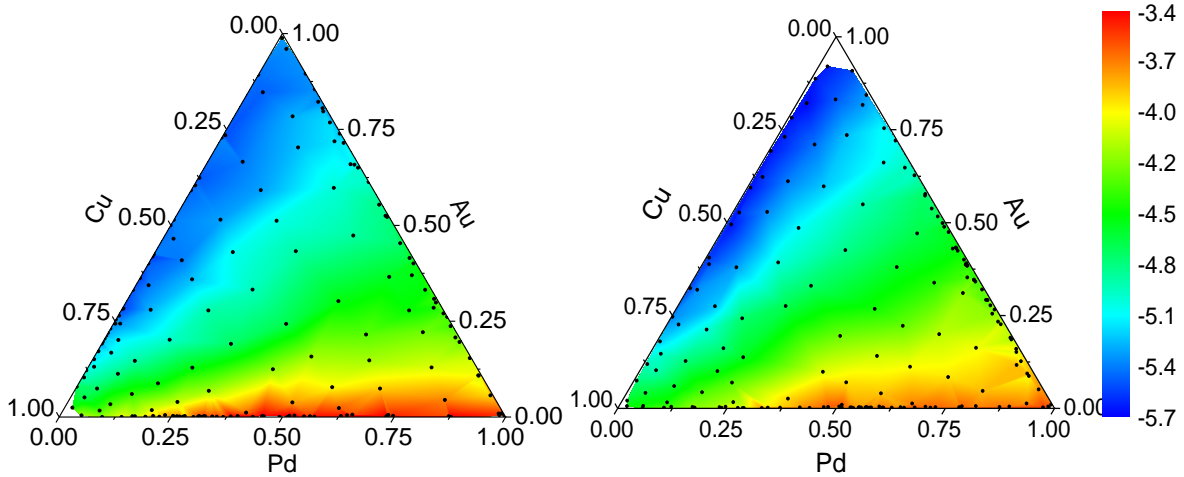


Figure 4.8. XPS-derived average energy of the filled v -band relative to the Fermi level of $\text{Cu}_x\text{Au}_y\text{Pd}_{1-x-y}$ CSAF versus Pd (at. %) compositions.

4.4.4 H₂-D₂ Exchange on the Cu_xAu_yPd_{1-x-y} CSAF

H₂-D₂ exchange over the Cu_xAu_yPd_{1-x-y} CSAF was carried out by feeding H₂, D₂, and Ar mixtures into the microreactor at constant temperature, partial pressures and flow rates, while monitoring the product gas composition by mass spectrometry. Mass spectrometer signals were converted to conversion, X , for 100 different Cu_xAu_yPd_{1-x-y} compositions, x and y , at 11 different temperatures, T , and 11 different flow conditions. Within these conditions, the Cu_xAu_yPd_{1-x-y} CSAF surface was found to give stable reactivity during successive experiments, as can be seen from the example in Figure 4.9. The measured conversions were plotted in Figure 4.9 as a function of T for four randomly selected alloy compositions for two successive experiments.

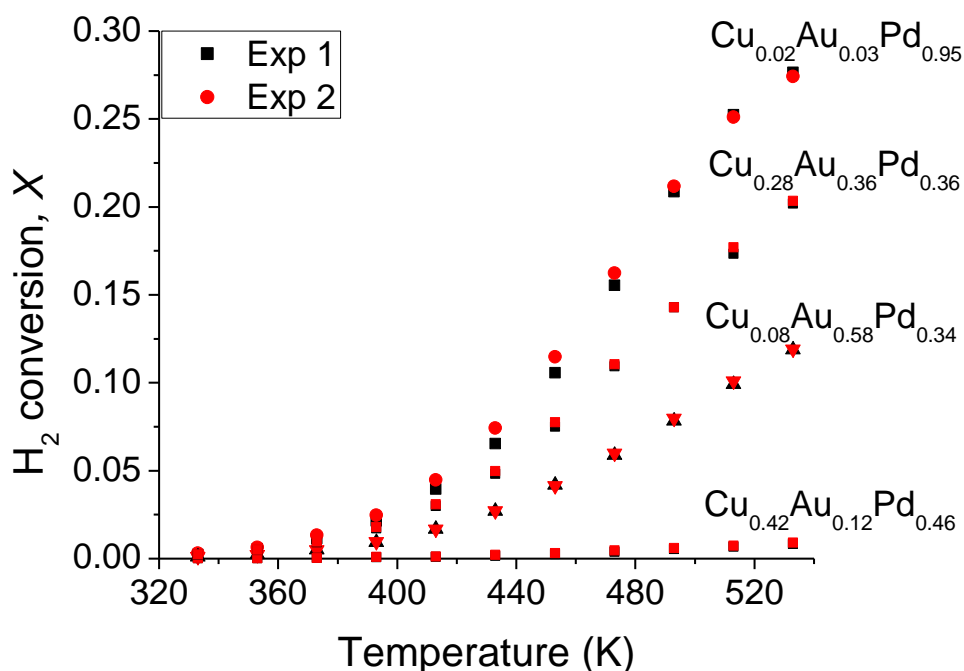


Figure 4.9. HD flow rate in the outlet measured at four different positions across the Cu_xAu_yPd_{1-x-y} CSAF versus temperature for two successive experiments. The inlet flow rate contains 0.05 mL/min H₂, 0.05 mL/min D₂ and 0.05 mL/min Ar per channel. The closeness of black and red data points shows that the surface is giving reproducible reactivity.

Collected X versus T for all the inlet conditions listed in Table 4.1 is then converted to the flow rate of produced HD using Equation 3.26. Calculated HD flow rates for all inlet flow conditions across all 100 different $\text{Cu}_x\text{Au}_y\text{Pd}_{1-x-y}$ compositions are given in Figure 4.10.

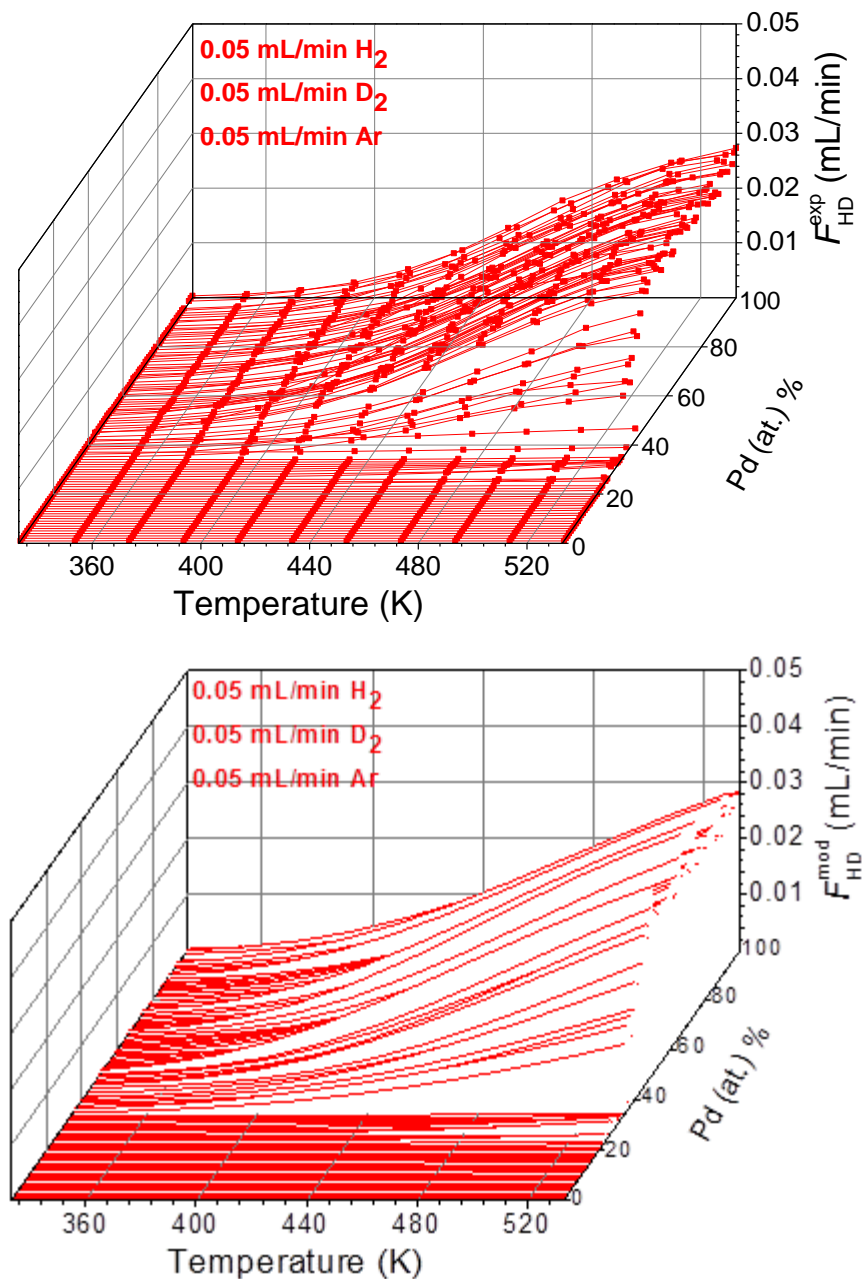


Figure 4.10. HD flow rate versus temperature measured across $\text{Cu}_x\text{Au}_y\text{Pd}_{1-x-y}$ composition space. For all 100 $\text{Cu}_x\text{Au}_y\text{Pd}_{1-x-y}$ compositions, conversion increases with increasing T and decreasing x and y . Flow conditions in one channel are labeled on each figure. ($P_{\text{tot}} = 1$ atm)

Across the CSAF, H₂-D₂ exchange activity increases with increasing T and decreasing Cu and Au content, x and y . At $T = 333$ K, the conversion was $X \approx 0$ at all alloy compositions. Experiments should be performed far below equilibrium conversion, since at equilibrium it is not possible to detect differences in catalytic activity across the CSAF. Therefore, the maximum temperature tested was $T = 533$ K. However, it is possible to test higher temperatures and lower flow rates if equilibrium conversion is desired. We made sure the H₂-D₂ exchange reaction progressed far enough so the product concentration would be easily measurable. Each data point in Figure 4.10 was collected under isothermal conditions; the CSAF was heated at 1 K/s and then held at constant temperature for ~4 min to reach steady state before sampling HD production across all 100 alloy compositions.

H₂ conversion as a function of alloy composition across the Cu _{x} Au _{y} Pd_{1- $x-y$} CSAF can better be represented using a ternary diagram. Waterfall plots given in Figure 4.10 show the collected data as a function of T at different Pd concentrations. Since we have a ternary alloy, this may not be useful in understanding the effect of Cu and Au addition to Pd on catalytic activity. One example of a ternary diagram showing how measured conversion changes with Cu, Au and Pd content for the inlet flow consisting of 0.05 mL/min H₂, 0.05 mL/min D₂, and 0.05 mL/min Ar (per channel) at 533 K is given in Figure 4.11. This diagram shows that as the color gradient changes from blue to green, which is also the direction of increasing Pd content, X increases. So, the highest conversions are achieved on the Pd-rich side of the CSAF. It should be noted that for the equimolar flow conditions at 533 K the equilibrium conversion is ~0.49.

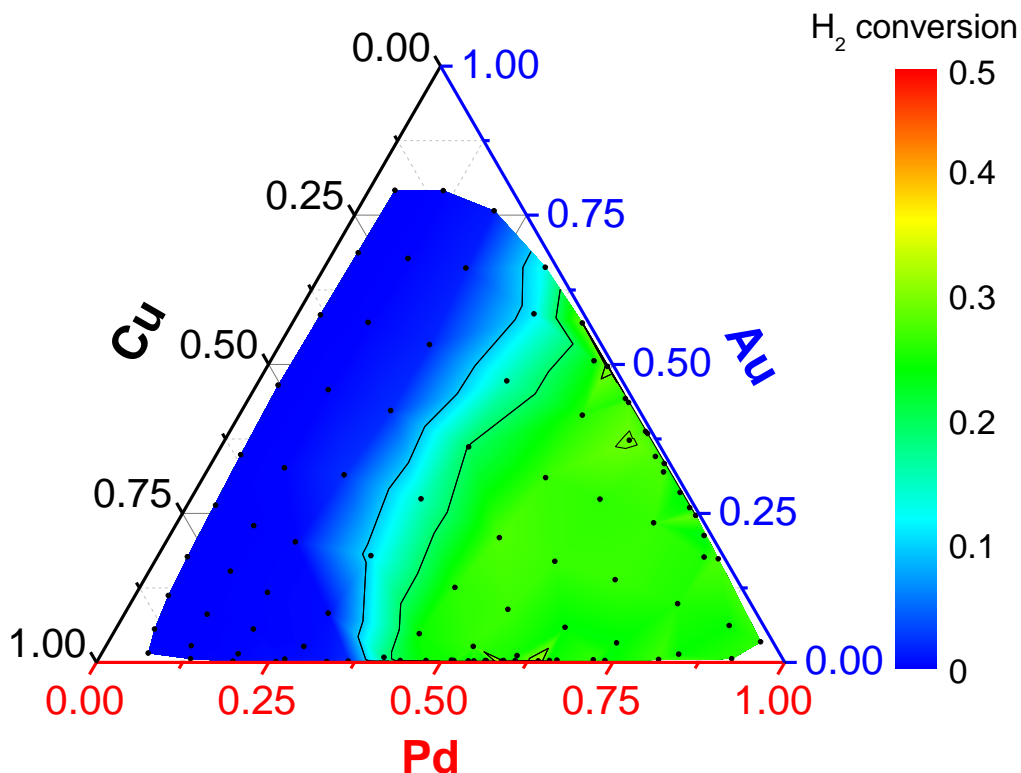


Figure 4.11. Ternary composition space showing how the catalytic activity of the H₂-D₂ exchange reaction changes with Cu, Au and Pd composition across the Cu_xAu_yPd_{1-x-y} CSAF. H₂ conversion was selected to be the indicator of activity and was measured at 533 K for the inlet flow 0.05 mL/min H₂ + 0.05 mL/min D₂ + 0.05 mL/min Ar.

The black edge of the triangle represents the Cu-Au binary alloy compositions on the CSAF, the blue edge represents Au-Pd binary compositions, and the red edge represents Cu-Pd binary compositions. In Figure 4.11, if one of the iso-activity lines is followed from the blue edge to red edge, i.e. from the Au-Pd binary region to the Cu-Pd binary region, one can see that Au-Pd binary alloys are slightly more active than Cu-Pd binary alloys because they give the same activity with less Pd content.

Figure 4.12 shows how H₂ conversion changes with temperature across the real physical space of the Cu_xAu_yPd_{1-x-y} CSAF. At $T = 333$ K, H₂ conversion is $X \approx 0$ across the entire CSAF. As T increases, the activity also increases, especially across the Pd-rich side of the CSAF. Further, when Figure 4.12 is compared with the CSAF's XPS composition map (Figure 4.4), there is higher activity for the Au-Pd binary region than for the Cu-Pd binary region. In Figure 4.12, the bottom edge represents the Cu-Pd binary region and the right edge represents the Au-Pd binary region. At 533 K, a wider green region is observed at the bottom edge, showing that side is more active than the right edge.

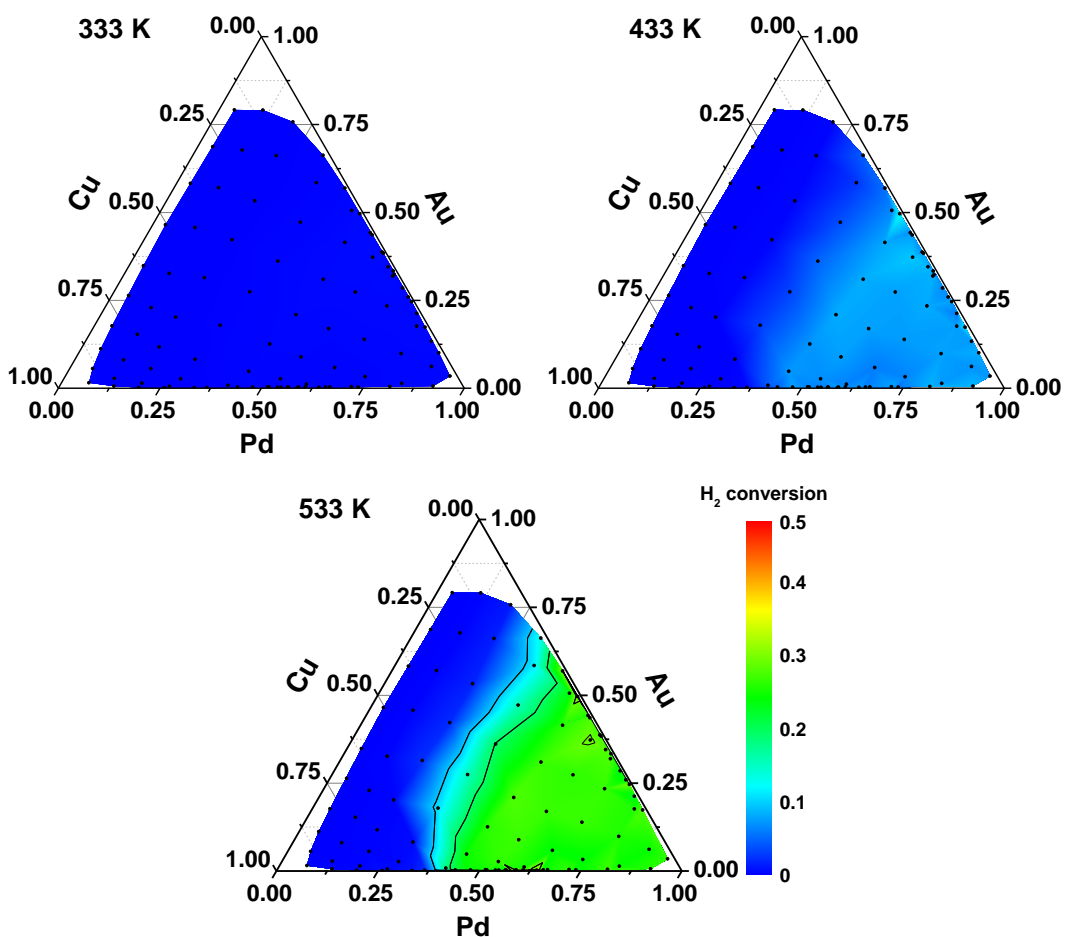


Figure 4.12. H₂-D₂ exchange conversion across Cu_xAu_yPd_{1-x-y} CSAF at $T = 333$ K, 433 K and 533 K. Inlet flow was 0.05 mL/min H₂, 0.05 mL/min D₂, and 0.05 mL/min Ar per channel.

The pressure dependence of HD production from H₂-D₂ exchange over Cu_xAu_yPd_{1-x-y} alloys has been investigated across the temperature range $T = 333 - 533$ K by varying P_{H_2} and P_{D_2} independently. The first 6 rows of Table 4.1 correspond to the inlet conditions where P_{D_2} was kept constant while changing P_{H_2} . Rows 6 to 9 of Table 4.1 correspond to the inlet conditions where P_{H_2} was kept constant while changing D . Rows 2, 10 and 11 belong to the set of experiments where the total pressure ($P_{D_2} + P_{H_2}$) changes for $P_{D_2}/P_{H_2} = 5$. For all experiments, activity was found to increase with T .

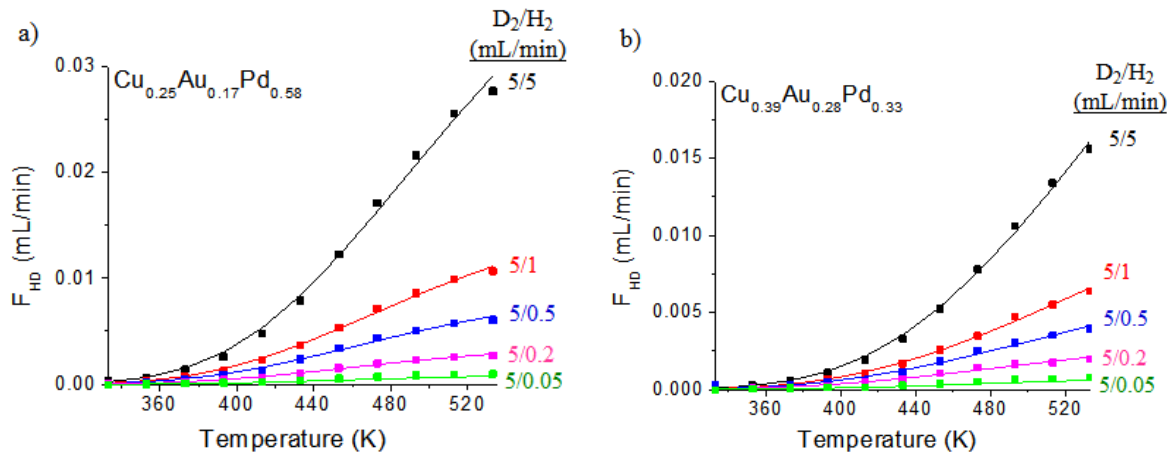


Figure 4.13. a), b) HD flow rate in the outlet measured for two Cu_xAu_yPd_{1-x-y} alloy compositions vs. T for five inlet flow conditions. Solid squares are the experimental measurement points and the solid lines are the fits of the data to the microkinetic model.

Figure 4.13 shows HD flow rates, F_{HD}^{out} obtained for two different Cu_xAu_yPd_{1-x-y} compositions and five different feed gas conditions, where F_{D_2} is kept constant at 5 mL/min (0.05 mL/min per channel). F_{D_2} is changed from 5 mL/min to 0.05 mL/min (0.05 mL/min to 0.0005 mL/min per channel). The total flow rate per channel is kept constant at 0.15 mL/min. The

experimental values of the HD flowrates for the five different feed conditions are shown as the discrete data points while the fits to the microkinetic model are represented as the solid lines. The quality of the fit can be assessed using these $F_{\text{HD}}^{\text{out}}$ versus T plots. A parity plot (Figure 4.14) comparison of the modeled HD flow rates (solid lines) and the experimental HD flow rates shows that the model fits the experimental data (12100 values of $F_{\text{HD}}^{\text{out}}$) well for all catalyst compositions across the entire temperature range of the experiment ($T = 333 - 593 \text{ K}$).

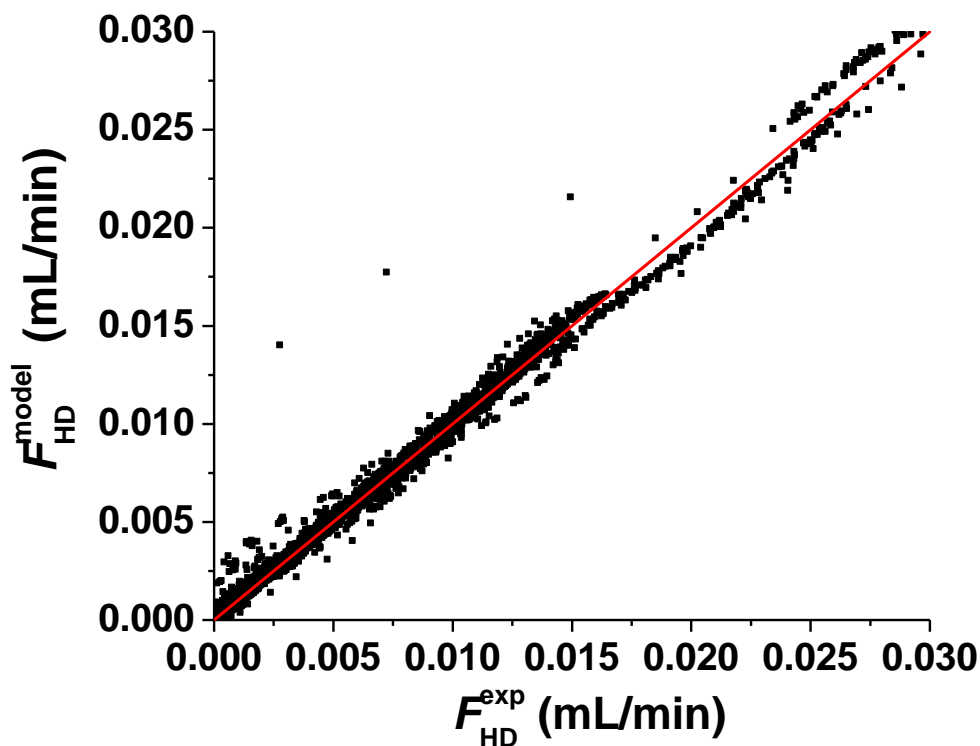


Figure 4.14. Parity plot of the HD flow rates predicted by the microkinetic model vs. experimental measurements. Data are shown for all 100 $\text{Cu}_x\text{Au}_y\text{Pd}_{1-x-y}$ compositions ($x = 0 - 1$, $y = 0 - (1 - x)$) at 11 different temperatures ($T = 333 - 533 \text{ K}$) and 11 inlet flow conditions (Table 4.1).

4.4.5 Kinetic Parameters for H₂-D₂ Exchange on the Cu_xAu_yPd_{1-x-y} CSAF

The comprehensive dataset obtained using high throughput methods and the microkinetic model have been used to estimate the kinetic parameters, v_{ads} , v_{des} , ΔE_{ads}^\ddagger and ΔE_{des}^\ddagger for each Cu_xAu_yPd_{1-x-y} alloy composition. Previous studies have shown that the pre-exponential factors are fairly independent of alloy composition [21, 46]. So in this study, model fitting was performed by fixing the pre-exponents to their transition state theory values of $v_{ads} = 10^{-4}$ mol/m²/s/Pa and $v_{des} = 10^6$ mol/m²/s [77] and only varying ΔE_{ads}^\ddagger and ΔE_{des}^\ddagger . Values for ΔE_{ads}^\ddagger are plotted in Figure 4.15-a and standard errors on estimated ΔE_{ads}^\ddagger are plotted in Figure 4.15-b. It was seen that the value of ΔE_{ads}^\ddagger decreases from ~0.6 eV to ~0.15 eV with increasing Pd content. When the Pd content is more than 50 at.%, similar ΔE_{ads}^\ddagger values were calculated for both Cu-Pd and Au-Pd binary regions, as well as for the Cu-Au-Pd ternary alloy compositions.

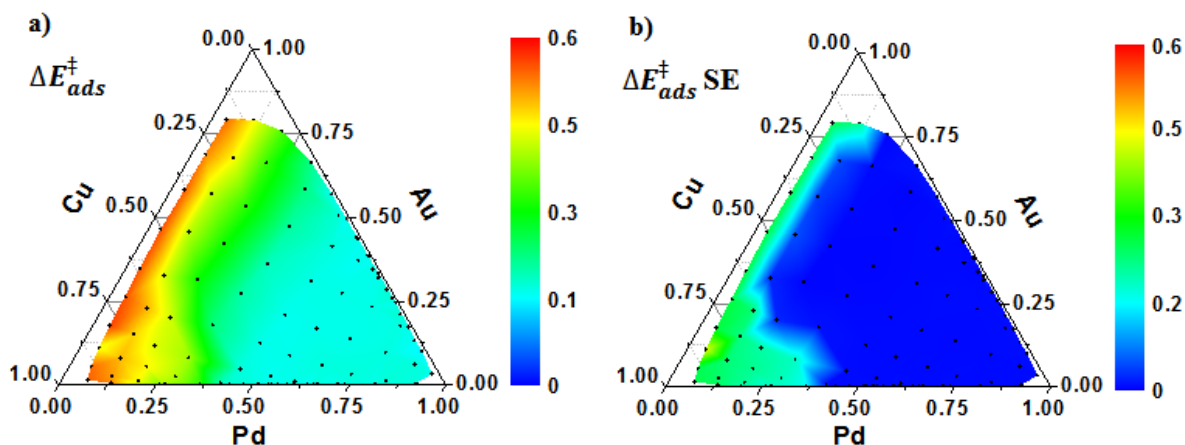


Figure 4.15. a) Barriers for H₂ adsorption as a function of Cu_xAu_yPd_{1-x-y} alloy composition and b) standard errors (SE) on estimated adsorption barriers.

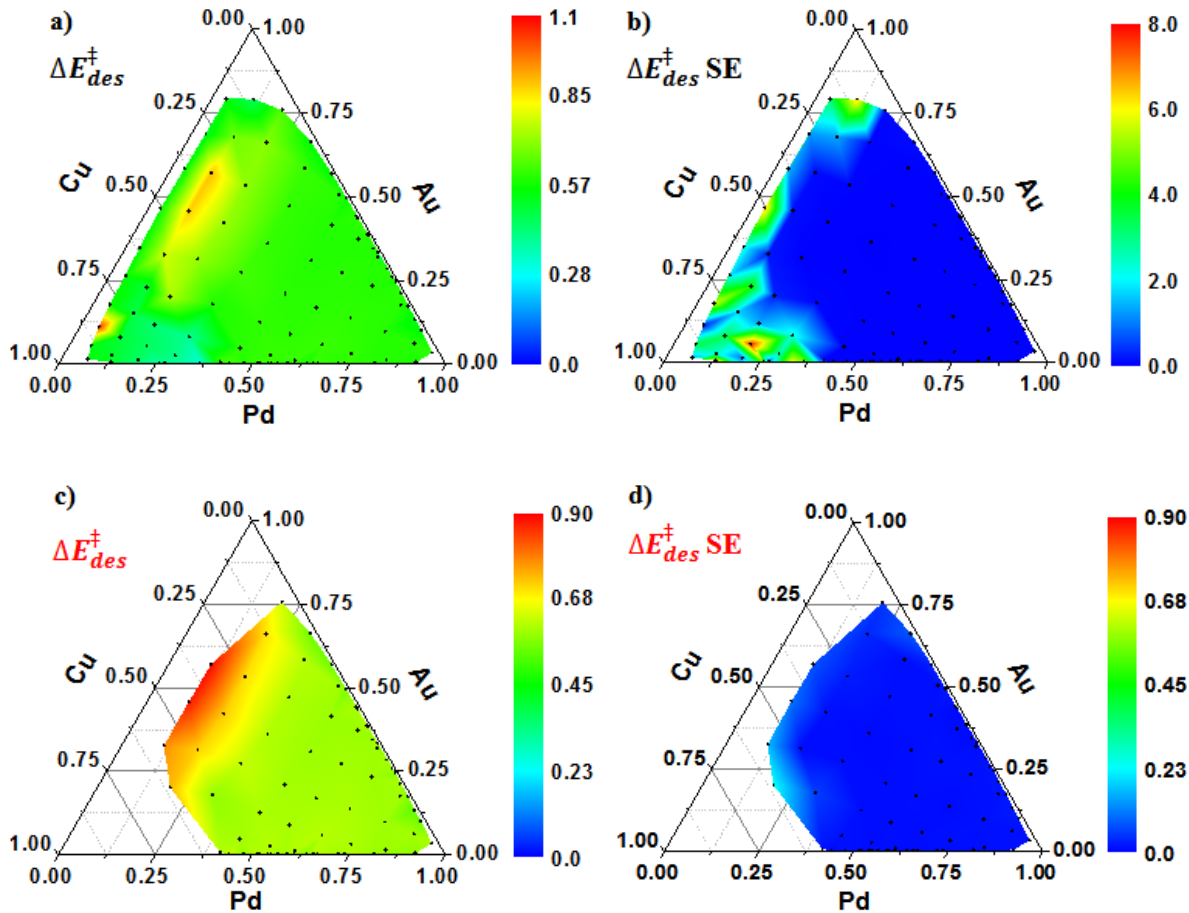


Figure 4.16. **a)** Barriers for H₂ desorption as a function of Cu_xAu_yPd_{1-x-y} alloy composition and **b)** standard errors (SE) on estimated desorption barriers for all 100 different points across the CSAF. **c)** $\Delta E_{des}^{\ddagger}$ as a function of Cu_xAu_yPd_{1-x-y} alloy composition and **d)** standard errors (SE) on estimated desorption barriers after discarding the points giving very high SEs.

Values for $\Delta E_{des}^{\ddagger}$ are plotted in Figure 4.16-a and standard errors on estimated $\Delta E_{des}^{\ddagger}$ are plotted in Figure 4.16-b for all 100 different alloy compositions across the Cu_xAu_yPd_{1-x-y} CSAF. However, the standard errors observed on $\Delta E_{des}^{\ddagger}$ showed a high degree of uncertainty when Pd content was less than ~20 at.%. So these points were not used for further discussion of $\Delta E_{des}^{\ddagger}$. Figure 4.16-c and Figure 4.16-d shows the calculated $\Delta E_{des}^{\ddagger}$ and their standard errors after the

erroneous points are discarded (the values across the white region in Figure 4.16c and d). It is observed that the value of ΔE_{des}^\ddagger decreases from ~ 0.9 eV to ~ 0.6 eV as Pd content increases. In the region where ΔE_{des}^\ddagger exhibits low SEs, ΔE_{des}^\ddagger is found to be greater than ΔE_{ads}^\ddagger , suggesting that the rate-limiting step for the H₂-D₂ exchange reaction is the recombinative desorption of HD. For the composition range Pd at.% < 20, the microkinetic modeling of H₂-D₂ exchange kinetics yielded high values of SE in ΔE_{des}^\ddagger that was greater than the magnitude of ΔE_{des}^\ddagger itself, $\sigma E_{des}^\ddagger > \Delta E_{des}^\ddagger$. This can be interpreted as an insensitivity of the H₂-D₂ exchange kinetics over Cu and Au to the value of ΔE_{des}^\ddagger due to dissociative adsorption being the rate-limiting step in this region. This observation suggests that in the region where Cu and Au dominates the composition of the alloy, the rate-limiting step changes from recombinative desorption of HD to dissociative adsorption of H₂/D₂. For Pd at.% > 50, both calculated values for ΔE_{ads}^\ddagger and ΔE_{des}^\ddagger are fairly independent of composition. For this region, ΔE_{ads}^\ddagger was calculated to be ~ 0.16 eV and ΔE_{des}^\ddagger was calculated to be ~ 0.6 eV. Very similar catalytic activities were also achieved for the H₂-D₂ exchange reaction for alloys containing 50 at.% Pd as for pure Pd. This observation is promising since it enables the preparation of reduced cost catalysts when comparing the \$0.01/g price of Cu [78] with Pd (\$32.43/g) [79] and Au (\$41.56/g) [80].

O'Brien et al. measured the values of v_{ads} , v_{des} , ΔE_{ads}^\ddagger and ΔE_{des}^\ddagger for the steady state catalytic H₂-D₂ exchange reaction over fixed beds of Cu, Cu_{0.53}Pd_{0.47}, Cu_{0.30}Pd_{0.70}, and Pd in a conventional flow reactor [21]. In that study, the adsorption barrier for Cu_{0.53}Pd_{0.47} was reported to be $\Delta E_{ads}^\ddagger = 0.15 \pm 0.02$ eV and the desorption barrier for Cu_{0.53}Pd_{0.47} was reported to be $\Delta E_{des}^\ddagger = 0.67 \pm 0.03$ eV. Gumuslu et al. measured the values of v_{ads} , v_{des} , ΔE_{ads}^\ddagger and ΔE_{des}^\ddagger for steady state catalytic H₂-D₂ exchange across a Cu_xPd_{1-x} CSAF. In that study, the adsorption barrier

for $\text{Cu}_{0.53}\text{Pd}_{0.47}$ was reported to be $\Delta E_{ads}^\ddagger \approx 0.11 \text{ eV}$ and the desorption barrier for $\text{Cu}_{0.3}\text{Pd}_{0.7}$ was reported to be $\Delta E_{des}^\ddagger \approx 0.6 \text{ eV}$. In our study, the adsorption barrier for $\text{Cu}_{0.28}\text{Au}_0\text{Pd}_{0.72}$ was reported to be $\Delta E_{ads}^\ddagger = 0.16 \text{ eV} \pm 0.01 \text{ eV}$ and the desorption barrier for $\text{Cu}_{0.28}\text{Au}_0\text{Pd}_{0.72}$ was reported to be $\Delta E_{des}^\ddagger = 0.6 \pm 0.01 \text{ eV}$. Both of these results display good agreement.

4.4.6 Reaction Rate Analysis of $\text{H}_2\text{-D}_2$ Exchange on $\text{Cu}_x\text{Au}_y\text{Pd}_{1-x-y}$ CSAF

Figure 4.17 displays the experimental HD production rate on five different $\text{Cu}_x\text{Au}_y\text{Pd}_{1-x-y}$ compositions at 433 K as a function of P_{H_2} , while P_{D_2} was held constant at 34 kPa. A positive dependence of the HD production rate was observed at all different temperatures tested, as well as on the growing P_{H_2} (from a small partial pressure), while P_{D_2} remained constant (at a relatively high pressure). The calculated slopes are very close to 1, which suggest that the reaction is first order with respect to P_{H_2} .

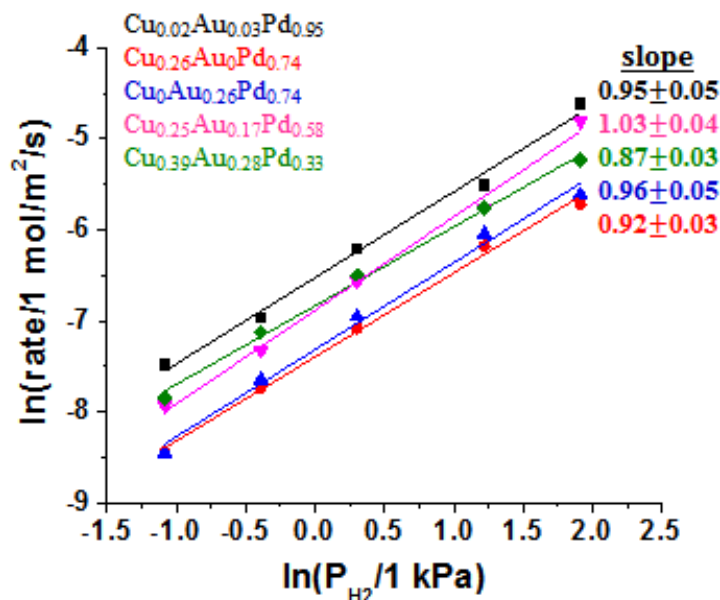


Figure 4.17. Plot of experimental HD production rate on five different $\text{Cu}_x\text{Au}_y\text{Pd}_{1-x-y}$ compositions (as listed on the figure) at 433 K as a function of P_{H_2} with P_{D_2} constant at 34 kPa.

Figure 4.18 displays the experimental HD production rate on five different $\text{Cu}_x\text{Au}_y\text{Pd}_{1-x-y}$ compositions at 433 K as a function of P_{D_2} , while P_{H_2} was held constant at 0.34 kPa. A zero slope was detected with increasing P_{H_2} (at a relatively high partial pressure), while P_{D_2} was held constant (at a small partial pressure).

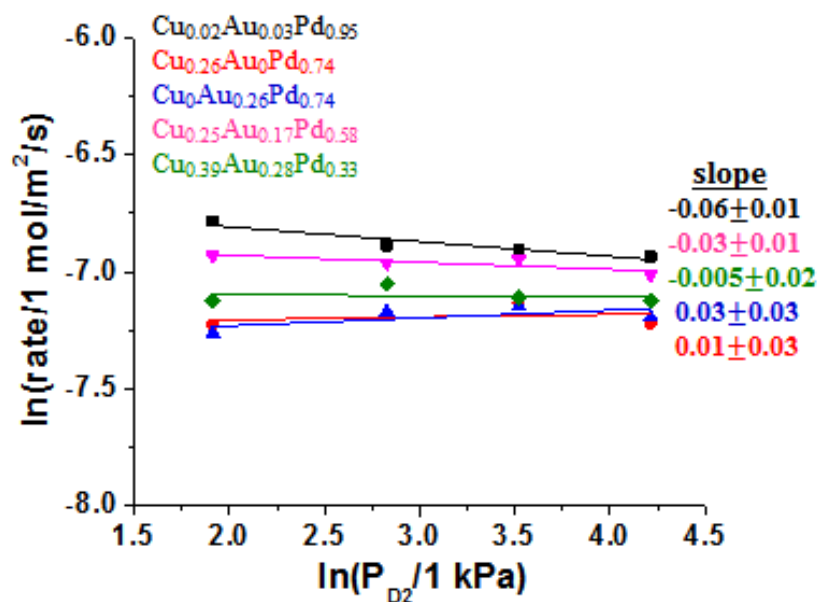


Figure 4.18. Plot of experimental HD production rate on five different $\text{Cu}_x\text{Au}_y\text{Pd}_{1-x-y}$ compositions (as listed on the figure) at 433 K as a function of P_{D_2} with P_{H_2} constant at 0.34 kPa.

The experimental formal reaction orders with the reaction orders predicted by the classical Langmuir-Hinshelwood model for the H_2/D_2 pressures are summarized in Table 4.2. The theoretical reaction orders are derived analytically using the microkinetic model described in the previous chapter (Section 3.4). For the inlet conditions, where P_{D_2} is constant and P_{H_2} is changing, the reaction orders obtained from experiment match the analytical solution of the Langmuir-Hinshelwood model. For the other case, where P_{H_2} is constant and P_{D_2} is changing, we observed zero order dependency of reaction order on P_{D_2} . When the surface coverage is close to 0,

$\theta_{H/D,surf} \approx 0$, the Langmuir-Hinshelwood model predicts the reaction order to be zero. So, it can be said that the classical Langmuir-Hinshelwood model predicts the HD production rate well when the coverage of the surface species is close to zero.

Table 4.2. Experimental and theoretical reaction orders for different inlet conditions.

Inlet conditions	Experiment	Langmuir-Hinshelwood
Constant P_{H_2} (Changing P_{D_2})	$+0.95 \pm 0.02$	$\sim \mathbf{1}$
Constant P_{D_2} (Changing P_{H_2})	-0.01 ± 0.01	$\sim -\mathbf{1 or 0}$

The total coverage of H and D atoms during H₂-D₂ exchange over 100 different Cu_xAu_yPd_{1-x-y} alloy compositions was calculated using Equation 3.14 and the kinetic parameters, ΔE_{ads}^\ddagger and ΔE_{des}^\ddagger , were extracted from the microkinetic model. Figure 4.20 shows the total coverage of H and D atoms on five different Cu_xAu_yPd_{1-x-y} alloy compositions, and Figure 4.20 shows the total coverage of H and D atoms on Cu_{0.02}Au_{0.03}Pd_{0.95} for four different inlet gas conditions over the temperature range $T = 333 - 533$ K. At low temperature (~ 350 K), the catalyst surface is nearly saturated with H and D atoms for different Cu_xAu_yPd_{1-x-y} alloy compositions. As temperature increases, the total coverage decreases for all feed conditions. Keeping P_{H_2} constant and reducing P_{D_2} (going from the red solid line to the pink solid line in Figure 4.21-b) reduces the rate of D₂ adsorption so that the total coverage of H and D atoms decreases. Since the coverage of H and D atoms are very low, it can be said that the Langmuir-Hinshelwood model does well at predicting the reaction order at high temperatures ($T > 360$ K). This is due to the fact that at high temperatures, only surface H and D species are present [81].

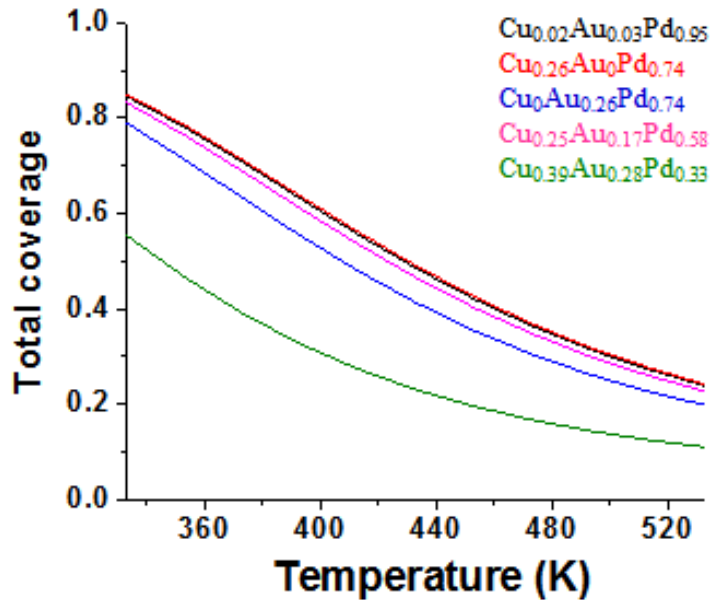


Figure 4.19. Total coverage of H and D atoms during H₂-D₂ exchange reaction over three different Ag_xPd_{1-x} alloy compositions ($x = 0.01, 0.2, 0.37$) as a function of T . The flow contains 9 mL/min H₂, 0.009 mL/min D₂ and 20.991 mL/min Ar.

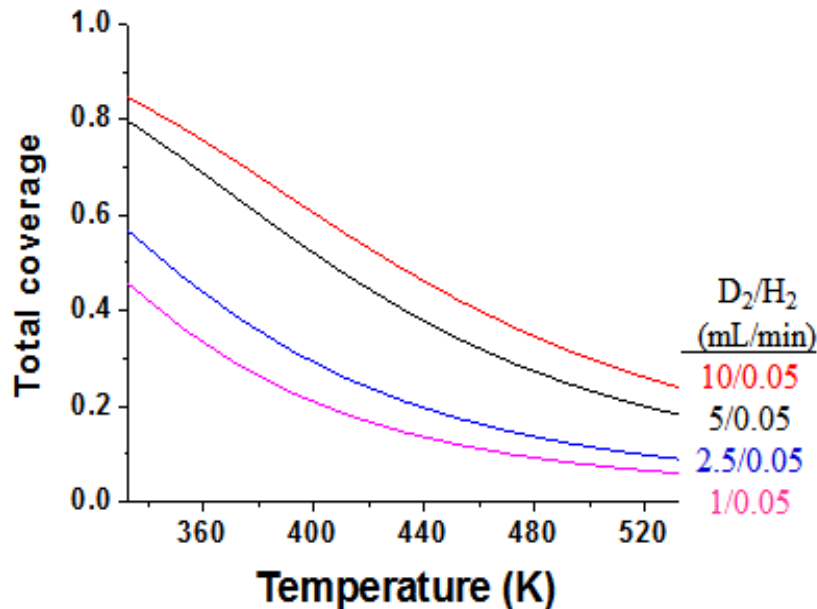


Figure 4.20. Total coverage of H and D atoms during H₂-D₂ exchange as a function of T for four different inlet flow compositions. The coverage is calculated using Equation (3.14) and the kinetic parameters, ν_{ads} , ν_{des} , $\Delta E_{ads}^{\ddagger}$ and $\Delta E_{des}^{\ddagger}$, are extracted from the microkinetic model.

4.4.7 Correlation of activity and structure across composition space

One of the goals of this study has been to correlate fundamental kinetic parameters for catalytic H₂-D₂ exchange over Cu_xAu_yPd_{1-x-y} alloys with characteristics of their electronic structure. Computationally, this can be achieved using DFT for various catalytic processes by correlating the calculated mean energy of the *d*-band, ε_d , of various metals with the calculated barriers, ΔE^\ddagger , to elementary reaction steps on their surfaces [1, 39, 73, 82]. In this work, we have used XP spectra from a Cu_xAu_yPd_{1-x-y} CSAF to measure the energy of the filled valence band center, $\varepsilon_v(x)$, and microkinetic modeling to calculate the ΔE_{ads}^\ddagger and ΔE_{des}^\ddagger for the H₂-D₂ exchange reaction. The correlation between these parameters are plotted in Figure 4.22 for different Cu_xAu_yPd_{1-x-y} alloy compositions. The correlation shows that as ε_v shifts toward the Fermi level, $\Delta E_{ads}^\ddagger(\varepsilon_v)$ and $\Delta E_{des}^\ddagger(\varepsilon_v)$ decrease slightly and then plateaus at $\Delta E_{ads}^\ddagger(\varepsilon_v) = \sim 0.16 \text{ eV}$ and $\Delta E_{des}^\ddagger(\varepsilon_v) = \sim 0.6 \text{ eV}$. As discussed in previous sections, these values correspond to the alloy compositions containing more than $\sim 40 \text{ at.}\%$ of Pd. To the best of our knowledge, this is the first experimental study that correlates fundamental kinetic parameters for the H₂-D₂ exchange reaction over Cu_xAu_yPd_{1-x-y} alloys with characteristics of their electronic structure.

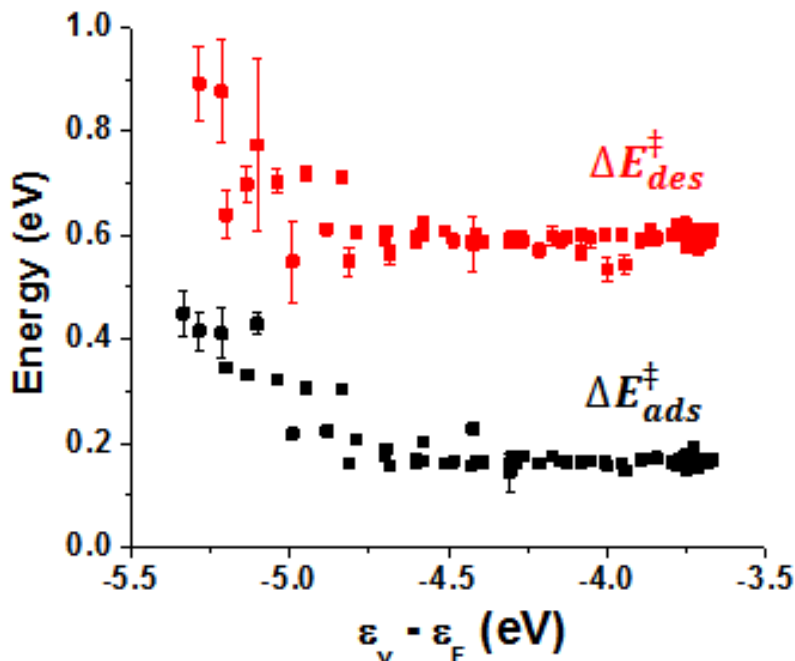


Figure 4.21. Energy barriers for dissociative adsorption of H₂, $\Delta E_{ads}^{\ddagger}(x, y)$, (black) and associative desorption of H₂, $\Delta E_{des}^{\ddagger}(x, y)$, (red) as a function of ν -band center energy measured across the Cu_xAu_yPd_{1-x-y} CSAF.

4.5 Conclusions

In this study, catalytic the H₂-D₂ exchange reaction was investigated across Cu_xAu_yPd_{1-x-y} composition space by using a high throughput methodology. A materials library spanning Cu_xAu_yPd_{1-x-y} composition space from $x = 0 - 1$ and $y = 0 - (1 - x)$ was prepared using the rotatable shadow mask deposition tool, as explained in Section 2.2.1.2. The characterization of composition and electronic structure across the CSAF was performed using XPS. Also, catalytic reactivity at 100 discrete positions (100 different alloy compositions) across the CSAF was measured using the multichannel microreactor array, as described in Section 2.2.2. Coupling spatially resolved characterization techniques and the high throughput reaction system, composition – catalytic activity – electronic structure correlation for Cu-Au-Pd ternary alloys has been investigated across

a continuous composition space. We found that the activity increased with increasing Pd at.%. Microkinetic analysis of the reaction showed that the H₂-D₂ exchange reaction was limited by the rate of desorption across the CSAF, except where Pd content is less than ~15 at.%. Obtained ν -band spectra showed that ν -band center moved closer to the Fermi level with increasing Pd content in the alloy. When correlating kinetic parameters and electronic structure, i.e. ΔE_{ads}^\ddagger and ΔE_{des}^\ddagger vs ϵ_ν , it was observed that both adsorption and desorption barriers decrease as ν -band center changes from -5.5 eV to -4.5 eV. At the Fermi level, both ΔE_{ads}^\ddagger and ΔE_{des}^\ddagger were found to be independent of the ν -band center of the alloy.

With these results, we were able to show that our high throughput methodology can be successfully applied to ternary, as well as binary alloys. Using this methodology, we were able to correlate the fundamental kinetic parameters for the H₂-D₂ exchange reaction with the electronic structure of the ternary alloy catalyst across a wide composition range.

4.6 Appendix: HD Flow Rate vs. Temperature across $\text{Cu}_x\text{Au}_y\text{Pd}_{1-x-y}$ Composition Space

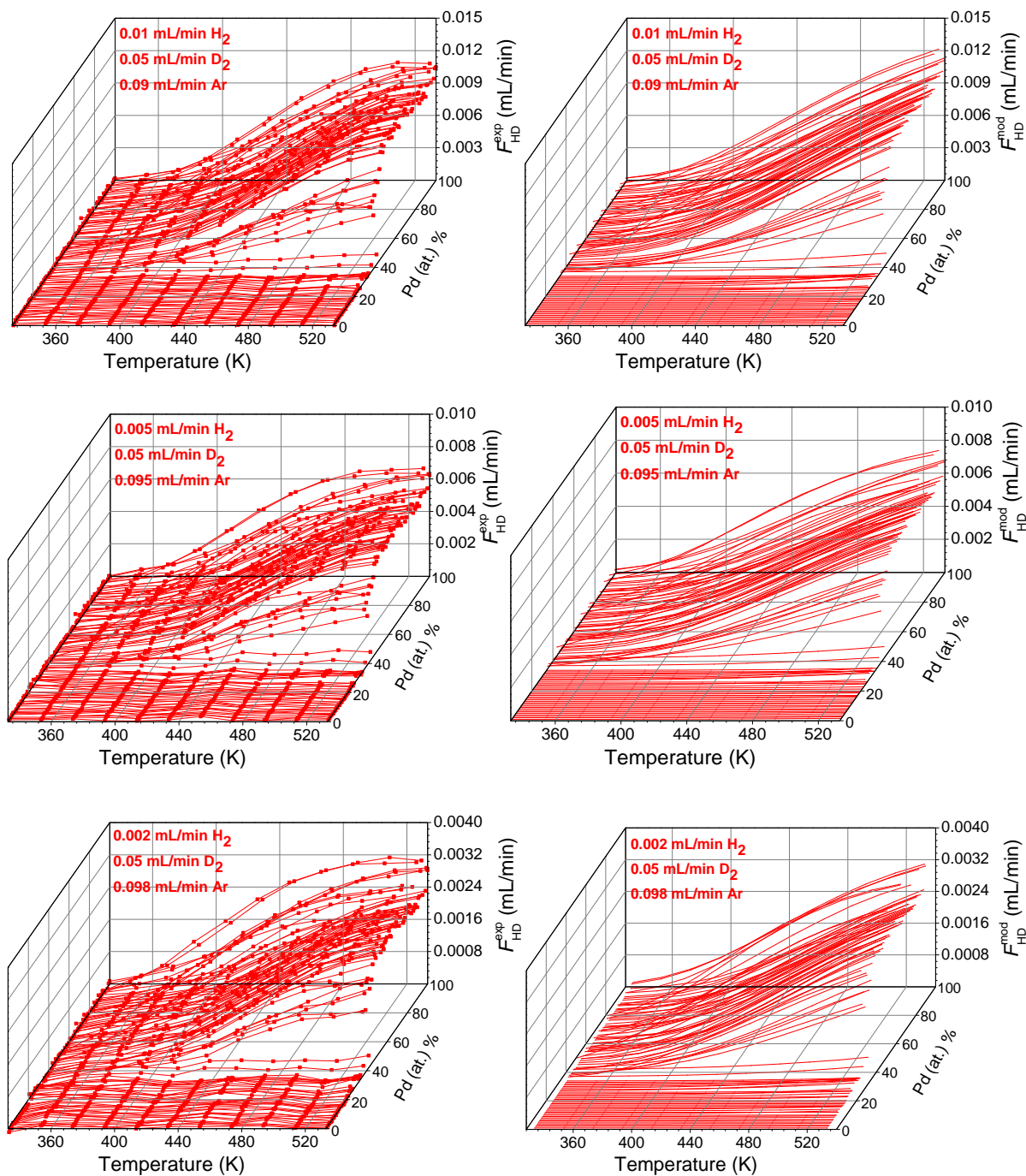


Figure 4.22. HD flow rate versus temperature measured across $\text{Cu}_x\text{Au}_y\text{Pd}_{1-x-y}$ composition space. For all 100 $\text{Cu}_x\text{Au}_y\text{Pd}_{1-x-y}$ compositions conversion increases with increasing T and decreasing x and y . Flow conditions in one channel are labeled on each figure. ($P_{\text{tot}} = 1$ atm)

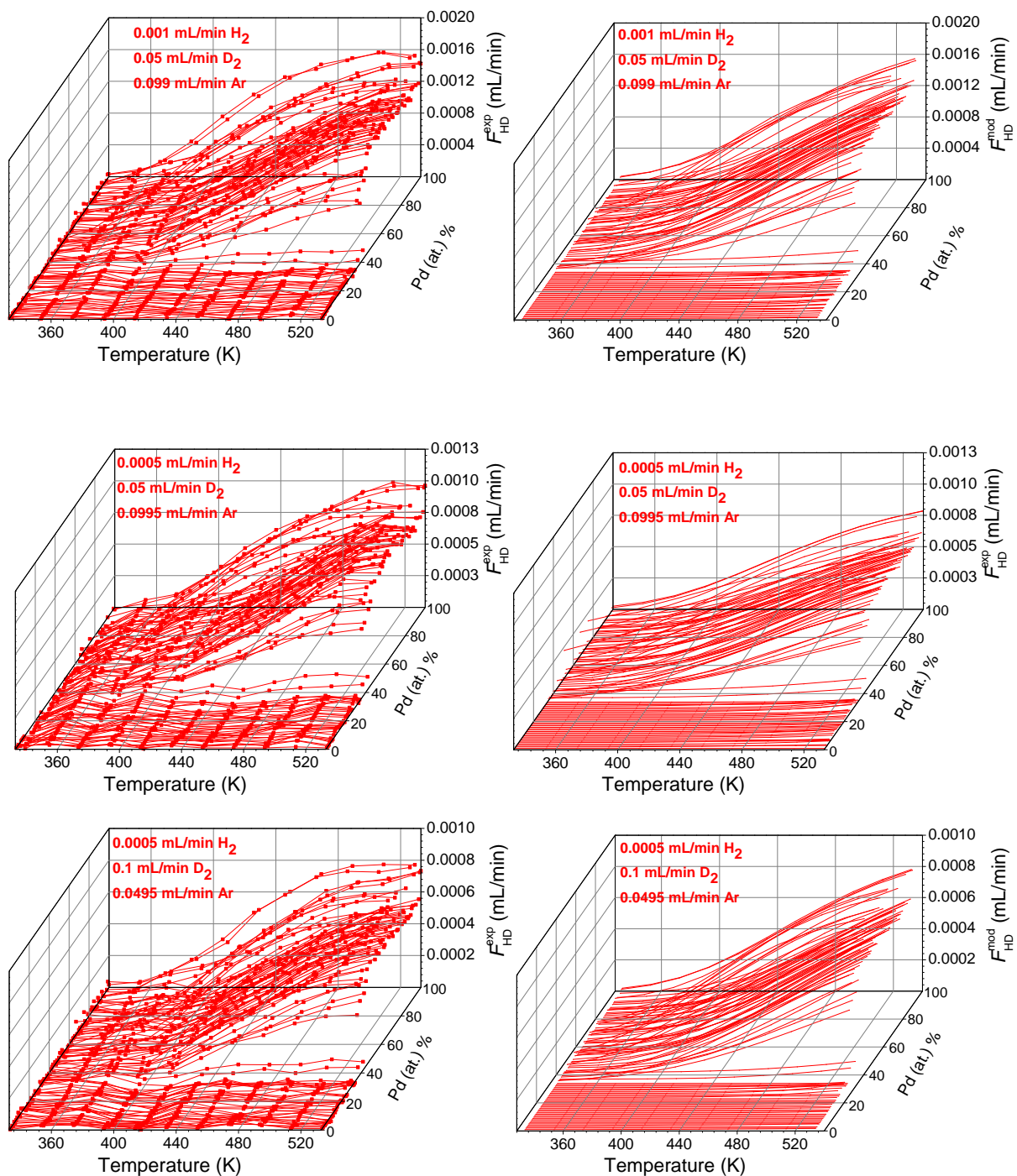


Figure 4.22. cont'd HD flow rate versus temperature measured across $\text{Cu}_x\text{Au}_y\text{Pd}_{1-x-y}$ composition space. For all 100 $\text{Cu}_x\text{Au}_y\text{Pd}_{1-x-y}$ compositions conversion increases with increasing T and decreasing x and y . Flow conditions in one channel are labeled on each figure. ($P_{\text{tot}} = 1 \text{ atm}$)

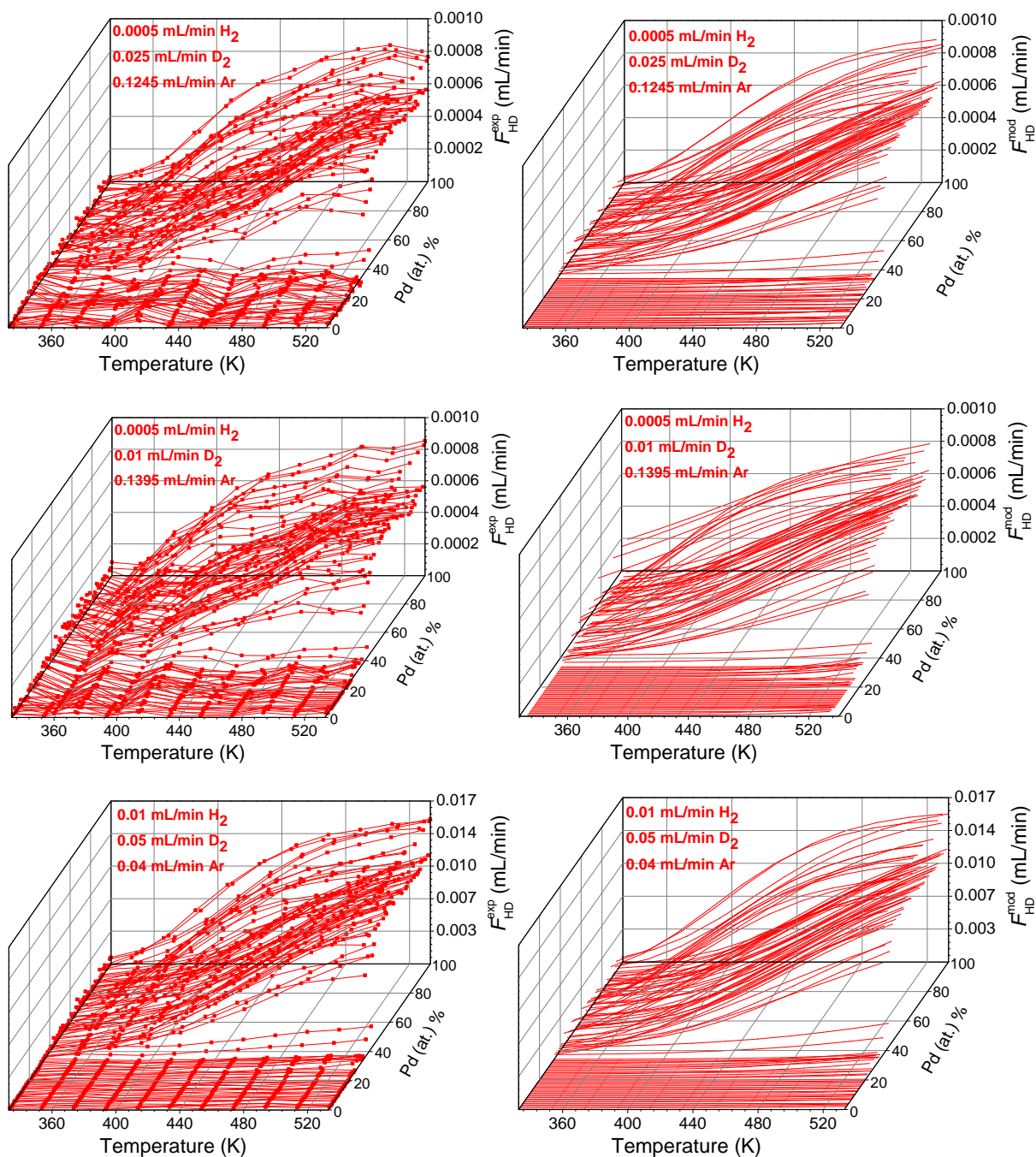


Figure 4.22. cont'd HD flow rate versus temperature measured across $\text{Cu}_x\text{Au}_y\text{Pd}_{1-x-y}$ composition space. For all 100 $\text{Cu}_x\text{Au}_y\text{Pd}_{1-x-y}$ compositions conversion increases with increasing T and decreasing x and y . Flow conditions in one channel are labeled on each figure. ($P_{\text{tot}} = 1 \text{ atm}$)

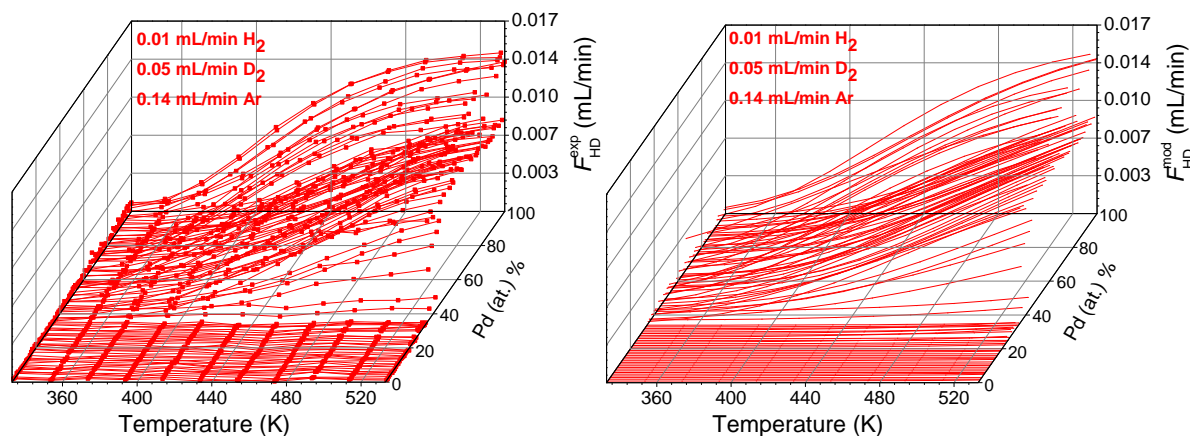


Figure 4.22. cont'd HD flow rate versus temperature measured across $\text{Cu}_x\text{Au}_y\text{Pd}_{1-x-y}$ composition space. For all 100 $\text{Cu}_x\text{Au}_y\text{Pd}_{1-x-y}$ compositions conversion increases with increasing T and decreasing x and y . Flow conditions in one channel are labeled on each figure. ($P_{\text{tot}} = 1 \text{ atm}$)

4.7 References

1. Hammer, B. and J.K. Norskov, *Why gold is the noblest of all the metals*. *Nature*, 1995. **376**(6537): p. 238-240.
2. Aasberg-Petersen, K., C.S. Nielsen, and S.L. Jørgensen, *Membrane reforming for hydrogen*. *Catalysis Today*, 1998. **46**(2): p. 193-201.
3. deRosset, A.J., *Diffusion of Hydrogen through Palladium Membranes*. *Industrial & Engineering Chemistry*, 1960. **52**(6): p. 525-528.
4. Paglieri, S.N. and J.D. Way, *INNOVATIONS IN PALLADIUM MEMBRANE RESEARCH*. *Separation and Purification Methods*, 2002. **31**(1): p. 1-169.
5. Lewis, F.A., *The palladium-hydrogen system: Structures near phase transition and critical points*. *International Journal of Hydrogen Energy*, 1995. **20**(7): p. 587-592.
6. Jayaraman, V. and Y.S. Lin, *Synthesis and hydrogen permeation properties of ultrathin palladium-silver alloy membranes*. *Journal of Membrane Science*, 1995. **104**(3): p. 251-262.
7. Shu, J., et al., *Catalytic palladium-based membrane reactors: A review*. *The Canadian Journal of Chemical Engineering*, 1991. **69**(5): p. 1036-1060.
8. Collins, J.P., et al., *Catalytic Dehydrogenation of Propane in Hydrogen Permselective Membrane Reactors*. *Industrial & Engineering Chemistry Research*, 1996. **35**(12): p. 4398-4405.

9. Roa, F., et al., *Preparation and characterization of Pd–Cu composite membranes for hydrogen separation*. Chemical Engineering Journal, 2003. **93**(1): p. 11-22.
10. Kamakoti, P., et al., *Prediction of Hydrogen Flux through Sulfur-Tolerant Binary Alloy Membranes*. Science, 2005. **307**(5709): p. 569-573.
11. Kulprathipanja, A., et al., *Pd and Pd–Cu membranes: inhibition of H₂ permeation by H₂S*. Journal of Membrane Science, 2005. **254**(1): p. 49-62.
12. Morreale, B.D., et al., *Effect of hydrogen-sulfide on the hydrogen permeance of palladium–copper alloys at elevated temperatures*. Journal of Membrane Science, 2004. **241**(2): p. 219-224.
13. Nam, S.-E. and K.-H. Lee, *Hydrogen separation by Pd alloy composite membranes: introduction of diffusion barrier*. Journal of Membrane Science, 2001. **192**(1): p. 177-185.
14. Piper, J., *Diffusion of Hydrogen in Copper-Palladium Alloys*. Journal of Applied Physics, 1966. **37**(2): p. 715-721.
15. Uemiya, S., T. Matsuda, and E. Kikuchi, *Hydrogen permeable palladium-silver alloy membrane supported on porous ceramics*. Journal of Membrane Science, 1991. **56**(3): p. 315-325.
16. Amandusson, H., L.-G. Ekedahl, and H. Dannetun, *Hydrogen permeation through surface modified Pd and PdAg membranes*. Journal of Membrane Science, 2001. **193**(1): p. 35-47.
17. L, M.D., *Method for hydrogen separation and purification*. 1969, Google Patents.
18. Yun, S. and S. Ted Oyama, *Correlations in palladium membranes for hydrogen separation: A review*. Journal of Membrane Science, 2011. **375**(1): p. 28-45.
19. Yang, J.Y., M. Komaki, and C. Nishimura, *Effect of overlayer thickness on hydrogen permeation of Pd₆₀Cu₄₀/V–15Ni composite membranes*. International Journal of Hydrogen Energy, 2007. **32**(12): p. 1820-1824.
20. Gao, H., et al., *Electroless plating synthesis, characterization and permeation properties of Pd–Cu membranes supported on ZrO₂ modified porous stainless steel*. Journal of Membrane Science, 2005. **265**(1): p. 142-152.
21. O'Brien, C.P., et al., *The Kinetics of H₂–D₂ Exchange over Pd, Cu, and PdCu Surfaces*. The Journal of Physical Chemistry C, 2011. **115**(49): p. 24221-24230.
22. O'Brien, C.P., et al., *H₂-D₂ Exchange Kinetics in the Presence of H₂S over Pd₄S, Pd₇₀Cu₃₀, and Pd₄₇Cu₅₃ Surfaces*. The Journal of Physical Chemistry C, 2012. **116**(33): p. 17657-17667.
23. Bartczak, W.M. and J. Stawowska, *Interaction of Dihydrogen with Transition Metal (Pd, Ni, Ag, Cu) Clusters*. Structural Chemistry, 2004. **15**(5): p. 447-459.
24. Cattania, M.G., et al., *Interaction of hydrogen with a palladium (110) surface*. Surface Science, 1983. **126**(1): p. 382-391.
25. Dong, W., G. Kresse, and J. Hafner, *Dissociative adsorption of H₂ on the Pd(111) surface*. Journal of Molecular Catalysis A: Chemical, 1997. **119**(1): p. 69-76.

26. Lozano, A., A. Groß, and H.F. Busnengo, *Molecular dynamics study of H_2 dissociation on H-covered Pd(100)*. Physical Review B, 2010. **81**(12): p. 121402.
27. Muschiol, U., P.K. Schmidt, and K. Christmann, *Adsorption and absorption of hydrogen on a palladium (210) surface: a combined LEED, TDS, $\Delta\Phi$ and HREELS study*. Surface Science, 1998. **395**(2): p. 182-204.
28. Iwao, Y., M. Naohiro, and K. Makoto, *Mechanism of Hydrogen Adsorption and Hydrogen-Deuterium Equilibration on Copper Surface*. Japanese Journal of Applied Physics, 1974. **13**(S2): p. 485.
29. Alexander, C.S. and J. Pritchard, *Chemisorption of hydrogen on evaporated copper films*. Journal of the Chemical Society, Faraday Transactions 1: Physical Chemistry in Condensed Phases, 1972. **68**(0): p. 202-215.
30. Mudiyansele, K., et al., *Adsorption of hydrogen on the surface and sub-surface of Cu(111)*. The Journal of Chemical Physics, 2013. **139**(4): p. 044712.
31. Sakong, S. and A. Groß, *Dissociative adsorption of hydrogen on strained Cu surfaces*. Surface Science, 2003. **525**(1): p. 107-118.
32. Wang, Z.S., G.R. Darling, and S. Holloway, *The surface temperature dependence of the inelastic scattering and dissociation of hydrogen molecules from metal surfaces*. The Journal of Chemical Physics, 2004. **120**(6): p. 2923-2933.
33. Abbott, H.L. and I. Harrison, *Microcanonical Transition State Theory for Activated Gas-Surface Reaction Dynamics: Application to $\text{H}_2/\text{Cu}(111)$ with Rotation as a Spectator*. The Journal of Physical Chemistry A, 2007. **111**(39): p. 9871-9883.
34. Hammer, B. and J.K. Nørskov, *Why gold is the noblest of all the metals*. Nature, 1995. **376**: p. 238.
35. Haruta, M. and M. Daté, *Advances in the catalysis of Au nanoparticles*. Applied Catalysis A: General, 2001. **222**(1): p. 427-437.
36. Vinod, C.P., J.W. Niemantsverdriet, and B.E. Nieuwenhuys, *Interaction of small molecules with Au(310): Decomposition of NO*. Applied Catalysis A: General, 2005. **291**(1): p. 93-97.
37. Okamoto, Y., *Density-functional calculations of atomic and molecular adsorptions on 55-atom metal clusters: Comparison with (111) surfaces*. Chemical Physics Letters, 2005. **405**(1): p. 79-83.
38. Sault, A.G., R.J. Madix, and C.T. Campbell, *Adsorption of oxygen and hydrogen on Au(110)-(1 × 2)*. Surface Science, 1986. **169**(2): p. 347-356.
39. Hammer, B. and J.K. Nørskov, *Theoretical surface science and catalysis—calculations and concepts*, in *Advances in catalysis*. 2000, Academic Press. p. 71-129.
40. Ruban, A., et al., *Surface electronic structure and reactivity of transition and noble metals* | Communication presented at the First Francqui Colloquium, Brussels, 19–20 February 1996.1. Journal of Molecular Catalysis A: Chemical, 1997. **115**(3): p. 421-429.

41. Nilsson, A., et al., *The electronic structure effect in heterogeneous catalysis*. Catalysis Letters, 2005. **100**(3): p. 111-114.
42. Nørskov, J.K., et al., *Density functional theory in surface chemistry and catalysis*. Proceedings of the National Academy of Sciences, 2011. **108**(3): p. 937-943.
43. Meyer, R., et al., *Surface chemistry of catalysis by gold*. Gold Bulletin, 2004. **37**(1): p. 72-124.
44. Tierney, H.L., A.E. Baber, and E.C.H. Sykes, *Atomic-Scale Imaging and Electronic Structure Determination of Catalytic Sites on Pd/Cu Near Surface Alloys*. The Journal of Physical Chemistry C, 2009. **113**(17): p. 7246-7250.
45. Ramos, M., A.E. Martinez, and H.F. Busnengo, *H₂ dissociation on individual Pd atoms deposited on Cu(111)*. Physical Chemistry Chemical Physics, 2012. **14**(1): p. 303-310.
46. Gumuslu, G., et al., *Correlation of Electronic Structure with Catalytic Activity: H₂-D₂ Exchange across CuxPd1-x Composition Space*. ACS Catalysis, 2015. **5**(5): p. 3137-3147.
47. Mei, D., E.W. Hansen, and M. Neurock, *Ethylene Hydrogenation over Bimetallic Pd/Au(111) Surfaces: Application of Quantum Chemical Results and Dynamic Monte Carlo Simulation*. The Journal of Physical Chemistry B, 2003. **107**(3): p. 798-810.
48. Greeley, J., et al., *Hydrogen Evolution Over Bimetallic Systems: Understanding the Trends*. Chemphyschem, 2006. **7**(5): p. 1032-1035.
49. Piccolo, L., A. Piednoir, and J.-C. Bertolini, *Absorption and oxidation of hydrogen at Pd and Pd-Au (111) surfaces*. Surface Science, 2006. **600**(18): p. 4211-4215.
50. Schmidt, T.J., et al., *Electrooxidation of H₂, CO and H₂/CO on well-characterized Au(111)-Pd surface alloys*. Electrochimica Acta, 2003. **48**(25): p. 3823-3828.
51. Venkatachalam, S. and T. Jacob, *Hydrogen adsorption on Pd-containing Au(111) bimetallic surfaces*. Physical Chemistry Chemical Physics, 2009. **11**(17): p. 3263-3270.
52. Fleutot, B., J.B. Miller, and A.J. Gellman, *Apparatus for deposition of composition spread alloy films: The rotatable shadow mask*. Journal of Vacuum Science & Technology A: Vacuum, Surfaces, and Films, 2012. **30**(6): p. 061511.
53. Wei, T., J. Wang, and D.W. Goodman, *Characterization and Chemical Properties of Pd-Au Alloy Surfaces†*. The Journal of Physical Chemistry C, 2007. **111**(25): p. 8781-8788.
54. Priyadarshini, D., et al., *High-Throughput Characterization of Surface Segregation in CuxPd1-x Alloys*. The Journal of Physical Chemistry C, 2011. **115**(20): p. 10155-10163.
55. He, J.W., et al., *Surface chemistry of monolayer metallic films on Re(0001) and Mo(110)*. Journal of Vacuum Science & Technology A, 1990. **8**(3): p. 2435-2444.
56. Park, C., E. Bauer, and H. Poppa, *Growth and alloying of Pd films on Mo(110) surfaces*. Surface Science, 1985. **154**(2): p. 371-393.
57. McQuarrie, D.A., *Statistical Mechanics*. 2000: University Science Books.

58. Payne, M.A., J.B. Miller, and A.J. Gellman, *High-throughput characterization of early oxidation across $Al_xFe_yNi_{1-x-y}$ composition space*. Corrosion Science, 2015. **91**(Supplement C): p. 46-57.
59. Saha, S.K.a.M., Sujit and Przybylski, Marek and Stepanyuk, Valeri S. and Kirschner, J\"urgen, *Sharply distinct d -band quantum-well states in palladium thin films*. Phys. Rev. B, 2014. **90**(8): p. 081404.
60. Li, X., Z. Zhang, and V.E. Henrich, *Inelastic electron background function for ultraviolet photoelectron spectra*. Journal of Electron Spectroscopy and Related Phenomena, 1993. **63**(3): p. 253-265.
61. Kratzer, P., B. Hammer, and J.K. Nørskov, *Geometric and electronic factors determining the differences in reactivity of H_2 on $Cu(100)$ and $Cu(111)$* . Surface Science, 1996. **359**(1): p. 45-53.
62. Mavrikakis, M., B. Hammer, and J.K. Nørskov, *Effect of Strain on the Reactivity of Metal Surfaces*. Physical Review Letters, 1998. **81**(13): p. 2819-2822.
63. Jeff Greeley, Jens K. Nørskov, and M. Mavrikakis, *ELECTRONIC STRUCTURE AND CATALYSIS ON METAL SURFACES*. Annual Review of Physical Chemistry, 2002. **53**(1): p. 319-348.
64. Xu, Y. and M. Mavrikakis, *Adsorption and dissociation of O_2 on $Cu(111)$: thermochemistry, reaction barrier and the effect of strain*. Surface Science, 2001. **494**(2): p. 131-144.
65. Michaelides, A. and P. Hu, *A density functional theory study of the reaction of $C+O$, $C+N$, and $C+H$ on close packed metal surfaces*. The Journal of Chemical Physics, 2001. **114**(13): p. 5792-5795.
66. Hammer, B. and J.K. Nørskov, *Electronic factors determining the reactivity of metal surfaces*. Surface Science, 1995. **343**(3): p. 211-220.
67. Lima, F.H.B., et al., *Catalytic Activity– d -Band Center Correlation for the O_2 Reduction Reaction on Platinum in Alkaline Solutions*. The Journal of Physical Chemistry C, 2007. **111**(1): p. 404-410.
68. Okada, M., et al., *Experimental and Theoretical Studies on Oxidation of $Cu-Au$ Alloy Surfaces: Effect of Bulk Au Concentration*. Scientific Reports, 2016. **6**: p. 31101.
69. Hofmann, T., et al., *Using Photoelectron Spectroscopy and Quantum Mechanics to Determine d -Band Energies of Metals for Catalytic Applications*. The Journal of Physical Chemistry C, 2012. **116**(45): p. 24016-24026.
70. Marek, G., E. Andreas, and H. Jürgen, *CO adsorption on close-packed transition and noble metal surfaces: trends from *ab initio* calculations*. Journal of Physics: Condensed Matter, 2004. **16**(8): p. 1141.
71. Visikovskiy, A., et al., *Electronic d -band properties of gold nanoclusters grown on amorphous carbon*. Physical Review B, 2011. **83**(16): p. 165428.

72. Gorzkowski, M.T. and A. Lewera, *Probing the Limits of d-Band Center Theory: Electronic and Electrocatalytic Properties of Pd-Shell–Pt-Core Nanoparticles*. The Journal of Physical Chemistry C, 2015. **119**(32): p. 18389-18395.
73. Hammer, B., Y. Morikawa, and J.K. Norskov, *CO chemisorption at metal surfaces and overlayers*. Phys Rev Lett, 1996. **76**(12): p. 2141-2144.
74. Zhou, W.P., et al., *Size effects in electronic and catalytic properties of unsupported palladium nanoparticles in electrooxidation of formic acid*. The Journal of Physical Chemistry B, 2006. **110**(27): p. 13393-13398.
75. Gajdoš, M., A. Eichler, and J. Hafner, *CO adsorption on close-packed transition and noble metal surfaces: trends from ab initio calculations*. Journal of Physics: Condensed Matter, 2004. **16**(8): p. 1141.
76. Toyoda, E., et al., *The d-Band Structure of Pt Nanoclusters Correlated with the Catalytic Activity for an Oxygen Reduction Reaction*. The Journal of Physical Chemistry C, 2011. **115**(43): p. 21236-21240.
77. James, A.D., *The Microkinetics of heterogeneous catalysis*. 1993: Washington, DC : American Chemical Society, 1993.
78. Copper unit price. Available from: <https://www.providentmetals.com/spot-price/chart/copper/>.
79. Palladium unit price. Available from: <https://www.apmex.com/spotprices/palladium-price>.
80. Gold unit price. Available from: <https://www.apmex.com/spotprices/gold-price>.
81. Wilde, M., et al., *Hydrogen absorption in oxide-supported palladium nanocrystals*. Physical Review B, 2008. **77**(11): p. 113412.
82. Hammer, B. and J.K. Nørskov, *Theoretical surface science and catalysis—calculations and concepts*. Advances in catalysis, 2000. **45**: p. 71-129.

CHAPTER 5

Characterization of Composition, Electronic Structure and Ethylene

Hydrogenation Activity across $\text{Cu}_x\text{Au}_y\text{Pd}_{1-x-y}$ Alloys

5.1 Chapter abstract

Hydrogenation processes are crucially important to the chemical industry and a significant fraction of these processes are performed on heterogeneous transition-metal catalyst. In order to understand the general mechanism and kinetics for hydrogenation reactions, ethylene hydrogenation has often been used as a probe reaction. Ethylene hydrogenation reaction ($\text{C}_2\text{H}_4 + \text{H}_2 \rightarrow \text{C}_2\text{H}_6$) has been one of the most widely studied reactions in heterogeneous catalysis. There is still much to learn about this relatively simple reaction since it possesses an extremely rich and complicated chemistry. Hence, investigating this reaction on alloy catalysts has major challenges.

In order to investigate ethylene hydrogenation reaction across multicomponent catalysts, thin multicomponent films called Composition Spread Alloy Films (CSAFs) are prepared, which have composition gradients parallel to their surfaces, $\text{A}_x\text{B}_y\text{C}_{1-x-y}$ with $x = 0 \rightarrow 1$ and $y = 0 \rightarrow 1 - x$. In order to study alloy catalysis across a CSAF, a 100 channel microreactor array has been developed to run steady state catalytic reactions at different positions or alloy compositions on the CSAF. $\text{Cu}_x\text{Au}_y\text{Pd}_{1-x-y}$ CSAFs spanning all of binary and ternary composition space have been prepared using a rotating shadow mask CSAF deposition tool developed in house.

High-throughput techniques have been used to characterize the activity of ethylene hydrogenation reaction over ternary alloy catalysts. Ethylene hydrogenation reaction has been chosen for this work since it is a simple reaction (producing only ethane) and it has been investigated on binary alloy catalysts before. Horiuti-Polanyi mechanism is widely accepted for this reaction. In this mechanism, ethylene adsorbs onto catalyst surface molecularly and H_2 adsorbs dissociatively. Adsorbed H atoms combine with adsorbed ethylene to form ethyl groups on the surface. As the last step, another H atom is added to the ethyl group, ethane is formed and immediately desorbed from the surface. The relationship between alloy catalyst activity and electronic structure is investigated experimentally across $Cu_xAu_yPd_{1-x-y}$ CSAFs.

C_2H_4 hydrogenation kinetics were measured at 100 discrete compositions on the CSAFs over a temperature range of 295 – 433 K. Characterization of the CSAFs was done using X-ray photoelectron spectroscopy. C_2H_4 conversion was chosen to be the indicator of activity and it was found to increase with increasing Pd content. A microkinetic model was used to estimate the energy barriers for all elementary steps in the mechanism as functions of alloy composition, x and y . Across the $Cu_xAu_yPd_{1-x-y}$ CSAF, ethyl hydrogenation was found to be the rate-limiting step. Spatially resolved X-ray photoelectron spectra obtained from the CSAFs were used to estimate the energy of the valence-band center as a function of alloy composition. The v-band center shifted monotonically from -3.4 to -5.6 eV across the $Cu_xAu_yPd_{1-x-y}$ CSAF. This data provides the first experimental correlation of elementary reaction barriers with valence band energy across a continuous span of ternary alloy composition space for C_2H_4 hydrogenation reaction.

5.2 Introduction

Ethylene hydrogenation has been one of the most widely studied reactions in heterogeneous catalysis. It has been used as a probe reaction for understanding the general mechanism and kinetics for olefin and aromatics hydrogenation [1-3]. Ethylene hydrogenation is one of the fastest heterogeneous catalytic reactions with the turnover rates of around $10 \text{ site}^{-1} \text{ s}^{-1}$ at room temperature and atmospheric pressures of ethylene and hydrogen [4]. There are a number of elegant studies investigating the kinetic behavior of ethylene hydrogenation on transition metal surfaces [5-10]. In various experimental studies conducted on Pt and Pd usually the apparent activation energies changing between 8-11 kcal/mol have been reported [1, 4, 11-17]. However there are still many unknowns about the basic elementary steps of the reaction.

The reaction order in both ethylene and hydrogen was found to be dependent on temperature and the partial pressures of the reactants on pure Pt and Pd [4, 5, 11-13, 18]. In these studies, the hydrogen kinetic order was reported to increase with increasing temperature from 0.5 to 1.1. The ethylene order was found to be nearly zero at low temperatures and high ethylene pressures, and as temperature increases and ethylene pressure decreases, the ethylene kinetic order becomes negative. This strong dependence of the kinetics of ethylene hydrogenation on reaction conditions and catalyst characteristics makes it complicated to study [19]. Horiuti-Polanyi mechanism has generally been used to model ethylene hydrogenation (Figure 5. 1) [20]. According to this mechanism ethylene adsorbs molecularly and hydrogen adsorbs dissociatively. Atomic hydrogen inserts into a metal-carbon bond to form ethyl intermediate. The ethyl intermediate then reacts with a second H atom to form ethane. Ethane desorbs from the surface into the gas phase. With the improvement in experimental and computational techniques, more details have been

added to this mechanism as explained in detail in Introduction section. However it is still very practical to capture the characteristics of fundamental elementary steps.

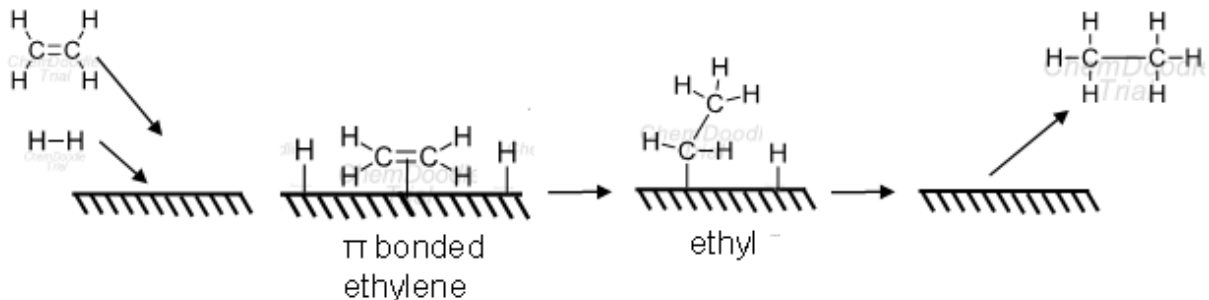
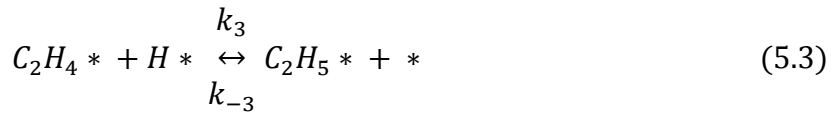
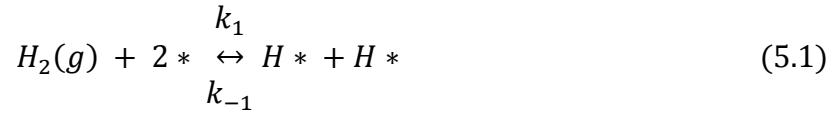


Figure 5. 1. Ethylene hydrogenation mechanism proposed by Horiuti-Polanyi. In this mechanism, H_2 adsorbs dissociatively and C_2H_4 (ethylene) adsorbs molecularly. Adsorbed H combine with adsorbed C_2H_4 to form C_2H_5 (ethyl) and then another H is added to C_2H_5 to produce C_2H_6 (ethane).

Alloying has been known to increase the selectivity and/or catalytic activity for other hydrogenation reactions over that from either of the pure metals (Pt and/or Pd). The effect of alloying Pd with Ag, Au and/or Cu on H_2 - D_2 exchange has been studied in the previous sections. Alloying Pd with Au was reported to enhance the selectivity for various industrial processes such as the trimerization of acetylene to benzene [21] and acetylene hydrogenation [22, 23]. When it comes to ethylene hydrogenation, Davis and Boudart have found that the addition of Au to Pd has no effect on catalytic activity, they reported no change of the activation barriers [24]. The effect of alloying Pd with Au was also studied using a first-principles-based dynamic Monte Carlo simulation method and the apparent turnover frequency was reported to remain constant with Au composition up to 12.5%. Alloying Pd with Cu was reported to suppress undesired ethylene hydrogenation during acetylene hydrogenation process [25]. For acetylene hydrogenation, when

the effects of alloying Pd with Cu, Au and Ag was compared, Cu was found to exceed both Au and Ag in conversion while Ag is the best one to enhance the selectivity [26].

In this study, a $\text{Cu}_x\text{Au}_y\text{Pd}_{1-x-y}$ CSAF that spans a continuous range of compositions ($x = 0 \rightarrow 1$ and $y = 0 \rightarrow 1-x$) was used to characterize the activity for C_2H_4 hydrogenation reaction. Quantitative kinetic data has been obtained and analyzed to elucidate the mechanism and extract fundamental kinetic parameters for C_2H_4 hydrogenation as functions of alloy composition. C_2H_4 hydrogenation has been parameterized by 7 rate constants: k_i ($i = 0 -7$) for each elementary reaction as given below. By measuring these seven rate constants over a range of temperature, the activation barriers to dissociative adsorption (ΔE_i^\ddagger) can be estimated across $\text{Cu}_x\text{Au}_y\text{Pd}_{1-x-y}$ alloy composition space.



In addition, the barriers have been correlated with the valence band electronic structure of the alloy at each composition. Using XPS we have estimated the average energy of the filled states of the valence band (*s*-, *p*-, and *d*-bands), $\epsilon_v(x)$, across composition space and used it as an experimental proxy for the *d*-band energy. By doing that, we can correlate reaction barriers (ΔE_i^\ddagger) with $\epsilon_v(x)$ across the entire $\text{Cu}_x\text{Au}_y\text{Pd}_{1-x-y}$ composition space. We have observed that as Cu and/or Au content decreases, the *v*-band center shifts toward the Fermi level. This work demonstrates a high-throughput experimental methodology for correlation of fundamental kinetic parameters, such as energy barriers, with the electronic structure of multicomponent alloy catalysts. This general methodology should be applicable to a wide-range of catalytic reactions.

5.3 Experimental

5.3.1 CSAF preparation

The CSAF samples were prepared by evaporative deposition of Cu, Au and Pd onto a $14 \times 14 \times 2 \text{ mm}^3$ polished Mo substrate (Valley Design Corp.) using a rotatable shadow mask CSAF deposition tool that has been described in detail previously [27]. Electron beam evaporation sources containing Cu, Au and Pd were positioned 120° apart from each other. Deposition rates from both sources were controlled by filament heating power and measured using a QCM. The film thickness ($\sim 100 \text{ nm}$ in this work) was controlled by the deposition time. The positions and orientations of the shadow masks between the sources and the substrate result in a flux gradient across the substrate. Mo was chosen as a substrate material because it does not alloy with Au, Cu or Pd and stabilizes the film against dewetting at annealing temperatures [28-31]. CSAFs were

deposited at room temperature over periods of 6 to 8 h, annealed at 800 K for 1 h to induce crystallization and sputtered using a He⁺ beam under ultrahigh vacuum conditions (UHV).

5.3.2 Characterization of CSAF composition and electronic structure

XPS analysis of the Cu_xAu_yPd_{1-x-y} CSAF was performed in a ThetaProbe™ (Thermo-Fisher Scientific Inc.) to map the local composition and the valence band electronic structure across the sample surface. XPS characterization process was the same as described in Section 3.3.2. Spatially resolved maps of the Cu 2p_{3/2}, Au 4f_{7/2} and Pd 3d_{3/2} XP spectra were obtained by lateral translation of the CSAF such that its plane intersected the source-analyzer focal point.

5.3.3 Characterization of C₂H₄ hydrogenation activity across Cu_xAu_yPd_{1-x-y} CSAF

The C₂H₄ hydrogenation activity of Cu_xAu_yPd_{1-x-y} CSAFs was measured by flowing H₂, C₂H₄, and Ar through a 100-channel microreactor array. The experimental setup used was explained in detail in Section 2.2.2. Cu_xAu_yPd_{1-x-y} was prepared as explained in Section 2.2.2. Mass flow controllers (Aalborg GFC 17) was used to regulate the flow rates of H₂ (99.999%, Valley National Gases), C₂H₄ (99.995%, Valley National Gases) and Ar (99.999%, Valley National Gases) through the microchannels to the CSAF surface. A surface area corresponding to one catalyst composition across the ternary CSAF was approximately 0.006 cm². The inlet flow rates of H₂, D₂, and Ar were adjusted to the conditions listed in Table 5. 1.

The CSAF was heated by a thermocouple spot-welded to one of its sides. The experiments were performed over a temperature range 333 to 533 K with 20 K increments and at atmospheric pressure. At each temperature, approximately 4 minutes were required to allow the system to

reach steady state. The product gas mixture from each of the 100 different reaction volumes was sent to the mass spectrometer for quantification. The CSAF surface was pretreated with H₂ prior

Table 5. 1. Flow rates of H₂ ($F_{H_2}^{in}$), C₂H₄ ($F_{C_2H_4}^{in}$), and Ar (F_{Ar}^{in}) in the eleven different gas conditions used during C₂H₄ hydrogenation experiments at $P_{tot} = 1$ atm. Flow rates in one channel can be found by dividing the listed values into 100. Total flow rate is kept constant at 0.1 mL/min per channel.

	$F_{C_2H_4}^{in}$ (mL/min)	$F_{H_2}^{in}$ (mL/min)	F_{Ar}^{in} (mL/min)	$P_{C_2H_4}$ (kPa)	P_{H_2} (kPa)
1	1.32	1.32	7.36	13.33	13.33
2	0.66	1.32	8.02	6.67	13.33
3	0.13	1.32	8.55	1.33	13.33
4	0.66	2.63	6.71	6.67	26.66
5	0.66	5.26	4.08	6.67	53.33
6	0.66	7.90	1.44	6.67	80.00
7	1.32	2.63	6.05	13.33	26.66
8	2.63	5.26	2.11	16.9	53.33

to the experiments. Also between different set of experiments the CSAF surface was left in contact with flowing H₂.

The composition of the reaction products were calculated by using the mass spectrometer signals at $m/q = 25, 26, 27, 29$ and 30 amu obtained from the product gas samples. Both ethylene (molar mass = 28) and ethane (molar mass = 30) have signals at $m/q = 25, 26, 27, 28, 29$ and 30 amu. The fragmentation patterns of these two compounds can be found in Figure 5.2 [32]. The two extra channels that were added to the microreactor system was used to obtain $25, 26, 27, 29$ and 30 signals at zero conversion (pure ethylene) and full conversion (pure ethane) cases after each

experiment. The signal at 28 amu was not used in the calculations due to the possible air penetration to the system and the ubiquitous presence of CO in all vacuum systems. Least squares estimation was used to calculate the fraction of signals derived from ethylene and ethane:

$$\begin{bmatrix} S_{25} \\ S_{26} \\ S_{27} \\ S_{29} \\ S_{30} \end{bmatrix} = (X_{C_2H_4}) \begin{bmatrix} S_{25} \\ S_{26} \\ S_{27} \\ S_{29} \\ S_{30} \end{bmatrix}_{C_2H_4} + (1 - X_{C_2H_4}) \begin{bmatrix} S_{25} \\ S_{26} \\ S_{27} \\ S_{29} \\ S_{30} \end{bmatrix}_{C_2H_6} \quad (5.5)$$

$$\beta = \begin{bmatrix} X_{C_2H_4} \\ 1 - X_{C_2H_4} \end{bmatrix} \quad (5.6)$$

$$\alpha = \begin{bmatrix} \begin{bmatrix} S_{25} \\ S_{26} \\ S_{27} \\ S_{29} \\ S_{30} \end{bmatrix}_{C_2H_4} & \begin{bmatrix} S_{25} \\ S_{26} \\ S_{27} \\ S_{29} \\ S_{30} \end{bmatrix}_{C_2H_6} \end{bmatrix} \quad (5.7)$$

$$\beta = (\alpha^T \alpha)^{-1} (\alpha^T S) \quad (5.8)$$

where α is a matrix of the mass spectrometer signals at each m/q for pure ethylene (obtained after each experiment from zero conversion channel) and pure ethane (obtained after each experiment from full conversion channel); S is a vector of measured signal intensities at $m/q = 25, 26, 27, 29$ and 30 ; β is the solution to the least squares estimation and gives the ethylene conversion $X_{C_2H_4}$.

C₂H₄ conversions were measured at 100 channels at T = 295-433 K at 8 different inlet flow conditions specified in Table 5. 1. The measured conversions were used to calculate the kinetic parameters, the activation barriers to dissociative adsorption (ΔE_{ads}^\ddagger) and recombinative desorption (ΔE_{des}^\ddagger) for the catalytic C₂H₄ hydrogenation reaction as a function of Cu_xAu_yPd_{1-x-y} alloy composition. The detailed explanation of the microkinetic model and calculation methods has been explained in Section 5.4.

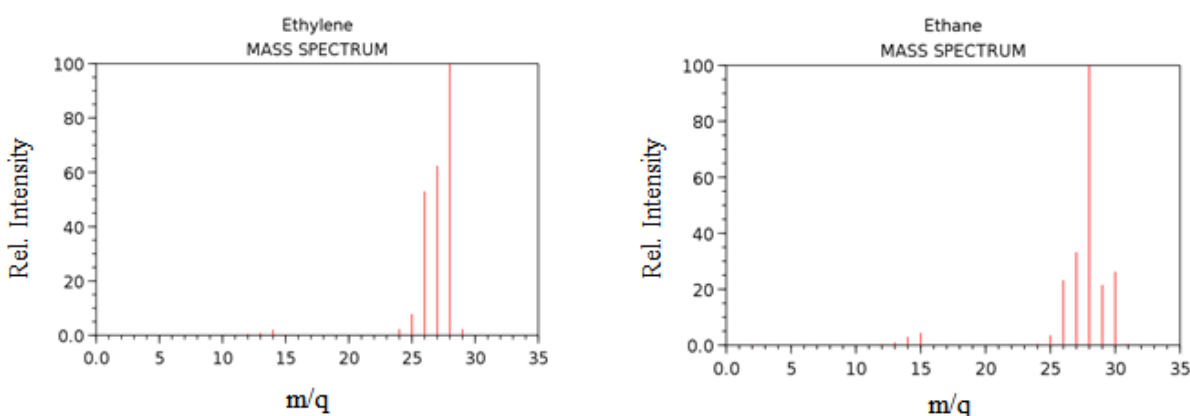
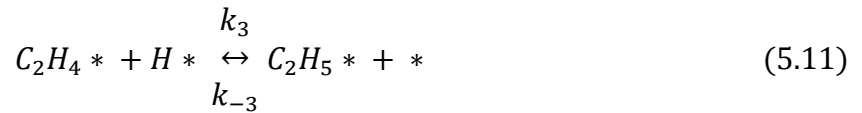
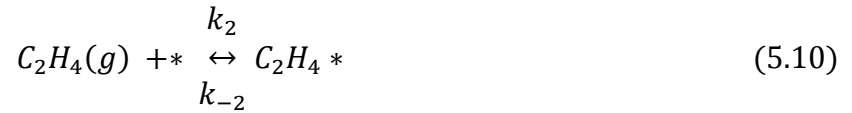
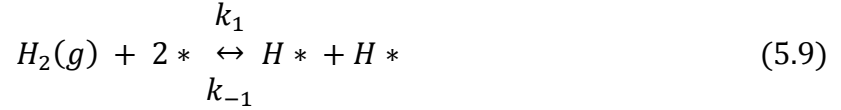


Figure 5.2. Fragmentation patterns of ethylene and ethane.

5.4 Microkinetic model

The primary mechanism for hydrogenation of simple alkenes over metal surfaces has been established as the Horiuti-Polanyi mechanism. In this mechanism, ethylene is adsorbed on the surface, and two sequential hydrogen addition steps take place from a reservoir of adsorbed hydrogen atoms. The resulting ethane desorbs spontaneously and the supply of hydrogen is restocked by the dissociative chemisorption of gaseous H₂. The proposed mechanism is given below:



where * denotes an empty surface site and the asterisk * with species denotes an adsorbed species. First two steps in the mechanism are dissociative adsorption of H₂ and molecular desorption of C₂H₄. Step 3 (Equation (5.11)) is the first hydrogenation step in which adsorbed ethylene and H atom combine to form ethyl species, leaving one vacant site. Step 4 (Equation (5.12)) is the second hydrogenation step in which ethyl combined with another H atom to form ethane which immediately desorbs from the surface. So this last step is modeled as an irreversible reaction, whereas, all the other steps are reversible.

The forward and reverse rate equations for all four steps can be written as

$$r_1 = k_1 P_{H_2} (1 - \theta_H - \theta_4 - \theta_5)^2 \quad (5.13)$$

$$r_{-1} = k_{-1} \theta_H^2 \quad (5.14)$$

$$r_2 = k_2 P_{C_2H_4} (1 - \theta_H - \theta_4 - \theta_5) \quad (5.15)$$

$$r_{-2} = k_{-2} \theta_4 \quad (5.16)$$

$$r_3 = k_3 \theta_H \theta_4 \quad (5.17)$$

$$r_{-3} = k_{-3} \theta_5 (1 - \theta_H - \theta_4 - \theta_5) \quad (5.18)$$

$$r_4 = k_4 \theta_H \theta_5 \quad (5.19)$$

where r_i 's are the rates of related reaction step; P_{H_2} and $P_{C_2H_4}$ are the partial pressures of H_2 and C_2H_4 , respectively; θ_H , θ_4 and θ_5 are the coverages of H atom, ethylene and ethyl species, respectively. Hence, $1 - \theta_H - \theta_4 - \theta_5$ describes the fraction of the vacant active sites on the surface. The k_i 's are the rate constants for each elementary step in the Arrhenius form

$$k_i = v_i \exp\left(-\frac{E_i}{k_B T}\right) \quad (5.20)$$

where v_i is the pre-exponential factor and E_i is the energy barrier of the reaction, i . k_B is the Boltzman constant and T is the temperature in K.

The rate of change of surface coverages of the species can be calculated by

$$\frac{d\theta_H}{dt} = k_1 P_{H_2} (1 - \theta_H - \theta_4 - \theta_5)^2 - k_{-1} \theta_H^2 + k_{-3} \theta_5 (1 - \theta_H - \theta_4 - \theta_5) - k_3 \theta_H \theta_4 - k_4 \theta_H \theta_5 \quad (5.21)$$

$$\frac{d\theta_4}{dt} = k_2 P_{C_2H_4} (1 - \theta_H - \theta_4 - \theta_5) - k_{-2} \theta_4 + k_{-3} \theta_5 (1 - \theta_H - \theta_4 - \theta_5) - k_3 \theta_H \theta_4 \quad (5.22)$$

$$\frac{d\theta_5}{dt} = k_3 \theta_H \theta_4 - k_{-3} \theta_5 (1 - \theta_H - \theta_4 - \theta_5) - k_4 \theta_H \theta_5 \quad (5.23)$$

The rate of change in the flow rates of H₂, C₂H₄ and C₂H₆ with respect to the surface area of the catalyst can be calculated as

$$\frac{dF_{H_2}}{dA} = -r_1 + r_{-1} \quad (5.24)$$

$$\frac{dF_{C_2H_4}}{dA} = -r_2 + r_{-2} \quad (5.25)$$

$$\frac{dF_{C_2H_6}}{dA} = r_4 \quad (5.26)$$

Ethylene conversion values can be calculated as

$$X_{model} = \frac{F_{C_2H_6}^{out}}{F_{C_2H_4}^{in}} \quad (5.27)$$

The model prediction of ethylene conversion, X_{model} , was fit to the experimental C_2H_4 conversion, X_{exp} , data at each catalyst composition, for all inlet flow conditions and temperatures simultaneously. The fit was performed by minimizing the sum of squared errors (SSE) between the calculated and experimental conversions by changing the fourteen parameters v_i and E_i (for each of the elementary steps in the mechanism of C_2H_4 hydrogenation reaction).

$$SSE = \sum_{i,j} [X_{\text{exp}}(F_i, T_j) - X_{\text{model}}(F_i, T_j)]^2 \quad (5.28)$$

The fit of the model prediction of conversions to experimental values was performed in MATLAB using non-linear fitting subroutine *lsqcurvefit* which utilizes a “trust-region-reflective” least squares algorithm which is based on an interior-reflective Newton Method. Initial guesses for 14 parameters (7 natural logarithm of pre-exponential factors and 7 energy barriers) were provided. In the optimization routine natural logarithm of pre-exponential factors were used in order to make the quantitative range of the parameters closer to each other. Using these initial guesses the rate constants were calculated using Equation 5.20. Using these rate constants the surface coverages of the species are calculated by using Equations 5.21-5.23. At steady state, these equations are equal to 0. MATLAB’s *fsolve* subroutine was used to calculate θ_H , θ_4 and θ_5 . The flow rates of H_2 , C_2H_4 and C_2H_6 were calculated by using Equations 5.24-5.26. As the last step, using Equation 5.27, ethylene conversion was calculated. This routine is done for all inlet flow conditions and all temperatures. After the optimum solution was found, MATLAB’s *nlparci* function was used to calculate the confidence intervals on the estimated parameters.

5.5 Results and discussion

5.5.1 Characterization of CSAF composition

Spatially resolved measurements of $\text{Cu}_x\text{Au}_y\text{Pd}_{1-x-y}$ composition were made using XPS across a 13×13 grid with 1 mm spacing. The generated composition maps for all three components Cu, Au, and Pd are given in Figure 5.3. Full composition range for Cu, Au and Pd was covered as seen from the composition map. Since Au gradient is quite narrow and our microreactor only covers $10 \times 10 \text{ mm}^2$ on the CSAF surface, we were not able to test AuPd binary alloy compositions on this particular CSAF. This situation can be captured by looking at the ternary composition space given in Figure 5.4. In Figure 5.4-a, the XPS measurement points are marked as black squares. The even distribution of the points shows that CSAF spans the entire ternary alloy composition. Having a good number of data points on the edges shows that we have all three binary alloys (Cu-Pd, Au-Pd, and Cu-Au) on the CSAF. Comparing the composition

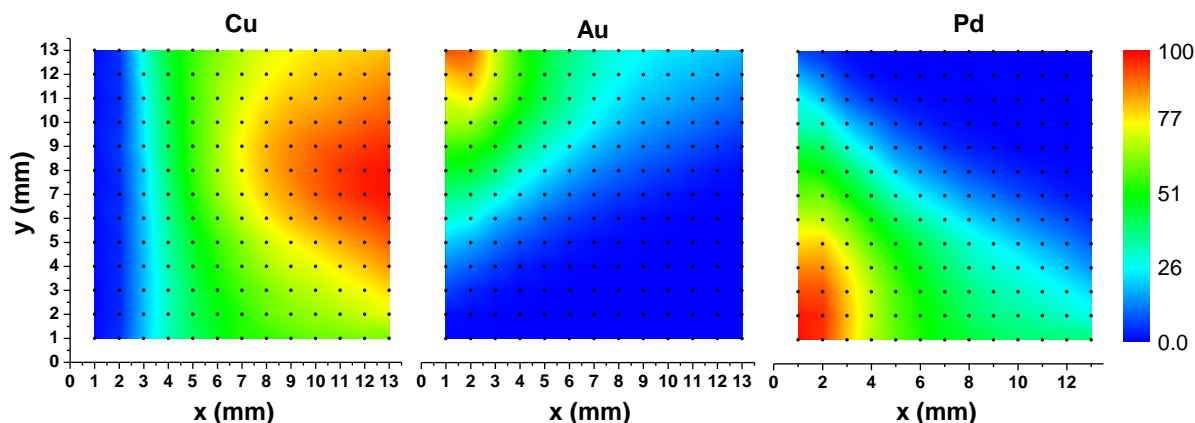


Figure 5.3. Concentration distribution (at. %) obtained with XPS for Cu, Au, and Pd across a $\text{Cu}_x\text{Au}_y\text{Pd}_{1-x-y}$ CSAF.

measurement points across the entire CSAF (Figure 5.4-a) and the points that corresponds to the microreactor reaction zones (Figure 5.4-b) clearly indicates that we are missing the AuPd binary region. The alloy compositions at the 10×10 reactor grid are determined using a composition distribution model (CDM) which is developed in our group. CDM provides a quantitative basis for estimating composition continuously at all locations across the CSAF from a set of discrete measurements, and is based on simplifying assumptions regarding the evaporative flux profiles produced by the rotatable shadow mask deposition tool. The details of the model can be found elsewhere [33]. The composition space showing all the 100 different alloy compositions that corresponds to each of the 100 channels in the multichannel microreactor array can be seen in Figure 5.4-b.

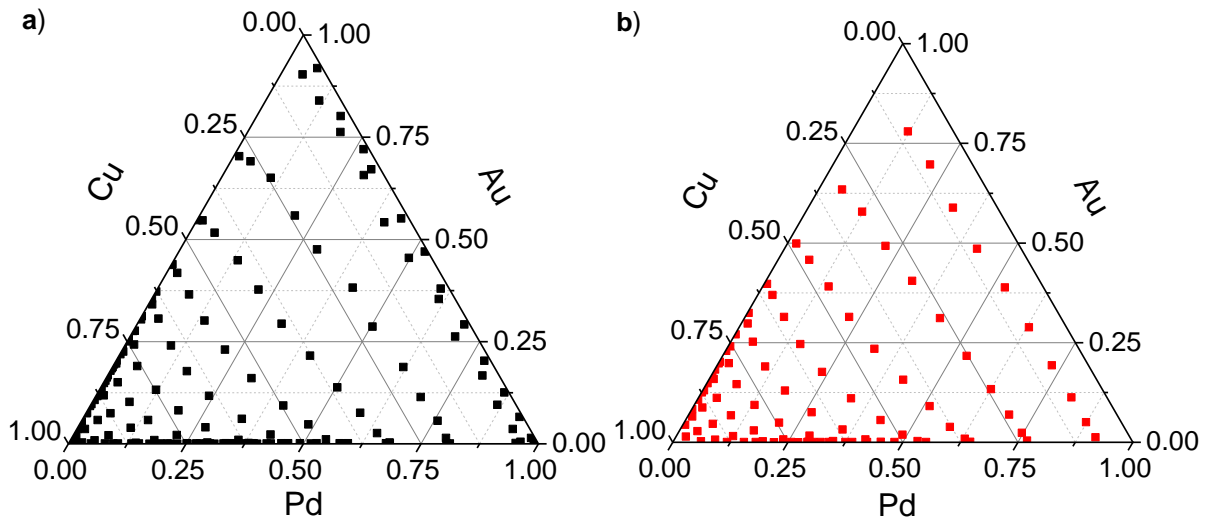


Figure 5.4. a) $\text{Cu}_x\text{Au}_y\text{Pd}_{1-x-y}$ alloy compositions across 14×14 mm² substrate surface (a 13×13 grid with 1 mm spacing). b) $\text{Cu}_x\text{Au}_y\text{Pd}_{1-x-y}$ alloy compositions covered in ternary space. Each of the red dots represent a different alloy composition corresponding to the 100 different microreactor channel.

5.5.2 Characterization of CSAF Electronic Structure

XPS was used to map the valence band electronic structure of the $\text{Cu}_x\text{Au}_y\text{Pd}_{1-x-y}$ CSAF across a 13×13 grid with 1 mm spacing. In previous chapter (Section 4.4.3), the background subtracted ν -band spectra mapped at 169 discrete locations across the $\text{Cu}_x\text{Au}_y\text{Pd}_{1-x-y}$ CSAF was given and how to interpret this spectra was explained in detail. The same procedure has been followed for this part of the study as well. The obtained ν -band spectra across $\text{Cu}_x\text{Au}_y\text{Pd}_{1-x-y}$ CSAF used in this part of the study is given in Figure 5.5. The average energy of the $\text{Cu}_x\text{Au}_y\text{Pd}_{1-x-y}$ ν -band shifts toward the Fermi level as the Pd content increases, i.e., as the color is changing from green to red.

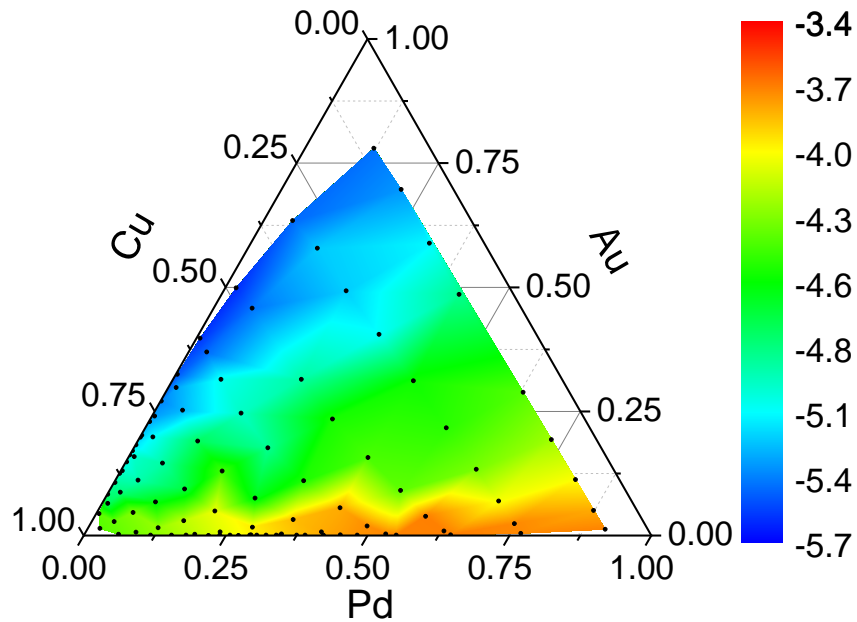


Figure 5.5. XPS-derived average energy of the filled ν -band relative to the Fermi level of $\text{Ag}_x\text{Pd}_{1-x}$ CSAF versus Pd (at. %) compositions.

5.5.3 C₂H₄ hydrogenation on Cu_xAu_yPd_{1-x-y} CSAF

C₂H₄ hydrogenation over Cu_xAu_yPd_{1-x-y} CSAF was carried out by feeding C₂H₄, H₂, and Ar mixtures into the microreactor at constant temperature, partial pressures and flow rates, while monitoring the product gas composition by mass spectrometry. Mass spectrometer signals were converted to conversion, X , for 100 different Cu_xAu_yPd_{1-x-y} compositions, x and y , at 8 different temperatures, T , and 8 different flow conditions. Within these conditions the Cu_xAu_yPd_{1-x-y} ternary CSAF surface was found to give a stable reactivity during successive experiments as can be seen from the example in Figure 5.6. In this figure, the measured conversion values of 3 randomly

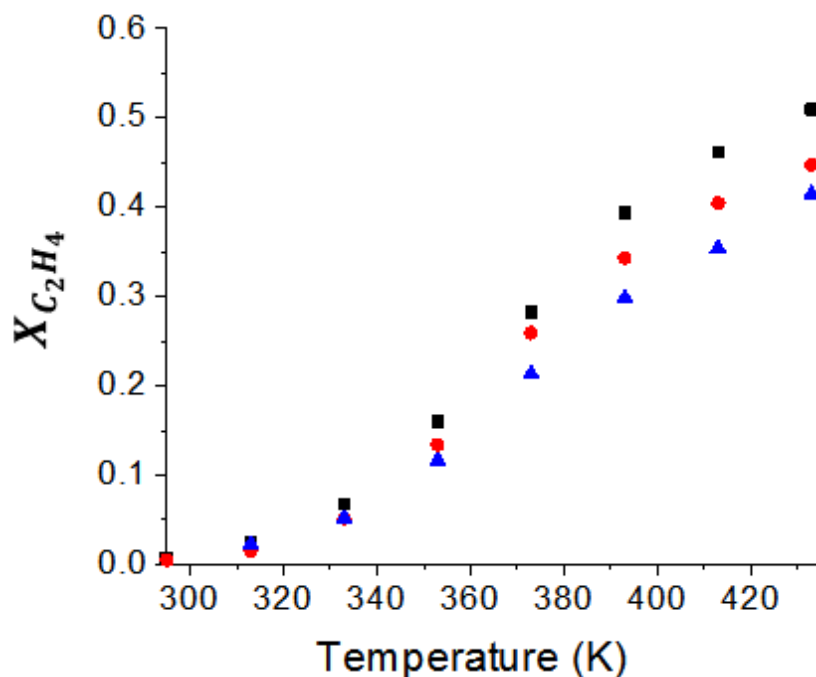


Figure 5.6. Ethylene conversion versus temperature measured at one randomly picked alloy composition (Cu_{0.26}Au_{0.01}Pd_{0.73}) across Cu_xAu_yPd_{1-x-y} composition space. The measured conversion values belong to 3 randomly picked experiments in order to show the reproducibility of the reactivity across the CSAF surface. The inlet flow rate contains 0.004 mL/min C₂H₄, 0.004 mL/min H₂ and 0.022 mL/min Ar per channel.

picked experiments from multiple successive experiments on $\text{Cu}_{0.26}\text{Au}_{0.01}\text{Pd}_{0.73}$ were given. Especially at high temperatures, the measured values may slightly differ from each other. Due to this fact, each experiment was repeated multiple times till the stable reactivity is obtained.

The deactivation of the CSAF surface was also tested. Standard reaction conditions are defined as 6.67 kPa of ethylene and 13.33 kPa of hydrogen for this study. Argon was used to balance the inlet flow at atmospheric pressure. In order to detect catalyst deactivation, conversion versus time data was collected with the standard flow conditions and at the 433 K. The results is shown in Figure 5.7. The deactivation study started at time zero at room temperature, then temperature is increased to 433 K and ethylene conversions were measured for about 1.5 hour. As can be seen from the graph, at 433 K no deactivation was observed within this time frame.

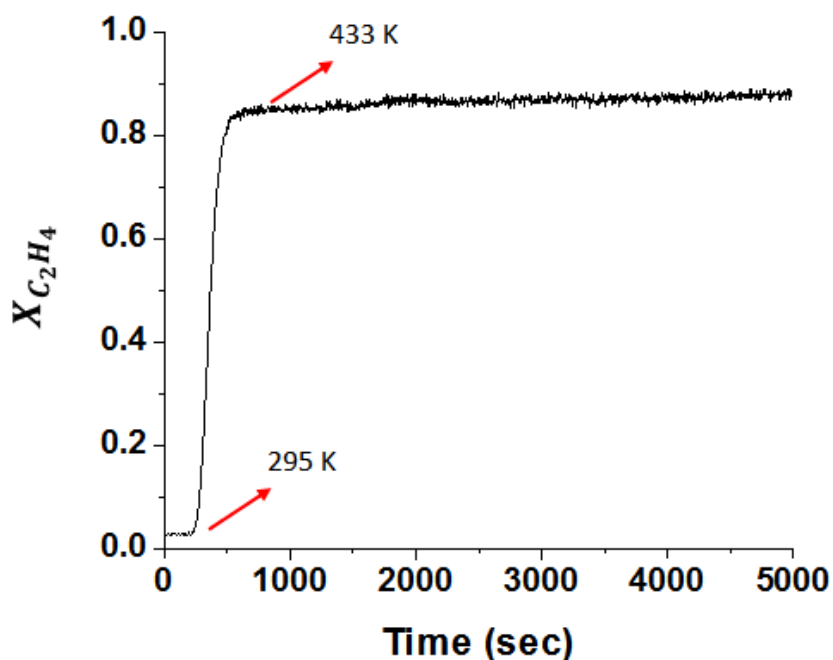


Figure 5.7. Ethylene conversion versus time measured at one randomly picked alloy composition ($\text{Cu}_{0.26}\text{Au}_{0.01}\text{Pd}_{0.73}$) across $\text{Cu}_x\text{Au}_y\text{Pd}_{1-x-y}$ composition space. No catalyst deactivation was observed.

Collected X versus T for all the inlet conditions listed in Table 5. 1 were then converted to the flow rate of produced C_2H_6 using Equation 5.23. Calculated C_2H_6 flow rates for all inlet flow conditions across all 100 different $Cu_xAu_yPd_{1-x-y}$ compositions are given in Figure 5.7.

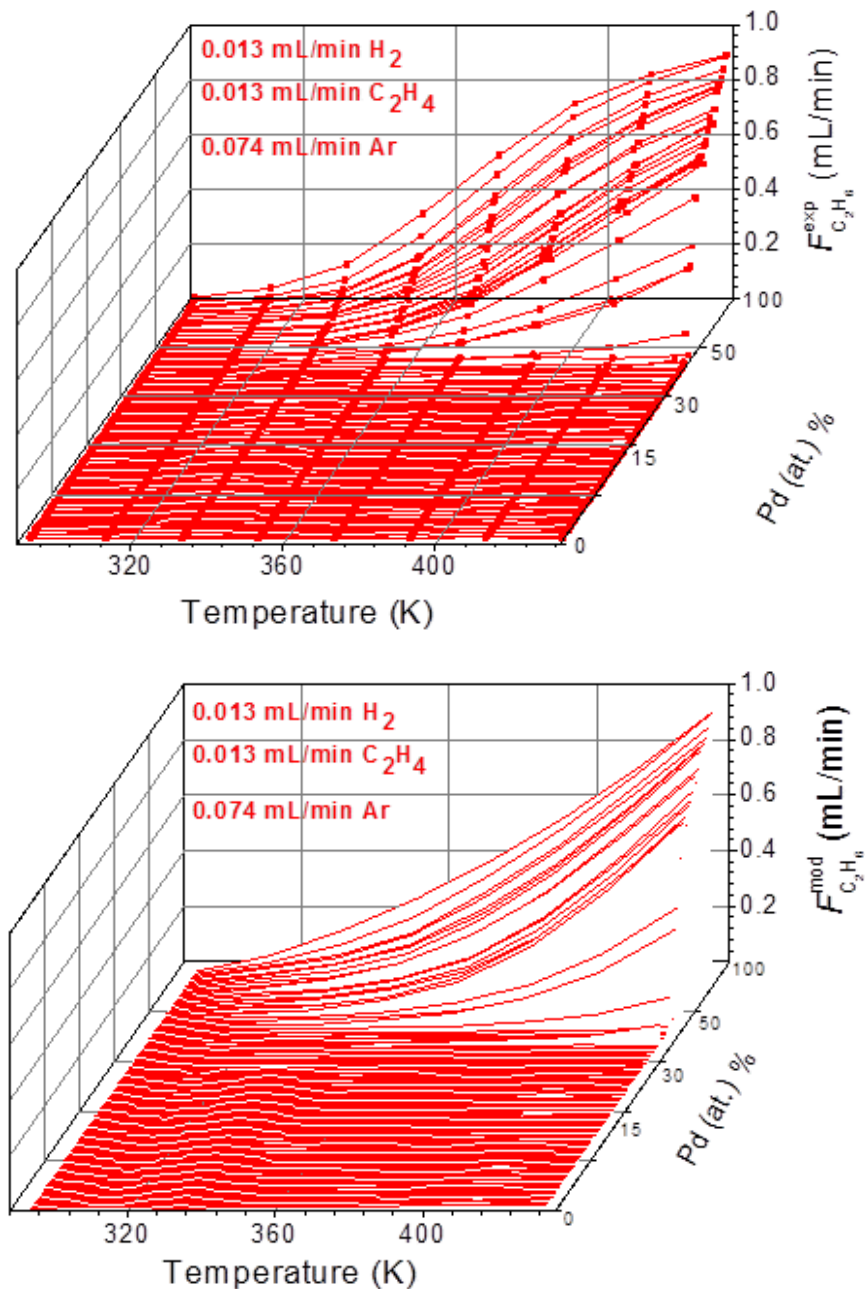


Figure 5.8. C_2H_6 flow rate versus temperature measured across $Cu_xAu_yPd_{1-x-y}$ composition space. For all 100 $Cu_xAu_yPd_{1-x-y}$ compositions activity increases with increasing T and decreasing x and y . Flow conditions in one channel are labeled on each figure. ($P_{tot} = 1$ atm) Top figure gives the experimentally measured values and the bottom one gives the model predictions.

Across the CSAF, C_2H_4 hydrogenation activity increases with increasing T and decreasing Cu and Au content, x and y . At $T = 295$ K, the conversion was $X < 5\%$ at all alloy compositions. It was avoided to reach equilibrium conversion, since at equilibrium it is not possible to detect the differences in catalytic activity across the CSAF. So, the maximum temperature tested was set to $T = 433$ K. Using our experimental set-up, it is possible to go higher temperatures and lower flow rates in order to reach equilibrium conversion if desired. We made sure that the C_2H_4 hydrogenation reaction progress far enough so that the product concentration can easily be measurable. Each data point in Figure 5.8 was collected under isothermal conditions; the CSAF was heated at 1 K/s and then held at constant temperature for ~ 4 min to reach steady-state before sampling C_2H_6 production across all 100 alloy compositions.

C_2H_4 conversion as a function of alloy composition across the $Cu_xAu_yPd_{1-x-y}$ ternary CSAF can better be represented using a ternary diagram. Waterfall plots given in Figure 5.8, shows the collected data as a function of T at different Pd concentrations. Since we have a ternary alloy this may not be useful to understand the effect of Cu and Au addition to Pd on catalytic activity. One example of ternary diagram showing how measured conversions change with Cu, Au and Pd content for the inlet flow consisting of 0.013 ml/min H_2 , 0.013 ml/min D_2 , and 0.074 ml/min Ar (per channel) at 433 K is given in Figure 5. 9. This diagram shows that as the color is changing from blue to green, X is increasing. This is also the direction of increasing Pd content. So basically we have achieved highest conversions across the Pd-rich side of the CSAF.

The black edge of the triangle represents the Cu-Au binary alloy compositions across the CSAF, the blue edge represents Au-Pd and the red edge represents Cu-Pd binary alloy compositions. In Figure 5. 9, if one of the iso-activity lines are followed from the blue edge to red edge, i.e., from Au-Pd binary region to Cu-Pd binary region, one can see that Cu-Pd binary alloys

are slightly more active than Au-Pd binary alloys because they are giving the same activity with less Pd content.

Figure 5. 10 shows how C_2H_4 conversion changes with temperature across the real physical space of the $Cu_xAu_yPd_{1-x-y}$ CSAF. At $T = 313$ K, C_2H_4 conversion is $X \approx 10\%$ at the most active point but usually $X \approx 0$ across the entire CSAF. As T increases, the activity also increases especially across the Pd-rich side of the CSAF. When Figure 5. 10 is compared with the XPS composition map of the CSAF (Figure 5.3), again the higher activity of Cu-Pd binary region than the Au-Pd binary region can be observed. At 533 K, a wider active region is observed at the bottom edge than the top edge that corresponds to mostly Cu-Pd binary and Cu-Au-Pd ternary alloy compositions across the CSAF.

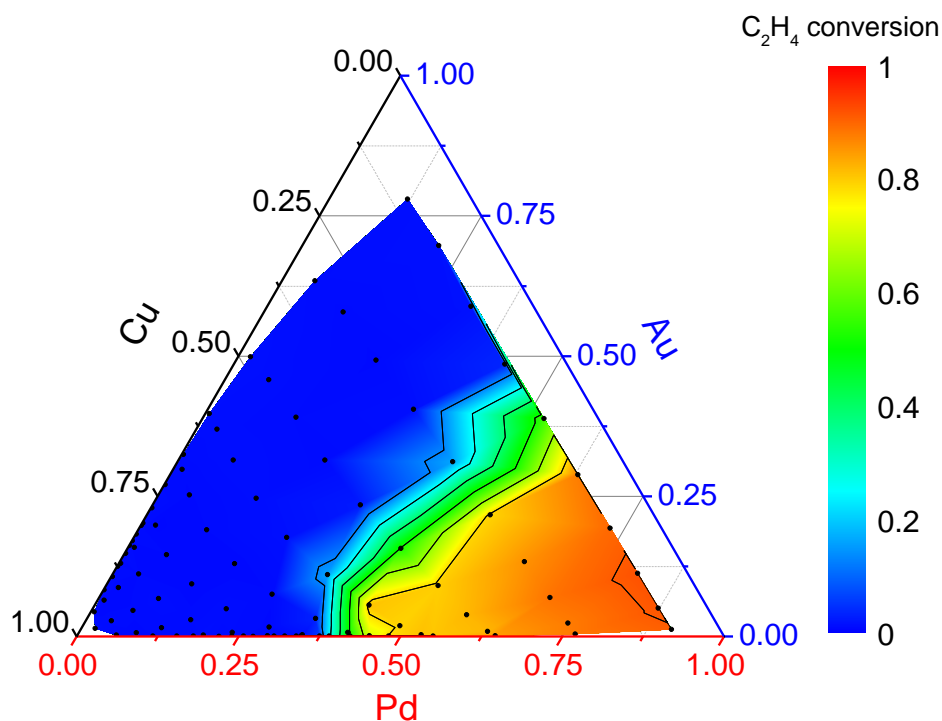


Figure 5. 9. Ternary composition space showing how the catalytic activity of the C_2H_4 hydrogenation reaction changes with Cu, Au and Pd composition across the $Cu_xAu_yPd_{1-x-y}$ CSAF. C_2H_4 conversion was selected to be the indicator of the activity and measured at 433K for the inlet flow 0.013 mL/min C_2H_4 + 0.013 mL/min H_2 + 0.076 mL/min Ar.

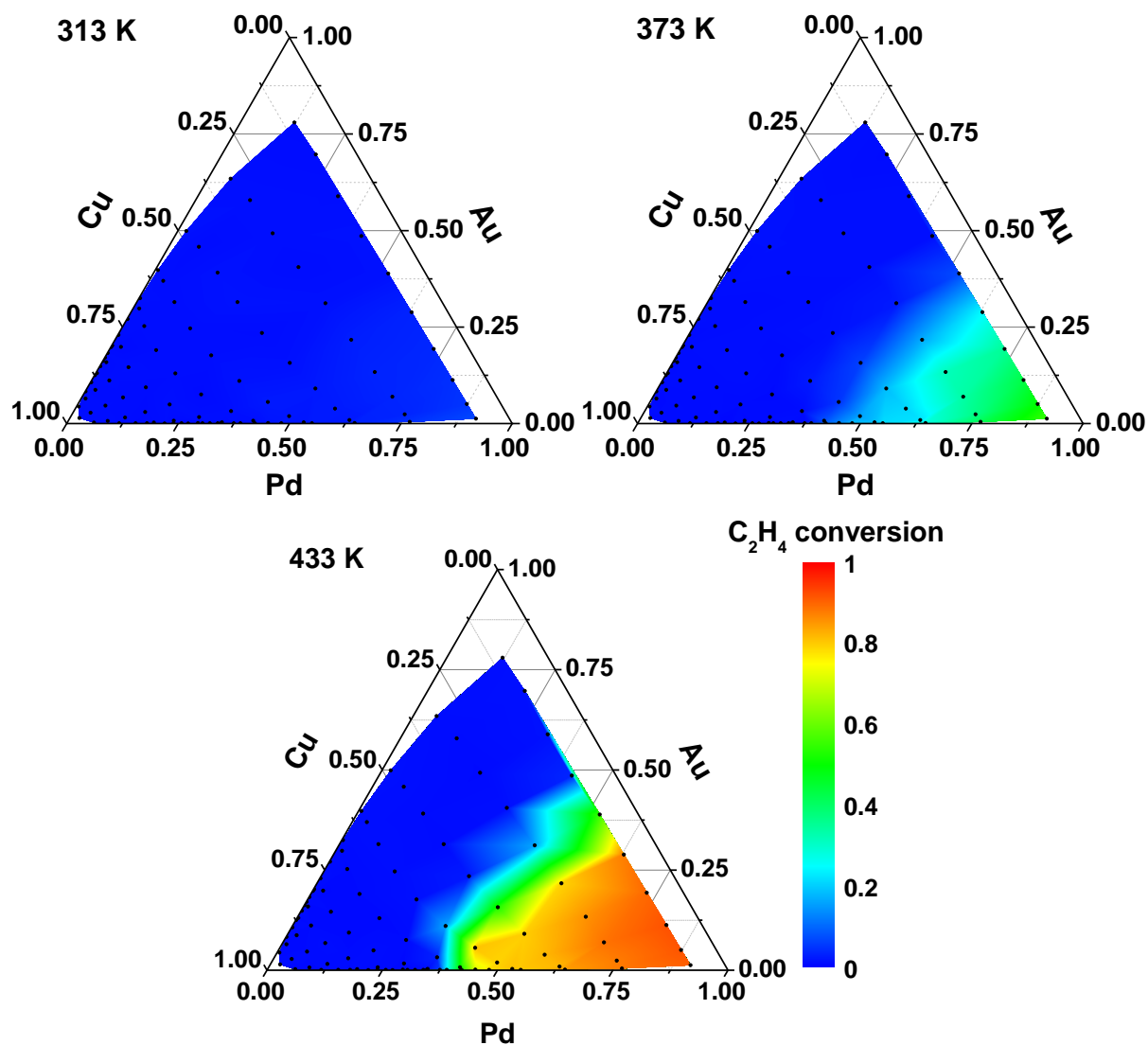


Figure 5. 10. C_2H_4 hydrogenation conversion across the $Cu_xAu_yPd_{1-x-y}$ CSAF at $T = 313$ K, 373 K and 433 K. Inlet flow was 0.013 mL/min C_2H_4 + 0.013 mL/min H_2 + 0.074 mL/min Ar per channel.

The pressure dependence of C_2H_6 production over $Cu_xAu_yPd_{1-x-y}$ alloys has been investigated across the temperature range $T = 295 - 433$ K by varying $P_{C_2H_4}$ and P_{H_2} independently. Three different $P_{C_2H_4}$ (1.33, 6.667, 13.33 kPa) was tested while keeping P_{H_2} constant at 13.33 kPa. Measured C_2H_6 flow rates at three sample alloy compositions are plotted in Figure 5.11. The flow rates have been normalized with respect to the activity at the standard conditions ($P_{C_2H_4} = 6.67$ kPa and $P_{H_2} = 13.33$ kPa). Figure 5.11 shows that as the $P_{C_2H_4}$ increases from 1.33 kPa, the ethane production decreases. The ethane production makes a plateau at around $P_{C_2H_4} = 5$ kPa. The decline in ethane production shows that ethylene kinetic order is negative with respect to $P_{C_2H_4}$. The kinetic order becomes less negative with increasing $P_{C_2H_4}$ and approaches zero at approximately 5 kPa. The similar observations are also reported in literature [4, 5, 12, 13].

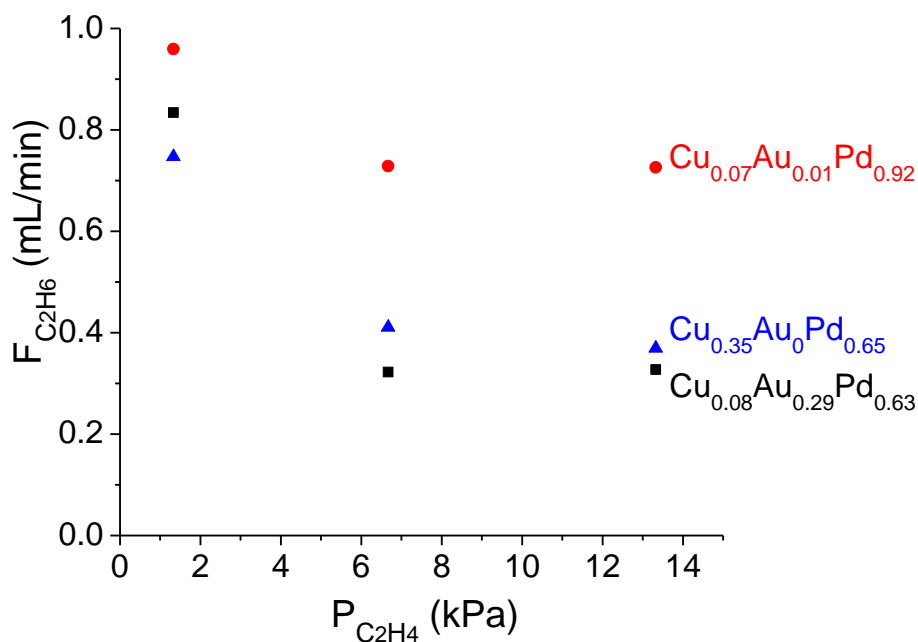


Figure 5.11. C_2H_6 flow rate in the outlet measured for three $Cu_xAu_yPd_{1-x-y}$ alloy compositions vs. $P_{C_2H_4}$. Catalytic activities are normalized to the catalytic activities observed at standard conditions ($T = 373$ K, $P_{H_2} = 13.33$ kPa, $P_{tot} = 1$ atm).

Figure 5.12 shows ethane flow rates $F_{C_2H_4}$, obtained for three different $Cu_xAu_yPd_{1-x-y}$ compositions. $P_{C_2H_4}$ is kept constant at 6.67 kPa and P_{H_2} is changed from 13.3 kPa to 80 kPa. The total flow rate per channel is kept constant at 0.1 mL/min. Figure 5.12 shows that ethane production increases with increasing P_{H_2} . The effect of total pressure was also investigated by keeping H_2/C_2H_4 ratio constant at 2 and by increasing $P_{C_2H_4}$ and P_{H_2} , however these experiments showed no significant change in activity.

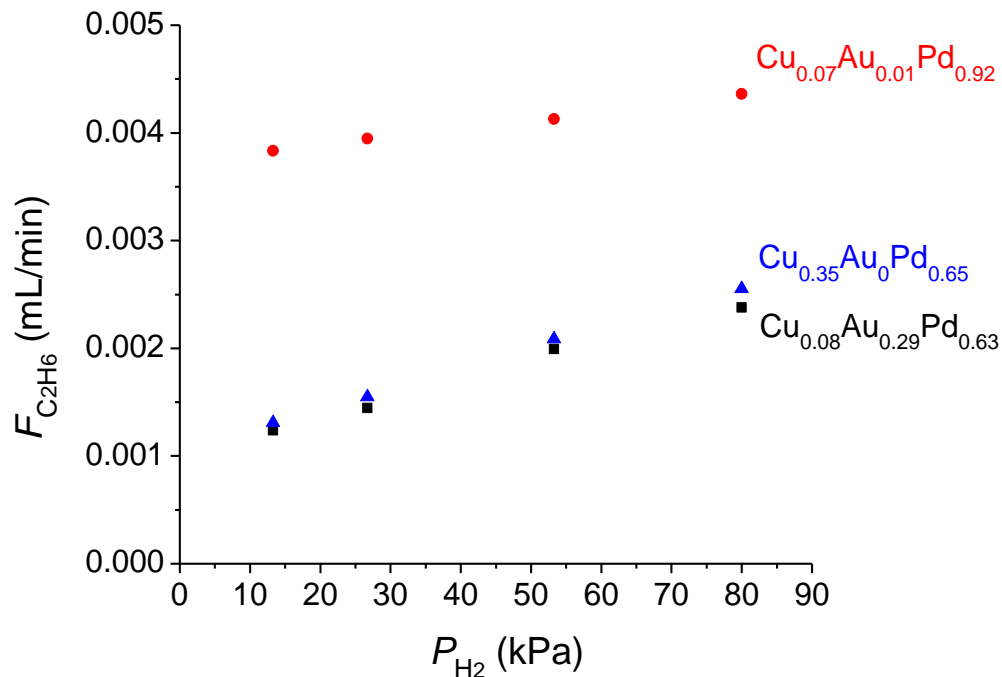


Figure 5.12. Effects of P_{H_2} on C_2H_6 flow rate in the outlet measured for three $Cu_xAu_yPd_{1-x-y}$ alloy compositions. ($T = 373$ K, $P_{C_2H_4} = 6.67$ kPa, $P_{tot} = 1$ atm).

5.5.4 Kinetic parameters for C₂H₄ hydrogenation on Cu_xAu_yPd_{1-x-y}

The comprehensive dataset obtained using high throughput methods and the microkinetic model have been used to estimate the kinetic parameters, ν_i and ΔE_i^\ddagger . These calculations were only carried out for the active region across the Cu_xAu_yPd_{1-x-y} alloy composition space (colored region on **Error! Reference source not found.**). In this study, model fit was performed by fixing the pre-exponents to their transition state theory values; for dissociative adsorption $\nu = 10^{-4}$ mol/m²/s/Pa, for molecular adsorption $\nu = 10^{-4}$ mol/m²/s/Pa, for Langmuir-Hinshelwood surface reactions $\nu = 10^6$ mol/m²/s and for molecular desorption $\nu = 10^6$ mol/m²/s [34].

Energy barriers for the first step of the mechanism are plotted in Figure 5. 13. This first step consists of dissociative adsorption and recombinative desorption of H₂ and their energy barriers are denoted as $\Delta E_{ads,H_2}^\ddagger$ and $\Delta E_{des,H_2}^\ddagger$, respectively. It was observed that the value of

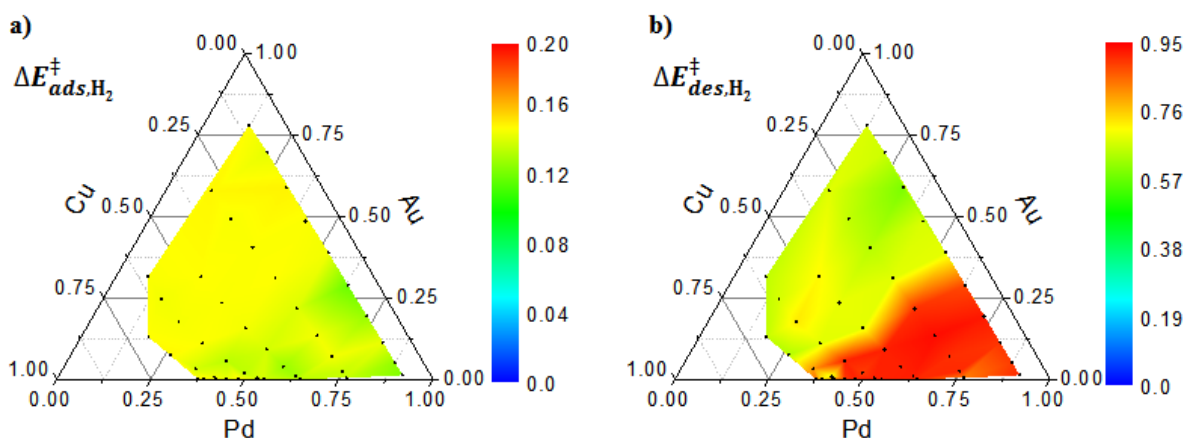


Figure 5. 13. a) Barriers for H₂ adsorption as a function of Cu_xAu_yPd_{1-x-y} alloy composition and b) Barriers for H₂ desorption as a function of Cu_xAu_yPd_{1-x-y} alloy composition.

$\Delta E_{ads,H_2}^\ddagger$ decreases and $\Delta E_{des,H_2}^\ddagger$ increases with increasing Pd content. The energetics of the elementary steps for C₂H₄ hydrogenation has usually been investigated in theoretical studies [35-37]. In one of those studies a first-principles-based dynamic Monte Carlo simulation method was used and the energy barriers for the elementary step in C₂H₄ hydrogenation mechanism was reported on pure Pd and two different AuPd binary alloys surfaces. For H₂ adsorption and desorption, barriers of 0.2 eV and 0.9 eV were reported, respectively [37]. Our desorption barriers are in good agreement with this study however we are calculating slightly lower adsorption barriers. In the same study, a decrease in $\Delta E_{des,H_2}^\ddagger$ was reported with increasing Au content in the alloy. We are also observing a similar pattern. In Figure 5. 13, $\Delta E_{des,H_2}^\ddagger$ is decreasing from ~0.9 eV to ~0.75 eV with increasing Cu and Au content in the alloy.

Energy barriers for C₂H₄ adsorption and desorption steps are plotted in Figure 5.14. C₂H₄ was reported to adsorb strongly on transition metal surfaces, especially on Pd and Pt both experimentally [38] and theoretically [39]. These studies showed that C₂H₄ bonds to Pd surface weaker than Pt surface. C₂H₄ adsorption barrier was reported to change in the range 0 – 0.3 eV in literature [40-43]. Our calculated $\Delta E_{ads,C_2H_4}^\ddagger$ values which are less than 0.2 eV across the CSAF is in good agreement with these studies. We calculated very low $\Delta E_{ads,C_2H_4}^\ddagger$ values especially on the Pd rich corner of the CSAF. Our experiments are carried out with excess H₂ and it is known that in a H₂-rich environment only π -bonded species are observed on Pd surfaces [38]. π -bonded species are very weakly bonded to the surface which can explain our low adsorption barriers. For C₂H₄ desorption, values in the range 0.3 – 0.9 eV were reported in literature [40-43]. We have calculated nearly flat desorption barrier which are approximately 0.4 eV. This number is again within the reported range. One interesting feature is that, $\Delta E_{des,C_2H_4}^\ddagger$ tends to decrease slightly with

increasing Pd content in the alloy. The relatively weak adsorption barriers of C₂H₄ on Pd may actually be promoting desorption.

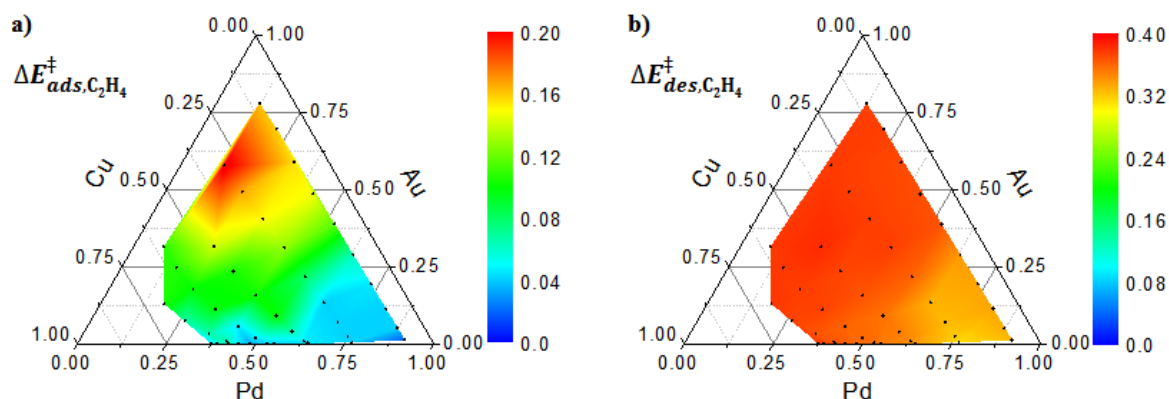


Figure 5.14. a) Barriers for C₂H₄ adsorption as a function of Cu_xAu_yPd_{1-x-y} alloy composition and b) Barriers for C₂H₄ desorption as a function of Cu_xAu_yPd_{1-x-y} alloy composition.

The comparison of Figure 5.13 and Figure 5.14 clearly states that calculated $\Delta E_{ads,H_2}^\ddagger$ is higher than $\Delta E_{ads,C_2H_4}^\ddagger$ when the Pd content is more than 20%. This result actually shows that H₂ plays an important role in C₂H₄ hydrogenation. Davis and Boudart suggests that H₂ adsorption was an irreversible and a possible rate limiting step in this reaction [44, 45]. In C₂H₄ mechanism, we cannot say that H₂ adsorption is the rate limiting step, however in order for the reaction to initiate H₂ adsorption step is putting a high energy barrier. The high barriers to H₂ adsorption is largely due to the difficulty to find two free sites that are adjacent to each other especially in the C-rich environments.

In Figure 5.15-a, the energy barrier for the first hydrogenation step, from C_2H_4 to C_2H_5 , is given. $\Delta E_{hyd,C_2H_4}^\ddagger$ was found to change in the range 0.2 – 0.4 eV across the $Cu_xAu_yPd_{1-x-y}$ CSAF. In Figure 5.15-b, the energy barrier for the decomposition of C_2H_5 is given. $\Delta E_{dis,C_2H_5}^\ddagger$ was found to vary in the range 0.23 – 0.33 eV. In the literature, on Pd $\Delta E_{hyd,C_2H_4}^\ddagger$ was reported to change in the range 0.4 – 0.88 eV and $\Delta E_{dis,C_2H_5}^\ddagger$ was reported to change in the range 0.3 – 0.75 eV [40-43]. Our values are comparable with those studies. In Figure 5.16, the energy barrier for the second hydrogenation step, from C_2H_5 to C_2H_6 , is given. $\Delta E_{hyd,C_2H_5}^\ddagger$ was found to be flat across the $Cu_xAu_yPd_{1-x-y}$ CSAF. It is calculated to be ~ 0.55 eV. Comparing the energetics of these two hydrogenation steps, tells us that ethyl hydrogenation step is the rate-limiting step for C_2H_4 hydrogenation reaction.

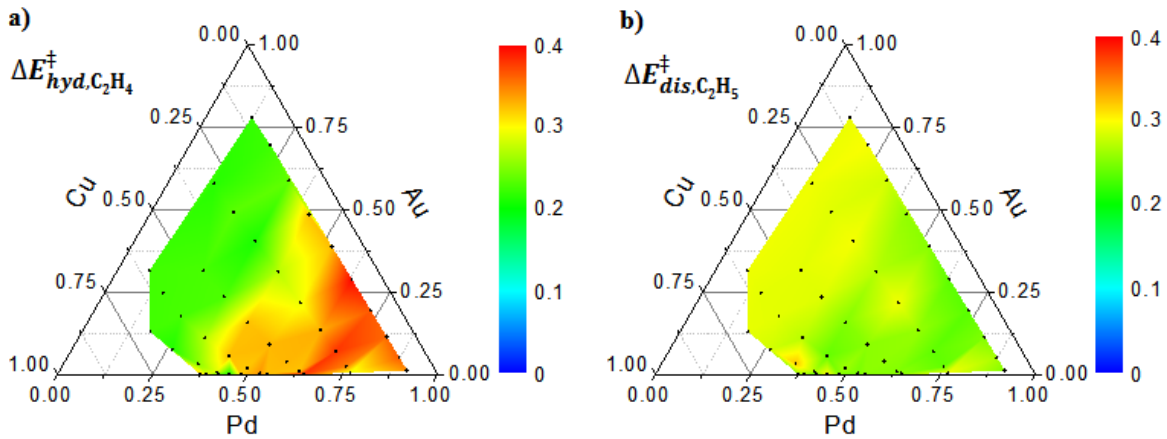


Figure 5.15. a) Barriers for C_2H_4 hydrogenation to C_2H_5 as a function of $Cu_xAu_yPd_{1-x-y}$ alloy composition and b) Barriers for C_2H_5 dissociation as a function of $Cu_xAu_yPd_{1-x-y}$ alloy composition.

For the first hydrogenation step, the barrier for the forward reaction was found to be slightly higher than the reverse reaction. This means ethyl is more likely to react back to form ethylene and hydrogen rather than continue on to hydrogenate and form ethane. So with this fact there occurs a hydrogen exchange cycle within the reaction pathway. Alloying Pd with Cu and Au, seems to be affecting the energetics of the forward reactions more than the reverse reactions. However when Pd content is more than 50%, usually flat energy barriers were calculated for all elementary steps. This result is in good agreement with the activity plot that we have obtained (**Error! Reference source not found.**). It is known that as Cu or Au surface composition is increased, the hydrogen binding energy decreases [37]. Lower binding energy means greater reactivity. Alloying Pd with Cu and Au on the other hand, decreases the surface coverage of hydrogen because it is known that H₂ does not have high affinity to adsorb on Cu and/or Au [46-52]. So these two kinetic factors compensate for each other and keep the activity more or less the same while alloying Pd with Cu and/or Au.

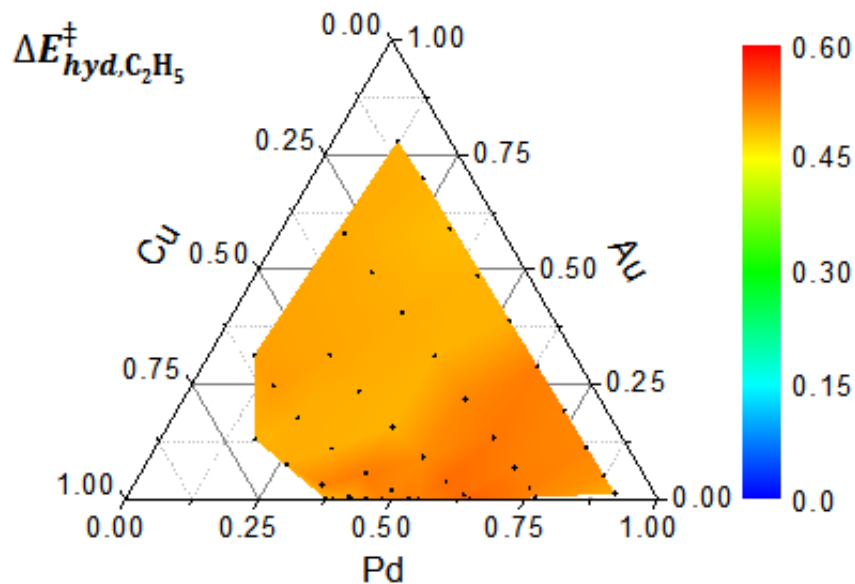


Figure 5.16. Barriers for C₂H₅ hydrogenation to C₂H₆ as a function of Cu_xAu_yPd_{1-x-y} alloy composition.

5.5.5 Correlation of activity and electronic structure across Composition Space

One of the goals of this study has been to correlate fundamental kinetic parameters for catalytic C_2H_4 hydrogenation reaction over $Cu_xAu_yPd_{1-x-y}$ alloys with characteristics of their electronic structure. Computationally this can be achieved using DFT for various catalytic processes by correlating the calculated mean energy of the d -band, ε_d , of various metals with the calculated barriers, ΔE^\ddagger , to elementary reaction steps on their surfaces [53-56]. In this work, we have used UP spectra from a $Cu_xAu_yPd_{1-x-y}$ CSAF to measure the energy of the filled valence band center, $\varepsilon_v(x)$, and microkinetic modeling to calculate the ΔE_i^\ddagger for C_2H_4 hydrogenation reaction.

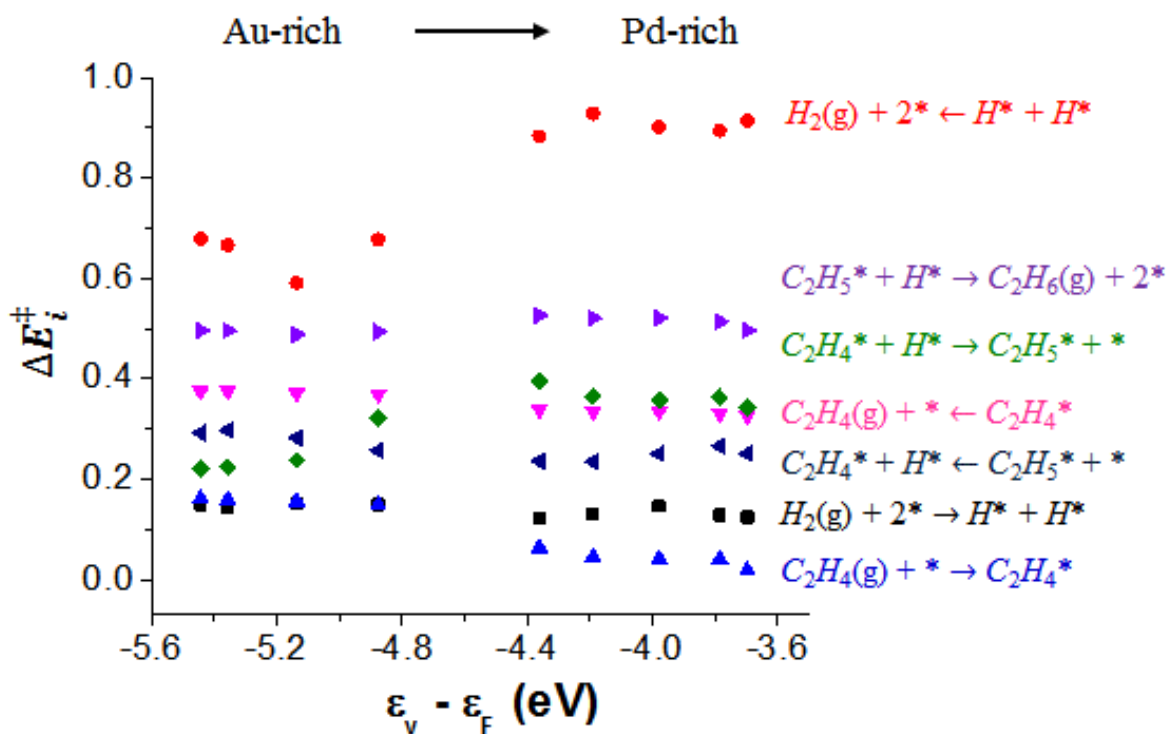


Figure 5.17. Energy barriers for all 7 elementary steps in the C_2H_4 hydrogenation mechanism, $\Delta E_i^\ddagger(x, y)$, as a function of v -band center energy measured across nine different alloy compositions across the $Cu_xAu_yPd_{1-x-y}$ CSAF. The corresponding elementary reaction is labeled next to each dataset.

The correlation between these parameters are plotted in Figure 5.17 for different $\text{Cu}_x\text{Au}_y\text{Pd}_{1-x-y}$ alloy compositions. For the sake of clear explanation, only 9 alloy compositions have been picked which have almost constant Cu content (8.5 ± 1 at.%) and changing Au (from 78 at.% to 1 at.%) and Pd (from 91 at.% to 12 at.%) content. For all the alloy compositions, the data is given in the Appendix. The calculated energy barriers for H_2 adsorption reaction ($\text{H}_2(\text{g}) + 2^* \rightarrow \text{H}^* + \text{H}^*$) was found to decrease slightly as ϵ_v shifts toward the Fermi level. However the energy barriers for H_2 desorption reaction ($\text{H}^* + \text{H}^* \rightarrow \text{H}_2(\text{g}) + 2^*$) was observed to increase. This is also the direction of increasing Pd content, and it is known that H atoms are more mobile on Pd. So as ϵ_v shifts toward the Fermi level, H atoms tend to engage in hydrogenation reaction instead of desorbing from the surface.

When the correlation between C_2H_4 adsorption and desorption barriers with ϵ_v was observed, it can be seen that the barrier to C_2H_4 desorption is independent of ϵ_v (pink data points in Figure 5.17). The barriers to C_2H_4 adsorption was found to decrease slightly as ϵ_v shifts toward the Fermi level. This can be explained with the increased mobility of H atoms on Pd-rich surfaces which opens active sites for C_2H_4 to adsorb slightly easier than on Cu- and Au-rich surfaces. Actually, alloying Pd with Cu and/or Au decrease the strength of metal-hydrogen and metal-carbon bonds, so one may expect to see a decrease in adsorption barriers as the Au content increases in the alloy (as ϵ_v moves further away from the Fermi level in Figure 5.17). We observed the opposite trend since Au addition is actually shutting down sites for H_2 adsorption.

For the hydrogenation steps first hydrogenation step where C_2H_4 is hydrogenated to C_2H_6 , the energy barrier was found to increase as ϵ_v shifts toward the Fermi level. And for the second hydrogenation step where C_2H_6 is produced, the energy barriers were found to be independent of ϵ_v . These observations are consistent with the discussion above. And it should be mentioned

that similar patterns were observed when Au content was kept constant and Cu and Pd contents were varied.

With these results, we were able to show that our high throughput methodology can be successfully applied to alkene hydrogenation reactions. Using this methodology, we were able to correlate the fundamental kinetic parameters for the C₂H₄ hydrogenation reaction with the electronic structure of the Cu_xAu_yPd_{1-x-y} ternary alloy catalyst across a wide composition range.

5.6 Conclusions

In this study, the catalytic C₂H₄ hydrogenation reaction was investigated across Cu_xAu_yPd_{1-x-y} composition space by using high throughput methodology. A materials library spanning Cu_xAu_yPd_{1-x-y} composition space from $x = 0 \rightarrow 1$ and $y = 0 \rightarrow 1-x$ was prepared using the rotatable shadow mask deposition tool, as explained in Section 2.2.1.2. The characterization of composition and electronic structure across the CSAF was done using XPS. Also catalytic reactivity at 100 discrete positions (100 different alloy compositions) across the CSAF was measured using the multichannel microreactor array, as described in Section 2.2.2. Coupling spatially resolved characterization techniques and the high throughput reaction system, composition – catalytic activity – electronic structure correlation for Cu-Au-Pd alloys has been investigated across a continuous composition space. We found that the activity increased with increasing Pd at.%. It was also found that alloying Pd with up to 50 at.% Cu and/or Au gives similar catalytic activities as pure Pd. Microkinetic analysis of the reaction showed that the C₂H₄ hydrogenation reaction was limited by the ethyl hydrogenation reaction. Obtained v-band spectra showed that the v-band center moved closer to the Fermi level with increasing Pd content in the alloy. With the correlation between the kinetic parameters and electronic structure, i.e. ΔE_i^\ddagger vs ϵ_v ,

it was observed that C_2H_4 adsorption barrier decreases more than H_2 adsorption barrier as the v -band center moved closer to the Fermi level. Energy barriers for ethyl hydrogenation step was found to be independent of the v -band center. With these results we were able to show that we have successfully developed a high throughput methodology that can be applied to catalysis studies. Using this technique, we were able to correlate the fundamental kinetic parameters for the C_2H_4 hydrogenation reaction with electronic structures of the ternary alloy catalysts across the entire composition range.

5.7 Appendix: Correlation of activity and electronic structure across composition space

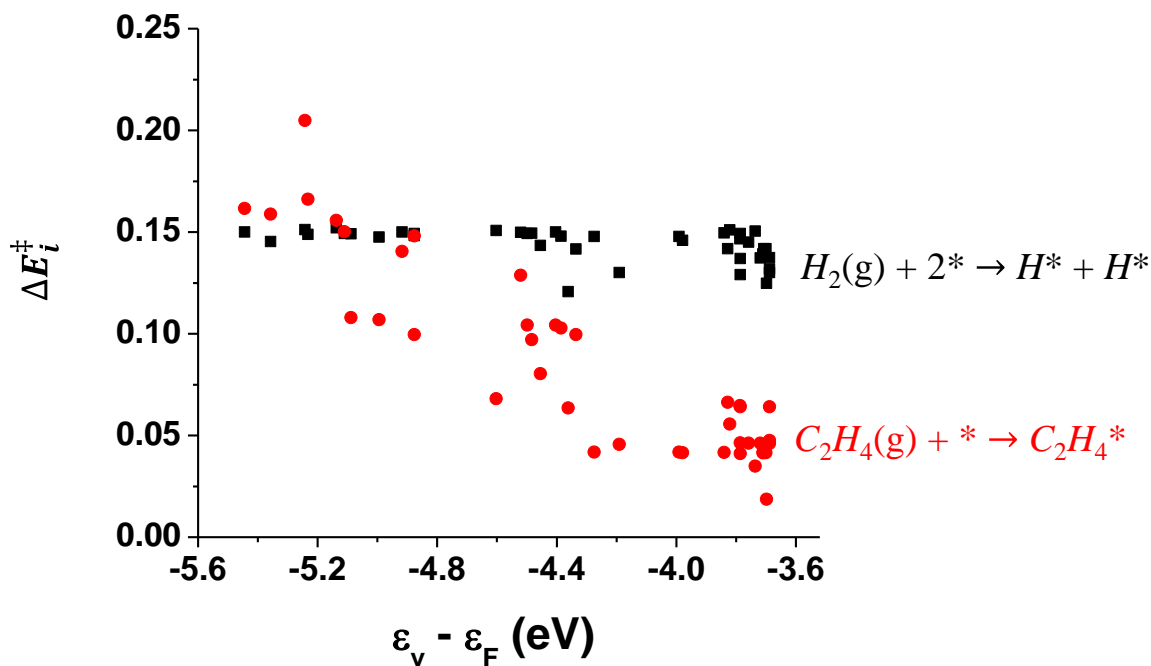


Figure 5. 18. Energy barriers for H_2 and C_2H_4 adsorption steps in the C_2H_4 hydrogenation mechanism, $\Delta E_i^\ddagger(x, y)$, as a function of v -band center energy measured across the $Cu_xAu_yPd_{1-x-y}$ CSAF. The corresponding elementary reaction is labeled next to each dataset.

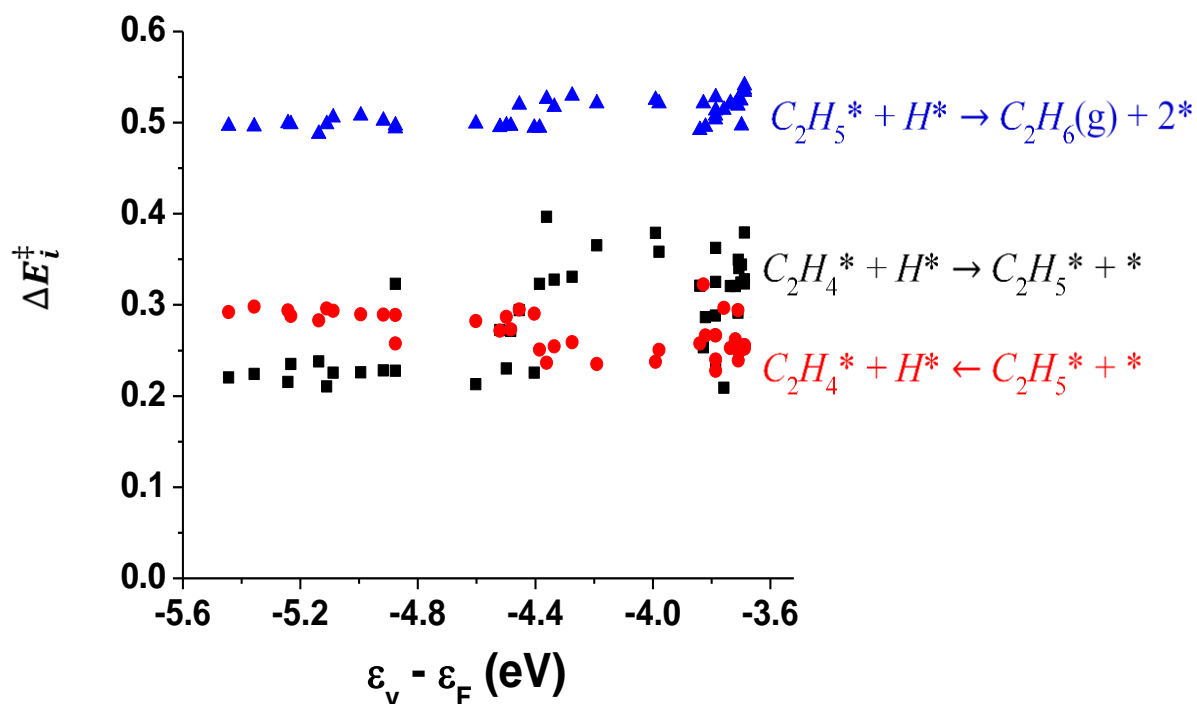


Figure 5. 19. Energy barriers for two successive hydrogenation steps in the C_2H_4 hydrogenation mechanism, $\Delta E_i^\ddagger(x, y)$, as a function of ν -band center energy measured across the $Cu_xAu_yPd_{1-x-y}$ CSAF. The corresponding elementary reaction is labeled next to each dataset.

5.8 References

1. Bond, G.C., et al., *Hydrogenation of olefins. Part 1.-Hydrogenation of ethylene, propylene and the n-butenes over alumina-supported platinum and iridium*. Transactions of the Faraday Society, 1964. **60**(0): p. 1847-1864.
2. Beeck, O., *Hydrogenation catalysts*. Discussions of the Faraday Society, 1950. **8**(0): p. 118-128.
3. Cremer, P.S. and G.A. Somorjai, *Surface science and catalysis of ethylene hydrogenation*. Journal of the Chemical Society, Faraday Transactions, 1995. **91**(20): p. 3671-3677.
4. Zaera, F. and G.A. Somorjai, *Hydrogenation of ethylene over platinum (111) single-crystal surfaces*. Journal of the American Chemical Society, 1984. **106**(8): p. 2288-2293.
5. Cortright, R.D., et al., *Kinetic study of ethylene hydrogenation*. Journal of Catalysis, 1991. **127**(1): p. 342-353.

6. Goddard, S.A., R.D. Cortright, and J.A. Dumesic, *Deuterium tracing studies and microkinetic analysis of ethylene hydrogenation over platinum*. Journal of Catalysis, 1992. **137**(1): p. 186-198.
7. Rekoske, J.E., et al., *Microkinetic analysis of diverse experimental data for ethylene hydrogenation on platinum*. The Journal of Physical Chemistry, 1992. **96**(4): p. 1880-1888.
8. Tysoe, W.T., G.L. Nyberg, and R.M. Lambert, *Structural, kinetic, and reactive properties of the palladium(111)-ethylene system*. The Journal of Physical Chemistry, 1984. **88**(10): p. 1960-1963.
9. Stuve, E.M. and R.J. Madix, *Bonding and dehydrogenation of ethylene on palladium metal. Vibrational spectra and temperature-programmed reaction studies on palladium(100)*. The Journal of Physical Chemistry, 1985. **89**(1): p. 105-112.
10. Yoshio, T., S. Tadashi, and M. Yoshiharu, *HYDROGENATION OF ETHYLENE ON SMALL PALLADIUM PARTICLES*. Chemistry Letters, 1985. **14**(8): p. 1179-1182.
11. Bond, G.C., *The reaction of ethylene with deuterium over various types of platinum catalyst*. Transactions of the Faraday Society, 1956. **52**(0): p. 1235-1244.
12. Dorling, T.A., M.J. Eastlake, and R.L. Moss, *The structure and activity of supported metal catalysts: IV. Ethylene hydrogenation on platinum/silica catalysts*. Journal of Catalysis, 1969. **14**(1): p. 23-33.
13. Schlatter, J.C. and M. Boudart, *Hydrogenation of ethylene on supported platinum*. Journal of Catalysis, 1972. **24**(3): p. 482-492.
14. Horiuti, J. and K. Miyahara, *Hydrogenation of ethylene on metallic catalysts*. 1968: US Department of Commerce, National Bureau of Standards.
15. Sinfelt, J.H., *Kinetics of Ethylene Hydrogenation over a Platinum—Silica Catalyst*. The Journal of Physical Chemistry, 1964. **68**(4): p. 856-860.
16. Schuit, G.C.A. and L.L. Van Reijen, *The Structure and Activity of Metal-on-Silica Catalysts*, in *Advances in Catalysis*, D.D. Eley, et al., Editors. 1958, Academic Press. p. 242-317.
17. Sato S., M.K., *Reaction Structure of Ethylene Hydrogenation on metallic Catalysts: Part I- The Reaction on Evaporated Copper Film*. Journal of the Research Institute for Catalysis Hokkaido University, 1975. **22**(1): p. 51-62.
18. Molero, H., D. Stacchiola, and W.T. Tysoe, *The kinetics of ethylene hydrogenation catalyzed by metallic palladium*. Catalysis Letters, 2005. **101**(3): p. 145-149.
19. Beebe, T.P. and J.T. Yates, *An in situ infrared spectroscopic investigation of the role of ethylidyne in the ethylene hydrogenation reaction on palladium/alumina*. Journal of the American Chemical Society, 1986. **108**(4): p. 663-671.
20. Horiuti, I. and M. Polanyi, *Exchange reactions of hydrogen on metallic catalysts*. Transactions of the Faraday Society, 1934. **30**(0): p. 1164-1172.

21. Mark Ormerod, R., C.J. Baddeley, and R.M. Lambert, *Geometrical and electronic effects in the conversion of acetylene to benzene on Au(111)/Pd and Au/Pd surface alloys*. Surface Science Letters, 1991. **259**(1): p. L709-L713.
22. Baddeley, C.J., et al., *Surface Structure and Reactivity in the Cyclization of Acetylene to Benzene with Pd Overlayers and Pd/Au Surface Alloys on Au{111}*. The Journal of Physical Chemistry, 1995. **99**(14): p. 5146-5151.
23. Lee, A.F., et al., *Structure–Reactivity Correlations in the Catalytic Coupling of Ethyne over Novel Bimetallic Pd/Sn Catalysts*. The Journal of Physical Chemistry B, 1997. **101**(15): p. 2797-2805.
24. R. J. Davis, M.B., *Catalysis Science and Technology* 1991. **1**(129).
25. Guzzi, L., et al., *Acetylene hydrogenation selectivity control using Pd/Cu catalysts*. Reaction Kinetics and Catalysis Letters, 1985. **27**(1): p. 147-151.
26. Pei, G.X., et al., *Performance of Cu-Alloyed Pd Single-Atom Catalyst for Semihydrogenation of Acetylene under Simulated Front-End Conditions*. ACS Catalysis, 2017. **7**(2): p. 1491-1500.
27. Fleutot, B., J.B. Miller, and A.J. Gellman, *Apparatus for deposition of composition spread alloy films: The rotatable shadow mask*. Journal of Vacuum Science & Technology A: Vacuum, Surfaces, and Films, 2012. **30**(6): p. 061511.
28. Wei, T., J. Wang, and D.W. Goodman, *Characterization and Chemical Properties of Pd–Au Alloy Surfaces†*. The Journal of Physical Chemistry C, 2007. **111**(25): p. 8781-8788.
29. Priyadarshini, D., et al., *High-Throughput Characterization of Surface Segregation in CuxPd1–x Alloys*. The Journal of Physical Chemistry C, 2011. **115**(20): p. 10155-10163.
30. He, J.W., et al., *Surface chemistry of monolayer metallic films on Re(0001) and Mo(110)*. Journal of Vacuum Science & Technology A, 1990. **8**(3): p. 2435-2444.
31. Park, C., E. Bauer, and H. Poppa, *Growth and alloying of Pd films on Mo(110) surfaces*. Surface Science, 1985. **154**(2): p. 371-393.
32. *NIST Chemistry WebBook*. . 2011; Available from: <http://webbook.nist.gov/chemistry/>.
33. Payne, M.A., J.B. Miller, and A.J. Gellman, *High-throughput characterization of early oxidation across AlxFeyNi1–x–y composition space*. Corrosion Science, 2015. **91**(Supplement C): p. 46-57.
34. James, A.D., *The Microkinetics of heterogeneous catalysis*. 1993: Washington, DC : American Chemical Society, 1993.
35. Neurock, M. and D. Mei, *Effects of Alloying Pd and Au on the Hydrogenation of Ethylene: An ab initio-Based Dynamic Monte Carlo Study*. Topics in Catalysis, 2002. **20**(1): p. 5-23.
36. Mei, D., et al., *First-principles-based kinetic Monte Carlo simulation of the selective hydrogenation of acetylene over Pd(111)*. Journal of Catalysis, 2006. **242**(1): p. 1-15.

37. Mei, D., E.W. Hansen, and M. Neurock, *Ethylene Hydrogenation over Bimetallic Pd/Au(111) Surfaces: Application of Quantum Chemical Results and Dynamic Monte Carlo Simulation*. The Journal of Physical Chemistry B, 2003. **107**(3): p. 798-810.
38. Stacchiola, D., L. Burkholder, and W.T. Tysoe, *Ethylene adsorption on Pd(111) studied using infrared reflection-absorption spectroscopy*. Surface Science, 2002. **511**(1): p. 215-228.
39. Bernardo, C.G.P.M. and J.A.N.F. Gomes, *The adsorption of ethylene on the (100) surfaces of platinum, palladium and nickel: a DFT study*. Journal of Molecular Structure: THEOCHEM, 2001. **542**(1): p. 263-271.
40. Masi, M., et al., *Kinetics of ethylene hydrogenation on supported platinum. Analysis of multiplicity and nonuniformly active catalyst particle behavior*. Chemical Engineering Science, 1988. **43**(8): p. 1849-1854.
41. Zaera, F., *On the Mechanism for the Hydrogenation of Olefins on Transition-Metal Surfaces: The Chemistry of Ethylene on Pt(111)*. Langmuir, 1996. **12**(1): p. 88-94.
42. Godbey, D., et al., *Hydrogenation of chemisorbed ethylene on clean, hydrogen, and ethylidyne covered platinum (111) crystal surfaces*. Surface Science, 1986. **167**(1): p. 150-166.
43. Hirschl, R., A. Eichler, and J. Hafner, *Hydrogenation of ethylene and formaldehyde on Pt (111) and Pt80Fe20 (111): a density-functional study*. Journal of Catalysis, 2004. **226**(2): p. 273-282.
44. Boudart, M., et al., *Kinetics of Heterogeneous Catalytic Reactions*. 1984: Princeton University Press.
45. Davis, R.J., *Ph.D. Thesis*. 1989, Stanford University.
46. Iwao, Y., M. Naohiro, and K. Makoto, *Mechanism of Hydrogen Adsorption and Hydrogen-Deuterium Equilibration on Copper Surface*. Japanese Journal of Applied Physics, 1974. **13**(S2): p. 485.
47. Alexander, C.S. and J. Pritchard, *Chemisorption of hydrogen on evaporated copper films*. Journal of the Chemical Society, Faraday Transactions 1: Physical Chemistry in Condensed Phases, 1972. **68**(0): p. 202-215.
48. Mudiyansele, K., et al., *Adsorption of hydrogen on the surface and sub-surface of Cu(111)*. The Journal of Chemical Physics, 2013. **139**(4): p. 044712.
49. Sakong, S. and A. Groß, *Dissociative adsorption of hydrogen on strained Cu surfaces*. Surface Science, 2003. **525**(1): p. 107-118.
50. Wang, Z.S., G.R. Darling, and S. Holloway, *The surface temperature dependence of the inelastic scattering and dissociation of hydrogen molecules from metal surfaces*. The Journal of Chemical Physics, 2004. **120**(6): p. 2923-2933.
51. Hammer, B. and J.K. Nørskov, *Electronic factors determining the reactivity of metal surfaces*. Surface Science, 1995. **343**(3): p. 211-220.

52. Abbott, H.L. and I. Harrison, *Microcanonical Transition State Theory for Activated Gas–Surface Reaction Dynamics: Application to H₂/Cu(111) with Rotation as a Spectator*. The Journal of Physical Chemistry A, 2007. **111**(39): p. 9871-9883.
53. Hammer, B., Y. Morikawa, and J.K. Nørskov, *CO chemisorption at metal surfaces and overlayers*. Phys Rev Lett, 1996. **76**(12): p. 2141-2144.
54. Hammer, B. and J.K. Nørskov, *Why gold is the noblest of all the metals*. Nature, 1995. **376**(6537): p. 238-240.
55. Hammer, B. and J.K. Nørskov, *Theoretical surface science and catalysis—calculations and concepts*, in *Advances in Catalysis*. 2000, Academic Press. p. 71-129.
56. Hammer, B. and J.K. Nørskov, *Theoretical surface science and catalysis—calculations and concepts*. Advances in catalysis, 2000. **45**: p. 71-129.

CHAPTER 6

General Conclusions

In this thesis we have developed a high throughput methodology that can be used in alloy catalysis studies. We have tested the performance of H₂-D₂ exchange reaction and C₂H₄ hydrogenation reaction across binary and ternary alloy libraries using a 100-channel microreactor array. With this method, we have collected a substantial amount of data at different temperatures and reactant partial pressures which led us calculate the fundamental kinetic parameters using the microkinetic models for each reaction.

We have focused on Pd-based alloys and prepared Ag_xPd_{1-x} binary and Cu_xAu_yPd_{1-x-y} ternary CSAFs using a rotatable shadow mask deposition tool. Spatially resolved X-ray photoelectron spectroscopy (XPS) was used to characterize the composition and electronic structure (ν -band center) across these CSAFs. Reactivity measurements were performed using the multichannel microreactor array that we have developed in our laboratory. During the course of this work, the multichannel microreactor array has been improved by changing the structure of the micromachined channels. The data collected has been fit to the microkinetic model and the energy barriers for each of the elementary steps in two different reactions were calculated as a function of alloy composition. These kinetic parameters were then correlated to the electronic structure data obtained from XPS.

For the H₂-D₂ exchange reaction, activity was found to increase with temperature and Pd content in the alloy for all compositions across both Ag_xPd_{1-x} and Cu_xAu_yPd_{1-x-y} CSAFs. On Ag_xPd_{1-x} CSAF, microkinetic analysis of the reaction showed that the H₂-D₂ exchange reaction

was limited by the rate of adsorption below 30 at. % Pd and desorption limited above that value. Obtained ν -band spectra showed that the ν -band center moved closer to the Fermi level with increasing Pd content in the alloy. With the correlation between the kinetic parameters and electronic structure, i.e. ΔE_{ads}^\ddagger and ΔE_{des}^\ddagger vs ϵ_ν , it was observed that both adsorption and desorption barriers decreased as the ν -band center moved closer to the Fermi level. With these results we were able to show that we have successfully developed a high throughput methodology that can be applied to catalysis studies. Using this technique, we were able to correlate the fundamental kinetic parameters for the H₂-D₂ exchange reaction with electronic structure of the binary alloy catalyst across the entire composition range.

On Cu_xAu_yPd_{1-x-y} CSAFs, microkinetic analysis of the reaction showed that the H₂-D₂ exchange reaction was limited by the rate of desorption across the CSAF, except where Pd content is less than ~15 at.%. Obtained ν -band spectra showed that ν -band center moved closer to the Fermi level with increasing Pd content in the alloy. When correlating kinetic parameters and electronic structure, i.e. ΔE_{ads}^\ddagger and ΔE_{des}^\ddagger vs ϵ_ν , it was observed that both adsorption and desorption barriers decrease as ν -band center changes from -5.5 eV to -4.5 eV. At the Fermi level, both ΔE_{ads}^\ddagger and ΔE_{des}^\ddagger were found to be independent of the ν -band center of the alloy. These results proved that we have successfully study reaction kinetics across ternary alloy libraries. It was found that the alloys containing approximately 50 at. % Pd exhibit similar adsorption and desorption barriers compared to pure Pd.

Through the experiments conducted in a multichannel microreactor array, kinetic parameter estimations of ethylene hydrogenation reaction on Cu_xAu_yPd_{1-x-y} CSAFs have been done successfully. We have provided kinetic data for about 50 compositions in the ternary portion of

the CSAF. At least two different samples of ternary CSAFs were tested in order to ensure that the expected composition range is scanned successfully. The 100 reactant streams consisting of C_2H_4 and H_2 balanced with Ar was identical to achieve a total pressure of 1 atm. The temperature range was kept to be between 295 and 433 K. Partial pressures of C_2H_4 and H_2 were varied to obtain comprehensive kinetic data. Steady state rate of C_2H_6 production was measured at low conversions. The obtained rate data over each of the CSAF was expressed as a function of $P_{C_2H_4}$, P_{H_2} , T , x and y . The energy barriers for each of the seven elementary steps in the mechanism was calculated by fitting the extensive experimental data into the microkinetic model. Using XPS, ν -band centers were calculated for each of the alloy compositions. So that, the correlation between the kinetic parameters, alloy composition and electronic structure has been done across the continuous composition space.

Starting from the simplest case, H_2 - D_2 exchange across binary alloy catalysts, and moving to a more complex system, C_2H_4 hydrogenation across $Cu_xAu_yPd_{1-x-y}$, we have validated the high throughput methodology that we have developed can be applied to other alloys and gas phase reactions to construct alloy composition-catalytic activity-alloy electronic structure relationship.

References

References are listed at the end of each chapter. Page numbers are listed below for convenience.

Chapter 1 p. 16

Chapter 2 p. 41

Chapter 3 p.81

Chapter 4 p. 123

Chapter 5 p. 163